At the beginning of 21th century, the range of solid state materials was extended by crystals featuring charge excitations with a chiral spin or pseudo-spin texture close to the Fermi energy. Such exceptional electronic properties can be found in graphene or topological insulators, which both render a great potential for upcoming electronic devices.

In this thesis, mesoscopic systems of such solid state materials are investigated by a time-dependent scheme, which describes the electronic excitations by the propagation of wave packets. Based on the time evolution of initial states dynamical and static observables are studied and new electronic phenomena are revealed. For example, the motion of electrons in graphene or topological insulators exhibit time-dependent features like Bloch-Zener oscillations or wave-packet revivals, which are not present in conventional electron gases. Also static properties, like transport characteristics, are encoded in the time evolution. For instance, the switching features of a topological insulator constriction can be extracted from a single wave-packet injected into a lead. The underlying effect builds the foundation of a novel charge and spin-transistor, which is presented in this thesis alongside other proposals for novel experiments in graphene or topological insulators.

Universitätsverlag Regensburg

a

ISBN 978-3-86845-097-2

gefördert von:

Alumni der physikalischen Fakultät der Universität Regensburg e.V.

Universität Regensburg

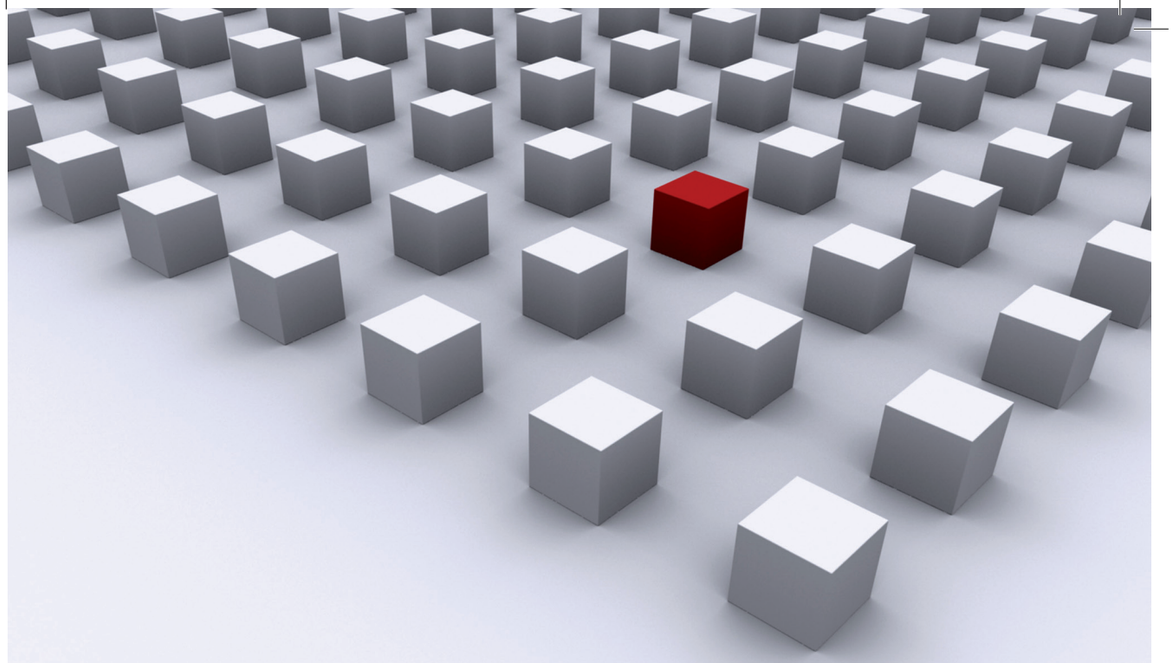

Viktor Krückl

Wave packets in mesoscopic systems:

From time-dependent dynamics to transport phenomena in graphene and topological insulators

Universitätsverlag Regensburg

Dissertationsreihe Physik - Band 31

Viktor Krückl

31

Dissertationsreihe Physik

Viktor Krückl

Wave packets in mesoscopic systems: From time-dependent dynamics to transport phenomena in graphene and topological insulators

Wave packets in mesoscopic systems: From time-dependent dynamics to transport phenomena in graphene and topological insulators

Dissertation zur Erlangung des Doktorgrades der Naturwissenschaften (Dr. rer. nat.)
der Fakultät für Physik der Universität Regensburg
vorgelegt von

Viktor Krückl
Regensburg
2012

Die Arbeit wurde von Prof. Dr. Klaus Richter angeleitet.
Das Promotionsgesuch wurde am 18.05.2012 eingereicht.
Das Promotionskolloquium fand am 18.03.2013 statt.

Prüfungsausschuss:

Vorsitzende:	Prof. Dr. Christoph Strunk
1. Gutachter:	Prof. Dr. Klaus Richter
2. Gutachter:	Prof. Dr. John Schliemann
weiterer Prüfer:	Prof. Dr. Andreas Schäfer

Dissertationsreihe der Fakultät für Physik der Universität Regensburg, Band 31

Herausgegeben vom Präsidium des Alumnivereins der Physikalischen Fakultät:
Klaus Richter, Andreas Schäfer, Werner Wegscheider, Dieter Weiss

Viktor Krückl

Wave packets in mesoscopic systems: From time-dependent dynamics to transport phenomena in graphene and topological insulators

Universitätsverlag Regensburg

Bibliografische Informationen der Deutschen Bibliothek.
Die Deutsche Bibliothek verzeichnet diese Publikation
in der Deutschen Nationalbibliografie. Detailierte bibliografische Daten
sind im Internet über http://dnb.ddb.de abrufbar.

1. Auflage 2013

Leibnizstraße 13, 93055 Regensburg

Konzeption: Thomas Geiger
Umschlagentwurf: Franz Stadler, Designcooperative Nittenau eG
Layout: Viktor Krückl
Druck: Docupoint, Magdeburg
ISBN: 978-3-86845-097-2

Weitere Informationen zum Verlagsprogramm erhalten Sie unter:
www.univerlag-regensburg.de

Wave packets in mesoscopic systems: From time-dependent dynamics to transport phenomena in graphene and topological insulators

Dissertation

zur Erlangung des Doktorgrades
der Naturwissenschaften (Dr. rer. nat.)
der Fakultät für Physik
der Universität Regensburg

vorgelegt von
Viktor Krückl
aus
Regensburg

im Jahr 2012

Die Arbeit wurde von Prof. Dr. Klaus Richter angeleitet.
Das Promotionsgesuch wurde am 18.05.2012 eingereicht.
Das Kolloquium fand am 18.03.2013 statt.

Prüfungsausschuss:	Vorsitzender	Prof. Dr. Christoph Strunk
	1. Gutachter:	Prof. Dr. Klaus Richter
	2. Gutachter:	Prof. Dr. John Schliemann
	weiterer Prüfer:	Prof. Dr. Andreas Schäfer

Contents

1 Introduction

The topics treated in this thesis can be subdivided into two parts according to the investigated material systems: "Graphene" and "Topological Insulators". Even though both material classes appear quite disconnected at first glance, they share several common characteristics. First of all, both of them represent very recent developments in the field of solid state physics. Although the earliest chemical preparation of few-layer graphene flakes dates back to 1962 [1] the first transport measurement based on a single graphene layer has only recently been established by the group of Geim in the year 2005 [2]. They found that a sheet of carbon atoms with a thickness of only one atomic layer can be isolated from a carbon crystal by a technique known as the 'Scotch® Tape Method' [3], which uses a conventional sticky tape to cleave off a single carbon layer from a bulk piece of graphite. This triggered various subsequent investigations and finally culminated in the awarding of the Nobel prize only five years later. The history of topological insulators is equally short and started in 2005 with the theoretical prediction of a novel quantized transport phenomenon in graphene, the so-called quantum spin Hall effect [4]. In contrast to the conventional quantum Hall effect, the conductance quantization already appears without an external magnetic field and is induced by the effective magnetic field given by the spin-orbit interaction.

The most significant similarity between graphene and topological insulators is based on their fundamental electronic properties. It has been found that due to the special lattice structure of graphene the low energy excitations of the charge carriers close to the Fermi level can be described by the Dirac equation, rather than the Schrödinger equation, which is conventionally used for electrons in solid state systems [5]. Since the Dirac equation for pristine graphene does not contain a mass term, no gap appears between electron and hole states and the type of charge carriers can easily be tuned between p-type and n-type via external gating [3]. In presence of a perpendicular magnetic field the Dirac nature of the electrons induces an anomalous Landau level structure with a peculiar square-root dependence compared to the equidistant level

spacing of conventional electron gases. It was this special Landau level structure, which served as the smoking gun experiment to verify the Dirac nature of charge carriers in graphene [2]. Graphene is also interesting for future applications due to its special physical properties. Owing to the high carrier mobility and saturation velocity of graphene it is a suitable material for high frequency electronic devices like radio-frequency transistors [6, 7].[1] Furthermore, graphene is only one layer of atoms thin and in this way transparent, but still mechanically very strong and flexible. This makes it possible to use graphene as transparent conducting electrode perfectly suited, for example, in organic light-emitting diodes [8, 9] and other optoelectronic devices [10].

The birth of topological insulators is strongly connected to graphene, since the first proposed topological insulator was based on graphene with strong spin-orbit interaction. The interplay of the Dirac nature of the charge carriers and the spin-orbit coupling leads to a new quantum state [4], manifesting itself in the aforementioned quantum spin Hall effect [11]. Topological insulators appear in two and three dimensions and feature conducting surface states at the boundaries of an insulating bulk crystal. These surface states arise if the ordering of the bands close to the band gap of the bulk insulator is inverted, which corresponds to an interchange of the electron-hole character between the valence and the conduction bands. However, the strength of the spin-orbit interaction and the associated band gap in graphene is not sufficiently strong to induce an experimentally accessible quantized current at reasonable temperatures. This created a new field of research, which is dedicated to the classification of materials with respect to their capabilities as topological insulators [12]. Furthermore, the appearance of such a new state of matter also triggered various fundamental investigations searching for further implications and possible applications, like spintronic devices or elements for quantum computation. In the year 2006, the first theoretical proposal for a promising two-dimensional topological insulator was based on a heterostructure of the material mercury telluride [13]. Only one year later, the presence of the topological insulator phase of this heterostructure was verified by the measurement of the quantum spin Hall effect [14]. For this two dimensional system the inverted electronic band structure of the quantum well leads to the formation of two spin-polarized edge states, which are protected from backscattering and can be described by a one-dimensional Dirac equation, as we will show in the following.

In this thesis we employ these two material systems and search for additional effects arising from the Dirac nature of the charge carriers. On the one side, we focus on time-dependent phenomena. Therefore, we have developed a rather general numerical framework to calculate the time-evolution of wave-packets governed by a wide class of Hamilton operators ranging from atomistic graphene over conventional electron-hole gases to topological insulators. This enables us to investigate dynamical effects like the revivals of wave packets, the Bloch oscillations in periodic potentials or the response of charge carries on external laser pulses. On the other side, besides these dynamical effects, we also consider static properties which are extracted from the time-evolution

[1] However, due to the lack of a band gap, the on-off ratio of graphene transistors is very low and a replacement of conventional Si transistors for logic operations appears not feasible.

of wave packets. We have developed a scheme that allows us to calculate observables like the density of states or the scattering matrix of mesoscopic systems. Using this framework, we have studied the weak localization signatures in diffusive transport and proposed a novel spin transistor based on HgTe constrictions.

In what follows, we will provide a brief outline of the different subjects treated in every single chapter of this thesis.

I. Graphene 7

In the first part, we study exceptional time-dependent phenomena in the two-dimensional semiconductor graphene.

2. Introduction to Graphene 9

We start with an introduction to the electronic structure of graphene based on an atomistic tight-binding Hamiltonian and introduce the low energy approximation used in this thesis. Furthermore, we derive the Landau level quantization of graphene in a perpendicular magnetic field and the corresponding eigenstates needed for the initial wave-packets in the following chapter.

3. Wave-Packet Revivals 17

This chapter is dedicated to the time-evolution of wave packets on a sheet of graphene in a perpendicular magnetic field. We reveal that an initially localized wave packet undergoes peculiar revival dynamics, attributable to the anomalous Landau level formation of graphene [15]. The effect is present in the center-of-mass motion as well as in the autocorrelation function and survives long-range impurity potentials. For experimental detection we propose a four-wave mixing scheme, which excites an initial state at the Fermi level by means of a single cycle laser pulse into a highly excited Landau level and probes the time evolution by a second time-delayed pulse.

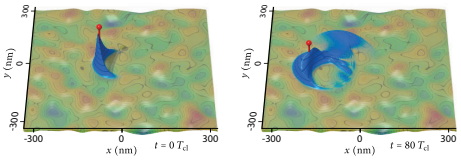

Revival on an impurity potential – The initial state as well as the state after 80 cyclotron orbits is localized, while the intermediate wave-packet is circularly distributed, as shown in more detail in Fig. 3.11.

4. Wave-Packet Transport Theory 47

In order to calculate the electronic properties of mesoscopic structures, we have developed a time-dependent scheme, which allows us to obtain different observables, like the density of states, the eigenstates or the transport characteristics using the time evolution of wave packets [16]. In this chapter, we give an insight into the numerical wave-packet propagation and present a comparison between four algorithms applied for different system constraints. Subsequently, we focus on the calculation of transport properties of a scattering system and present how the time evolution of a wave packet, initially localized in a lead, can be employed to deduce the scattering amplitudes, that serve as basis for various transport characteristics between the attached leads.

In this chapter, we show that charge carriers in zero-gap semiconductors like graphene feature, beyond conventional Bloch oscillations, so-called Bloch–Zener oscillations in presence of a periodic superstructure. We demonstrate by means of a model Hamiltonian, that these oscillations are characterized by a rich frequency spectrum, which arises from the periodic Bloch oscillations in momentum space combined with the coherent Zener tunneling between the electron and hole branches [17]. In order to reveal the peculiarities of these oscillations in an existing semiconductor environment, we investigate the time evolution of wave packets and the corresponding frequency spectrum in periodically modulated graphene nanoribbons. Furthermore, we point out that the presence of Bloch–Zener oscillations can also be deduced from the current-voltage characteristics, induced by the superstructure, for sufficiently high applied bias voltages. We show that the full frequency spectrum can be as well extracted, if the current is considered in presence of an external radiation field.

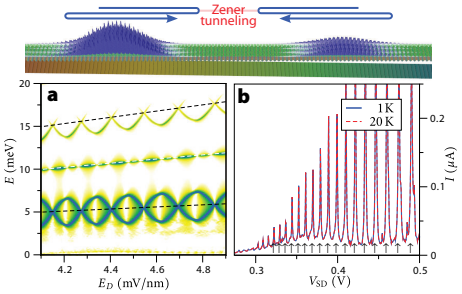

Bloch–Zener oscillations on a nanoribbon – The dynamics of Bloch–Zener oscillations are characterized by a combined motion of an electron (right) and a hole wave-packet (left) connected through a periodic Zener tunneling, leading to a (**a**) characteristic frequency pattern and (**b**) pronounced current peaks.

In this part of the thesis we study the transport properties of the two-dimensional topological insulator mercury telluride (HgTe).

At first, we introduce a 6×6 Luttinger-Kohn model to describe the electronic structure of the quantum well constituents HgTe and CdTe. Then we search for the transversal eigenstates of the quantum well to establish the concept of inverted band ordering for the states close to the Fermi energy. Based on these eigenstates we develop different two-dimensional approximations for the electronic states of the quantum well, which will be used throughout this thesis for our transport considerations. Furthermore, we derive the edge states arising at transitions between conventional and inverted ordered bands and use these states to prove, why scattering between different spin-states is not possible in presence of time-reversal symmetry.

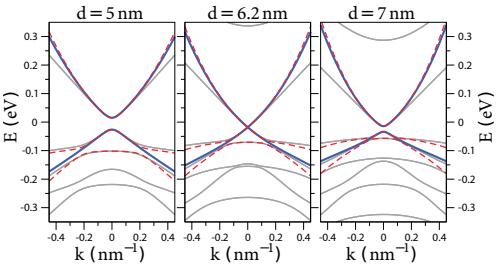

Band structure of a HgTe quantum well – Series of band structures for different HgTe layer width d featuring from left to right a conventional band ordering, a gapless Dirac spectrum and an inverted band ordering.

7. Switching Edge-States in HgTe Constrictions 103

In this chapter, we investigate the switching properties of a constriction etched out of the topological insulator HgTe and propose a novel spin-transistor action by means of two different gating configurations [18]. Therefore, we derive the edge states arising at a HgTe boundary and use the states as a basis for a quasi one-dimensional model. Using this approximate description we outline the switching properties using a transfer-matrix approach [19] and confirm the spin-transistor action with full two-dimensional calculations comprising impurities and edge disorder. Furthermore, we investigate the possibility to downscale the device and reveal that a reduced length of the switching channel can be achieved by additional spin-orbit interaction terms induced by structure-inversion asymmetry.

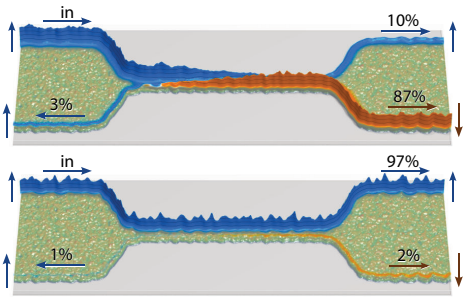

Switching states of a HgTe constriction – Depending on the chemical potential within the constriction the spin-polarized edge states entering from the upper left edge undergo a full spin flip (upper panel) or stay unaltered (lower panel).

8. Weak Localization in HgTe Heterostructures 127

We analyze the weak localization properties of a HgTe heterostructure in the diffusive regime for different band topologies. Our results reveal different transitions between weak localization and weak anti-localization depending on the Fermi energy and the band topology, which is explained by a Berry phase argument [20]. The weak localization minimum is shifted by an interplay of Berry phases and correlations of backscattered trajectories, which is also visible in transport through ballistic cavities [21]. Besides, we assess that the two-band model for HgTe heterostructures is insufficient to describe the Berry phase of the hole states and present an improved description. Furthermore, we study the influence of spin-orbit interactions and reveal a similar energy dependent weak anti-localization transition. Based on these findings we point out that the inverted band ordering of a topological insulator can also be probed experimentally by the energy dependence of the magneto-conductance outside the bulk band gap, in addition to the measurement of the quantum spin Hall effect.

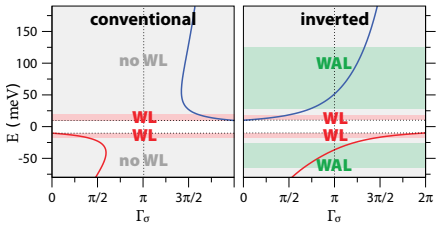

Energy dependent weak localization – Different weak localization (WL) and weak anti-localization (WAL) regimes based on the Berry phase Γ_σ depending on the Fermi energy E and the band topology.

Part I.

Graphene

2 Introduction to Graphene

In the following part of this thesis, we study novel effects in the electronic system of a two-dimensional atomically-thin layer of carbon atoms, called graphene. The chemical and physical properties of carbon are determined by its six electrons which occupy the $1s^2$, $2s^2$ and $2p^2$ atomic orbitals. Those electrons can hybridize into an sp^3 (*e.g.* methane [CH_4]), sp^2 (*e.g.* ethene [C_2H_4]) and sp (*e.g.* acetylene [C_2H_2]) orbitals allowing for single, double and triple bonds. Because of these universal capabilities for different bondings, an inexhaustible amount of carbon-based compounds exists, which can be synthesized by methods of organic chemistry. Furthermore, all known life forms are composed of carbon-based structures. In ambient conditions pure carbon crystallizes in several structures with different dimensionality, ranging from quasi zero-dimensional C_{60} fullerenes [22] via quasi one-dimensional carbon nanotubes [23] to three dimensional crystals. In the latter case, diamond and graphite exhibit two types of crystal structures, which result in significantly different physical properties.

Around 2005 the variety of crystallized manifestations of carbon has been extended to the quasi two-dimensional case. By means of mechanical exfoliation, a single layer of atoms can be separated from a bulk graphite crystal, which builds an atomically thin film of carbon atoms arranged in a hexagonal structure, called graphene[3]. Because of the hexagonal arrangement the new material features exceptional electronic properties, which can be described by a two-dimensional Dirac equation for ultrarelativistic particles [5]. This leads to various novel phenomena in quantum transport, different from conventional two-dimensional electron gases, like for example an anomalous quantum Hall effect in a perpendicular magnetic field [24]. These exceptional quantization characteristics of graphene were demonstrated by the smoking gun experiments of two experimental groups, at the University of Manchester [2] and at Columbia University [25], proving the Dirac nature of electronic excitations in graphene.

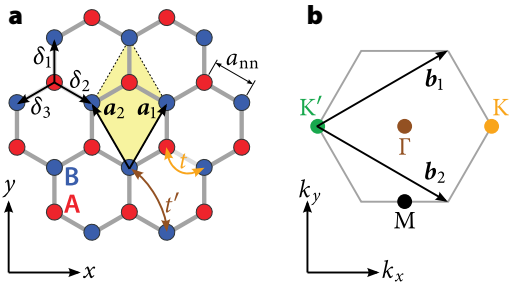

Figure 2.1. | Atomic structure of graphene and its Brillouin zone
a, Primitive unit cell (yellow) containing two basis atoms (A, B), generating the lattice structure by means of the two basis vectors $\boldsymbol{a}_1$ and $\boldsymbol{a}_2$. t and t' depict the hopping terms for Eq. (2.4); δ_i represent the nearest-neighbor vectors (i=1, 2, 3).
b, Corresponding momentum space representation. The two Dirac cones are situated at the K and K′ point.

At first we introduce the tight-binding model that describes the electronic properties of graphene on an atomistic basis, which is used in the upcoming calculations of the next chapters. Furthermore, we employ this atomistic model to deduce an approximate description of the electronic structure close to the Fermi energy similar to a two-dimensional Dirac equation. Additionally, we derive the quantization of electrons into Landau levels in presence of a perpendicular magnetic field, which is a key ingredient for the wave-packet revivals in the next chapter.

2.1. Elementary electronic properties

In theoretical studies the electronic properties of graphene are commonly described by means of two different levels of approximation [26]. The full physics can be captured by an atomistic description, which takes different sets of electronic orbitals into account, either as part of an ab initio investigation with density functional theory [27, 28], or by means of a tight-binding approximation [29, 30]. In the following we introduce the tight-binding Hamiltonian based on the p_z orbitals forming π bonds between neighboring carbon atoms. This Hamiltonian is used for the atomistic description of graphene throughout this work and will be further employed to derive the low-energy approximation applied in the forthcoming chapters.

2.1.1. Tight-binding approach

The carbon atoms in a sheet of graphene are arranged in a hexagonal lattice, as shown in Fig. 2.1 (**a**), with a spacing of $a_{\mathrm{nn}} \approx 1.42\,\text{Å}$ between neighboring atoms. This type of structure is described by a unit cell, depicted as yellow shaded diamond in Fig. 2.1 (**a**), which is displaced multiple times by two lattice vectors,

$$\boldsymbol{a}_1 = \frac{a}{2}\begin{pmatrix} 1 \\ \sqrt{3} \end{pmatrix} \quad \text{and} \quad \boldsymbol{a}_2 = \frac{a}{2}\begin{pmatrix} -1 \\ \sqrt{3} \end{pmatrix}, \tag{2.1}$$

of length $a = |\boldsymbol{a}_1| = |\boldsymbol{a}_1| = \sqrt{3}\, a_{\mathrm{nn}} \approx 2.46\,\text{Å}$. Each unit cell contains two carbon atoms A and B attributed to two basis vectors, *e.g.* $^2/_3\,(\boldsymbol{a}_1 + \boldsymbol{a}_2) = (0, {}^{2a}/\sqrt{3})$ and $(0, 0)$. This

basis generates together with the two lattice vectors a hexagonal structure. The reciprocal vectors $\boldsymbol{b}_j$, which represent the lattice in momentum space, are determined by $\boldsymbol{a}_i \cdot \boldsymbol{b}_j = 2\pi\delta_{ij}$, depending on the real space vectors $\boldsymbol{a}_i$. This sets the reciprocal vectors to

$$\boldsymbol{b}_1 = \frac{2\pi}{\sqrt{3}a}\begin{pmatrix}\sqrt{3}\\1\end{pmatrix} \quad \text{and} \quad \boldsymbol{b}_1 = \frac{2\pi}{\sqrt{3}a}\begin{pmatrix}\sqrt{3}\\-1\end{pmatrix}, \tag{2.2}$$

defining the Brillouin zone of the honeycomb lattice, as sketched in Fig. 2.1 (**b**). Since many properties of the charge carriers are predominantly governed by the electronic band structure close to the Fermi energy, the corners of the Brillouin zone [K and K′ in Fig. 2.1 (**b**)] are of particular importance, because the gap between the electron- and hole-like states closes at these points. For graphene two inequivalent corners can be found, which are located at

$$\mathrm{K} = \frac{4\pi}{3a}\begin{pmatrix}1\\0\end{pmatrix} \quad \text{and} \quad \mathrm{K}' = \frac{4\pi}{3a}\begin{pmatrix}-1\\0\end{pmatrix}, \tag{2.3}$$

and are commonly named different valleys, or Dirac points, because the spectrum in their vicinity can be described by a two-dimensional Dirac equation.

The simplest tight-binding Hamiltonian for the electronic states of graphene can be found by neglecting all atomic orbitals of the carbon atoms except the p_z ones. Allowing these p_z electrons to hop between nearest and next-nearest lattice sites results in the Hamiltonian [29]

$$\begin{aligned} H = &- t \sum_{\langle i,j\rangle} \left(a_i^\dagger b_j + b_j^\dagger a_i\right) \\ &- t' \sum_{\langle\langle i,j\rangle\rangle} \left(a_i^\dagger a_j + a_j^\dagger a_i + b_i^\dagger b_j + b_j^\dagger b_i\right), \end{aligned} \tag{2.4}$$

where a_i ($a_i^\dagger$) and b_i ($b_i^\dagger$) are the creation (annihilation) operators for the A and B carbon atoms at the lattice positions $\boldsymbol{R}_\mathrm{A} = n\boldsymbol{a}_1 + m\boldsymbol{a}_2 + {}^2\!/_3\,(\boldsymbol{a}_1 + \boldsymbol{a}_2)$ and $\boldsymbol{R}_\mathrm{B} = n\boldsymbol{a}_1 + m\boldsymbol{a}_2$ ($n, m \in \mathbb{N}$). This Hamiltonian contains entries which connect nearest neighbors $\langle i, j\rangle$ of different sublattice type with the hopping element t, and next-nearest neighbors $\langle\langle i, j\rangle\rangle$ of the same sublattice type with the hopping element t', as sketched in Fig. 2.1 (**a**). The values of the hopping elements t and t' used in the literature differ slightly. Throughout this work we assume the nearest-neighbor hopping element $t \approx 2.8\,\mathrm{eV}$ [26] and the next-nearest-neighbor hopping element $t' \approx 0.1t$ [31].

2.1.2. Dirac fermions

In the following we employ the tight-binding description introduced previously to derive an effective Hamiltonian for small excitations around the Fermi energy, which will show a distinct similarity to a two-dimensional Dirac equation. An infinitely

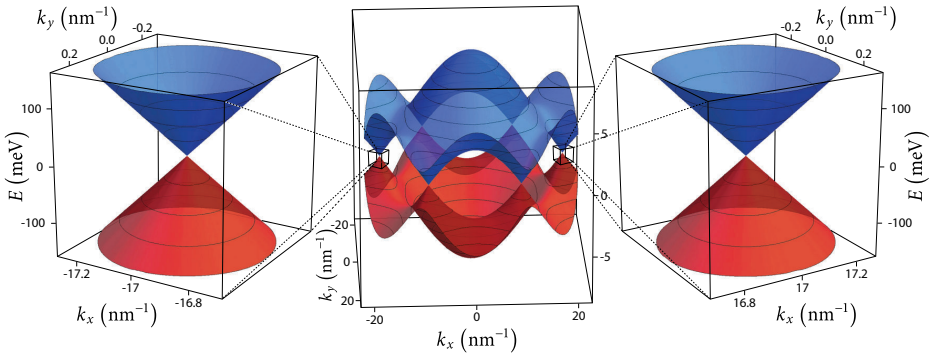

Figure 2.2. | Electronic bandstructure of graphene – The central panel displays the energy spectrum of the full Brillouin zone [see Fig. 2.1 (**b**)] for hopping matrix elements $t = 2.8\,\mathrm{eV}$ and $t' = 0$. Left and right panels show a zoom into the energy bands close to the K′ and K Dirac point respectively.

extended system features translational invariance along the lattice vectors $\boldsymbol{a}_1$ and $\boldsymbol{a}_2$, which allows one to express the wave functions by the Bloch ansatz

$$\psi(\boldsymbol{R}) = \mathrm{e}^{\mathrm{i}\boldsymbol{k}\boldsymbol{R}} \begin{pmatrix} \psi_{\mathsf{A}}(\boldsymbol{k}) \\ \psi_{\mathsf{B}}(\boldsymbol{k}) \end{pmatrix}. \tag{2.5}$$

Here, the wave function located at the two sublattices A and B is cast into the spinor $(\psi_{\mathsf{A}}(\boldsymbol{k}), \psi_{\mathsf{B}}(\boldsymbol{k}))$. The Hamiltonian for the bulk system can be derived from the Hamiltonian of one primitive cell by taking the Bloch phases of the bonds to all the atoms of neighboring unit cells into account. This leads to the Hamiltonian [5, 32]

$$H(\boldsymbol{k}) = -2t' \left(\sum_{i=1}^{3} \cos\left(\boldsymbol{k} \cdot \boldsymbol{a}_i\right) \right) \mathbb{1}_{2\times 2} - t \left(\sum_{i=1}^{3} \cos\left(\boldsymbol{k} \cdot \delta_i\right) \right) \sigma_x + t \left(\sum_{i=1}^{3} \sin\left(\boldsymbol{k} \cdot \delta_i\right) \right) \sigma_y, \tag{2.6}$$

containing the unit matrix $\mathbb{1}_{2\times 2}$ and the Pauli matrices σ_x, σ_y. The phase values attributed to each bond are expressed by means of the connecting vectors δ_i for nearest neighbors and $\boldsymbol{a}_i$ for next-nearest neighbors,[1] as defined in Fig. 2.1 (**a**). This Hamiltonian features an electron and a hole branch given by

$$E_{\pm} = \pm t\sqrt{3 + f(\boldsymbol{k})} - t' f(\boldsymbol{k}), \tag{2.7}$$

with

$$f(\boldsymbol{k}) = 2\cos\left(a\, k_x\right) + 4\cos\left(\frac{a}{2} k_x\right) \cos\left(\frac{\sqrt{3}\, a}{2} k_y\right). \tag{2.8}$$

The resulting band structure exhibits six points in the first Brillouin zone where electron and hole bands touch each other, as shown in the middle panel of Fig. 2.2. Since every touching point can be connected by the reciprocal lattice vectors $\boldsymbol{b}_1$ and $\boldsymbol{b}_2$ with two

[1] The lattice vector $\boldsymbol{a}_3 = \boldsymbol{a}_2 - \boldsymbol{a}_1$ is introduced to allow for the compact notation of Eq. (2.6).

other ones [see Fig. 2.1 (**b**)], there are only two groups which feature inequivalent physical properties. In the following those are labeled by $\boldsymbol{K}_\tau$ with the valley index τ ($\boldsymbol{K}_+$ = K, $\boldsymbol{K}_-$ = K′):

$$\boldsymbol{K}_\tau = \frac{4\pi}{3a}\begin{pmatrix}\tau\\0\end{pmatrix}. \tag{2.9}$$

A zoom into the band structure close to these points reveals two cones linear in the momentum $|\boldsymbol{k}-\boldsymbol{K}_\tau|$, as displayed in the left and right panel of Fig. 2.2. This immediately suggests an expansion of Eq. (2.6) for small momenta $\boldsymbol{q} = \boldsymbol{k} - \boldsymbol{K}_\tau$ around the different valleys $\boldsymbol{K}_\tau$. Up to linear order in $\boldsymbol{q}$ the resulting Hamiltonian [33]

$$H(\boldsymbol{K}_\tau + \boldsymbol{q}) \approx H_\tau := \hbar v_F\,(\tau q_x\sigma_x + q_y\sigma_y) \tag{2.10}$$

is similar to a two-dimensional Dirac Hamiltonian with a Fermi velocity of $v_F = \frac{\sqrt{3}ta}{2\hbar}$. For given material parameters $v_F \approx 10^6$ m/s, which is about 300 times smaller than the speed of light.

2.2. Landau levels

In the following chapter, we will apply the Dirac approximation of graphene to study the time evolution of a wave-packet in presence of a perpendicular magnetic field. Therefore it is suitable to introduce at first how electronic states condense into Landau levels. To this end, we study the effect of a magnetic field $\boldsymbol{B} = B\boldsymbol{e}_z$ on the Dirac Hamiltonian H_τ of Eq. (2.10) in a similar fashion as in Refs. [24, 26, 34]. We will show how the initial problem can be transformed to a differential equation containing the creation and annihilation operators of a harmonic oscillator problem, and derive the corresponding eigenstates and energies of the system.

The effect of a magnetic field is incorporated into a Hamiltonian by "minimal coupling", which amounts to replacing the momentum $\boldsymbol{p} \to \boldsymbol{p} - e\boldsymbol{A}$ using a vector potential $\boldsymbol{A}$ associated with the magnetic field by $\boldsymbol{B} = \nabla \times \boldsymbol{A}$. Without loosing generality, we choose the vector potential in a Landau gauge

$$\boldsymbol{A} = -By\boldsymbol{e}_x. \tag{2.11}$$

This results in a Hamiltonian with a translational invariance in x-direction and a broken one in y-direction, which allows for the Bloch ansatz,

$$\psi_k(x,y) = \mathrm{e}^{\mathrm{i}\,k\,x}\phi(y), \tag{2.12}$$

for the eigenstates of the system. After combination of this wavefunction with the two-dimensional Dirac equation (2.10), the momentum operator in x-direction gets replaced by

$$k_x \to k + \frac{eA_x}{\hbar} = k + \frac{y}{l_B^2}, \tag{2.13}$$

using the magnetic length $l_B = \sqrt{\frac{\hbar}{eB}}$. This leads to the following differential equation for the wave function in y-direction:

$$\hbar v_F \begin{pmatrix} 0 & -\partial_y + \tau\left(k - \frac{y}{l_B^2}\right) \\ \partial_y + \tau\left(k - \frac{y}{l_B^2}\right) & 0 \end{pmatrix} \phi(y) = E\phi(y). \tag{2.14}$$

We introduce a dimensionless length scale $\xi = l_B k - y/l_B$, which allows us to substitute the differential operator ∂_y and the position dependence of the preceding equation. In doing so, we are able to define the ladder operators

$$\mathcal{O} = \frac{1}{\sqrt{2}}\left(\partial_\xi + \tau\xi\right), \tag{2.15a}$$

$$\mathcal{O}^\dagger = \frac{1}{\sqrt{2}}\left(-\partial_\xi + \tau\xi\right), \tag{2.15b}$$

similar to those of the quantum harmonic oscillator. The operators fulfill the canonical commutation relation $\left[\mathcal{O}, \mathcal{O}^\dagger\right] = \tau$, which reveals that they change their character between raising and lowering operator depending on the valley index τ. For $\boldsymbol{K}_+$ the raising operator is given by $\mathcal{O}$ and the lowering operator by $\mathcal{O}^\dagger$, which is inverted for $\boldsymbol{K}_-$. In terms of these operators the differential equation for the states $\phi(\xi)$ reads

$$\sqrt{2}\frac{\hbar v_F}{l_B} \begin{pmatrix} 0 & \mathcal{O}^\dagger \\ \mathcal{O} & 0 \end{pmatrix} \phi(\xi) = E\phi(\xi). \tag{2.16}$$

By means of the eigenstates of the harmonic oscillator

$$\varphi_n(\xi) = \pi^{-1/4}\, 2^{-n/2}\, (n!)^{-1/2}\, \mathrm{e}^{-\xi^2/2}\, \mathrm{H}_n(\xi), \tag{2.17}$$

where $\mathrm{H}_n(\xi)$ are Hermite polynomials of the first kind, we are able to derive the energy eigenstates.

An inspection of the matrix comprised of the raising and lowering operators in Eq. (2.16) reveals why zero-energy Landau levels exist for massless Dirac fermions. In the case of the valley $\boldsymbol{K}_+$, the lowering operator is given by $\mathcal{O}^\dagger$ acting on the second spinor entry as shown in Eq. (2.16). If the eigenstate is described by the first harmonic oscillator eigenfunction $\varphi_0(\xi)$ in the lower spinor entry, this state is completely annihilated by $\mathcal{O}^\dagger$. The right-hand side of Eq. (2.16) vanishes and consequently the state represents a zero energy eigenstate. For the opposite valley $\boldsymbol{K}_-$, the lowering operator is given by $\mathcal{O}$ allowing for a zero-energy eigenstate in the upper spinor entry. Finally, the Landau levels for zero energy are given by

$$\phi_{0,\tau=+}(\xi) = \begin{pmatrix} 0 \\ \varphi_0(\xi) \end{pmatrix} \quad \text{and} \quad \phi_{0,\tau=-}(\xi) = \begin{pmatrix} \varphi_0(\xi) \\ 0 \end{pmatrix}. \tag{2.18}$$

Also the higher excited states can be derived using a similar construction. For the valley $\boldsymbol{K}_+$ the ladder operators in the matrix of Eq. (2.16) lead to a lowering of the

second spinor entry, $\mathcal{O}^\dagger \varphi_{n+1}(\xi) = \sqrt{n}\,\varphi_n(\xi)$, and to a raising of the first spinor entry, $\mathcal{O}\,\varphi_n(\xi) = \sqrt{n}\,\varphi_{n+1}(\xi)$, resulting in the eigenstates

$$\phi_{n,\tau=+}(\xi) = \begin{pmatrix} \varphi_{n-1}(\xi) \\ \operatorname{sgn}(n)\,\varphi_n(\xi) \end{pmatrix}. \tag{2.19}$$

In case of the opposite valley $\boldsymbol{K}_-$ the operators $\mathcal{O}$ and $\mathcal{O}^\dagger$ swap their raising and lowering character leading to the eigenstates

$$\phi_{n,\tau=-}(\xi) = \begin{pmatrix} -\operatorname{sgn}(n)\,\varphi_n(\xi) \\ \varphi_{n-1}(\xi) \end{pmatrix}. \tag{2.20}$$

For both cases the energies of the Landau levels are determined by the $\sqrt{n}$ factor of the ladder operators, giving rise to the eigenenergies

$$\mathcal{E}_n = \frac{\hbar\, v_F}{l_B} \operatorname{sgn}(n) \sqrt{2\,|n|} = v_F \operatorname{sgn}(n) \sqrt{2\,e\,B\,\hbar\,|n|}. \tag{2.21}$$

A similar quantization is still present if an additional electric field is applied, leading to a splitting of the Landau levels as we have shown in Ref. [35].

The foregoing considerations reveal that the energies of Landau levels in graphene significantly differ from those in conventional two-dimensional electron gases. Not only the spacings between Landau levels, which are equidistant in electron gases, are determined by a square-root dependence, but also the relation between the energies and the magnetic field shows a square-root behavior, which would be linear for conventional systems. These exceptional properties have been employed in two seminal works to experimentally prove the Dirac nature of charged particles in graphene [2, 25]. In the following chapter, we will show that the special properties of the Landau levels lead to further implications like for example a revival dynamics in the time evolution of wave packets in graphene.

3 Wave-Packet Revivals

In this section we study the dynamics of wave packets on a sheet of graphene in a perpendicular magnetic field. Because of the similarities between the effective low-energy Hamiltonian of graphene and the Dirac equation for massless particles, some "relativistic effects" have a close counterpart in the time evolution of charge carriers in graphene [36]. We start with the so-called *zitterbewegung* which gives rise to a non-transient rapid oscillatory motion in presence of a perpendicular magnetic field [37, 38]. Subsequently, we show that in a similar setting an initially excited wave packet undergoes collapses and revivals, comparable to the dynamics of the outer electron in a Rydberg atom [15]. We present a detailed analysis of the effect in the autocorrelation function as well as the center-of-mass motion and offer an intuitive, trajectory-based explanation for the process. Furthermore, the influence of random electrostatic impurities on the revival-dynamics is studied by means of numerical wave-packet propagations. We also investigate how wave-packet revivals can be verified experimentally and propose a pump-probe setup. To this end, we analyze the impact of a few-cycle laser pulse on the wave-packet dynamics in a sheet of graphene placed in a perpendicular magnetic field. We study the necessary conditions to excite an initial state from the Fermi level into a highly excited Landau level and present a non-perturbative scheme to simulate a four-wave mixing experiment. In doing so we are able to trace back the revival dynamics of the wave packets to the dependence of the four-wave mixing signals on the delay time of the second laser.

3.1. Zitterbewegung

As shown in the previous chapter, graphene features two inequivalent points in the electronic band structure where the gap between electron and hole states closes. These points are located at the corners of the Brillouin zone at K and K' [5, 26]. In the following we consider wave packets with excitation energies of a few 100 meV above or below the Fermi level. As a consequence, the electronic properties can be perfectly described by the effective Dirac Hamiltonian (2.10), since the linear approximation of the spectrum is quite accurate for energies between ±700 meV. For higher excitations the trigonal warping, which exists due to the hexagonal structure, gains in importance and higher-order terms have to be taken into account [39].

Here, we will study the time evolution of a wave packet on an infinitely extended sheet of graphene in presence of a perpendicular magnetic field $\boldsymbol{B}(\boldsymbol{r}) = B\boldsymbol{e}_z$. Such a system has been proposed by T. M. Rusin, W. Zawadzki [37] and J. Schliemann [38] to study the non-transient *zitterbewegung* of a wave packet. As initial state a kicked Gaussian wave packet of the form

$$\psi(\boldsymbol{r}, t = 0) = \frac{1}{\sqrt{\pi} a_0} \exp\left(-\frac{(\boldsymbol{r} - \boldsymbol{r}_0)^2}{2a_0^2} + \mathrm{i}\boldsymbol{k}\boldsymbol{r}\right)\begin{pmatrix} 1 \\ \mathrm{e}^{\mathrm{i}\varphi} \end{pmatrix} \tag{3.1}$$

is considered. The width of the wave packet is taken as $a_0 = \sqrt{\hbar/(eB)}$ and the initial momentum $\boldsymbol{k}$, which is often referred to as initial kick, can point along any direction in the x-y plane, but is set to $\boldsymbol{k} = k_0\boldsymbol{e}_y$ in the following. The pseudospin $\boldsymbol{\sigma}\boldsymbol{k}$ of the wave packet is determined by the phase-relation between the two spinor entries. For $\varphi = \pi/2$ the wave packet is mostly electron like since the momentum and the pseudo spin are pointing along the y-direction. In case of the opposite phase $\varphi = 3\pi/2$ the wave packet is mostly hole like. For intermediate angles all different superpositions of hole and electron states can be achieved.

In the following, we calculate the time-evolution of this Gaussian wave packet in presence of a perpendicular magnetic field. Therefore, the action of the time-evolution operator on the wavefunction

$$\psi(t) = \exp\left(-\frac{\mathrm{i}}{\hbar}\hat{H}_\tau t\right)\psi(0), \tag{3.2}$$

has to be evaluated. In principle there exist several possibilities to determine the time-evolution of the wave packet, like an expansion in eigenstates [40], split-step techniques [41] or polynomial propagators [42]. The expansion in eigenstates leads to a very accurate time evolution even for long propagation times, yet can only be efficiently applied to systems with a known set of eigenstates, which is in general not the case when impurity potentials or special confining shapes are considered. For such cases algorithms which are not based on eigenstates are preferable, like for example split-step techniques [43]. However, those are generally not very accurate and only lead to sufficient numerical quality for short propagation times. Thus, we have developed

several algorithms which do not require any knowledge of the eigenstates but are still very accurate, due to an expansion of the time-evolution operator in polynomials up to high orders. In the following, we will employ a propagation using Chebyshev polynomials [42], which will be introduced amongst other propagators in the next chapter.

During the time evolution we track several observables, including the expectation value of the position operator

$$\boldsymbol{r}(t) = \langle \psi(t) | \hat{\boldsymbol{r}} | \psi(t) \rangle. \tag{3.3}$$

Throughout this work we refer to $\boldsymbol{r}(t)$ as the "center-of-mass", although the calculated motion describes massless particles. If we consider the time evolution of the initial Gaussian wave packet (3.1), the center-of-mass movement reveals a distinct trembling motion known as *zitterbewegung*. This is apparent in the snapshots of the videos shown in Fig. 3.1 (**a**), which present the time evolution for different initial setups. Another interesting property, the local pseudospin, is given by the expectation value $\langle \psi(\boldsymbol{r}, t) | \boldsymbol{\sigma} \hat{\boldsymbol{k}} | \psi(\boldsymbol{r}, t) \rangle$ at each point $\boldsymbol{r}$, which is color coded on the surface of the wave packets in the videos. This pseudospin reveals the local electron or hole character of the wave packet. Furthermore, we are able to employ this method to extract stationary properties from the time-evolution, like the local density of states (LDOS) and the Green's function [44]. For example, the relative strength of each energy eigenstate with respect to the initial state is given by the Fourier transform of the autocorrelation function

$$C(t) = \langle \psi(t = 0) | \psi(t) \rangle. \tag{3.4}$$

The same concept allows us to calculate the $\boldsymbol{E} \times \boldsymbol{B}$ drift motion and eigenstates in the quantum Hall regime of graphene for high bias currents [35]. The LDOS is given by the Laplace transformation of the autocorrelation function

$$n(E) \propto \mathfrak{Re} \int_0^\infty dt \, \mathrm{e}^{\mathrm{i}Et/\hbar} C(t), \tag{3.5}$$

which will be introduced in Appendix A.4. As shown in Fig. 3.1 (**b**) the LDOS of the trembling wave packet reveals pronounced peaks at the energies of the Landau levels $\mathcal{E}_n = v_F \operatorname{sign}(n) \sqrt{2eB\hbar|n|}$ depicted by red dots. The peak height, which is proportional to the enclosed area of the peak in the LDOS, indicates the overlap of the initial Gaussian wave packet with the different Hermite polynomials of the Landau levels. For $\varphi = \pi/2$ more electron than hole states are occupied, leading to a wave-packet trajectory with an initial motion into positive y-direction passing over to an erratic motion, as shown in Figs. 3.2 (**a, b**). Because of the choice of the initial pseudospin parallel to the initial momentum, the wave packet is predominantly electron like, which is either identifiable in the large orange regions of the wavefunction in the video on the left side of Fig. 3.1 (**a**), or directly by the stronger weight of the electron states in the spectrum of Fig. 3.1 (**b**). In case of $\varphi = \pi$, hole and electron states are equally represented in the initial state, leading to a trajectory with a vanishing motion of the center-of-mass in y-direction. This is caused by a mirror symmetry between the time evolution of the

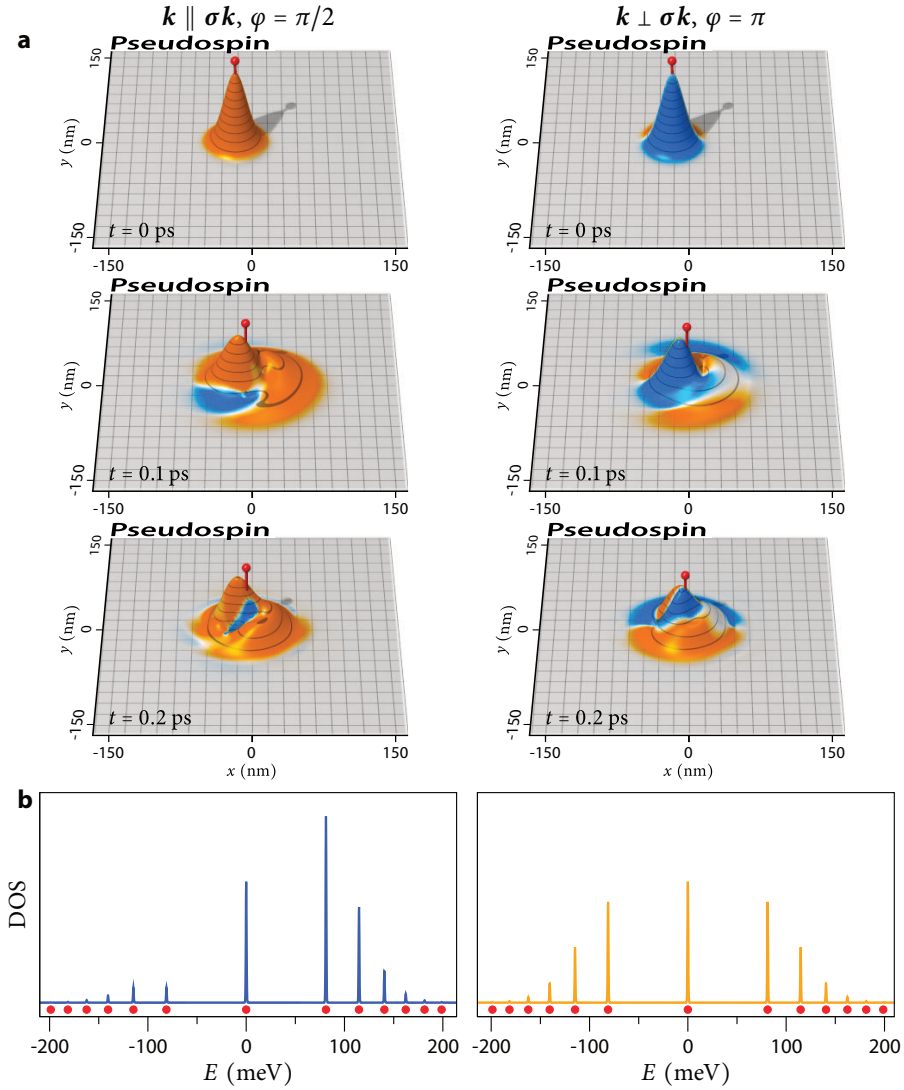

Figure 3.1. | Zitterbewegung of a wave packet on graphene – a, Snapshots of the time-evolution of a kicked Gaussian wave packet for different initial pseudospin configurations ($B = 5\,\mathrm{T}$, $k_0 = \sqrt{eB/\hbar}$, $a_0 = \sqrt{\hbar/(eB)}$). The red pin represents the center-of-mass of the wave packet, the height for the absolute value and the color the local pseudospin given by $\langle\psi(\boldsymbol{r},t)|\boldsymbol{\sigma}\hat{\boldsymbol{k}}|\psi(\boldsymbol{r},t)\rangle$, with orange corresponding to electron-like parts and blue to hole-like parts. Videos of the propagation are available at http://doi.krueckl.de/phd/0001 for initial pseudospin $\boldsymbol{\sigma k} \parallel \boldsymbol{k}$ (movie1a.flv, 5.0 MB) and $\boldsymbol{\sigma k} \perp \boldsymbol{k}$ (movie1b.flv, 5.3 MB). **b,** Local density of states calculated from the wave-packet propagation. The spectrum shows strong peaks for positive energies if the initial pseudospin is parallel to the momentum and a mirror symmetry if pseudospin and momentum are orthogonal to each other. Red dots denote the analytical energies of the Landau levels and coincide up to a very high accuracy with the numerical positions.

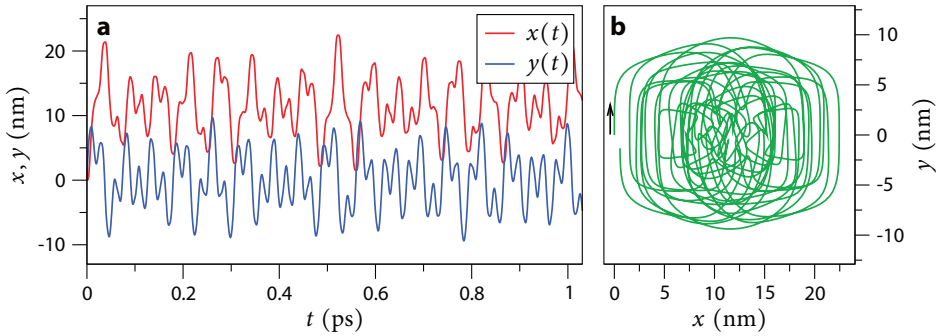

Figure 3.2. | Trajectory of a kicked Gaussian wave packet – a, Time evolution of the center-of-mass of a kicked Gaussian wave packet ($k_0 = \sqrt{eB/\hbar}$, $a_0 = \sqrt{\hbar/(eB)}$) for an initial pseudospin of $\boldsymbol{\sigma k} \parallel \boldsymbol{k}$ in a perpendicular magnetic field $B = 5\,\mathrm{T}$. **b,** Projection of the same trajectory on the x-y plane revealing an erratic trembling motion corresponding to the results in Ref. [38].

hole and the electron states, which is also visible in the local pseudospin, featuring an antisymmetry with respect to the x-axis, which can be verified in the video on the right side of Fig. 3.1 (**a**). A trembling motion of the wave packet is present in both cases, since for any initial condition a finite amount of electron- and hole-like states contributes to the initial configuration, as displayed by the spectra in Fig. 3.1 (**b**). More information about the trembling motion in semiconductor systems and especially graphene can be found in a recent review [45]. In the following, the setting is slightly changed by increasing the initial momentum of the wave packet to reveal additional revival effects in the time evolution.

3.2. Model for wave-packet revivals

The appearance of wave-packet revivals has been initially introduced in the field of atomic physics. In this context revivals are commonly observed for the valence electron in the Coulomb potential of Rydberg atoms and have been studied in theory [46] as well as in experiments [47, 48]. In general, wave-packet revivals are coined by a characteristic time evolution of the system, which can be split into three different time domains. For short times, the initial time evolution is well described by a quasiclassical approximation, expressed by a localized wave packet which follows the trajectory of the underlying classical system [49]. After some time the state disperses, leading to a wave packet distributed over several orbits. During this phase the state can often be subdivided into smaller copies of the initial state, giving rise to fractional revivals [50]. If a sufficient amount of time has passed, the dispersion of the state is reversed and a wave packet with the initial shape is recreated. For a recent review about quantum revivals of wave packets in various settings see Ref. [49].

In the following, we will show why wave packets on graphene in a perpendicular

magnetic field feature such quantum revivals. In order to get an impression about the rich revival dynamics, it is advisable to first inspect the numerical results presented in Fig. 3.3 and the corresponding video. It is worth mentioning that conventional semiconducting materials usually do not show revival features in presence of a perpendicular magnetic field, since the dispersion is dominated by quadratic terms, leading to cyclotron frequencies independent of the Landau level index. Graphene and topological insulators form their own class because of the linear dispersion and the resulting different Landau level spectrum.

3.2.1. Wave-packet revivals in the center-of-mass motion

First, we study the appearance of collapses and revivals in the center-of-mass motion of a wave packet in graphene. The quantum mechanical expectation value of the center-of-mass $\boldsymbol{r}(t)$, Eq. (3.3), cannot be written in a simple analytical expression. Thus we introduce a classical picture which approximates the center-of-mass as a weighted sum over the center-of-masses of different Landau level contributions moving along quantized cyclotron orbits. We define the center-of-mass motion of a classical cyclotron orbit in the n-th Landau level by

$$z_n(t) = x_n(t) + \mathrm{i}y_n(t) = l_n e^{\mathrm{i}\omega_n t}, \tag{3.6}$$

with a cyclotron radius and angular frequency of

$$l_n = \operatorname{sign}(n)\sqrt{2\frac{\hbar}{eB}|n|}, \qquad \omega_n = v_F \operatorname{sign}(n)\sqrt{\frac{eB}{2\hbar|n|}} \quad \text{if} \quad n \neq 0, \tag{3.7}$$

as derived in Appendix A.1. If the initial momentum of the Gaussian wave packet (3.1) is large compared to the momentum used for the *zitterbewegung*, the index of the average occupied Landau level can be approximated by

$$\bar{n} \approx \frac{\hbar}{2eB}k_0^2, \tag{3.8}$$

which can be deduced from the semiclassical quantization condition (A.16). The numerically calculated LDOS supports this assertion, as shown in Fig. 3.4. A strongly kicked Gaussian wave packet mostly occupies one energy branch if the initial pseudospin is parallel to the initial momentum. For an initial momentum $k_0 = 7\sqrt{eB/\hbar}$ the wave packet is excited into the 24.5^{th} Landau level, and hole contributions can be neglected, since they are 400 times smaller than the electron parts. Additionally, the trembling motion disappears, as only one charge carrier type dominates the initial state. The occupation P_n of the n-th Landau level depends on the initial momentum k_0, the initial pseudospin and the width a_0 of the wave packet. As an approximation we infer from numerical calculations for high average Landau levels a Gaussian distribution of the form

$$P(n) = \frac{1}{\sqrt{2\pi}\sigma}\exp\left(-\frac{(n-\bar{n})^2}{2\sigma^2}\right), \tag{3.9}$$

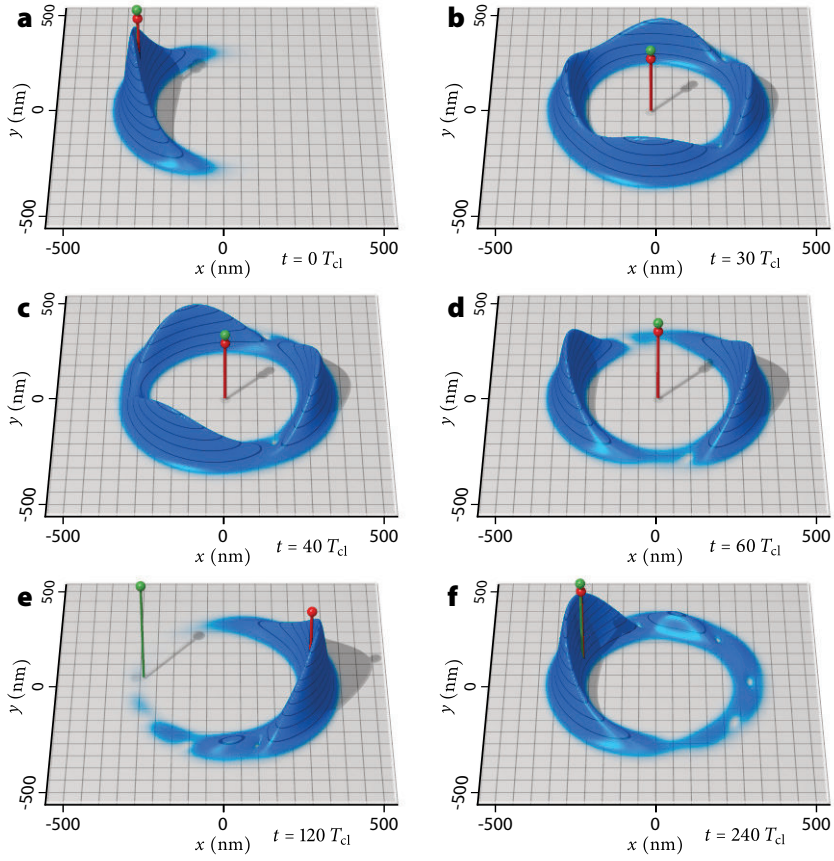

Figure 3.3. | Revivals and fractional revivals of a cyclotron wave packet – The red pin depicts the quantum mechanical center-of-mass, whereas the green pin represents the center-of-mass calculated by the semiclassical expression (3.10). A video of the time evolution is available at http://doi.krueckl.de/phd/0002 (movie2.flv, 20 MB). **a,** The initial wave packet is chosen such that the contributing eigenstates follow the Gaussian distribution (3.9) with $\bar{n} = 60$, $\sigma = 1$, leading to a Poincaré cyclotron time of $T_{\mathrm{cl}} \approx 1.77\,\mathrm{ps}$ ($B = 1\,\mathrm{T}$). During the time-evolution the center-of-mass collapses to the center of a circular wavefunction and subsequently shows pronounced revivals. **b,** Quarter revival at $t = 1/2\bar{n}\,T_{\mathrm{cl}}$, **c**, third revival at $t = 2/3\bar{n}\,T_{\mathrm{cl}}$ and **d,** half revival at $t = \bar{n}\,T_{\mathrm{cl}}$. All revivals have specific symmetries which also occur in the subsequent revivals. **e,** After a certain time a localized wave packet emerges as a mirror revival at $t = 2\bar{n}\,T_{\mathrm{cl}}$. In this case, the quantum mechanical center-of-mass is at the opposite side compared to the semiclassical center-of-mass. This phenomenon has already been observed in Rydberg revivals [51]. **f,** The full revival where the semiclassical and the quantum mechanical center-of-mass coincide occurs for $t = 4\bar{n}\,T_{\mathrm{cl}}$.

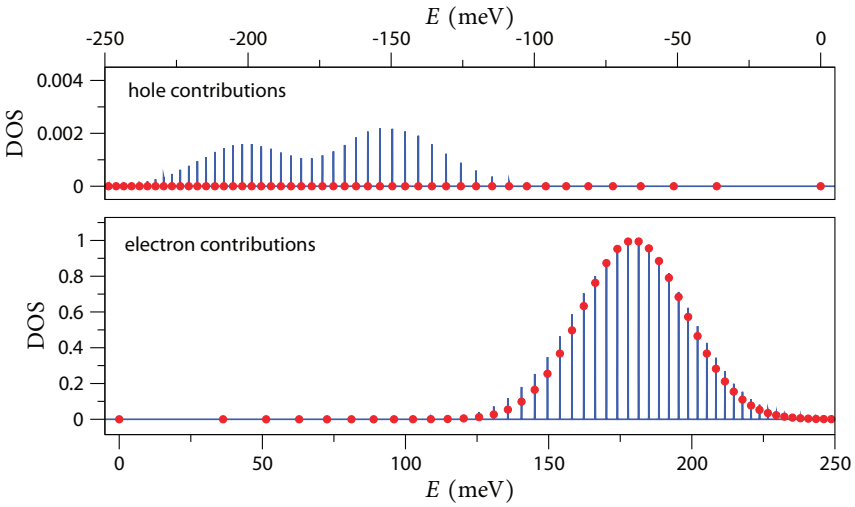

Figure 3.4. | Spectrum of a kicked Gaussian wave packet – Initial kick chosen to produce an average occupied Landau level of $\bar{n} = 24.5$ ($B = 1T$, $k_0 = 7\sqrt{eB/\hbar}$). The hole-like contributions are approximately 400 times smaller than the electron-like parts. The red dots show the position of the analytical Landau levels as well as the probability distribution of Eq. (3.9) used in the following approximations.

as depicted in Fig. 3.4 by the red dots. Here $\bar{n}$ specifies the average occupied Landau level and σ denotes the Landau level spread, which is approximately $\sigma \approx 5$ for the Gaussian wave-packet in Fig. 3.4. The sum over the Landau levels is normalized if $\bar{n} \gg \sigma$ is fulfilled. Within this limit the cyclotron radii l_n do not differ substantially from the cyclotron radius $l \equiv l_{\bar{n}}$ of the average occupied Landau level $\bar{n}$, leading to the approximation

$$z(t) = l \sum_{n=-\infty}^{\infty} P_n e^{i\omega_n t}. \tag{3.10}$$

In the following we will show that this sum contains both effects, the collapse of the center-of-mass as well as its revival. Numerical results of the computed classical center-of-mass motion are shown in Fig. 3.3. In the corresponding video the classical approximation is marked by the green pin, which almost perfectly coincides with the exact quantum mechanical result indicated by the red pin.

Collapse:

Next, we extract the characteristics of the initial collapse of the center-of-mass given by Eq. (3.10). To this end we expand the discrete set of cyclotron frequencies ω_n around the average Landau level $\bar{n}$ by the smooth function

$$\omega(n) \approx v_F \sqrt{\frac{eB}{2\hbar}} \bar{n}^{-1/2} \left(1 - \frac{1}{2}\frac{n-\bar{n}}{\bar{n}} + \frac{3}{8}\frac{(n-\bar{n})^2}{\bar{n}^2} - \dots\right). \tag{3.11}$$

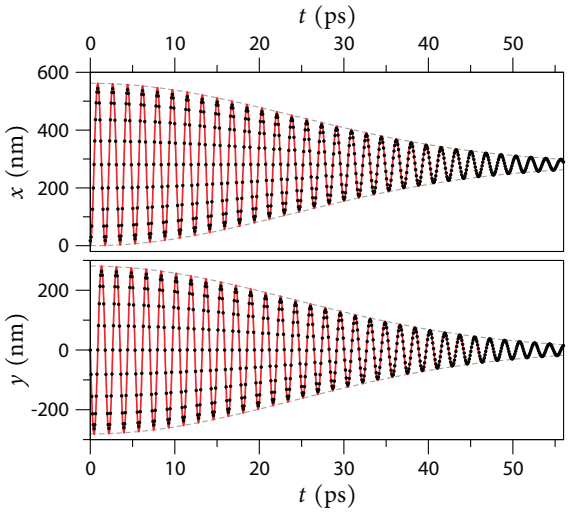

Figure 3.5. | Collapse of a Dirac wave packet – Both panels show the time-evolution of the x- and the y-position of the wave packet ($\bar{n} = 60$, $\sigma = 1$, $B = 1\,\mathrm{T}$). The black dots are obtained from a quantum mechanical calculation and fit to the classical center-of-mass (red line) given by Eq. (3.12) quite well. The slightly smaller amplitude stems from the fact that the center-of-mass of the initial wave packet has already a strong angular dispersion (see Fig. 3.3) and thus the average cyclotron radius l is overestimated.

For high Landau levels the energy spectrum becomes denser and the sum can be approximated by an integral which can be evaluated analytically after the series is reduced to the first two terms:

$$\begin{aligned} z(t) &= l\int_{-\infty}^{\infty} dn\, P(n) e^{\mathrm{i}\omega(n)t} \\ &\approx \frac{l}{\sqrt{2\pi}\sigma}\int_{-\infty}^{\infty} dn \exp\left(-\frac{(n-\bar{n})^2}{2\sigma^2}\right)\exp\left(\mathrm{i}v_F\sqrt{\frac{eB}{2\hbar}}\frac{1}{\sqrt{\bar{n}}}\left(1-\frac{1}{2}\frac{n-\bar{n}}{\bar{n}}\right)t\right) \\ &= l\exp\left(\mathrm{i}\omega_{\bar{n}}t\right)\cdot\exp\left(-\frac{eBv_F^2}{8\hbar}\frac{\sigma^2t^2}{\bar{n}^3}\right). \end{aligned} \tag{3.12}$$

Eq. (3.12) reveals that the center-of-mass motion passes through one cyclotron orbit during the cyclotron time of the average Landau level $\bar{n}$,

$$T_{\mathrm{cl}} = \frac{2\pi}{v_F}\sqrt{\frac{2\hbar}{eB}|\bar{n}|}, \tag{3.13}$$

damped by a Gaussian decay on the timescale

$$T_{\mathrm{coll}} = \frac{4}{v_F\sigma}\sqrt{\frac{\hbar}{eB}|\bar{n}|^3}. \tag{3.14}$$

Our numerical calculations in Fig. 3.5 show the same behavior. The slightly reduced amplitude of the center-of-mass motion given by Eq. (3.12) compared to the exact result stems from the initial radial dispersion of the wave packet created. The initial wave packet is created with a Gaussian probability distribution and exhibits a half-moon shape, as shown in Fig. 3.3 (**a**). This leads to a small reduction of the initial Landau level radius l, which is not included in the classical theory.

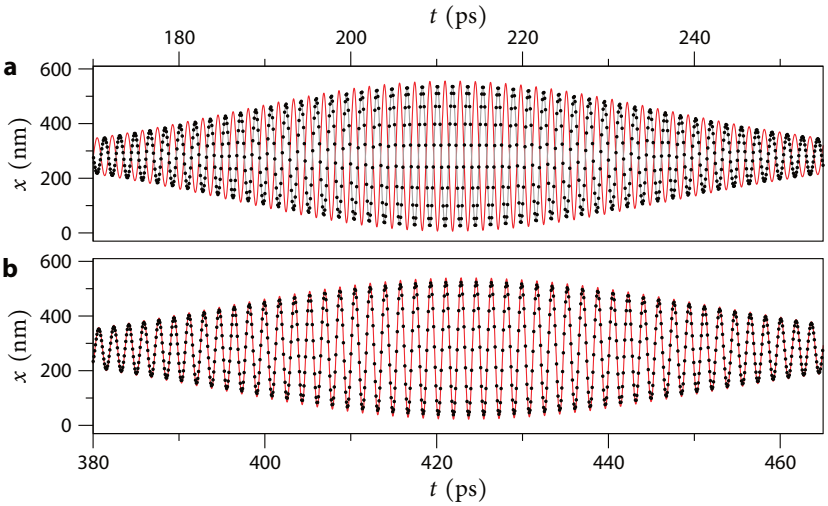

Figure 3.6. | First two revivals of the center-of-mass – The red line shows the (**a**) first and (**b**) second revival of the center-of-mass given by the semiclassical approximation (3.10) ($\tilde{n} = 60$, $\sigma = 1$, $B = 1\,\mathrm{T}$). This result is compared with a full quantum mechanical calculation shown by the black dots. Both results fit well with the remarkable difference for odd revivals. For the first revival (**a**) the classical result is shifted by a phase of π from the quantum mechanical result, which has already been seen in Rydberg atoms.

Revivals:

A revival of the classical center-of-mass motion occurs when all parts orbiting along the contributing Landau levels reunite at a common position. We calculate the revival time from the Taylor expansion of the classical center-of-mass motion inserted into Eq. (3.10). In order to meet the conditions for a revival $|z(T_{\mathrm{rev(CM)}})| = l$, all elements of the sum

$$z(t) = l \sum_{n=-\infty}^{\infty} P_n \exp\left(\mathrm{i}\omega_{\tilde{n}} t + \mathrm{i}(n-\tilde{n})\omega'_{\tilde{n}} t + \ldots\right) \tag{3.15}$$

must share a common phase. Thus, the n-dependent addend of the exponent $\mathrm{i}n\omega'_{\tilde{n}} t$ must be a multiple of $2\pi\mathrm{i}$. This leads to a revival time of the classical center-of-mass given by

$$T_{\mathrm{rev(CM)}} = \frac{2\pi}{\omega'_{\tilde{n}}} = \frac{4\pi}{\nu_F}\sqrt{\frac{2\hbar}{eB}|\tilde{n}|^3} = 2|\tilde{n}|\, T_{\mathrm{cl}}. \tag{3.16}$$

In this case, the classical center-of-mass of the wave packet is on the opposite side compared to the center-of-mass of the quantum mechanical calculation. This phenomenon is visible in the comparison between the classically and the quantum mechanically calculated expectation value of the x-coordinate for the first revival time shown in Fig. 3.6 (**a**). Exactly the same effect occurs for Rydberg atoms known as mirror revivals [51, 52], featuring a center-of-mass motion which is seemingly out of phase

compared to classical calculations. However, for the second revival the classical and the quantum mechanical center-of-mass motion coincide again, as is evident from Fig. 3.6 (**b**).

3.2.2. Revivals in the autocorrelation function

In contrast to the center-of-mass revivals, the revivals in the autocorrelation function can be understood without a semiclassical approximation. By definition the time-evolution of the autocorrelation function is given by

$$C(t) = \langle \phi(t=0) | \phi(t) \rangle = \sum_{n=-\infty}^{\infty} \mathrm{e}^{-\mathrm{i}\mathcal{E}_n t/\hbar} P(n). \tag{3.17}$$

As for the center-of-mass motion, we expand the square root dependence in a Taylor series

$$\mathcal{E}_n \approx v_F \sqrt{2eB\hbar|\tilde{n}|} \left(1 + \frac{1}{2}\frac{n-\tilde{n}}{\tilde{n}} - \frac{1}{8}\frac{(n-\tilde{n})^2}{\tilde{n}^2} + \frac{1}{16}\frac{(n-\tilde{n})^3}{\tilde{n}^3} + \ldots\right), \tag{3.18}$$

leading to an approximate autocorrelation function

$$C(t) \approx \sum_{n=-\infty}^{\infty} \mathrm{e}^{-\mathrm{i}\left(\mathcal{E}_{\tilde{n}} + (n-\tilde{n})\mathcal{E}'_{\tilde{n}} + \frac{1}{2}(n-\tilde{n})^2\mathcal{E}''_{\tilde{n}} + \frac{1}{6}(n-\tilde{n})^3\mathcal{E}'''_{\tilde{n}} + \ldots\right)t/\hbar} P(n), \tag{3.19}$$

where $\mathcal{E}'_{\tilde{n}}$ stands for the first derivative of the dispersion and $\mathcal{E}''_{\tilde{n}}$, $\mathcal{E}'''_{\tilde{n}}$ denote the higher-order derivatives. It is astonishing that all orders are prominently encoded in the quantum mechanical motion and influence the picture at the relevant revival times. From the term $\mathrm{i}\mathcal{E}_{\tilde{n}} t/\hbar$ in the exponent of equation (3.19) we obtain phase oscillations of the autocorrelation function on the timescale

$$T_{\mathrm{osc}} = \frac{2\pi\hbar}{|\mathcal{E}_{\tilde{n}}|} = \frac{\pi}{v_F}\sqrt{\frac{2\hbar}{eB|\tilde{n}|}}. \tag{3.20}$$

These oscillations take place when the wave packet passes through its initial position. At the classical cyclotron time

$$T_{\mathrm{cl}} = \frac{2\pi\hbar}{|\mathcal{E}'_{\tilde{n}}|} = \frac{2\pi}{v_F}\sqrt{\frac{2\hbar|\tilde{n}|}{eB}}, \tag{3.21}$$

the wave packet returns to the initial position and thus the oscillations of the autocorrelation function approximately retain their initial strength, as shown in Fig. 3.7 (**a**). For a revival the terms proportional to the second derivative have to be a multiple of 2π. This leads to a revival for

$$T_{\mathrm{rev}} = 2\frac{2\pi\hbar}{|\mathcal{E}''_{\tilde{n}}|} = \frac{8\pi}{v_F}\sqrt{\frac{2\hbar|\tilde{n}|^3}{eB}} = 4|\tilde{n}|\, T_{\mathrm{cl}}, \tag{3.22}$$

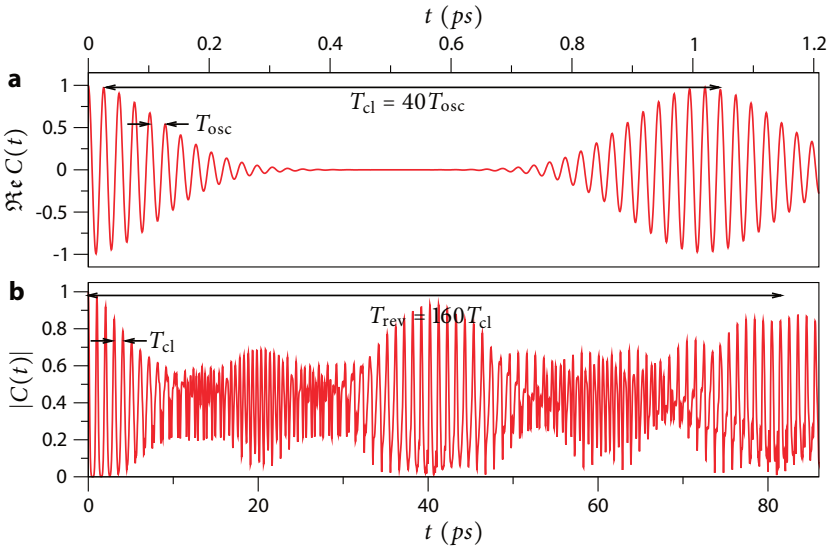

Figure 3.7. | Revivals in the autocorrelation function – a, The real part of the autocorrelation function $C(t)$ shows fast oscillations on the timescale T_{osc} and exhibits revivals every T_{cl} corresponding to the time of a classical cyclotron orbit ($\bar{n} = 20$ $\sigma = 1$, $B = 1\,\mathrm{T}$). **b,** The absolute value of the autocorrelation function shows a continuous peak structure depending on the classical cyclotron time T_{osc}. In the course of time the spread of the initially localized wave packet grows, leading to a uniform distribution which recovers to a full revival after T_{rev}, recognizable as more pronounced $|C(t)|$ peaks.

which is readily identifiable in the time-evolution for the absolute value of the autocorrelation function, as depicted in Fig. 3.7 (**b**). In the same manner, the revival hierarchy can be continued to higher orders of the Landau level expansion (3.18). In atomic physics the next time is the so-called "super revival time"

$$T_{\mathrm{super}} = 6\frac{2\pi\hbar}{|\mathcal{E}'''_{\bar{n}}|} = \frac{16\pi}{v_F}\sqrt{\frac{2\hbar|\bar{n}|^5}{eB}} = 8\bar{n}^2\,T_{\mathrm{cl}} = 2|\bar{n}|\,T_{\mathrm{rev}}. \tag{3.23}$$

The large range of different timescales, comparing the small phase oscillations with the final revival times, requires a highly accurate wave-packet propagation, since the phase of the propagated wave packet needs to be accurate for at least $4|\bar{n}|^2$ phase oscillations in the autocorrelation function. The used Chebychev propagation scheme, which will be introduced in Chapter 4.1.1, is well suited for this task, since the accumulated error is reduced by using only very few but long time steps.

3.2.3. Fractional revivals

Interestingly, we can also identify fractional revivals occurring between the full revivals [50] in the dynamics of the autocorrelation function [53]. For the first time,

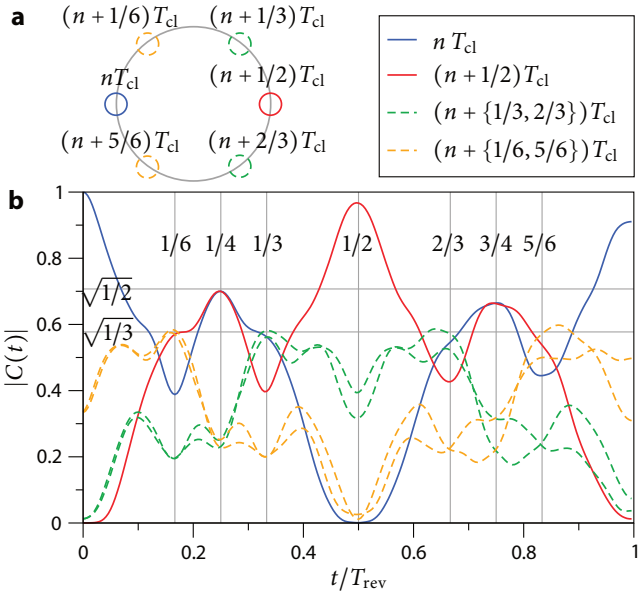

Figure 3.8. | Poincaré sections of the autocorrelation function
a, Sketch illustrating the correspondence between locations and timings of fractional revivals.
b, The autocorrelation function calculated for successive classical cyclotron times n and suitable subdivisions p/q ($\tilde{n}=60$, $\sigma=1$, $B=1\,\mathrm{T}$) featuring a full revival at $t=T_{rev}$, a mirror revival at $t=T_{rev}/2$ and several fractional revivals. For these times $\left|C\left((n+p/q)T_{cl}\right)\right|$ features local extremal points which are labeled in the plot.

fractional revivals were experimentally observed in Rydberg atoms [54]. The underlying phase effect can also be employed for prime number factorization [55, 56], which has recently been implemented in several experiments using various setups, like for example nuclear magnetic resonance spectroscopy [57], cold atoms [58] or optically with ultrashort laser pulses [59]. Note that the phase properties for wave packets in graphene differ from those of the aforementioned experiments so that the revival dynamics on graphene cannot be utilized for such tasks.

In order to extract the fractional revivals, it is advantageous to calculate the autocorrelation function in a Poincaré map for a step size given by the classical cyclotron time. Fig. 3.8 displays the fractional revivals for several points in time $t = (n + p/q)\,T_{cl}$, where n is an integer and p/q represents an irreducible fraction. Suitable fractions for different fractional revivals can be found by dividing a circle into equal sections, as depicted in Fig. 3.8 (**a**). For a full revival the autocorrelation function at $p/q = 0$ needs to be studied, whereas for $p/q = 1/2$ mirror revivals can be identified. Fractional revivals, which show a higher order rotational symmetry, like for example the triangular shape in Fig. 3.3 (**c**), can be extracted by time shifts of $p/q = 0$, $p/q = 1/3$, $p/q = 2/3$ and $p/q = 1/2$, $p/q = 1/6$, $p/q = 5/6$. The absolute value of the autocorrelation for these times is shown in Fig. 3.8 (**b**) and indicates moments which feature a revival. For example, a full revival, as displayed in Fig. 3.3 (**f**), takes place if the absolute value of the correlation for $p/q = 0$ reaches unity, which is the case for $t = T_{rev}$, as shown by the blue line in Fig. 3.8 (**b**). The revival for $t = 1/2\,T_{rev}$ has a minimum for $p/q = 0$ and a maximum for $p/q = 1/2$, thereby explaining the discrepancy between the classical center-of-mass and the quantum mechanical result. Fractional revivals with two peaks are visible at times $t = 1/4\,T_{rev}$ and $t = 3/4\,T_{rev}$. In this case the absolute value of the

autocorrelation function has to reach almost $\sqrt{1/2}$, which is the case for the blue and red line in Fig. 3.8 (**b**). Fractional revivals with a triangular shape, as shown in Fig. 3.3 (**c**), can occur in two different fashions. For the first type one maximum is located at the opposite side of the initial starting point, which is the case for the autocorrelation function at $p/q = 1/2$, $p/q = 1/6$, $p/q = 5/6$. At these points $|C(t)|$ reaches values up to $\sqrt{1/3}$, as depicted by the red and orange lines in Fig. 3.8 (**b**). This suggests the absolute value of the wave packet to be divided into three equal parts, which is also identifiable in the real-space picture of the wave packet in Fig. 3.8 (**c**). As a second possibility for a triangular revival the right phase constellation occurs for $p/q = 0$, $p/q = 1/3$, $p/q = 2/3$. Also the next higher fractional revivals like the four-fold state of Fig. 3.3 (**b**) can be extracted from the numerical data for higher fractions p/q.

3.3. Effect of impurities

To this day, the physical properties of experimentally available graphene are still strongly affected by several external influences like the substrate, impurities or ripples [60]. The highest mobilities, with mean free paths of up to $2\,\mu$m, are achieved in suspended graphene samples [61] or by means of ultraflat boron nitride substrates [62]. However, the remaining defects influence the electronic properties of graphene, and mask its low energy description by a single Dirac equation. For example, short-range disorder leads to resonant scattering and midgap states close to the Dirac point [63]. Furthermore, grain boundaries, yielding topological defects in large scale graphene flakes, can generate transport gaps [64]. Additionally, the mobility is reduced by the formation of intrinsic ripples which are supposed to stabilize the two-dimensional system [65]. Moreover, deformations of the hexagonal lattice can introduce additional spin-orbit interactions [30] as well as a position-dependent pseudo gauge-field [66, 67], which can reach values up to 300 Tesla in graphene nanobubbles [68].

In this thesis we restrict ourselves to the effect of long-range disorder by charged impurities, which is often used in literature since scattering between the valleys K and K′ is absent for this kind of disorder [69–71]. As a model we apply a Gaussian correlated random potential and analyze the propagation of a cyclotron wave packet through this perturbed environment. The potential is generated by the convolution of a random white noise potential U_n at each grid point $\boldsymbol{r}_n$ of a square lattice:

$$U_{\mathrm{imp}}(\boldsymbol{r}) = \sum_n U_n \exp\left(-\frac{|\boldsymbol{r}-\boldsymbol{r}_n|^2}{2\xi^2}\right). \tag{3.24}$$

The resulting potential features a vanishing average expectation value $\langle U_{\mathrm{imp}}(\boldsymbol{r})\rangle = 0$ and a variance of $\langle U_{\mathrm{imp}}(\boldsymbol{r})^2\rangle = U_0^2$. Furthermore, it is correlated on a length scale of ξ by means of $\langle U_{\mathrm{imp}}(\boldsymbol{r})U_{\mathrm{imp}}(\boldsymbol{r}')\rangle = U_0^2 \exp\left(-|\boldsymbol{r}-\boldsymbol{r}'|^2/(2\xi^2)\right)$. We focus on cases where the correlation length ξ is longer than the grid spacing leading to a potential which is a smooth function with respect to the graphene unit cell, resulting in a vanishing scattering probability between the two valleys.

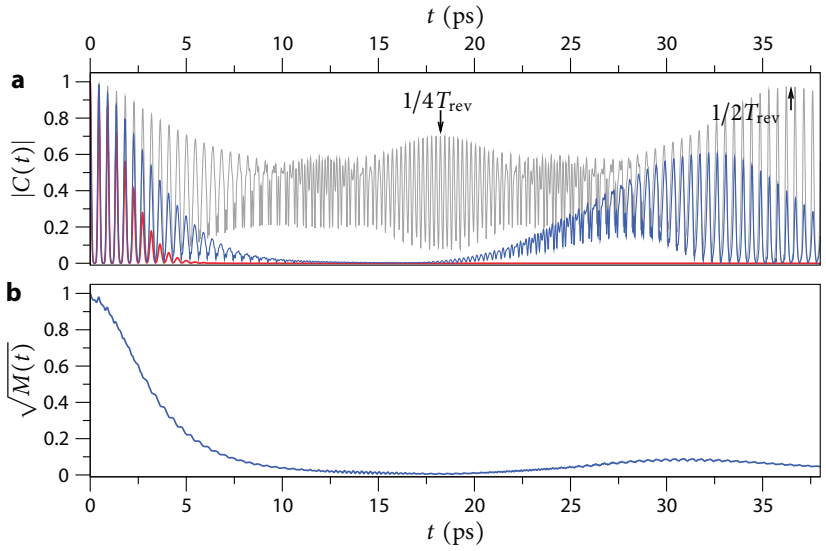

Figure 3.9. | Autocorrelation and fidelity in presence of impurities – a, Comparison between the autocorrelation function of two different impurity configurations (blue and red line, $\xi = 42\,\mathrm{nm}$, $U_0 = 5\,\mathrm{meV}$) and the autocorrelation function of the clean system (gray line). The numerical data shows that the potential strongly suppresses $|C(t)|$ of a cyclotron wave packet ($\bar{n} = 40$, $\sigma = 1$) after a few orbits in a magnetic field of $B = 10\,\mathrm{T}$. Revivals in the blue line are not due to the phase relations between the addends of equation (3.19) but stem from a global motion of the wave packet which by chance returns to the initial position. **b,** The fidelity $M(t)$ averaged over 10 different impurity configurations for the same initial cyclotron wave packet ($\bar{n} = 40$, $\sigma = 1$, $B = 10\,\mathrm{T}$) features a similar decay.

In the following, we study several impurity configurations and calculate the propagation of a wave packet with the same initial shape as the Landau level wave-packets used before in the clean system. First, we investigate the autocorrelation function, which generally vanishes much faster in the perturbed system compared to the results of the bare Dirac equation. The gray line in Fig. 3.9 (**a**) shows the autocorrelation function of the clean system with prominent revivals, whereas the autocorrelation function in the presence of an impurity potential decays after a few picoseconds, as depicted by the red and blue line. This phenomenon happens for many different setups and can be attributed to the local potential gradient at the origin of the initial state, leading to a drift of the wave packet. However, for some impurity configurations the wave packet returns to its initial position quite accidentally after some time, which is mainly determined by the impurity configuration. The return results in an increased autocorrelation function, but differs from the revivals occurring in the clean systems, since the revival time is not determined by the initial occupation of the Landau levels, but solely depending on the impurity potential.

As a measure for the deviation of the time evolution given by a disordered system

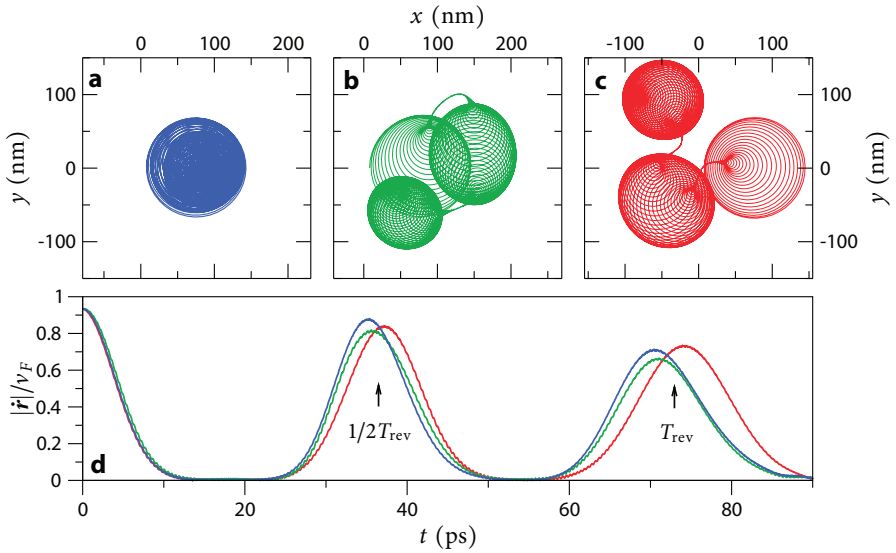

Figure 3.10. | Center-of-mass motion in presence of impurities – a-c, center-of-mass motion of a cyclotron wave packet ($\bar{n} = 40$, $\sigma = 1$, $B = 10\,\mathrm{T}$) for different impurity configurations ($\xi = 42\,\mathrm{nm}$, $U_0 = 5\,\mathrm{meV}$). The time-evolution shows the collapse of the localized wave packet by a shrinking spiral. The evenly distributed circular wave packet shows much smoother movement leading to a connecting line between two revivals. **d,** Velocity of the center-of-mass for the depicted wave-packet trajectories from above. The velocity approaches the Fermi velocity of graphene v_F for each revival. Revivals appear at the same time as in the clean system. Although the impurity potential reduces the velocity of the wave packet for $1/2T_{\mathrm{rev}}$ and T_{rev} the effect of revivals is still very pronounced in the time-evolution of the center-of-mass velocity.

compared to the clean system, we calculate the fidelity

$$M(t) = \left| \langle \psi(0) | \mathrm{e}^{\mathrm{i}\hat{\mathcal{H}}' t/\hbar} \mathrm{e}^{-\mathrm{i}\hat{\mathcal{H}} t/\hbar} | \psi(0) \rangle \right|^2 . \tag{3.25}$$

To this end, we track the overlap between the wave packet propagated by the perturbed Hamiltonian $\hat{\mathcal{H}}' = \hat{\mathcal{H}} + U_{\mathrm{imp}}$ and the propagation in the unperturbed Hamiltonian $\hat{\mathcal{H}}$. For the free electron gas, expressions are known which describe the fidelity decay in disordered systems for differently correlated impurity potentials [72]. We obtain similar numerical results, as shown in Fig. 3.9 (**b**). For short times the fidelity is approximately unity and then proceeds in an exponential decay. For longer propagation times, the fidelity does not follow the exponential decay when approaching zero, since there is a non-vanishing probability to return to the initial position due to the perpendicular magnetic field. However, we cannot infer from the autocorrelation function whether a wave-packet revival occurs or not, since the exponential fidelity decay removes all relevant information from the calculated data.

Consequently, we have to find other observables which characterize the revivals even if an impurity potential is present. One particularly suitable observable is the center-

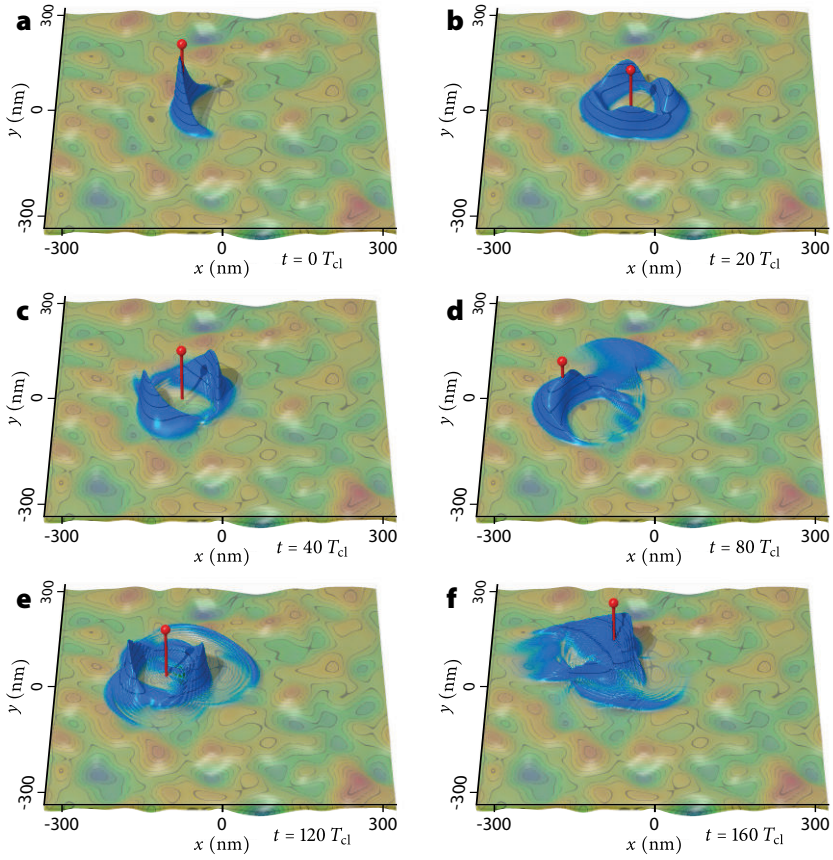

Figure 3.11. | Revivals and fractional revivals in an impurity potential – The red pin marks the quantum mechanical center-of-mass ($\xi = 42\,\mathrm{nm}$, $U_0 = 5\,\mathrm{meV}$). **a,** The initial wave packet with a Gaussian eigenstate contribution ($\bar{n} = 40$, $\sigma = 1$). The magnetic field $B = 10\,\mathrm{T}$ leads to a Poincaré cyclotron time of $T_{\mathrm{cl}} \approx 0.32\,\mathrm{ps}$. During the time evolution the center-of-mass collapses to the center of a circular wavefunction featuring pronounced revivals. In panel (**b**) a quarter revival occurs at $t = 1/2\bar{n}\,T_{\mathrm{cl}}$ and in panel (**c**) a half revival at $t = \bar{n}\,T_{\mathrm{cl}}$. After a certain time a localized wave packet emerges again and (**d**) shows a mirror revival for $t = 2\bar{n}\,T_{\mathrm{cl}}$. In this case some part of the wavefunction is already detached from the localized cyclotron wave packet. **e,** The center-of-mass collapses again and forms a fractional revival. **f,** The full revival, where the semiclassical and the quantum mechanical center-of-mass coincide, occurs at $t = 4\bar{n}\,T_{\mathrm{cl}}$. At this time the wavefunction shows pronounced branches. However, the probability distribution is clumped around the center-of-mass showing the characteristics of a revival in the velocity expectation value.

of-mass motion of the wave packet. In Fig. 3.10 (**a-c**) the center-of-mass motion of a Dirac wave packet is shown for different impurity potentials. In Fig. 3.10 (**a**) the impurity potential is chosen such that the wave packet does not drift away from its origin and thus the revivals occur on top of each other. This leads to a revival in the autocorrelation function shown as blue line in Fig. 3.9 (**a**), which has nothing in common with the wave-packet revivals of the clean system, since the revival time depends crucially on the exact choice of the impurity potential. However, for the majority of the disorder configurations the time evolution features a drift of the wave packet, as shown in Fig. 3.10 (**b,c**). In all cases the wave packet moves at the beginning on a shrinking spiral, since the center-of-mass is located at the position with the highest probability density [see Fig. 3.11 (**a**)]. Already at this state of the time evolution, the center of the spiral shows a random drift. After a few picoseconds, the center-of-mass collapses to the center of a rotating circular wave packet, as shown in Fig. 3.11 (**b,c**). In the following, the wave packet is moving without oscillations on a smooth line, because the density is equally distributed along a circular orbit. As in the clean system, the first revival occurs as a mirror revival at the time $1/2\, T_{\mathrm{rev}}$ and as a full revival at T_{rev}. In order to remove the structure of the impurity potential form the center-of mass motion, it is advantageous to extract its corresponding velocity

$$\boldsymbol{v}(t) = \frac{\partial}{\partial t}\langle\psi(t)|\hat{\boldsymbol{r}}|\psi(t)\rangle, \tag{3.26}$$

which is shown in Fig. 3.10 (**d**). The initial wave packet moves on a circular orbit with a velocity slightly smaller than the "speed of light" of graphene. During the timespan of a collapse, this velocity drops down to the drift velocity of the wave packet, which is governed by the potential gradient and thus at least two orders of magnitude smaller. The revivals occur at the same time for all the impurity configurations, as shown by the common peak for different impurity configurations in Fig. 3.10 (**d**). However, fractional revivals cannot be extracted from the center-of-mass motion but are nevertheless present, as displayed by the shapes of the wavefunction for different times in Fig. 3.11.

3.4. Pump-probe detection

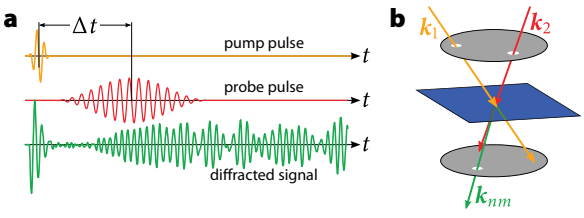

Figure 3.12. | Pump-probe setup **a,** Electric field of a pump and probe laser delayed by Δt, resulting in a persistent diffracted signal. **b,** Geometry of pump and probe wave vector $\boldsymbol{k}_1$ and $\boldsymbol{k}_2$ impinging on a sheet of graphene, leading to the diffracted signal $\boldsymbol{k}_{nm}$ selected by an aperture.

In Ref. [37] the center-of-mass motion of a wave packet was employed to establish a dipole moment, which is closely connected to external electric radiation fields and may

serve as an experimentally accessible observable for the *zitterbewegung* of the electrons in graphene. In case of wave-packet revivals, it seems reasonable that this dipole moment can be used likewise to reveal the different revival states, since it is maximal during a revival and almost zero when the wave packet is collapsed, similar to the velocity of the wave packet in Fig. 3.10 (**d**). In the following, we propose a pump-probe setup using two laser pulses separated by a time delay Δt to reveal wave-packet revivals in a graphene system, as sketched in Fig. 3.12. At first, we determine in Section 3.4.1 the influence of a femtosecond laser pulse with a wave vector $\boldsymbol{k}_1$. This pump pulse can be chosen such that the generated excited state populates high Landau levels, leading to wave-packet revivals in the course of the subsequent picoseconds. By varying the delay time Δt of the second laser pulse with a slightly different wave vector $\boldsymbol{k}_2$, we examine the higher-order diffracted signals arising in a four-wave-mixing setup, which display a close connection to the underlying revival dynamics, as we will demonstrate in Section 3.4.2.

In a four-wave-mixing arrangement higher order processes, which are induced by an interaction of at least four photons, are selectively probed by an arrangement of different lasers and apertures, as sketched in Fig. 3.12 (**b**). The system is excited by two laser pulses corresponding to the wave vectors $\boldsymbol{k}_1$ and $\boldsymbol{k}_2$. The total diffracted radiation contains several higher order signals, which can be separately probed by an aperture. In this way only photons with an outgoing wave vector $\boldsymbol{k}_{nm} = n\boldsymbol{k}_1 + m\boldsymbol{k}_2$ can reach the detector, as shown in Fig. 3.12 (**b**). A typical pump-probe experiment combines a short laser pulse with a wave-vector $\boldsymbol{k}_1$, used to excite the system, with a second time-delayed laser pulse with a wave vector $\boldsymbol{k}_2$, which probes the system at a later time. Time-resolved signals can be recorded by repeating the pulse sequence with different delay times Δt, allowing for an indirect determination of the time evolution by an integrating measurement of the emitted radiation in to the direction $\boldsymbol{k}_{nm}$. Since the connection between the shape of a wave packet performing a revival and the diffracted signal for a delay Δt is by no means obvious, we have extended a scheme used in theoretical chemistry [73] to calculate non-perturbatively the occurring time-resolved pump-probe signals of a four-wave mixing experiment. To this end, we calculate the time evolution of a system in presence of two lasers pulses for different phases of the laser and extract from the polarization response the diffracted radiation in certain directions. A detailed explanation of this scheme will be presented in the following section. The results suggest a pump-probe setup as a promising way to measure wave-packet revivals in a sheet of graphene, since the diffracted radiation, which is typically determined in time-resolved experiments, shows clear-cut signatures of wave-packet revivals.

3.4.1. Excitation into high Landau levels

The developments in ultrafast optics allow for the generation of ultraintense laser pulses with durations as short as a few femtoseconds. As a result, the associated electric field

only oscillates a few cycles with respect to the laser carrier frequency, as sketched in Fig. 3.12 (**a**) for the pump pulse. At the turn of the millennium such pulses became routinely available, and have been even shortened to a few hundred attoseconds [74, 75], allowing for example a tracking of the electron motion on the atomic scale [76]. In the following, we will employ such few-cycle laser pulses for the optical excitation of wave-packet revivals in graphene. A recent review about the theoretical modeling of ultrashort laser pluses can be found in Ref. [77]. Advances in the experimental realization of attosecond pulses steering the electronic motion in atoms, molecules and nanostructures are reviewed in Ref. [78].

At first, we study how an initial state at the Fermi level can be excited into a high Landau level by means of a single ultrashort laser pulse. Therefore we assume the Fermi level to be located at zero energy and search for maximally localized wave packets representing this state. The Landau level eigenstates (2.12), calculated in the previous chapter, are chosen to be infinitely extended by a plain wave part resulting from the translational invariance in x-direction, due to the Landau gauge. In order to get localized initial states we integrate different plane waves to form a Gaussian wave packet by

$$\psi(x,y) = \frac{1}{\sqrt{2\pi}} \int_{-\infty}^{\infty} \psi_k(x,y)\, \pi^{-1/4} \mathrm{e}^{-\frac{1}{2}k^2 l_B^2}\, dk. \tag{3.27}$$

For the Landau level at zero energy this results in the wave packet[1]

$$\psi(x,y) = \frac{1}{\sqrt{2\pi}a_0} \mathrm{e}^{-\frac{x^2+2\mathrm{i}xy+y^2}{4a_0^2}} \begin{pmatrix} 0 \\ 1 \end{pmatrix}, \tag{3.28}$$

which serves as initial state for the following calculations.

The electric field of a short laser pulse i peaked at time t_i with a carrier frequency ω_i and a wave vector $\boldsymbol{k}_i$ can be described by

$$\boldsymbol{E}_i(\boldsymbol{r},t) = \mathfrak{Re}\left(\boldsymbol{\epsilon}_i\, f_i(t-t_i)\, \mathrm{e}^{\mathrm{i}(\boldsymbol{k}\boldsymbol{r}-\omega_i(t-t_i))}\right), \tag{3.29}$$

where the product of polarization and amplitude is given by $\boldsymbol{\epsilon}_i$ [77]. The circularly polarized pump pulse used for the excitation of the initial state is described by the complex-valued polarization $\boldsymbol{\epsilon}_i = E_i(\boldsymbol{e}_x + \mathrm{i}\boldsymbol{e}_y)/\sqrt{2}$, and the temporal restriction is modeled by the envelope function

$$f_i(t) = \begin{cases} \sin\left(\pi\, t/\tau_i\right)^2, & \text{if } 0 < t < \tau_i \\ 0, & \text{else} \end{cases}, \tag{3.30}$$

on a timescale of τ_i. This envelope strictly suppresses the electrical field for times larger than the main pulse duration, which is numerically advantageous, since a highly

[1] Note, this initial state is given in Landau gauge. However, the numerical calculations are carried out in a symmetric gauge, since the error is equally distributed on both momentum directions. Applying the gauge transformation on the initial state compensates the phase term $2\mathrm{i}\,xy$ in the exponent, leading to a real wavefunction.

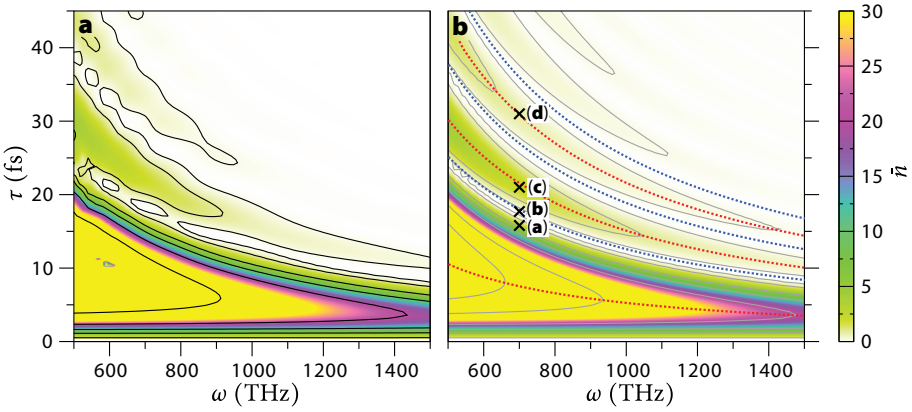

Figure 3.13. | Average occupied Landau level by laser excitation – Both panels show the final Landau level index in a perpendicular magnetic field of $B = 8\,\mathrm{T}$ after a circularly polarized laser pulse of peak field $E_1 = 700\,\mathrm{kV/cm}$ with different laser frequency ω and pulse length τ. The color code represents the final Landau level $\tilde{n}$. **a,** Quantum mechanical result calculated by a mixed Lanczos and Chebychev propagation, see Section 4.1.1 and 4.1.3. The average Landau level is extracted using Eq. (3.32). **b,** Classical time-evolution by a Gragg-Bulirsch-Stoer algorithm leading to a final Landau level given by Eq. (3.35). Black crosses represent the pulse properties used for the classical trajectories in Fig. 3.14. Dashed lines show the expected maxima (red) and minima (blue) of Eq. (3.36).

efficient Chebychev propagator can be used for the time evolution after the laser pulse. During the pulse the timeline is split into sufficiently small steps of $dt = 0.1\,\mathrm{fs}$ and the propagation is calculated with a Lanczos algorithm [79], which will be introduced in Chapter 4.1.3.

The influence of an external laser field is commonly incorporated into the time independent Hamiltonian by means of two different gauges: The length gauge or the velocity gauge [80]. Here, we employ the length gauge which couples the time-dependent electric field $\boldsymbol{E}(t)$ of the radiation into the Dirac Hamiltonian (2.10) with the dipole operator $\boldsymbol{\mu}$, leading to the time-dependent Hamiltonian

$$H_\tau(t) = H_\tau + \boldsymbol{\mu} \cdot \boldsymbol{E}(t). \tag{3.31}$$

To this end, we use a dipole approximation which assumes a weak spacial variation of the applied laser field in comparison to the spread of the wave packet. This is justified for wave vectors $\boldsymbol{k}_i$ perpendicular to the graphene layer, leading to a location-independent description of the electric field $\boldsymbol{E}(\boldsymbol{r}, t) \approx \boldsymbol{E}(t)$. Since the circular field of the pump laser is preserving the translational invariance of the system, we can use a single origin $\boldsymbol{r} = 0$ for the dipole approximation without loss of generality.

In the following, we study how a short mid-infrared laser pulse excites an initial zero-energy state (3.28) into a high Landau level. For this purpose, we calculate the exact time evolution in presence of the laser field by a Lanczos propagation algorithm and

extract the energy distribution $D(E)$ of the wave packet after the application of the laser pulse. This allows for the calculation of the average occupied Landau level

$$\bar{n}_{\mathrm{quant}} = \int D(E) \frac{E^2}{2v_F^2 eB\hbar} \mathrm{d}E. \tag{3.32}$$

For sufficiently short pulse durations τ the initial zero-energy state is strongly excited into states with a Landau level index higher than 30, as shown for short- to mid-infrared laser frequencies in Fig. 3.13 (**a**). For longer pulse durations fringes with alternating strength of the average excited Landau level are emerging. To gain insight into the excitation process, we study the time evolution of the associated classical system governed by the two coupled differential equations for the position $\boldsymbol{r}$ and the momentum $\boldsymbol{k}$ of a charged particle:

$$\dot{\boldsymbol{r}} = \frac{\partial \mathcal{E}(\boldsymbol{k})}{\hbar \partial k} - \dot{\boldsymbol{k}} \times \boldsymbol{\Omega}(\boldsymbol{k}), \tag{3.33a}$$

$$\hbar \dot{\boldsymbol{k}} = -e\boldsymbol{E}(t) - e\dot{\boldsymbol{r}} \times \boldsymbol{B}. \tag{3.33b}$$

The electric field $\boldsymbol{E}(t)$ of the laser as well as the Lorentz force exerted by the magnetic field $\boldsymbol{B}$ enter the differential equations similarly to free electrons. The special electronic properties of graphene are considered by the band dispersion $\mathcal{E}(\boldsymbol{k})$ and the Berry curvature $\boldsymbol{\Omega}$, which is absent for graphene without mass gap [81]. Consequently, the only graphene specific component in this level of approximation is the momentum derivative of the band dispersion

$$\frac{\partial \mathcal{E}}{\hbar \partial k} = v_F \frac{\boldsymbol{k}}{|\boldsymbol{k}|}, \tag{3.34}$$

which indicates that electron-like particles travel with speed of light in momentum direction, and hole-like particles perform the opposite motion against the momentum direction. We solve this set of coupled equations for an initial state in the zeroth Landau level ($\boldsymbol{k} = \boldsymbol{r} = 0$) in presence of a laser pulse (3.29) using a numerical integration with a Gragg-Bulirsch-Stoer algorithm [82]. From the momentum after the pulse we extract the final Landau level index

$$\bar{n}_{\mathrm{cl}} = \frac{\hbar k^2}{2eB}, \tag{3.35}$$

as color coded in Fig. 3.13 (**b**). A comparison between the results of the quantum and the classical calculation reveals only small deviations, which arise especially for long pulse lengths. However, we are not interested in long pulses, since the resulting excited Landau level is generally not sufficiently high to feature wave-packet revivals in this limit.

The trajectories during the pump pulse give information about the dynamics of the excitation process from the zeroth Landau level, as shown in Fig. 3.14. For strong laser pulses, the center of mass follows directly the electric field of the laser, leading to small circles in the trajectories. After the pump process, the radius of the final orbit depends

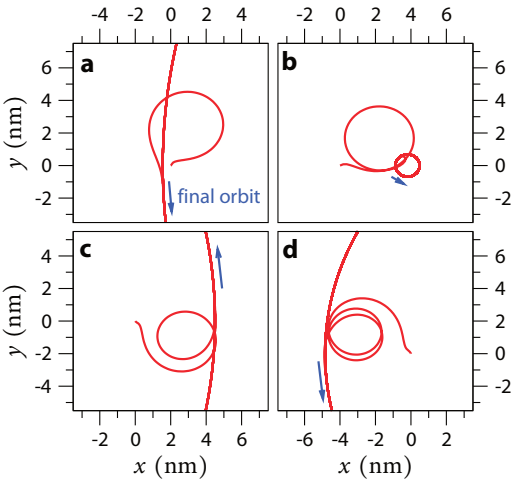

Figure 3.14. | Trajectories of a pumping event – Classical pumping from the zeroth Landau level in a perpendicular magnetic filed $B = 8\,\mathrm{T}$ for a circularly polarized laser pulse of peak field $E_1 = 700\,\mathrm{kV/cm}$ and central frequency $\omega = 700\,\mathrm{THz}$. Panels (**a**-**d**) show different pulse durations. **a,** The trajectory traverses a three-quarter cycle during the pump pulse leading to a circular orbit with big radius (blue arrow, only partial segment is shown) equivalent to a high Landau level ($\tau = 16\,\mathrm{fs}$). **b,** Trajectory produces a full cycle resulting in a negligible energy transfer ($\tau = 18\,\mathrm{fs}$). **c,** 1.5-cycle ($\tau = 21\,\mathrm{fs}$) **d,** 2.5-cycle ($\tau = 31\,\mathrm{fs}$).

strongly on the deposited energy during the pump event. One criterion for the energy transfer is the average electric field $\langle \boldsymbol{E} \rangle$ of the laser pulse. For the used pulse shape this leads to

$$\langle \boldsymbol{E} \rangle \propto \int \mathrm{e}^{\mathrm{i}\omega t} f(t) dt = -\frac{4\sin(\tau\omega\pi/2)}{\tau^2\omega^2 - 4}. \tag{3.36}$$

The maxima and minima of this expression readily deliver the extrema of the average occupied Landau levels $\bar{n}$, as sketched by the red and blue dotted lines in Fig. 3.13 (**b**). However, the final Landau level also depends nontrivially on the other external parameters, like the magnetic field, the laser frequency and the peak electric field. The numerical calculations demonstrate that for sufficiently short pulse durations τ excitations much higher than the 30th Landau level can be achieved, as shown in Fig. 3.13 (**a**). Such highly excited states are best generated by single-cycle laser pulses, which are experimentally challenging, but have already been achieved in a few setups [74, 75]. However, excitations into lower Landau levels are sufficient for a detection of the mirror revival in the center-of-mass motion, which can be obtained by few-cycle laser pulses, as suggested by the excitation fringes in Fig. 3.13 (**a**).

3.4.2. Four-wave mixing

In the following we study the relation between the revivals of wave packets on a sheet of graphene in a perpendicular magnetic field and the full polarization dynamics, which can be probed by angle-resolved pump-probe spectroscopy. Therefore, we consider the interaction of a sheet of graphene with two lases pulses separated by a variable time delay Δt and calculate the diffracted radiation arising in a typical four-wave-mixing experiment. In doing so we extract from the non-perturbative time-evolution of wave packets the dependence of the 16 strongest diffracted signals on the time delay Δt, which is adopted from a scheme used in theoretical chemistry [83] and will be introduced in this section.

The subsequent calculations contain a second probe laser, which is added to the total applied time-dependent electric field

$$\boldsymbol{E}(\boldsymbol{r},t) = \sum_{i=1}^{2} \boldsymbol{E}_i(\boldsymbol{r},t). \tag{3.37}$$

For this second laser we choose the same carrier frequency $\omega_2 = \omega_1$, but a linear polarization $\boldsymbol{\epsilon}_2 = E_2\,\boldsymbol{e}_x$ with a much weaker peak electric field E_2. The pulse duration τ_2 of the second laser is prolonged compared to the first pulse and delayed in time by $\Delta t = t_2 - t_1$. Furthermore, the wave vector $\boldsymbol{k}_2$ of the probe laser must differ from the wave vector $\boldsymbol{k}_1$ of the pump laser to allow for a separation of the generated higher-order diffracted signals in a four-wave mixing setup.

The response of the electrons on the two laser pulses can be described by the polarization of the system, which is given by the expectation value of the dipole moment $\boldsymbol{\mu}$:

$$\boldsymbol{P}(\boldsymbol{r},t) = \langle\psi(t)|\boldsymbol{\mu}|\psi(t)\rangle. \tag{3.38}$$

Conventionally, this polarization is calculated by means of time-dependent perturbation theory, which separates the time evolution of the initial state into different order processes given by a recursive N-fold propagation of the state

$$\psi^{(N)}(\boldsymbol{r},t) = \frac{\mathrm{i}}{\hbar}\int_{-\infty}^{t} dt' \mathrm{e}^{-\mathrm{i}H_\tau(t-t')/\hbar}\boldsymbol{\mu}\boldsymbol{E}(t')\psi^{(N-1)}(\boldsymbol{r},t). \tag{3.39}$$

As a result, the polarization response can be expressed by the perturbative expansion

$$\boldsymbol{P}(\boldsymbol{r},t) = \sum_{N} \boldsymbol{P}^{(N)}(\boldsymbol{r},t), \tag{3.40}$$

which comprises the polarizations $\boldsymbol{P}^{(N)}$ of order N containing all processes involving N photons respectively. The different contributions are given by the expectation value of the dipole moment $\langle\psi^{(M)}(\boldsymbol{r},t)|\boldsymbol{\mu}|\psi^{(M')}(\boldsymbol{r},t)\rangle$, which are depending on the perturbative time evolution $\psi^{(M)}(\boldsymbol{r},t)$ and $\psi^{(M')}(\boldsymbol{r},t)$, leading to a total order $N = M + M'$. Consequently the linear polarization is given by

$$\boldsymbol{P}^{(1)}(\boldsymbol{r},t) = \left\langle\psi^{(0)}(\boldsymbol{r},t)\middle|\boldsymbol{\mu}\middle|\psi^{(1)}(\boldsymbol{r},t)\right\rangle + \text{h.c.}\,, \tag{3.41}$$

which describes the absorption of a single photon. Since the polarization response of all processes with an even amount of involved photons vanishes, the first non-linear term is given by

$$\boldsymbol{P}^{(3)}(\boldsymbol{r},t) = \left\langle\psi^{(0)}(\boldsymbol{r},t)\middle|\boldsymbol{\mu}\middle|\psi^{(3)}(\boldsymbol{r},t)\right\rangle + \left\langle\psi^{(1)}(\boldsymbol{r},t)\middle|\boldsymbol{\mu}\middle|\psi^{(2)}(\boldsymbol{r},t)\right\rangle + \text{h.c.}\,. \tag{3.42}$$

This expression contains processes involving three photons, known as coherent emission, stimulated emission and stimulated Raman. Further higher-order events can be calculated likewise by the perturbative N-fold time evolution [84, 85].

If the wave vectors $\boldsymbol{k}_1$ and $\boldsymbol{k}_2$ of the two laser pulses are different, the resulting photon processes can be further separated by the final wave vector $\boldsymbol{k}_{nm}$, which allows for the selective measurement of higher-order process in experimental setups. The perturbative polarization of Eq. (3.40) separated into N photon processes can also be regrouped into different total wave vectors $\boldsymbol{k}_{nm}$ by

$$\boldsymbol{P}(\boldsymbol{r},t) = \sum_N \boldsymbol{P}^{(N)}(\boldsymbol{r},t) = \sum_{n,m} \boldsymbol{P}_{nm}(t) \mathrm{e}^{\mathrm{i}(n\boldsymbol{k}_1 + m\boldsymbol{k}_2)\boldsymbol{r}} = \sum_{\boldsymbol{k}_{nm}} \boldsymbol{P}_{nm}(t) \mathrm{e}^{\mathrm{i}\boldsymbol{k}_{nm}\cdot\boldsymbol{r}}. \tag{3.43}$$

The resulting wave vectors $\boldsymbol{k}_{nm} = n\boldsymbol{k}_1 + m\boldsymbol{k}_2$ represent the processes absorbing or emitting $n, m \in \mathbb{Z}$ photons of the first and second laser pulse, respectively. A selective measurement of different diffraction directions $\boldsymbol{k}_{nm}$ can be achieved experimentally by using apertures that blank out all directions except the one corresponding to the higher-order signal of interest, as sketched in Fig. 3.12 (**b**). Thereby small signals can be extracted from the total polarization, which is usually dominated by unscattered photons and first-order processes. Furthermore, photodetectors usually do not allow for a time-resolved tracking of the polarization, but measure the time-integrated radiated energy. From a classical point of view, this energy is given by the energy change $\dot{W}$ of the system, which can be determined by the expectation value of the Hamiltonian [85]

$$\dot{W} = \frac{\partial}{\partial t} \langle \psi(t) | H(t) | \psi(t) \rangle. \tag{3.44}$$

However, the numerical calculations do not take into account energy changes due to emission of photons and consequently we rely on the approximation

$$\dot{W} \approx \langle \psi(t) | \boldsymbol{\mu} \cdot \dot{\boldsymbol{E}}(t) | \psi(t) \rangle = \boldsymbol{P}(t) \cdot \dot{\boldsymbol{E}}(t). \tag{3.45}$$

Following this, we assume the total emitted intensity I and the intensity I_{nm} emitted into the direction $\boldsymbol{k}_{nm}$ to be given by

$$I = \int \boldsymbol{P}(t) \cdot \dot{\boldsymbol{E}}(t)\, dt \quad \text{and} \quad I_{nm} = \int \boldsymbol{P}_{nm}(t) \cdot \dot{\boldsymbol{E}}(t)\, dt. \tag{3.46}$$

The scheme using the perturbative time evolution to gain different angular resolved polarization signals $\boldsymbol{P}_{nm}$ is especially applicable if only low-order processes are excited by the laser pulses. For more complicated systems and higher excitations a non-perturbative method was introduced in theoretical chemistry to calculate the spectra of molecules [83, 86] and has been further extended to include four-wave mixing setups [87–89], which we will apply to calculate the pump-probe response of graphene.

In the following we want to show that all orders of the polarization components $\boldsymbol{P}_{nm}$ can be extracted from non-perturbative wave-packet calculations. Therefore, we go back to the application of the dipole approximation $\boldsymbol{E}(\boldsymbol{r},t) \approx \boldsymbol{E}(t)$. It is well suited to assume a position independent electric field $\boldsymbol{E}(t)$, since the extent of the wave packet (3.28) and the cyclotron radius are much smaller than the spacial variation of the electric field due to $\mathrm{e}^{\mathrm{i}\boldsymbol{k}\boldsymbol{r}}$. For the following numerical calculations we use an

Table 3.1. | Considered photon processes – All photon processes $\alpha_i = (n, m)$ considered in the calculation for the pump-probe polarization $\boldsymbol{P}_{\alpha_i}$ of Eq. (3.48) shown in Fig. 3.15.

	1	2	3	4	5	6	7	8	9	10	11	12	13	14	15	16
n	1	2	1	3	0	2	4	2	-1	-2	-1	-3	0	-2	4	-2
m	0	-1	-2	-2	1	-3	3	1	0	1	2	2	-1	3	-3	-1

experimentally reasonable magnetic field of $B = 8\,\mathrm{T}$, which corresponds to an initial zero-energy state with an extent of about 10 nm.[2] The system is probed by a laser with a carrier frequency of $\omega = 700\,\mathrm{THz}$, leading to a spacial variation of the laser field with a periodicity of about 4000 nm, if the laser is tilted away from perpendicular incidence by 10°. As a consequence, it is justified to use the approximation $\mathrm{e}^{\mathrm{i}\boldsymbol{kr}} \approx 1$, since the spacial variation of $\boldsymbol{E}(\boldsymbol{r}, t)$ occurs on a length scale, which is a few orders of magnitude larger than the dimensions of the area the wave packet is exploring during the propagation. However, due to the translational invariance of the graphene sheet we are not restricted to $\boldsymbol{r} = 0$ as origin for the dipole approximation and therefore any starting point $\boldsymbol{r}_s$ of the initial wave packet can be chosen. The scalar products $\boldsymbol{k}_1\boldsymbol{r}_s = \varphi_1$ and $\boldsymbol{k}_2\boldsymbol{r}_s = \varphi_2$ in the definition of the electric field (3.29) of the two laser pulses can be replaced by two phases $\Phi = (\varphi_1, \varphi_2)$. By means of numerical propagation of wave packets under the influence of different laser phases Φ, we are able to calculate the time evolution of the polarization $\boldsymbol{P}(t, \varphi_1, \varphi_2)$. In this way it is possible to extract the direction-dependent polarization

$$\boldsymbol{P}_{nm}(t) = \frac{1}{(2\pi)^2} \int_0^{2\pi} \mathrm{d}\varphi_1 \int_0^{2\pi} \mathrm{d}\varphi_2 \mathrm{e}^{-\mathrm{i}(n\varphi_1 + m\varphi_2)} \boldsymbol{P}(t, \varphi_1, \varphi_2), \tag{3.47}$$

using a two-dimensional Fourier transform [83].

For moderate laser peak fields E_1 and E_2 higher-order processes, involving more than eight photons of a single laser, are strongly suppressed. As a result, we are able to restrict the number of phases φ_1 and φ_2 to a limited set and apply a discrete Fourier transform. For the results of the pump-probe calculations we present in the following, only processes involving four photons of the pump and the probe laser are considered, which requires the calculation of 8×8 independent propagations. A comparison between results using 16×16 instead of 8×8 phases revealed no change of the various polarizations $\boldsymbol{P}_{nm}$, suggesting that processes with a total of more than eight photons are very unlikely.

The numerical effort can be further reduced if all impossible or strongly suppressed processes are explicitly forbidden in the Fourier transform. A closer look reveals that only a few signals contribute significantly to the total polarization which allows us to express the phase dependent polarization by

$$\boldsymbol{P}(t, \Phi_j) = \sum_i \mathrm{e}^{\mathrm{i}\Phi_j\alpha_i} \boldsymbol{P}_{\alpha_i}(t). \tag{3.48}$$

[2] The extent of higher order Landau levels grows with $\sqrt{n}$.

Table 3.2. | Set of phases for pump-probe calculation – Restricted set of phases $\Phi_j = (\varphi_1, \varphi_2)$ allowing for the extraction of all photon processes summarized in Table 3.1 from the phase-dependent polarization $\boldsymbol{P}(t, \Phi_j)$ by means of Eq. (3.48).

	1	2	3	4	5	6	7	8
$\varphi_1/2\pi$	0	1/4	0	0	1/8	1/8	1/8	0
$\varphi_2/2\pi$	0	0	1/4	1/2	0	1/8	1/4	1/8
	9	10	11	12	13	14	15	16
$\varphi_1/2\pi$	1/8	1/8	1/2	3/4	1/4	3/4	5/8	1/2
$\varphi_2/2\pi$	3/8	5/8	1/8	1/4	5/8	5/8	0	7/8

We assume that the first 16 contributions $\alpha_i = (n, m)$ summarized in Table 3.1 are sufficient to describe the direction dependent polarization $\boldsymbol{P}_{\alpha_i}$. Based on this selection we search for the minimal set of phases Φ_j, allowing for an extraction of all polarization signals. This corresponds to the determination of a set Φ_j, which creates an invertible matrix $(\exp(\mathrm{i}\Phi_j\alpha_i))_{ij}$. The set of phases we use to extract the relevant $\boldsymbol{P}_{nm}$ are summarized in Table 3.2. This method allows an efficient calculation of all important higher-order polarization signals and reduces the computational effort, as forbidden and negligibly small contributions are removed from the calculation.

In the following, we use this method to calculate the signatures of wave-packet revivals in the pump-probe signals of a four-wave mixing experiment. Therefore, we employ a short circular-polarized pumping laser, whose pulse duration $\tau_1 = 17\,\mathrm{fs}$ and frequency $\omega_1 = 700\,\mathrm{THz}$ is chosen based on the calculation of the average occupied Landau level presented in Fig. 3.13 (**a**), such that the resulting excited state performs wave-packet revivals. By modifying the laser intensity and the associated peak electric field E_1 the timing of the revival can be tuned, as displayed in Fig. 3.15 (**a-c**). The three panels show the center-of-mass motion of the x-coordinate (gray line) as well as the time-evolution of the oscillation radius (blue line) without second probe pulse. For the weakest electric field $E_1 = 500\,\mathrm{kV/cm}$ of the pump laser the excited state features an average Landau level of $\bar{n} \approx 11$ leading to a revival time of $T_{\mathrm{rev(CM)}} \approx 6\,\mathrm{ps}$. This is in good correspondence with the center-of-mass motion shown in Fig. 3.15 (**a**). With increasing peak field of $E_1 = 700\,\mathrm{kV/cm}$ ($E_1 = 900\,\mathrm{kV/cm}$) the Landau level index rises to $\bar{n} \approx 20$ ($\bar{n} \approx 29$) providing a revival time of $T_{\mathrm{rev(CM)}} \approx 15\,\mathrm{ps}$ ($T_{\mathrm{rev(CM)}} \approx 25\,\mathrm{ps}$). For such high excitations the revival is very pronounced and the motion during the collapse is strongly suppressed, as depicted by Fig. 3.15 (**b,c**).

Subsequently we add a probe laser with a peak intensity of $E_2 = 2\,\mathrm{kV/cm}$ and a pulse length of $\tau_2 = 50\,\mathrm{fs}$ to study the different diffracted signals. In experimental pump-probe setups the relation between the diffracted radiation in the direction of a certain wave vector $\boldsymbol{k}_{nm}$ and the delay time $\Delta t = t_2 - t_1$ between the two laser pulses is studied. By means of the time-dependent polarization $\boldsymbol{P}_{nm}(t)$ and the electric field of the laser

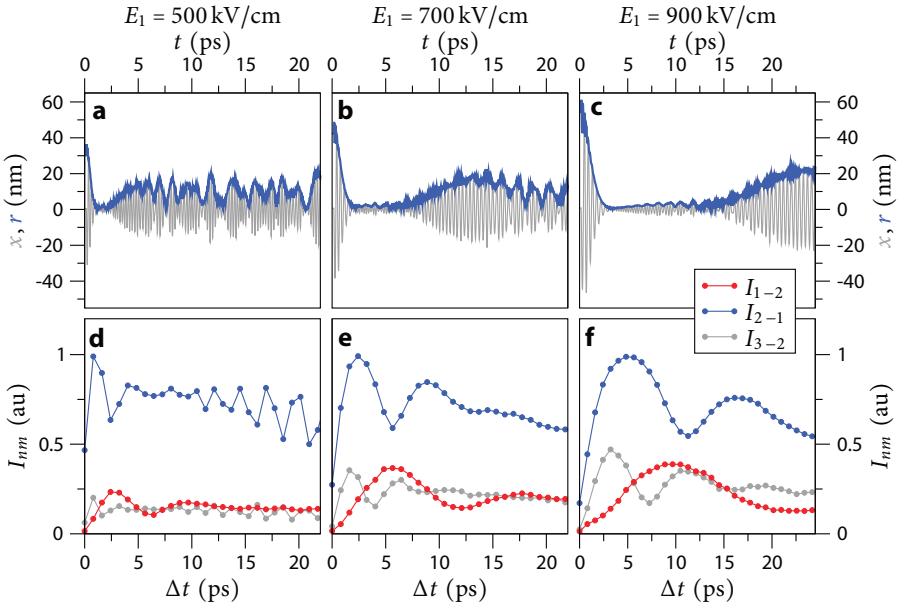

Figure 3.15. | Revival signatures in pump-probe signals – a-c, Center-of-mass motion $x(t)$ and radius of the motion $r(t)$ for a wave packet (3.27) initially in the lowest Landau level excited by a circularly polarized pump laser ($\tau_1 = 17$ fs, $\omega_1 = 700$ THz). The time evolution reveals pronounced revival features in the considered observables ($B = 8$ T). **d-f,** Corresponding higher-order integrated four-wave mixing signals I_{nm} induced by a probe laser ($\tau_1 = 50$ fs, $E_2 = 2$ kV/cm) with a variable time delay Δt.

pulses $\boldsymbol{E}(t)$ the integrated intensity is given by [85]

$$I_{nm}(\Delta t) = \int_0^{t_{\max}} \dot{\boldsymbol{E}}(t, \Delta t) \boldsymbol{P}_{nm}(t, \Delta t) dt. \tag{3.49}$$

For the numerical results presented in Fig. 3.15 (**d-f**) we use an integration window of $t_{\max} = 80$ ps to obtain the integrated signal. All three panels display the intensity I_{nm} for three different directions given by n representing one, two and three multiples of the pump wave vector. The index m of the probe wave-vector is chosen to obtain the lowest non-vanishing contribution still depending on the probe laser ($|m| > 0$) and not forbidden by the selection rule ($n + m \bmod 2 = 1$). A comparison between the first-order pump-probe signal $I_{1-2}(\Delta t)$ in the lower panels and the underlying real-space motion in the corresponding upper panels reveals a close connection between both observables [see gray and blue lines in Fig. 3.15 (**a-c**) and red dots in Fig. 3.15 (**d-f**)]. If the center-of-mass motion is pronounced, corresponding to a localized wave packet during the initial stage of the motion or the revival phase, the diffracted signal induced by a properly time-delayed probe laser pulse is small. However, if the wave packet is maximally delocalized, as it is the case during a collapse, the diffracted signal is strongly enhanced. This feature is observable in all three panels of Fig. 3.15 (**d-f**), even for very low excited Landau levels, where the revival dynamics happen within the first few

picoseconds. A closer look at the higher-order signals reveals an approximate relation between the different diffracted signals. Higher-order process of the pump laser show an increasing oscillation frequency depending on the wave vector multiple n. Furthermore, the intensity of the contribution linear in the probe laser pulse I_{2-1} is stronger than the other two presented signals, since the single photon process is more likely than the two photon process, because of the low intensity of the probe pulse. In view of this close connection between the pump-probe signals and the wave-packet revivals we think that pump-probe experiments are a promising approach to detect magnetically induced wave-packet revivals in graphene.

In the future we want to develop a scheme which connects the semiclassical time-evolution with the polarization of the system allowing for a quantitative explanation of the arising higher-order diffracted signals. Furthermore, the influence of the Landau levels below the Fermi energy should be studied in more detail and relaxation mechanisms from phonons or electron-electron interactions can be taken into account in upcoming investigations.

3.5. Summary

In this chapter we have shown that wave packets on a sheet of graphene feature revivals in presence of a perpendicular magnetic field, which can be explained by the special Landau level structure of the electrons described by an effective two-dimensional Dirac Hamiltonian. Besides the full revivals we revealed additional fractional revivals and gave detailed explanations for the centre-of-mass motion as well as the autocorrelation function connected to the revival phenomenon. Furthermore, we have studied the effect of correlated electrostatic impurities, which suppress revivals in the autocorrelation function. However, the centre-of-mass revivals, which are most important for the signatures in a pump-probe scenario, are still present if the correlation length of the impurity potential is long enough with respect to the average cyclotron radius. Subsequently, we have shown how few- and single-cycle laser pulses can be employed to excite an initial wave packet into a high Landau level, featuring pronounced revival signatures in the following time evolution. We have extended a non-perturbative scheme to calculate the higher-order diffracted signals arising in a pump-probe setup and revealed in this context a close connection between the revival phenomenon and the signals induced by the second time-delayed laser pulse. Our findings suggest that four-wave mixing setups are promising candidates for the detection of wave-packet revivals in graphene.

4 Wave-Packet Transport Theory

The advances in material fabrication allow for the preparation of heterostructures providing two-dimensional electron and hole gases [90] or atomically thin graphene layers [62] with decreasing amounts of defects leading to higher mobilities. By techniques like electron beam lithography very small structures can be created from those materials, such that the phase coherence length of the confined charge carriers starts to exceed the system size. This limit is denoted as the mesoscopic regime which is characterized by substantial quantum corrections to the electronic properties of the underlying classical system, because of the long quantum phase coherence. Most quantum treatments of the electronic properties, such as Green's function techniques, are based on stationary solutions of the wavefunctions [91]. In this chapter we will introduce a complementary approach, which utilizes the time evolution of wave packets in mesoscopic systems and allows for the calculation of various observables like transmission amplitudes, density of states or scattering eigenstates, just as in a conventional Green's function approach, but also amendable to explicitly time-dependent systems.

In the following we will introduce all necessary requirements to treat mesoscopic systems with a wave-packet approach. In Section 4.1 we commence with four different propagation algorithms, which are specialized for disjunct system properties, such as the boundaries of the system, being either open or closed, or an explicit time dependence of the system Hamiltonian. Subsequently, the propagation schemes are used in Section 4.2 to describe how transmission properties of a mesoscopic system can be extracted from the time evolution of a wave packet. The necessary procedures are demonstrated using the example of the valley-valve effect of a zigzag graphene nanoribbon. All presented algorithms are implemented among other necessary program parts like different Hamilton operators in the time-dependent quantum transport (TQT) library.

4.1. Wave-packet propagation

The description of a quantum mechanical system evolving in time builds the foundation of modern quantum mechanics and represents one of the groundbreaking achievements of the last century [92–94]. For any system determined by the Hamiltonian operator $\hat{H}(t)$ the quantum time-evolution of an initial state $\psi(\boldsymbol{r}, t = t_0)$ is governed by the time-dependent Schrödinger equation

$$\mathrm{i}\hbar \frac{d}{dt}\psi(\boldsymbol{r}, t) = \hat{H}\,\psi(\boldsymbol{r}, t), \tag{4.1}$$

where $\psi(\boldsymbol{r}, t)$ is the wavefunction and $\hbar$ the reduced Planck constant. If the Hamiltonian $\hat{H}(t)$ contains terms which are explicitly time dependent, like for example the field of a driving laser, the time-evolution operator is formally given by

$$U(t, t_0) = T\left[\exp\left(-\frac{\mathrm{i}}{\hbar}\int_{t_0}^{t}\hat{H}(\tau)d\tau\right)\right], \tag{4.2}$$

using the time-ordering operator T. For a time-independent Hamiltonian $\hat{H}$, this expression can be simplified to

$$\hat{U}(t, t_0) = \exp\left(-\frac{\mathrm{i}}{\hbar}\hat{H}\cdot(t - t_0)\right). \tag{4.3}$$

In both cases the time-evolution operator $U(t, t_0)$ propagates the initial state $\psi(\boldsymbol{r}, t_0)$ to the state $\psi(\boldsymbol{r}, t) = \hat{U}(t, t_0)\psi(\boldsymbol{r}, t_0)$ at any time t. For a few basic problems, mostly if all eigenstates of the system are known, the propagation can be solved analytically. However, this is not the focus of this thesis, since in mesoscopic systems the influence of impurities and complicated boundaries usually hinders an exact analytical solution. Moreover, we want to employ numerical schemes to evaluate the quantum time-evolution and extract related physical observables, which are then compared to the expectations gained from analytical approximations of the corresponding model systems.

In many cases the electronic properties of crystalline solids can be described by low energy approximations of the band structure at special points in momentum space known as $\boldsymbol{k}\cdot\boldsymbol{p}$ perturbation theory [95]. All arising Hamilton operators can be written in the form

$$\hat{H} = \sum_{m_x, m_y} c_{m_x m_y}(\boldsymbol{r})\ \hat{k}_x^{m_x}\ \hat{k}_y^{m_y}, \tag{4.4}$$

where $c_{m_x m_y}(\boldsymbol{r})$ are matrices which represent position dependent material parameters and $\hat{k}_x^{m_x}$, $\hat{k}_y^{m_y}$ momentum operators of different orders m_x and m_y. For conventional recursive Green's function algorithms this Hamiltonian is transformed into a matrix representation by using discretized momentum operators leading to various off-diagonal entries in the Hamilton matrix [91, 96]. In this thesis we pursue a different way by applying all $\boldsymbol{k}$ operators in momentum space leading to the Hamiltonian

$$\hat{H} = \sum_{m_x, m_y} c_{m_x m_y}(\boldsymbol{r})\ \ \mathcal{F}_x^{-1} k_x^{m_x} \mathcal{F}_x\ \ \mathcal{F}_y^{-1} k_y^{m_y} \mathcal{F}_y, \tag{4.5}$$

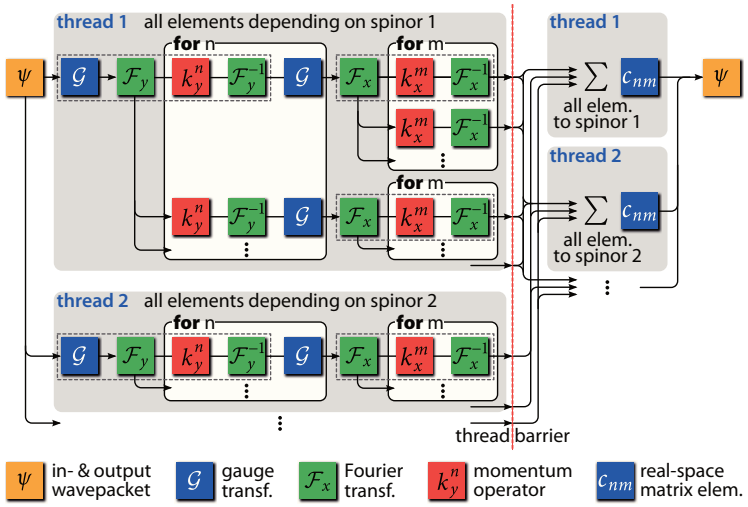

Figure 4.1. | Sequence to calculate the action of the Hamiltonian operator – In the first step all matrix elements $k_y^n\, k_x^m\, \psi_i$ from Eq. (4.5) are simultaneously calculated by different threads depending on the spinor index i. One-dimensional Fourier transformations $\mathcal{F}_{x/y}^{\pm 1}$ are used for the momentum operators and a magnetic field is added by a gauge transformation $\mathcal{G}$ (see Eq. (A.31) of Appendix A.2). To reduce the computational cost parts with common power n are collected and only calculated once for all matrix elements. Steps framed by a gray dashed line are skipped for $n = 0$ or $m = 0$ and directly passed to the next step. After the thread barrier the different matrix elements $k_y^n\, k_x^m\, \psi_i$ are added up with the factor c_{nm} to provide $\hat{H}\psi$.

using the Fourier transformations

$$\mathcal{F}_x^{\pm 1}\psi(\boldsymbol{r}) = \frac{1}{\sqrt{2\pi}} \int dx\, \mathrm{e}^{\mp \mathrm{i} k_x x} \psi(\boldsymbol{r}) \quad \text{and} \quad \mathcal{F}_y^{\pm 1}\psi(\boldsymbol{r}) = \frac{1}{\sqrt{2\pi}} \int dy\, \mathrm{e}^{\mp \mathrm{i} k_y y} \psi(\boldsymbol{r}), \tag{4.6}$$

to convert the wavefunction between the momentum-space and real-space representation [43]. In momentum space the operators $\hat{k}_x^{m_x}$ and $\hat{k}_y^{m_y}$ are described by the scalars $k_x^{m_x}$ and $k_y^{m_y}$ and consequently, their respective action can be computed by a multiplication of the wavefunction with a vector of the same size. For the numerical calculations the wavefunction is discretized on a square lattice, which allows an efficient conversion of the representation by means of Fast Fourier transforms [97]. The advantages of this technique are especially present for Hamilton operators with dominant terms linear in momentum, as it is the case for graphene or topological insulators. On the one hand, the derivative operator in momentum space exceeds the precision of the discretized operator based on the wavefunction of neighboring lattice sites, and on the other hand the fermion doubling is strongly suppressed [15]. The fermion doubling problem arises, for example, if the momentum operator is approximated by $\hat{k}\,\psi_i \propto \psi_{i+1} - \psi_{i-1}$, because of the local description of the derivative and is absent if a nonlocal operator is chosen [98], which is the case if $\hat{k}$ is applied in momentum space.

Table 4.1. | Choice of propagation algorithms depending on the time dependence of the Hamilton operator and the presence of open/closed system boundaries.

	time-independent $\hat{H}$	time-dependent $\hat{H}$
closed system	Chebychev	Lanczos
open system	Chebychev / Faber	Arnoldi

The central numerical step for all time-evolution algorithms we will employ in this thesis is $\hat{H}\psi$, the action of the Hamiltonian operator on a wavefunction. Many interesting electronic properties of novel materials can only be described by taking the spin states of the charge carries or even combinations of electron and hole bands into account, leading to $\boldsymbol{k}\cdot\boldsymbol{p}$ Hamilton operators with an increasing amount of basis states represented by growing c_{m_x,m_y} matrices. Therefore the TQT library contains algorithms, which evaluate the action of the Hamilton operator by computing fully threaded all necessary momentum matrix elements $\hat{k}_x^{m_x}\hat{k}_y^{m_y}\psi_i$ of the different spinor components ψ_i, considering the reusable intermediate results shared by different matrix elements. This is achieved by a sequence of fast Fourier transformations between position and momentum space with intermediate multiplications with the vectors k_x^n and k_y^m, as sketched in Fig. 4.1. The effect of the magnetic field is introduced by means of the gauge transformations $\mathcal{G}$, which allow the implementation of anisotropic magnetic fields without a major impact on the computational time by two additional vector multiplications, as we will show in Appendix A.2. Furthermore, the implementations are not restricted to the aforementioned mixed representation but can also handle a matrix representation of the Hamiltonian to calculate, for example, the time evolution and corresponding observables of a wave packet in a graphene nanoribbon based on an atomistic tight-binding approach.

In the following the different propagation algorithms will be introduced, which have been applied to study the time evolution of the systems treated in this thesis. All of them have disjunct fields of applications and a proper choice should be made to warrant the numerical efficiency. If the accuracy of the propagated wavefunction is of minor importance, the time evolution can be calculated by a split-step technique, which is fast but inaccurate and does not allow for position dependent coefficients $c_{m_x,m_y}(\boldsymbol{r})$ if $m_x, m_y > 0$. We employ higher-order polynomial expansions to calculate the propagator, since the quality of the propagation should only be restricted by numerical errors due to the floating point arithmetic and not by an approximation. The different covered problems can then be separated into systems with time-independent $\hat{H}$, as for the wave-packet revivals in graphene, and systems with explicitly time-dependent $\hat{H}(t)$, like the laser induced pump-probe calculations. Once open boundary conditions are included in the Hamiltonian, which is for example necessary to calculate the transport properties of open mesoscopic structures, the spectrum of the system is not restricted to real eigenvalues and the propagation algorithms have to be modified to converge also in the complex plane. For all different cases suitable propagation algorithms are integrated into the TQT library and the choice should be made based on Table 4.1.

4.1.1. Chebychev propagator

Several numerically accessible implementations of the time-evolution operator (4.3) are based on the expansion of the exponential function in a polynomial series of the operator $-\frac{\mathrm{i}}{\hbar}\hat{H}t$. Since the expansion of a function containing operators is equivalent to an expansion for all eigenvalues of the operator [99], it is instructive to establish at first a polynomial approximation of the function

$$f(z) = \mathrm{e}^{-\mathrm{i}\,\alpha\, z} \approx \sum_{n=0}^{N} a_n(\alpha)\, P_n(z), \tag{4.7}$$

comprising the polynomials $P_n(z)$ of degree n with the expansion coefficients a_n up to a total degree N. Compared to the time-evolution operator (4.3), the parameter α represents the frequency of the oscillation depending on the size of the time step. The easiest set of polynomials are the different powers of z, leading to the Taylor expansion of the complex exponential function

$$f(z) = \mathrm{e}^{-\mathrm{i}\,\alpha\, z} \approx \sum_{n=0}^{N} \frac{(-\mathrm{i}\,\alpha)^n}{n!} z^n. \tag{4.8}$$

However, this type of approximation is not well suited for the purpose of a time evolution, since the result is not converging evenly for different z. The approximation is based on smooth functions, as depicted in Fig. 4.2 (**a**), but is attempted to resemble a rapidly oscillating function. As a result, the Taylor expansion only converges for z close to the origin and diverges for larger $|z|$, as displayed in Fig. 4.2 (**b**). A closer look at the deviation between the exact result and the polynomial expansion,

$$\left| \frac{\mathrm{e}^{-\mathrm{i}\,\alpha\, z} - \sum_{n=0}^{N} \frac{(-\mathrm{i}\,\alpha)^n}{n!} z^n}{\mathrm{e}^{-\mathrm{i}\,\alpha\, z}} \right|, \tag{4.9}$$

reveals that the error is growing exponentially with $|z|$, as shown in Fig. 4.2 (**c**). As a consequence, the Taylor expansion is not suitable for a propagator and other expansions should be employed.

Well suited polynomials should oscillate on variation of z and be generated by short recursion relations, to keep the memory requirements for numerical implementations as low as possible. For example, these requirements are fulfilled by Chebyshev polynomials, which makes these functions particularly applicable for the numerical time evolution [42, 100]. Chebyshev polynomials of the first kind are given by the recursion relation

$$\mathrm{T}_0(z) = 1, \qquad \mathrm{T}_1(z) = z, \qquad \mathrm{T}_n(z) = 2z\,\mathrm{T}_{n-1}(z) - \mathrm{T}_{n-2}(z), \tag{4.10}$$

which only depends on the last two foregoing polynomials. The resulting functions feature rapid oscillations increasing with their degree n, as shown in Fig. 4.2 (**d**). They build an orthogonal basis set in the interval $(-1, 1)$ with respect to the scalar product

$$\langle f|g\rangle = \int_{-1}^{1} \frac{f(z)\, g(z)}{\sqrt{1-z^2}}\, dz, \tag{4.11}$$

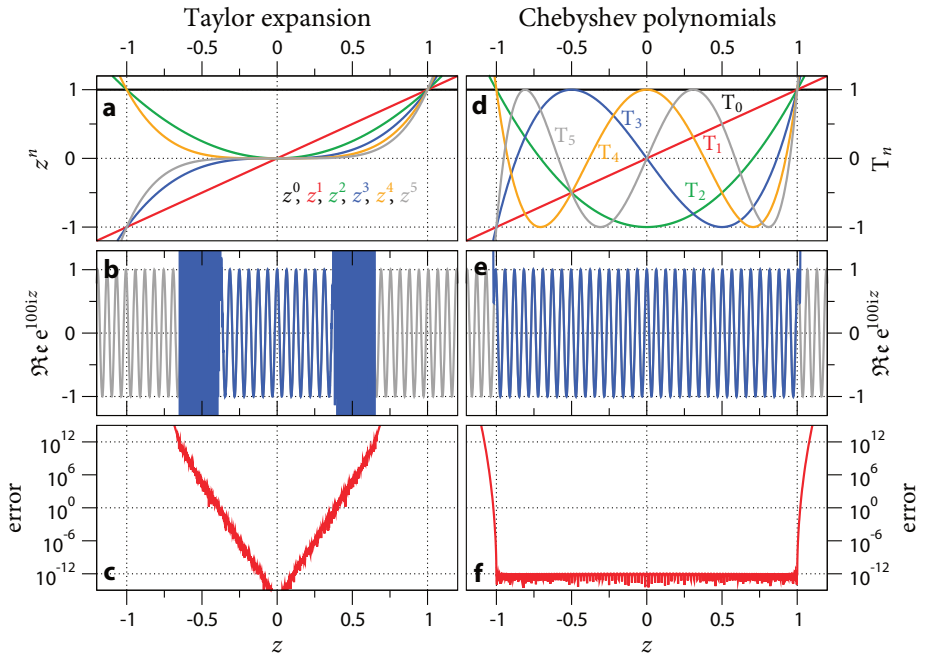

Figure 4.2. | Error of a polynomial expansion – Comparison between the Taylor expansion (4.8) and the Chebyshev expansions (4.12) of $f(z) = \exp(100\,\mathrm{i}\,z)$ with polynomials up to order $N = 140$. **a,** Polynomials used for a Taylor expansion. **b,** Comparison between the real part of the exponential function (gray) and its approximation (blue). **c,** Deviation between approximation and original function given by Eq. (4.9). **d,** Chebyshev polynomials employed at the expansion. **e,** Comparison between the real part of the original function (gray) and the Chebyshev expansion (blue). **f,** Error distribution for an expansion with Chebyshev polynomials.

and can therefore be employed for an expansion in this interval by the polynomial series

$$f(z) = \mathrm{e}^{-\mathrm{i}\,\alpha\,z} \approx \sum_{n=0}^{N} a_n(\alpha)\,\mathrm{T}_n(z). \tag{4.12}$$

By means of the scalar product the expansion coefficients are given by

$$a_n(\alpha) = \frac{2-\delta_{n,0}}{\pi}\int_{-1}^{1}\frac{\exp(-\mathrm{i}\alpha z)\mathrm{T}_n(z)}{\sqrt{1-z^2}}dz = (2-\delta_{n,0})(-i)^n J_n(\alpha), \tag{4.13}$$

with the Bessel functions of the first kind $\mathrm{J}_n(\alpha)$, which can also be computed by a short recursion relation $[J_n(\alpha) = 2\frac{n}{\alpha}J_{n-1}(\alpha) - J_{n-2}(\alpha)]$. A numerical evaluation of the resulting approximation is depicted in Fig. 4.2 (**e**) and shows a convergence in the entire interval $(-1,1)$, although the maximal degree N of the used polynomials is the same as for the Taylor expansion in Fig. 4.2 (**b**). The detailed analysis of the deviation between expansion and original function reveals that the error is distributed equally for all values of $z \in (-1,1)$, as shown in Fig. 4.2 (**f**). For increasing α the number of added

polynomials has to be extended to achieve unchanged low numerical errors. The series is conventionally truncated once the expansion coefficients $a_n(\alpha)$ are smaller than the machine precision. For high order polynomials the expansion coefficients vanish like

$$|a_n(\alpha)| = J_n(\alpha) \approx \frac{2^{-n}\,\alpha^n}{\Gamma(n+1)}, \tag{4.14}$$

and as a consequence the truncation of the series is guaranteed. The implemented routines use a maximal polynomial degree N, which is chosen as $N = 1.04\,\alpha + 40$.

In order to apply this expansion to the physical system of interest, all eigenvalues of the Hamiltonian $\hat{H}$ must be mapped into the interval $(-1, 1)$ leading to the normalized Hamiltonian

$$\hat{H}_{\text{norm}} = 2\frac{\hat{H} - E_0}{\Delta E}, \tag{4.15}$$

with the energy range of the eigenvalues ΔE and their average value E_0. By replacing the argument z of the polynomial expansion with the normalized Hamiltonian, the time evolution of an initial state $\psi(t_0)$ can be calculated by

$$\psi(t) = \sum_{n=0}^{N} e^{-\frac{\mathrm{i}}{\hbar}E_0(t-t_0)}\, a_n\left(\frac{\Delta E(t-t_0)}{2\hbar}\right) \underbrace{\mathrm{T}_n(-\mathrm{i}\hat{H}_{\text{norm}})\psi(t_0)}_{P_n}, \tag{4.16}$$

where the polynomials P_n are given by the action of the Hamiltonian $\hat{H}_{\text{norm}}$ on the state $\psi(t_0)$ via the recursion relations

$$P_0 = \psi(t_0), \qquad P_1 = -\mathrm{i}\,\hat{H}_{\text{norm}}\psi(t_0), \qquad P_n = -2\mathrm{i}\,\hat{H}_{\text{norm}}\,P_{n-1} + P_{n-2}. \tag{4.17}$$

Very long propagation times can be achieved by this type of expansion, because of the high numerical quality of the approximation for abitary $\alpha = \Delta E(t - t_0)/2\hbar$. In this way it is possible to reduce the total error of the propagation, since the time is not split into very small steps. Instead, a few quite large leaps are sufficient to calculate the total time evolution. As a result, the accumulated error is strongly reduced compared to split-step techniques [100], and all observables can be extracted with arbitrary time resolution from the polynomials during the time step.[1] We apply this propagator for all closed systems with a time-independent Hamiltonian like the wave-packet revivals in the previous chapter. However, if open systems are considered another expansion might be more efficient.

[1] For numerical stability the expansion coefficients $a_n(\Delta E(t' - t_0)/(2\hbar))$ for time sub-steps t' should be already truncated at a lower degree, since the numerical implementation of Bessel functions shows some instability for very high orders.

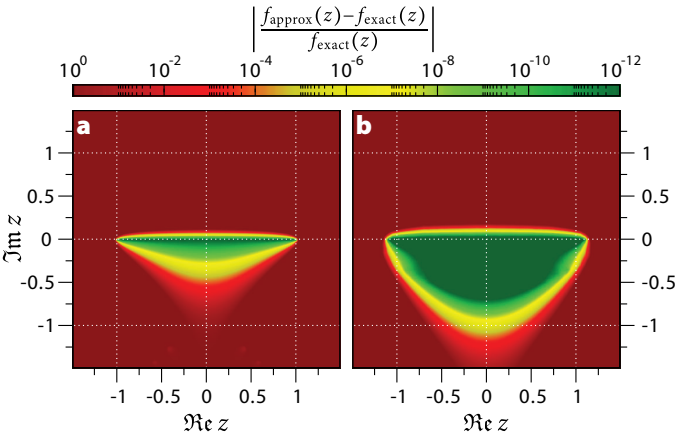

Figure 4.3. | Error of polynomial expansions in the complex plane
Deviation between the function $f(z) = \exp(-\mathrm{i}\,\alpha\, z)$ for $\alpha = 100$ and two truncated expansions ($N = 200$) by means of (**a**) Chebychev polynomials (4.12) or (**b**) Faber polynomials (4.20) for complex values of z.

4.1.2. Faber propagator

The physical properties of a mesoscopic system, consisting of a scattering region which is coupled to an environment by leads, is usually described by a non-unitary Hamiltonian, which we will discuss in Appendix A.3. The expansion in Chebyshev polynomials given by Eq. (4.12) with complex arguments z only converges to the time-evolution operator for real values in the interval $(-1, 1)$, as shown by the error distribution in the complex plane of Fig. 4.3 (**a**). However, an open system features complex eigenvalues with small negative parts corresponding to a finite lifetime of the states within the scattering region. Consequently, the polynomial expansion has to be extended to the complex plane. A possible choice are Faber polynomials [101], which can be generated recursively by the relation

$$F_{k+1}(z) = z\, F_k(z) - \sum_{j=0}^{k} \gamma_j\, F_{k-j} - k\, \gamma_k, \qquad F_0 = 1. \tag{4.18}$$

Each set of Faber polynomials is associated with a conformal map Ψ describing a connected space in the complex plane, which defines the coefficients γ_j of the recursion relation. It was shown that any regular function $f(z)$ in S can be described by an expansion in these polynomials depending on the surface of S, which is defined by a unit cycle $z = \exp(it)$ transformed by the conformal map Ψ. For the purpose of the time-evolution operator the conformal mapping

$$\Psi(\omega) = \omega - E_0 + d/\omega \tag{4.19}$$

is used, which describes an elliptic domain with an origin shifted by E_0 and an eccentricity depending on d. Because of the elliptic domain the polynomials $F_k(z)$ can be generated by a short recursion relation, which is favorable for an numerical expansion

of the time-evolution operator [102]. This leads to an approximation of the complex exponential function

$$f(z) = \mathrm{e}^{-\mathrm{i}\,\alpha\, z} \approx \sum_{n=0}^{N} \underbrace{\frac{1}{2\pi\mathrm{i}} \int_{|\omega|=1} \frac{\exp(-\mathrm{i}\,\alpha\,\psi(\omega))}{\omega^{n+1}} d\omega}_{a_n(z)} F_n(z), \tag{4.20}$$

with the starting polynomials

$$F_0(z) = 1, \qquad F_1(z) = z, \qquad F_2(z) = z\,F_1(z) - 2d\,F_0(z), \tag{4.21}$$

and the recursion relation

$$F_{n+1}(z) = z\,F_n(z) - d\,F_{n-1}(z). \tag{4.22}$$

For this particular choice of mapping, the expansion coefficients $a_n(z)$ can be calculated analytically leading to

$$a_n = \exp\left(-\mathrm{i}/\sqrt{d}\right)^n \cdot J_n\left(\frac{\Delta E\,(t-t_0)}{\hbar}\sqrt{d}\right). \tag{4.23}$$

The region with deviations smaller than 10^{-12} is not restricted to the interval $(-1,1)$ for this type of expansion, but features a semicircle of convergence into the negative complex plane, as shown in Fig. 4.3 (**b**). Furthermore, the error distribution can be tuned by the eccentricity d. For $d = 0$ the generated Polynomials $F_n(z)$ are equal to those of a Taylor expansion, leading to an approximation which is almost equivalent for the real and the imaginary axis. The set of Faber polynomials for $d = 1/2$ matches renormalized Chebyshev polynomials and the resulting expansion is only a good approximation on the real axis. If an intermediate value is chosen, as for example $d = 1/4$ in Fig. 4.3 (**b**), the approximation is a mixture of both and also convergence in the complex plane is achieved.

As in the case of the Chebyshev propagator, the expansion can also be used to calculate the time evolution of the wavefunction

$$\psi(t) = \sum_{n=0}^{N} e^{-\frac{\mathrm{i}}{\hbar}E_0(t-t_0)}\, a_n \underbrace{\mathrm{F}_n(\hat{H}_{\mathrm{norm}})\psi(t_0)}_{P_n}, \tag{4.24}$$

with the Faber polynomials $\mathrm{F}_n(\hat{H}_{\mathrm{norm}})$, which are recursively constructed from the initial state $\psi(t_0)$ by means of the normalized Hamiltonian H_{norm}:

$$P_0 = \psi(t_0), \qquad P_1 = \hat{H}_{\mathrm{norm}}\psi(t_0), \qquad P_2 = \hat{H}_{\mathrm{norm}}P_1 - 2d \cdot P_0,$$
$$P_{k+1} = \hat{H}_{\mathrm{norm}}P_k - d \cdot P_{k-1}. \tag{4.25}$$

In order to achieve convergence, the number of polynomials in the series has to be increased compared to the Chebyshev expansion by a factor of $(2d)^{-1/2}$ $(d < 1/2)$.

Hence, including eigenvalues with small negative complex parts into the convergence region causes a small calculation overhead, which is why Chebychev polynomials should be employed if the eigenvalues are strictly real. In this thesis we apply the Faber propagation to calculate the time evolution for long propagation steps and open boundary conditions. Similar to the expansion in Chebychev polynomials we are able to extract any observable during these time steps from the polynomials of the expansion with arbitrary time resolution.

4.1.3. Lanczos propagator

If the Hamiltonian $\hat{H}(t)$ is explicitly time dependent the time-evolution operator is given by Eq. (4.2) and the time ordering of the Hamiltonian has do be taken into account during the propagation. In this cases, the time evolution can be calculated by splitting the time t into N small steps of size δt and describe the total propagation by a sequence of short time steps using a piecewise constant Hamiltonian,

$$U(t = N\,\delta t) \approx \prod_{n=0}^{N} \exp\left(-\frac{\mathrm{i}}{\hbar}\,\hat{H}(n\,\delta t)\,\delta t\right). \tag{4.26}$$

Since the time evolution cannot be calculated in a few long propagation steps, the advantages of the aforementioned Chebyshev and Faber expansions vanish. In this context it is better to employ polynomial expansions, which still describe the exponential function very accurately, but need a low amount of polynomials for short time steps. These requirements can be satisfied by an expansion of the time-evolution operator in an N-dimensional Krylov subspace $\mathcal{K} = \mathrm{span}\{\psi, \hat{H}\psi, \ldots, \hat{H}^{N-1}\psi\}$ [103, 104]. In order to achieve the best numerical stability, the basis vectors k_n of the Krylov space $\mathcal{K}$ are orthonomalized by a Gram-Schmidt procedure during the recursive creation:

$$k_0 = \frac{\psi(t_0)}{|\psi(t_0)|}, \tag{4.27a}$$

$$k_1 = \frac{\hat{H}k_0 - \alpha_0 k_0}{\beta_1}, \tag{4.27b}$$

$$k_{n+1} = \frac{\hat{H}k_n - \alpha_n k_n - \beta_{n-1}k_{n-1}}{\beta_n}. \tag{4.27c}$$

The overlap between successive Krylov vectors $\alpha_n = \langle k_n|\hat{H}|k_n\rangle$ and $\beta_{n-1} = \langle k_{n-1}|\hat{H}|k_n\rangle$ are not only necessary for the orthonormalization of the basis, but also generate the tridiagonal matrix

$$H_{\mathcal{K}} = \begin{pmatrix} \alpha_0 & \beta_0 & 0 & \cdots & 0 \\ \beta_0 & \alpha_1 & \beta_1 & & 0 \\ 0 & \beta_1 & \alpha_2 & & \vdots \\ \vdots & & & \ddots & \beta_{N-2} \\ 0 & 0 & \cdots & \beta_{N-2} & \alpha_{N-1} \end{pmatrix}, \tag{4.28}$$

which represents the Hamilton operator $\hat{H}$ in the Krylov space. This procedure enables the calculation of approximate eigenvalues of the initial operator $\hat{H}$ based on the eigenvalues of $H_{\mathcal{K}}$ [79], which can be computed by conventional algorithms for dense matrices, since the Krylov space is usually restricted to 10 – 40 basis vectors.

Furthermore, this basis can be used to calculate the time evolution of the initial state $\psi(t_0)$. In the Krylov space the wavefunction at t_0 is represented by $\psi_{\mathcal{K}}(t_0) = (1, 0, \ldots, 0)$ and the corresponding time evolution is given by

$$\psi_{\mathcal{K}}(t) = \mathrm{e}^{-\frac{\mathrm{i}}{\hbar} H_{\mathcal{K}}(t-t_0)}\, \psi_{\mathcal{K}}(t_0). \tag{4.29}$$

Because of the small number of basis vectors generating $\mathcal{K}$, the time evolution of $\psi_{\mathcal{K}}(t)$ can be calculated by an expansion in the eigenstates of $H_{\mathcal{K}}$. Using the matrix of eigenstates $\mathbf{T}$ and the eigenvalues $\mathbf{E}$ of the reduced Krylov space $H_{\mathcal{K}}$, the time evolution of the initial state in the original basis is constituted by

$$\psi(t) = \sum_{n=0}^{N-1} \left[\mathbf{T}^t \exp\left(-\tfrac{\mathrm{i}}{\hbar}\mathbf{E}(t-t_0)\right)\mathbf{T}\ \psi_{\mathcal{K}}(t_0)\right]_n \cdot k_n, \tag{4.30}$$

depending on the basis vectors k_n of the Krylov space given by Eq. (4.27). It has been shown that this Krylov space approach converges to the exponential operator much faster than a conventional Taylor expansion [105]. In this thesis the Lanczos propagator is used for the numerical time evolution of all closed systems with a fast time dependence, like for example the pump-probe detection of wave-packet revivals in the preceding chapter.

4.1.4. Arnoldi propagator

The propagation scheme using a Lanczos method to create an orthonormal basis for the Krylov space only requires small modifications once open boundary conditions are added to the system. Because of the additional complex part of the eigenvalues, the orthogonalization process of the Krylov space (4.27) cannot be truncated after the first vector. In fact all previously created Krylov vectors have to be used for the Gram–Schmidt process, which was already introduced by Arnoldi for the iterative solution of the eigenvalue problem for non-Hermitian matrices [106]. Accordingly, the matrix $H_{\mathcal{K}}$ representing the Hamilton operator in the Krylov space is no longer tridiagonal but changes into an upper Hessenberg form, because of the additional entries recording the overlap with lower-order basis vectors in the upper right of the matrix. However, it is equally possible to calculate the eigenvectors and eigenstates of this rather small matrix $H_{\mathcal{K}}$ and use it for the expansion of the time-evolution operator [107]. As for the unitary system the time evolution of the initial wavefunction is given by Eq. (4.30). This type of propagation mechanism can be used if an open system with a time-dependent Hamiltonian is considered, like for example an open mesoscopic system in the presence of a driving laser field.

4.2. Transport

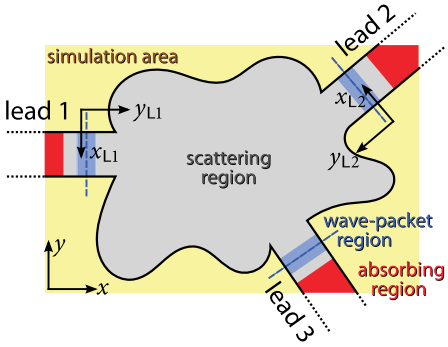

Figure 4.4. | Setup for wave-packet transport calculations in mesoscopic systems
Scattering region coupled to $N = 3$ semi-infinite leads embedded in a large simulation area (yellow). Each lead features a sufficient overlap with the simulated area to allow the placement of absorbing boundaries (red) and incoming and outgoing wave packets (blue). The wave packets are created by a diagonalization of the interpolated system Hamiltonian along the x_{Li} axis of the coordinate system (x_{Li}, y_{Li}) of lead i.

A central point of this thesis is the theoretical description of electron- and spin-transport properties of mesoscopic systems as arising in quantum transport experiments. For a proper theoretical definition of quantum transport the structures of interest are generally divided into a finite scattering region, which is connected to the environment by several semi-infinite leads, as sketched in Fig. 4.4. Scattering theory describes how an initial state in a certain mode of an asymptotic lead is scattered through the central region into all attached leads, which is expressed by means of a scattering matrix S. For mesoscopic systems this scattering matrix S is calculated conventionally by means of a Green's function approach based on the steady states for a fixed energy [91]. In this thesis we use a complementary approach which extracts the elements of the scattering matrix from the time evolution of wave packets. Therefore we have extended a scheme used in quantum chemistry for a conventional free electron Hamiltonian to spin-orbit coupled systems comprising several leads. This approach launches incoming wave packets in the leads and extracts the scattering matrix by tracking the correlations between the propagating state with a set of outgoing wave packets [108].

4.2.1. Time-dependent quantum scattering

In the following we commence with a general introduction to time-dependent scattering theory, which describes how the time evolution of a quantum state is related to the scattering matrix.[2] For a setup which consists of N leads attached to a scattering region, it is possible to describe the time evolution of a localized wave packet by different local Hamilton operators, depending on the position of the state. To this end, we separate the full Hamilton operator

$$\hat{\mathcal{H}} = \hat{\mathcal{H}}_{\mathrm{L}n} + \hat{\mathcal{H}}'_{\mathrm{L}n}, \tag{4.31}$$

into a superposition of the lead Hamiltonian $\hat{\mathcal{H}}_{\mathrm{L}n}$ and a scattering Hamiltonian $\hat{\mathcal{H}}'_{\mathrm{L}n}$, which is given by the difference of the two operators $\hat{\mathcal{H}}'_{\mathrm{L}n} = \hat{\mathcal{H}} - \hat{\mathcal{H}}_{\mathrm{L}n}$ for every lead n. In

[2] For a pedagogical introduction to the time-dependent scattering theory, also in combination with proofs and further mathematical properties, the reader may consider Ref. [109].

its own coordinate system $(x_{\mathsf{L}n}, y_{\mathsf{L}n})$, as sketched in Fig. 4.4, every lead Hamiltonian features an infinite translational invariance

$$\hat{\mathcal{H}}_{\mathsf{L}n}(x_{\mathsf{L}n}, y_{\mathsf{L}n} = 0) = \hat{\mathcal{H}}_{\mathsf{L}n}(x_{\mathsf{L}n}, y_{\mathsf{L}n}). \tag{4.32}$$

However, in numerical calculations the simulation area is usually truncated, as it is the case for the yellow shaded region in Fig. 4.4, and absorbing boundary conditions are implemented to model the infinite extent. The time evolution of the lead subsystem is given by the operator

$$\hat{U}_{\mathsf{L}n}(t) = \exp\left(-\frac{\mathrm{i}}{\hbar}\hat{\mathcal{H}}_{\mathsf{L}n}t\right), \tag{4.33}$$

similar to $\hat{U}(t)$, the time-evolution operator (4.3) of the full system.

If an arbitrary state ψ is propagated by the time-evolution operator $\hat{U}(t)$, the state tends to leave the scattering region. For very long propagation times, only an infinitesimal amount of the wavefunction is left in the scattering region and the time evolution is only governed by the lead propagators $U_{\mathsf{L}n}(t)$,

$$\hat{U}(t)\,\psi \xrightarrow{t\to\infty} \sum_{n=1}^{N} \hat{U}_{\mathsf{L}n}(t)\,\psi_n^-, \tag{4.34}$$

with the outgoing states ψ_n^- in lead n. The same argument holds for a propagation backwards in time,

$$\hat{U}(t)\,\psi \xrightarrow{t\to-\infty} \sum_{n=1}^{N} \hat{U}_{\mathsf{L}n}(t)\,\psi_n^+, \tag{4.35}$$

which is only depending on the time evolution of the incoming states ψ_n^+ by the lead propagators $\hat{U}_{\mathsf{L}n}(t)$ for very early times t. This justifies the definition of the so called Møller operators $\mathbf{\Omega}_n^{\mp}$ by

$$\psi = \sum_{n=1}^{N} \underbrace{\lim_{t\to+\infty} \hat{U}^\dagger(t)\,\hat{U}_{\mathsf{L}n}(t)}_{\mathbf{\Omega}_n^-}\,\psi_n^- \quad \text{and} \quad \psi = \sum_{n=1}^{N} \underbrace{\lim_{t\to-\infty} \hat{U}^\dagger(t)\,\hat{U}_{\mathsf{L}n}(t)}_{\mathbf{\Omega}_n^+}\,\psi_n^+, \tag{4.36}$$

which project an arbitrary state on the outgoing and incoming states of different channels. A proof of the convergence of these operators for the electron gas and important mathematical properties, like the invertibility, can be found in Ref. [109]. Most important, the Møller operators can be used to define a scattering matrix. Since all states ψ in the scattering region can be either mapped onto outgoing states $\psi^- = \Omega^{-\dagger}\psi$ or expressed in terms of an incoming state by $\psi = \Omega^+\psi^+$, the Møller operators allow a connection between the incoming and outgoing channels by $\psi^- = \Omega^{-\dagger}\Omega^+\psi^+$ without referring to the states ψ of the scattering region. By means of wave packets ψ_n and ψ_m, which are supposed to be localized in the leads n and m, the scattering between the different channels is determined by

$$\langle\psi_m|S|\psi_n\rangle = \langle\psi_m|\mathbf{\Omega}_m^{-\dagger}\mathbf{\Omega}_n^+|\psi_n\rangle = \langle\psi_m^-|\psi_n^+\rangle. \tag{4.37}$$

This expression provides the scattering amplitude of an entire wave packet, which is a superposition of different lead momenta and modes. However, in mesoscopic systems the scattering amplitude for a fixed Fermi energy is an experimentally important quantity, which will be extracted from the wave packets in Section 4.2.3.

4.2.2. Asymptotic wave packets

A time-dependent mode-resolved transport scheme relies on wave packets, which correspond to the typical mode structure of the semi-infinite leads. For the purpose of a numerical implementation we assume a simulation area discretized on a square grid, which encloses the scattering region and a sufficient long section of each lead, as sketched in Fig. 4.4. Within the scattering region and the leads (gray area) the material parameters allow for propagating solutions for energies close to the Fermi level, whereas no traveling waves are allowed in the boundary regions (yellow area). This can be achieved by a change of material parameters, which is commonly applied for Hamilton operators in a mixed position and momentum space representation, or by an absence of grid points in the case of a tight-binding description. Every lead has a separate coordinate system defined by the transverse coordinate $x_{\mathrm{L}n}$ and the longitudinal coordinate $y_{\mathrm{L}n}$, which is tilted by the angle $\alpha_{\mathrm{L}n}$ to point in the direction of the lead towards the scattering region. The longitudinal origin is located in the asymptotic region and thus the Hamilton operator of the system is independent of $y_{\mathrm{L}n}$,

$$\hat{\mathcal{H}}\big|_{x_{\mathrm{L}n},\, y_{\mathrm{L}n}=0} = \hat{\mathcal{H}}\big|_{x_{\mathrm{L}n},\, |y_{\mathrm{L}n}|<\delta}\,, \tag{4.38}$$

for a finite region δ, which is shaded blue in Fig. 4.4. This justifies a plane wave ansatz for the asymptotic wavefunctions

$$\psi_{\mathrm{L}n}(x_{\mathrm{L}n}, y_{\mathrm{L}n}) = \chi(x_{\mathrm{L}n}, k_{y_{\mathrm{L}n}})\ \mathrm{e}^{\mathrm{i}k_{y_{\mathrm{L}n}} y_{\mathrm{L}n}}, \tag{4.39}$$

with the transverse wavefunction $\chi(x_{\mathrm{L}n}, k_{y_{\mathrm{L}n}})$ for the wave vector $k_{y_{\mathrm{L}n}}$. For the mixed representation a new Hamilton operator can be extracted for each lead n by replacing the momentum operators of the two-dimensional Hamiltonian (4.4) with

$$\hat{k}_x \to \cos(\alpha_{\mathrm{L}n})\ \hat{k}_{x_{\mathrm{L}n}} - \sin(\alpha_{\mathrm{L}n})\ k_{y_{\mathrm{L}n}}, \tag{4.40a}$$

$$\hat{k}_y \to \sin(\alpha_{\mathrm{L}n})\ \hat{k}_{x_{\mathrm{L}n}} + \cos(\alpha_{\mathrm{L}n})\ k_{y_{\mathrm{L}n}}, \tag{4.40b}$$

using a rotated operator $\hat{k}_{x_{\mathrm{L}n}}$ in the transverse direction and the wave vector $k_{y_{\mathrm{L}n}}$ of the plane wave. This determines a one-dimensional Hamilton operator

$$\hat{\mathcal{H}}_{\mathrm{L}n}(k_{y_{\mathrm{L}n}}) = \sum_m c'_m(x_{\mathrm{L}n}, k_{y_{\mathrm{L}n}})\hat{k}^m_{x_{\mathrm{L}n}}, \tag{4.41}$$

which describes the transverse modes by the new matrix elements $c'_m(x_{\mathrm{L}n}, k_{y_{\mathrm{L}n}})$ arising from the condensation of the two momentum operators by Eq. (4.40),

$$\begin{aligned} c'_m(x_{\mathrm{L}n}, k_{y_{\mathrm{L}n}})\hat{k}^m_{x_{\mathrm{L}n}} &= \sum_{m_x m_y} c_{m_x m_y}(x_{\mathrm{L}n}, y_{\mathrm{L}n}) \left(\cos(\alpha_{\mathrm{L}n})\hat{k}_{x_{\mathrm{L}n}} - \sin(\alpha_{\mathrm{L}n})k_{y_{\mathrm{L}n}}\right)^{m_x} \\ &\quad \cdot \left(\sin(\alpha_{\mathrm{L}n})\hat{k}_{x_{\mathrm{L}n}} + \cos(\alpha_{\mathrm{L}n})k_{y_{\mathrm{L}n}}\right)^{m_y}\Big|_{\mathrm{order}\left(\hat{k}_{x_{\mathrm{L}n}}\right)= m} \\ &= \sum_{m_x m_y} c_{m_x m_y}(x_{\mathrm{L}n}, y_{\mathrm{L}n}) \sum_{l=0}^{m_x} (-1)^l \binom{m_x}{l} \binom{m_y}{m_x+m_y-m-l} \\ &\quad \cdot \cos^{m_x}(\alpha_{\mathrm{L}n})\ \sin^{m_y}(\alpha_{\mathrm{L}n})\ k_{y_{\mathrm{L}n}}^{m_x+m_y-m}\ \hat{k}^m_{x_{\mathrm{L}n}}. \end{aligned} \tag{4.42}$$

To get a finite lead Hamiltonian the matrix elements $c_{m_x m_y}$ of the two-dimensional system are only evaluated on a restricted line parallel to the $x_{\mathrm{L}n}$ axis,[3] as sketched by the blue dashed line in Fig. 4.4. In the following we calculate the eigensystem of the lead Hamiltonian for all momenta $k_{y_{\mathrm{L}n}}$,

$$\hat{\mathcal{H}}_{\mathrm{L}n}(k_{y_{\mathrm{L}n}})\chi_{ni}(x_{\mathrm{L}n}, k_{y_{\mathrm{L}n}}) = \epsilon_{ni}(k_{y_{\mathrm{L}n}})\chi_{ni}(x_{\mathrm{L}n}, k_{y_{\mathrm{L}n}}), \tag{4.43}$$

and use the transverse eigenstates $\chi_{ni}(x_{\mathrm{L}n}, k_{y_{\mathrm{L}n}})$ and the energy dispersion $\epsilon_{ni}(k_{y_{\mathrm{L}n}})$ to create wave packets for different modes i. Algorithms for the eigenstates of dense matrices can be applied in the case of a tight-binding Hamilton operator, which are for example provided by the linear algebra package (Lapack). However, if the full Hamiltonian is expressed in a mixed position and momentum space representation, the kinetic part of the lead Hamiltonian (4.41) should be treated on an equal footing and also be calculated in momentum space by means of Fourier transforms. It is possible to derive the eigenstates of the mixed operator with an implicitly restarted Lanczos method as implemented in the Arpack library [106, 111]. This numerical approach extracts (almost) all eigenstates $\chi_{ni}(x_{\mathrm{L}n}, k_{y_{\mathrm{L}n}})$ by means of random trial wavefunctions χ_r and the action of the operator $\hat{\mathcal{H}}_{\mathrm{L}n}(k_{y_{\mathrm{L}n}})\chi_r$.

The transverse eigenstates χ_{ni} serve as the basis for the wave packets Φ_{ni}, which are assembled in momentum space by

$$\Phi_{ni} = \int_{-\infty}^{\infty} \eta_{ni}(k_{y_{\mathrm{L}n}})\ \chi_{ni}(k_{y_{\mathrm{L}n}})\ \mathrm{e}^{\mathrm{i}k_{y_{\mathrm{L}n}} y_{\mathrm{L}n}}\ \mathrm{d}k_{y_{\mathrm{L}n}}, \tag{4.44}$$

and represent the mode i in lead n weighted by $\eta_{ni}(k_{y_{\mathrm{L}n}}) \in \mathbb{R}$ for different momenta. The states $\chi_{ni}(k_{y_{\mathrm{L}n}})$ are calculated with a step size of δk for discrete $k_{y_{\mathrm{L}n}}$ and therefore have to be connected to continuous bands, which is achieved by a maximization of the overlap $|\langle\chi_{ni}(k_{y_{\mathrm{L}n}})|\chi_{nj}(k_{y_{\mathrm{L}n}} + \delta k)\rangle|$ between adjacent momenta for different band

[3] The grid points of the lead Hamiltonian are chosen by a Bresenham line algorithm[110]. Thus no interpolation errors occur for the lead angles $\alpha_{\mathrm{L}n} = \pi/4 \cdot m$ with $m \in \mathbb{N}$. For intermediate angles we use a five point interpolation to derive the material parameters of the tilted lead.

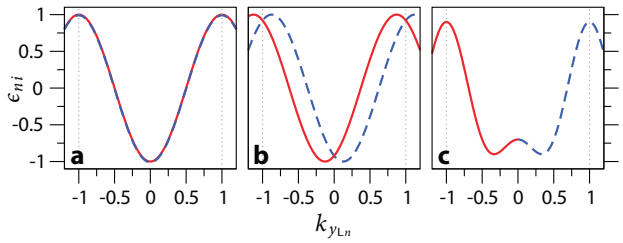

Figure 4.5. | Band-structure degeneracies – a, Bands degenerate in entire momentum space. **b,** Degeneracies at single points. **c,** Multiple k feature common energy for positive or negative group velocity.

indices i and j. In order to assure the wave packets to be localized at $y_{\mathrm{L}n} = 0$ the phase ambiguity of the transverse states $\chi_{ni}(k_{y_{\mathrm{L}n}})$ is removed by rotating the phase with

$$\chi_{ni}(k_{y_{\mathrm{L}n}} + \delta k) \to \chi_{ni}(k_{y_{\mathrm{L}n}} + \delta k) \cdot \frac{|\langle \chi_{ni}(k_{y_{\mathrm{L}n}}) | \chi_{ni}(k_{y_{\mathrm{L}n}} + \delta k)\rangle|}{\langle \chi_{ni}(k_{y_{\mathrm{L}n}}) | \chi_{ni}(k_{y_{\mathrm{L}n}} + \delta k)\rangle}. \tag{4.45}$$

The continuity of the lead wave-packets in momentum space can only be achieved if all degeneracies of the band structure are characterized by additional expectation values.[4] In the following we reveal how the transverse eigenstates $\chi_{ni}(x_{\mathrm{L}n}, k_{y_{\mathrm{L}n}})$ are processed to fulfill these requirements.

Basically two types of degeneracies between different bands can occur, as sketched in Fig. 4.5 (**a,b**). If several bands are degenerate for the entire range of momenta $k_{y_{\mathrm{L}n}}$, it is possible to find an operator $\mathcal{S}$, which commutes with the Hamilton operator of the leads $\hat{\mathcal{H}}_{\mathrm{L}n}(k_{y_{\mathrm{L}n}})$ and allows for a classification. For example, the HgTe Hamilton operator, which we will study in the next part of this thesis, owns a commuting polarization operator $\mathcal{S} = \sigma \otimes \mathbb{I}_{2\times 2}$, using the Pauli matrices σ. To introduce the quantization into the lead basis a conventional diagonalization of the degenerate states can be applied. For a given set of N degenerate orthonormal eigenvectors $\chi_{ni}(k_{y_{\mathrm{L}n}})$ it is possible to deduce from the eigenvectors $\boldsymbol{o}_i$ of the overlap matrix

$$O_{ij} = \langle \chi_{ni}(k_{y_{\mathrm{L}n}}) | \mathcal{S} | \chi_{nj}(k_{y_{\mathrm{L}n}})\rangle, \tag{4.46}$$

a new set of rotated eigenstates

$$\chi'_{ni}(k_{y_{\mathrm{L}n}}) = \sum_{j=1}^{N} [\boldsymbol{o}_i]_{nj}\, \chi_j(k_{y_{\mathrm{L}n}}), \tag{4.47}$$

which are also eigenstates of the operator $\mathcal{S}$. After this classification step the majority of degeneracies are distinguishable by the expectation values of the spin operator $\mathcal{S}$.

Nevertheless, there are still ambiguities left at special points in momentum space where two bands cross, as shown in Fig. 4.5 (**b**). For these momenta $k_{y_{\mathrm{L}n}}$ the velocity operator can be used to find an unambiguous representation, since the bands have to

[4] If several degenerate states are present, the overlap maximization and the phase correction (4.45) do not generally lead to a localized wave packet, since erratic fluctuations between different degenerate eigenstates, which are commonly present after a numerical diagonalization, hinder the creation of smooth wave packets in momentum space.

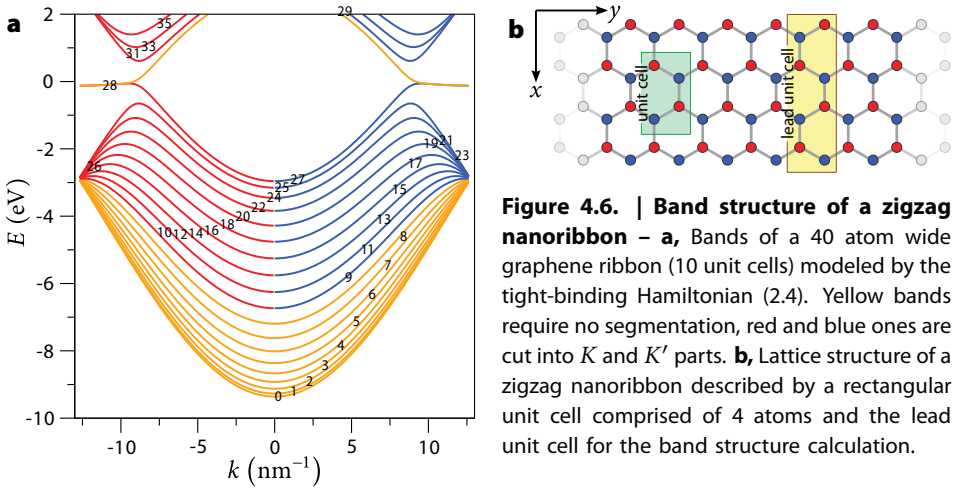

Figure 4.6. | Band structure of a zigzag nanoribbon – a, Bands of a 40 atom wide graphene ribbon (10 unit cells) modeled by the tight-binding Hamiltonian (2.4). Yellow bands require no segmentation, red and blue ones are cut into K and K' parts. **b,** Lattice structure of a zigzag nanoribbon described by a rectangular unit cell comprised of 4 atoms and the lead unit cell for the band structure calculation.

cross with different slopes [112]. An additional rotation into states with different group velocities enables a continuation of the bands through level crossings.

These two steps assure continuous bands throughout the whole momentum space, which makes it possible to create mode-resolved lead wave-packets. However, there are circumstances where the continuity of the bands is not desired, which occurs when a single band features too many extrema, as sketched in Fig. 4.5 (**c**). In general, a single band is only allowed to change the sign of the group velocity

$$v_i = \frac{1}{\hbar}\frac{\partial \epsilon_i}{\partial k} \tag{4.48}$$

for different $k_{y_{\mathrm{L}n}}$ once. If more sign changes appear, there are regions where right or left moving states can exist for different $k_{y_{\mathrm{L}n}}$ with the same energy, as it is the case at the band minima in Fig. 4.5 (**c**). This leads to an increased amount of open channels, which all have to be treated independently, since every channel carries a single conductance quantum. From a mathematical point of view this expresses the requirement of an invertible dispersion $\epsilon_{ni}(k_{y_{\mathrm{L}n}})$ for a given sign of the group velocity, which is also needed in the following derivation of the transmission amplitudes. To fulfill this condition the bands are divided into parts, such that the new bands only change the sign of the group velocity once, as shown in Fig. 4.5 (**c**).

Example:

This situation appears, for example, in graphene nanoribbons with a zigzag edge termination. The electronic structure of such a nanoribbon can best be described by the tight-binding Hamiltonian (2.4), which uses a single p_z basis function for every carbon atom in the hexagonal grid of the ribbon,[5] as sketched in Fig. 4.6 (**b**). In the following

[5] Since the code is relying on square grids, the basis is extended to four atoms as marked in Fig. 4.6 (**b**).

passages we will use this type of nanoribbon as a model system to demonstrate the capabilities of the wave-packet transport algorithm. Since the zigzag boundary condition does not mix the valleys K and K' of the bulk system, the electronic structure of a nanoribbon still exhibits these symmetry points [71]. Accordingly, the bands feature two minimal gaps between the electron and the hole states for the momenta $k_{y_{\mathrm{L}n}} = \pm 2\pi/3a$, as shown in Fig. 4.6 (**a**). This allows to choose a wave-packet with positive group velocity either from the K or the K' valley, if the excitation energy E is close to the charge neutrality point. In view of transport this doubles the number of open channels and also results in an increased conductivity through a ballistic sample. The algorithm takes this into account by an automatic search for valley degeneracies, which leads to an appropriate splitting of the states, as occurred for the red and blue bands in Fig. 4.6 (**a**). Accordingly, the wave packets used in the transport calculation are automatically chosen valley polarized if possible.

4.2.3. Scattering matrix

Based on the preliminary studies in the previous section we are able to define wave packets

$$\Phi_\alpha = \int_{-\infty}^{\infty} \eta_\alpha(k)\ \chi_\alpha(k)\ \mathrm{e}^{\mathrm{i}ky}\ \mathrm{d}k, \tag{4.49}$$

which represent a single mode and are assembled by the transverse eigenstates $\chi_\alpha(k)$ in momentum space weighted by the factor $\eta_\alpha(k)$. To keep clarity the indices for the mode i and lead n of the previous wave-packet definition (4.44) are condensed into the index α and all expressions which indicate independent lead coordinate systems are omitted. In the following those wave packets are used to calculate the matrix elements of the scattering matrix (4.37). Therefore, the states Φ_α are mapped using the Møller operators $\mathbf{\Omega}_\alpha^\pm$ of Eq. (4.36) on the incoming wave packets Φ_α^+ and the outgoing wave packets Φ_α^-:

$$\Phi_\alpha = \mathbf{\Omega}_\alpha^\pm \Phi_\alpha^\pm. \tag{4.50}$$

Since the initial states Φ_α are localized by construction in the appropriate lead α, the entire backward (forward) propagation of the time evolution necessary to compute the Møller operator $\mathbf{\Omega}_\alpha^+$ ($\mathbf{\Omega}_\alpha^-$) is only governed by the lead Hamiltonian, if just states with positive (negative) group velocity are represented by the wave packet. Accordingly, the projected wave packets can be expressed as

$$\Phi_\alpha^\pm = \int_{-\infty}^{\infty} \eta_\alpha^\pm(k)\ \chi_\alpha(k)\ \mathrm{e}^{\mathrm{i}ky}\ \mathrm{d}k, \tag{4.51}$$

with a vanishing weight $\eta_\alpha^\pm(k) = 0$ if $\pm v_\alpha(k) < 0$. The incoming and outgoing wave packets $\Phi_\alpha^\pm$ are built up from many different k vectors, which all correspond to a certain energy. In order to obtain an energy-resolved transmission from the total scattering amplitude (4.37), the transfer between different plane wave contributions $\psi_\alpha^\pm(E)$ has to be calculated. Since the weight of the these contributions is specified by the term

$\eta_\alpha^\pm(k)$ in momentum space, the right conversion into the energy domain has to be found. For the wave packet $\Phi_\alpha^\pm$ the plane wave contribution for a fixed energy E can be extracted by

$$\psi_\alpha^\pm(E) = \frac{1}{\mu_\alpha^\pm(E)} \int_{-\infty}^{\infty} \mathrm{e}^{-\mathrm{i}\hat{H}_\alpha t/\hbar}\, \Phi_\alpha^\pm\, \mathrm{e}^{\mathrm{i}Et/\hbar}\, \mathrm{d}t, \tag{4.52}$$

using the propagation of the wave packet $\Phi_\alpha^\pm$ with the lead Hamiltonian H_α.[6] For the purpose of the scattering matrix the plane waves $\psi_\alpha^\pm(E)$ and $\psi_\beta^\pm(E')$ must be orthonormal

$$\langle \psi_\beta^+(E') | \psi_\alpha^+(E) \rangle = \langle \psi_\beta^-(E') | \psi_\alpha^-(E) \rangle = \delta_{\beta\alpha}\, \delta(E - E'), \tag{4.53}$$

with respect to their energies E, E' and the combined lead and mode index α, β. This determines a correction factor

$$\mu_\alpha^\pm(E) = \frac{\eta_\alpha^\pm(E)(2\pi\hbar)^{3/2}}{\sqrt{v_\alpha^\pm(E)}}, \tag{4.54}$$

which specifies the weight of different energies in the lead wave-packets and is derived in Appendix A.5. For this purpose the group velocity $v_\alpha^\pm(E)$ and weight $\eta_v^\pm(E)$ at the energy $E = \epsilon_\alpha^\pm(k)$ of the band α are required, which have been initially defined in momentum space. To get an unique assignment between the momentum and the energy representation of both quantities a cutting of the bands is sometimes necessary, as discussed in the previous section.

The plane wave parts of the wave packets can be further employed to express the elements of the energy-resolved transmission amplitude $t_{\beta\leftarrow\alpha}(E', E) = \langle \psi_\beta^-(E') | \psi_\alpha^+(E) \rangle$ from the state α at energy E to the state β at energy E', which represents a single entry of the scattering matrix S. In terms of wave packets this expression reads

$$\begin{aligned} \langle \psi_\beta^-(E') | \psi_\alpha^+(E) \rangle = & \frac{\sqrt{v_\beta^-(E')\, v_\alpha^+(E)}}{(2\pi\hbar)^3 \mu_\beta^-(E') \mu_\alpha^+(E)} \int_{-\infty}^{\infty} dx \int_{-\infty}^{\infty} dy \int_{-\infty}^{\infty} dt_\alpha \int_{-\infty}^{\infty} dt_\beta \\ & \cdot \left(\mathrm{e}^{-\mathrm{i}\hat{H}t_\beta/\hbar} \Phi_\beta^- \mathrm{e}^{\mathrm{i}Et_\beta/\hbar} \right)^\dagger \left(\mathrm{e}^{-\mathrm{i}\hat{H}t_\alpha/\hbar} \Phi_\alpha^+ \mathrm{e}^{\mathrm{i}Et_\alpha/\hbar} \right), \end{aligned} \tag{4.55}$$

which amounts to a double Fourier transform of the overlap between two independently propagating wave packets at time t_α and t_β determined by the Hamiltonian $\hat{H}$.

This expression can be further simplified. If the Hamiltonian does not explicitly depend on time, the propagators at t_α and t_β commute with each other and the overlap is only depending on the time difference $t_\alpha - t_\beta$:

$$\langle \psi_\beta^-(E') | \psi_\alpha^+(E) \rangle = \frac{\sqrt{v_\beta^-(E')\, v_\alpha^+(E)}}{(2\pi\hbar)^3 \mu_\beta^-(E') \mu_\alpha^+(E)} \int_{-\infty}^{\infty} dt_\alpha \int_{-\infty}^{\infty} dt_\beta \left\langle \Phi_\beta^- \middle| \mathrm{e}^{-\mathrm{i}\hat{H}(t_\alpha - t_\beta)/\hbar} \middle| \Phi_\alpha^+ \right\rangle \mathrm{e}^{\mathrm{i}(Et_\alpha - E't_\beta)/\hbar}. \tag{4.56}$$

[6] Similar spectral methods based on a propagation can be for example used to calculate the eigenstates or scattering states, which will be shown in Appendix A.4.2.

Furthermore, the integration variables can be substituted by $t = t_\alpha - t_\beta$ and $t' = t_\alpha + t_\beta$ and the energies can be replaced by the average energy $E_+ = (E + E')/2$ and the energy difference $E_- = (E - E')/2$. After this transformation the t' integral can be easily carried out, which results in the energy δ function

$$\int_{-\infty}^{\infty} dt' \, \mathrm{e}^{\mathrm{i}E_- t'/\hbar} = 2\pi\hbar\delta(E - E'). \tag{4.57}$$

This reveals that scattering between states with different energies is forbidden, which is a basic property for time-independent Hamiltonian. Furthermore, the two propagations in Eq. (4.55) can be reduced to a single one. As a result, the quantum transmission from the mode α at energy E to the state β is given by

$$t_{\beta\alpha}(E) = \langle \psi_\beta^-(E) | \psi_\alpha^+(E) \rangle = \frac{\sqrt{v_\beta^-(E)\, v_\alpha^+(E)}}{(2\pi\hbar)^2 \mu_\beta^-(E) \mu_\alpha^+(E)} \int_{-\infty}^{\infty} dt \underbrace{\left\langle \Phi_\beta^- \middle| \mathrm{e}^{-\mathrm{i}\hat{H}t/\hbar} \middle| \Phi_\alpha^+ \right\rangle}_{C_{\beta\alpha}(t)} \mathrm{e}^{\mathrm{i}Et/\hbar}. \tag{4.58}$$

Each scattering amplitude depends on the time-dependent correlation $C_{\beta\alpha}(t)$ between a static outgoing wave packet Φ_β^- and an incoming wave packet Φ_α^+, which is propagated by the time-evolution operator of the full Hamiltonian $\hat{H}$. In order to obtain the total transmission $T_{mn}(E)$ between the leads n and m,

$$T_{mn}(E) = \sum_{i,j} \left| t_{\beta=(m,j)\,\alpha=(n,i)}(E) \right|^2, \tag{4.59}$$

the time-evolutions of all wave packets $\Phi_{\alpha=(n,i)}^+$, which represent the open mode i of lead n, have to be calculated. During these propagations the correlation $C_{\beta\alpha}(t)$ with the outgoing wave packet $\Phi_{\beta=(m,j)}^-$ of mode j in lead m is tracked and subsequent Fourier transformations lead to the single quantum transmission amplitudes. This scheme is constructed to resolve the transmission for the whole energy range represented by the incoming and outgoing wave packets depending on the weighting terms $\eta_\alpha^\pm(k)$. To obtain the entire structure of the transmission amplitudes the propagation has to be evaluated until all correlation functions $C_{\beta\alpha}(t)$ approach zero, which in most cases corresponds to a vanishing norm of the wave packet in the simulated area.

Example:

In order to give a deeper insight into the procedures necessary to calculate the transmission properties of a mesoscopic system, we will apply the wave-packet transport scheme on a p-n junction in a graphene nanoribbon and compare the results with a well established recursive Green's function algorithm [96]. The corresponding implementation of the required steps using the wave-packet approach of the TQT library are represented by the sample program in Appendix A.6.

In the following the transport properties of a zigzag terminated graphene nanoribbon are studied, which is described by the tight-binding Hamiltonian (2.4) comprising

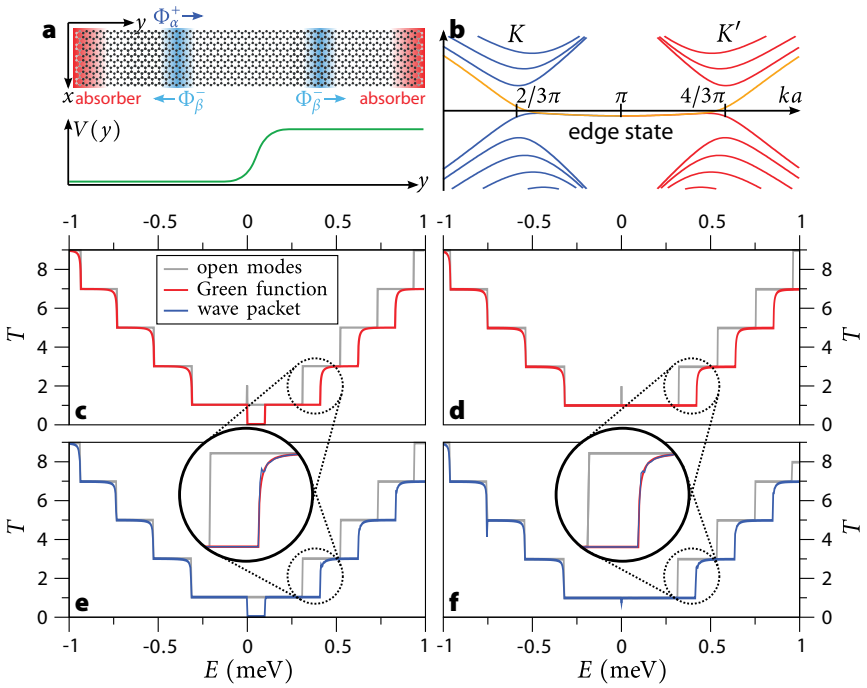

Figure 4.7. | Valley-valve effect with wave packets – a, Sketch of the setup to calculate the transmission through a p-n junction in a zigzag graphene nanoribbon. **b,** Band structure of the leads featuring the two valleys K and K' and a linking pair of edge states. **c, d,** Transmission pattern calculated by means of a recursive Green's function algorithm for a p-n junction ($V_0 = 0.1\,\mathrm{eV}$, $\delta y = 1.5\,\mathrm{nm}$). **e, f,** Transmission pattern obtained by the wave-packet transport algorithm. The graphene nanoribbon contains (**c,e**) 20 unit cells or (**d,f**) 19 unit cells.

carbon atoms arranged in a honeycomb lattice, as shown in Fig. 4.6 (**b**). The p-n junction is modeled by a position dependent electrostatic potential

$$V(y) = \frac{V_0}{1 + \mathrm{e}^{-y/\delta y}}, \tag{4.60}$$

with a step size V_0 and a broadening of the transition δy. The numerically simulated area of the nanoribbon is truncated at both sides. Therefore complex absorbing potentials are added to the Hamiltonian at the left and right boundaries to mimic the infinite extent of the leads, as illustrated by the red areas in Fig. 4.7 (**a**).[7]

On both sides of the potential step surfaces are defined, which separate the system into scattering region and leads and provide the location of the periodic system (4.43), necessary to calculate the asymptotic eigenstates $\chi_\alpha(k)$ and eigenenergies $\epsilon_\alpha(k)$ for the lead wave-packets. Several bands in the band structure of a zigzag nanoribbon

[7] An introduction to the applied absorbing boundary conditions can be found in Appendix A.3.

feature multiple maxima and minima and therefore have to be split into two parts leading to valley polarized wave packets, as shown in Fig. 4.6 (**a**). The incoming and outgoing wave packets are assembled from the transverse states $\chi_\alpha(k)$ in momentum space by Eq. (4.44) and the corresponding weighting factors $\eta_\alpha(k)$ to select only wave vectors k with positive or negative group velocity.[8] Every number in the band structure of Fig. 4.6 (**a**) corresponds to a single initial wave packet Φ_α^+, which will be propagated in presence of the potential step. In the same way, outgoing wave packets Φ_β^- are constructed and placed into the left and the right lead, as depicted in Fig. 4.7 (**a**). Subsequently, the time evolution of every incoming wave packet is calculated individually and the different correlation functions $C_{\beta\alpha}(t)$ between the propagated wave and the static outgoing wave packets are tracked. Afterwards, the time-dependent correlation functions are transformed into energy-dependent transmission amplitudes by taking the weighting factors $\eta_\alpha(k)$ into account, which compensates the variable energy contributions of the wave packets.

Fig. 4.7 shows the resulting transmission through the p-n junction for two nanoribbons with an even or odd number of transverse unit cells at different Fermi energies calculated by means of a recursive Green's function method in panel (**c,d**) and the wave-packet scheme in panel (**e,f**). The data only feature small deviations between the two methods, which exclusively occur at the band edges, the energies where new modes start to contribute to transport. At these points the group velocity of the lead states approaches zero, which calls for particular propagation times to bring these parts of the wavefunction from the scattering region through the lead surface into the absorbing boundaries. If parts of the wave packet remain in the simulated area the correlation functions $C_{\beta\alpha}(t)$ between the incoming and outgoing wave packets still feature small oscillations. As a consequence, the Fourier transformation used to obtain the transmission amplitudes (4.58) exhibits spurious oscillations due to the finite time window, which predominantly occur at the opening of new bands, as revealed in the zoomed regions in Fig. 4.7 (**e,f**).

Furthermore, an interesting phenomenon is captured by the transmission results presented in Fig. 4.7, which is known as the valley-valve effect [113]. Close to zero energy the transmission shows a noticeable change between unity and zero depending on the width of the nanoribbon, which is consistently revealed by both methods. Because of the potential difference induced by the p-n junction an energy window between 0 and V_0 exists, where the right moving states of both leads feature different valley polarizations, which again suggests no transmission if a scattering between the valleys is forbidden. However, the two valleys are linked by the edge states in momentum space, as shown by the band structure in Fig. 4.7 (**b**). As a result, the different symmetries of the edge state wavefunctions and their propagation in momentum space between K and K' lead to a total reflection if the opposite edges of the nanoribbon are made of the same type of basis atoms and a perfect transmission for the other case, which is

[8] The weighting terms $\eta_\alpha(k)$ also contain an energy cutoff to restrict every single wave packet into a uniform energy domain and to avoid rapid oscillations of the calculated correlation functions.

explained in more detail in Ref. [114]. The corresponding time-dependent picture of the valley-valve effect, showing a pronounced time delay of the K to K' scattering is presented in Appendix A.4.3, as an example of the mode-resolved current observable.

4.3. Summary

In the foregoing chapter we established the time-dependent description of the quantum mechanical scattering problem with a particular focus on mesoscopic systems. Therefore we have introduced four different algorithms to calculate the quantum time evolution of wave packets governed by multi-band Hamilton operators, which are used throughout this thesis to model various materials with different combinations of open/closed boundaries and possible time-dependent external fields. Subsequently, a scheme is presented which is capable of calculating the quantum transmission through mesoscopic systems by means of the propagation of wave packets, which are tailored to model the mode structure of the attached leads. The example of a p-n junction in a zigzag terminated graphene nanoribbon was employed to illustrate the algorithms for the wave-packet generation and the necessary steps to evaluate the total transmission. The arising transport characteristics have been compared with a well established recursive Green's function algorithm and all results are in very good accordance.

From a numerical point of view the wave-packet transport scheme can be implemented very efficiently, since all steps which determine the runtime require no matrix inversions or eigenstate decompositions. Additionally, a single wave-packet run reveals the transmission properties for a broad energy range. Problems arise for band edges and localized states, which both lead to conditions with small decay rates into the leads and require especially long propagation times. However, if properties like weak localization are investigated, it is sufficient to calculate the energy-averaged transmission, which can be extracted already from the integrated current once most parts of the propagated wave packet have left the scattering region and thus circumvents long propagation times. From a physical point of view the time-dependent scheme to quantum transport represents a very intuitive approach and allows a straightforward insight into the occurring processes, which are often hidden in a static formulation.

5 Bloch–Zener Oscillations

Electrons in a periodic potential, which are accelerated by a constant external field, undergo a coherent oscillatory motion, known as Bloch oscillations. This phenomenon predicted in the early days of quantum mechanics [115, 116], has been already observed in various fields of physics. A periodic motion was first demonstrated in biased semiconductor superlattices by optical pump-probe measurements using the dependence of the diffracted radiation on the time-delay between the two pulses [117–119]. Furthermore, Bloch oscillations have been directly detected in the time evolution of a wave packet consisting of cold atoms by the analysis of the momentum distribution of the state after a certain propagation time [120, 121]. More recently the experimental fields showing Bloch oscillations have been extended to classical optical [122, 123] and acoustic [124] waves. Additional interesting effects arise when the dynamics of conventional Bloch oscillations in a single miniband are coupled to another band which is close in energy [125]. In most cases this leads to an avoided band crossing, which induces a coherent superposition of Bloch oscillations due to the Zener tunneling between adjoining bands [126, 127]. The splitting of the wave packet and the subsequent phase-coherent recombination after a Bloch cycle gives rise to several Rabi-type interference phenomena and in particular a double-periodic motion known as Bloch–Zener oscillations [128–130].

In order to generate these oscillations two coupled minibands have to be engineered, which is generally achieved by binary lattices. The consequences of this effect in such especially tailored systems have already been demonstrated in the THz emission of AlGaAs superlattices [131], and even the population dynamics have been measured very recently for light [132] and atomic matter waves [133]. However, materials with

a linear Dirac spectrum [5] exhibit a strong coupling between the electron and hole states, which naturally creates the necessary band structure, since the gap generated by a spatially periodic modulation still allows for Zener tunneling between electron and hole states. In recent years materials with such a linear band structure attained great interest, due to the discovery of graphene [3, 25] and the advent of topological insulators [11]. For graphene based periodic superstructures novel features have been theoretically predicted like the emergence of extra Dirac cones [134–136] and the appearance of a negative differential conductance [137].

The following chapter will reveal that in view of Bloch oscillations further novel features arise in graphene superlattices. It will be shown that multiple Zener tunneling events between the coupled electron and hole branch lead to distinct Bloch–Zener oscillations that emerge naturally in superlattices made of systems with a Dirac-like dispersion. In Section 5.1 the influence of Bloch–Zener oscillations on the wave packet motion in a graphene nanoribbon and the arising frequency spectrum is studied. Subsequently, a two-band model is introduced in Section 5.2, which explains the additional features in the frequency spectrum and the peculiarities of the transitions between electron and hole states in presence of Bloch–Zener oscillations. In Section 5.3 we reveal that Bloch–Zener oscillations also give rise to distinct features in the current through graphene nanoribbons. The influence of an external driving radiation field on the transmission through the superstructure is investigated in Section 5.4 Furthermore, we will show in Section 7.5 of the topological insulator part that also nanoribbons made of mercury telluride feature Bloch–Zener oscillations, which are visible in the frequency patterns as well as in the transport signatures.

5.1. Wave-packet motion in graphene superlattices

In the next section we will study the dynamics of a single electron in a periodic potential under the influence of an additional force. In the case of a free electron in presence of a periodic potential $V(x) = V(x+a)$ with a periodicity length a described by the Hamiltonian

$$H = \frac{p^2}{2m} + V(x) - eE_D\, x \tag{5.1}$$

the resulting motion is already very special. Instead of a constant acceleration induced by the applied electric field E_D, the electron undergoes an oscillatory motion with a frequency of

$$\omega_B = \frac{eE_D a}{\hbar}. \tag{5.2}$$

This dynamics is created by the lattice periodicity and the associated miniband structure in reciprocal space, leading to a periodic motion within one miniband and also oscillations in the corresponding real space picture, which is known as Bloch oscillations. An overview of the dynamics of conventional Bloch oscillations can be found in Ref. [138].

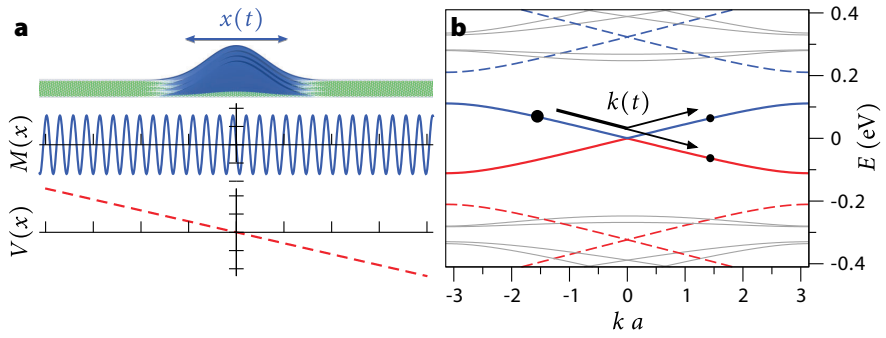

Figure 5.1. | Setup for Bloch–Zener oscillations in a graphene nanoribbon – a, Sketch of a Gaussian wave packet in presence of a periodic mass potential $M(x) = M_0 \sin(2\pi x/a)$ and an electrostatic drift potential $V(x) = -eE_D x$. **b,** Bandstructure of the superlattice with a small avoided crossing at $k = 0$ (nanoribbon width $W = 10\ a_0 \approx 2.5\,\mathrm{nm}$, $a = 10\sqrt{3}\ a_0 \approx 4.3\,\mathrm{nm}$, $M_0 = 0.1\ t \approx 0.28\,\mathrm{eV}$). The thick lines and the dashed lines show the first and the second Bloch band from the metallic armchair mode, respectively. The gray lines represent higher transversal modes.

The dynamics of Bloch–Zener oscillations is more complicated and can be for example tracked in the time-evolution of a wave packet on a graphene nanoribbon in presence of a periodic mass potential $M(x)$ and a linear electrostatic drift potential $V(x)$, as sketched in Fig. 5.1 (**a**). Throughout this chapter the electronic structure of graphene is modeled by the tight-binding Hamiltonian [139]

$$H_{\mathrm{tb}} = \sum_{\langle i\ j\rangle,\beta} t\ c^{\dagger}_{i,-\beta} c_{j,\beta} + V\ c^{\dagger}_{i,\beta} c_{i,\beta} + M\ \beta\ c^{\dagger}_{i,\beta} c_{i,\beta}, \tag{5.3}$$

where $\langle i\ j\rangle$ denotes neighbouring unit cells and $\beta = \pm 1$ the sublattice degree of freedom. In addition to the basic Hamiltonian (2.4) an electrostatic potential $V(x)$ as well as a mass potential $M(x)$ are added to every lattice site, with $M(x)$ changing its sign β for different basis atoms. As introduced in Section 4.2.2 the initial wave packet is created by diagonalizing the periodic Hamiltonian $H(k)$ (4.41), which has already been used to create the asymptotic wave packets for the quantum transport calculations. The initial state for the following time-evolution,

$$\psi(t=0) = \int_{-\infty}^{\infty} \chi_i(y,k)\ \mathrm{e}^{\mathrm{i}kx}\ \mathrm{e}^{-\frac{1}{2}k^2\delta^2}\,\mathrm{d}k, \tag{5.4}$$

is assembled in momentum space by means of the transversal eigenfunctions $\chi_i(y,k)$ of the mode i and represents an electron-like Gaussian wave packe of width δ. Since the motion of the wave packet is confined by the Bloch oscillations, no absorbing boundaries are needed and the time-evolution of the initial state can be calculated by an expansion of the time-evolution operator in Chebychev polynomials, as introduced in Section 4.1.1. In presence of the periodic mass potential

$$M(x) = M_0 \sin(2\pi x/a), \tag{5.5}$$

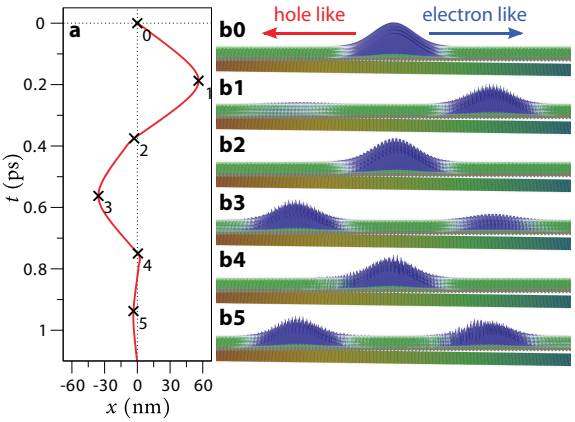

Figure 5.2. | Snapshots of Bloch–Zener oscillations
a, Center-of-mass motion of a wave packet on a periodically modulated graphene nanoribbon ($W = 10\,a_0$, $a = 10\sqrt{3}\,a_0$, $M_0 = 0.1\,t$).
b, Snapshots of the probability distribution of the wave packet for the corresponding times marked with crosses in panel (**a**). A video of the dynamics is available at http://doi.krueckl.de/phd/0003.

with a strength M_0 and a periodicity length a, the band structure of the resulting superlattice exhibits a small anti-crossing at $k = 0$ and a large gap between the first and the second Bloch band, as depicted in Fig. 5.1 (**b**).[1] An additional drift potential

$$V(x) = -eE_D x, \tag{5.6}$$

with E_D as the strength of the electric drift field, leads to a constant acceleration of the wave packet. Because of its Gaussian shape in the x-direction, $\psi(t)$ is also localized in momentum space with a distinct average momentum $k(t)$, which is growing linearly in time due to the applied drift field E_D. At the boundaries of the Brillouin zone the state is not able to tunnel into higher bands, since the gap between the first Bloch band, represented by the solid blue/red in Fig. 5.1 (**b**), and the next higher ones (dashed blue/red lines) is sufficiently large to induce perfect Bragg reflections between opposite momenta in the reciprocal space, leading to a periodic sawtooth motion of $k(t)$. Due to the strong coupling between electron and hole states the dynamics of Bloch oscillations in a graphene nanoribbon exhibit additional features, which is indicated by the typical trajectory

$$x(t) = \langle \psi(t) | \hat{x} | \psi(t) \rangle \tag{5.7}$$

of the center-of-mass as shown in Fig. 5.2 (**a**). A wave packet $\psi(t = 0)$ is initialized in the first electron branch of the nanoribbon using a Gaussian probability distribution, as shown in Fig. 5.2 (**b0**). During the first Bloch cycle the shape of the wave packet stays mostly unaltered and the center-of-mass $x(t)$ only travels to the right of the initial position [see Fig. 5.2 (**b1**)]. The electrostatic potential of this region is negative and accordingly the parts of the wave packet performing Bloch oscillations in this potential region are electron like. In Fig. 5.2 (**b2**) the wave packet is again localized at $x = 0$ and $k = 0$ and as a consequence tunneling from the electron to the hole branch is possible,

[1] For the wave-packet calculations we use a periodic mass potential, since the gap between the first and the second miniband is much larger than for an electrostatic modulation This allows for long propagation times necessary for the frequency analysis in Fig. 5.3.

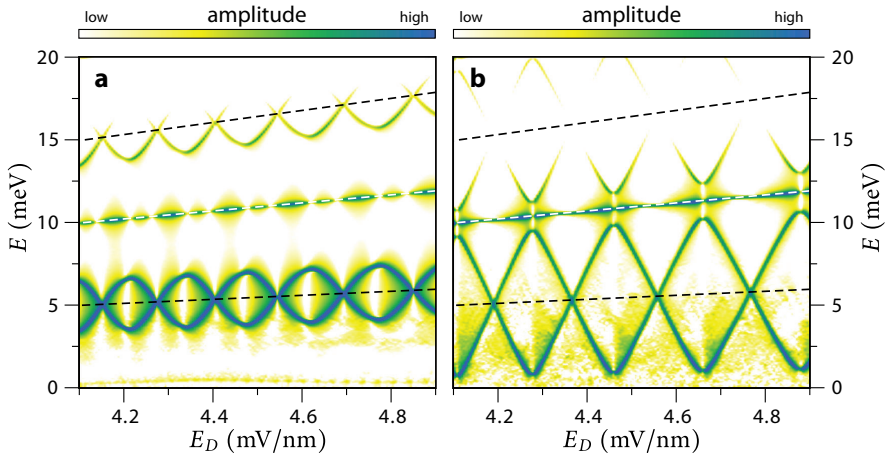

Figure 5.3. | Frequency spectrum of Bloch–Zener oscillations – Frequency spectra $\mathcal{A}(E = \hbar\omega)$ from the center-of-mass motion of a wave packet for varying drift field E_D for (**a**) moderate ($M_0 = 0.1t$) and (**b**) stronger periodic potential ($M_0 = 0.2t$). Dark colors denote strong intensities. The dashed lines correspond to {1/2, 1, 3/2} times the conventional Bloch frequency.

as sketched by the bullets in Fig. 5.1 (**b**). This leads to an increase of the hole-like contributions to $\psi(t)$, which allows the wave packet to propagate into regions with positive potential values and a negative center-of-mass. The corresponding snapshot at the turning point of the wavefunction in Fig. 5.2 (**b3**) reveals predominantly a hole-like state on the left side and a smaller electron-like state on the right side. After the next tunneling the probability distribution between electron and hole states is almost equal, thus the center-of-mass motion is strongly suppressed. Because of the periodic mass potential, the gaps between the first Bloch band and the higher bands are bigger than the gaps between electron and hole states, as shown in Fig. 5.1 (**b**). For the applied drift potentials this results in a negligible tunneling into higher bands and thus the Bloch–Zener oscillations are not dampened.

To study the dynamics of the tunneling between the electron and the hole branch in more detail we perform a frequency analysis of the center-of-mass motion for different drift fields E_D. The Fourier amplitudes

$$\mathcal{A}(\omega) = \left| \int_0^T x(t)\, \mathrm{e}^{\mathrm{i}\omega t}\, \mathrm{e}^{-4t^2/T^2}\, dt \right| \tag{5.8}$$

are extracted from $x(t)$ for a propagation of about 1000 classical Bloch cycles and the dominant frequency contributions are visualized by dark colors in Fig. 5.3. Besides the conventional Bloch frequency (white dashed line), the resulting spectrum shows a pronounced interweaving pattern around half of this frequency (black dashed line). With increasing periodic mass potential the gap between electron and hole branch rises, which also leads to a transition from the smooth pattern to a more abrupt rhombic structure, as shown in Fig. 5.3 (**b**). These periodic features in the frequency spectrum

arise from the interplay between Bloch oscillations and the splitting of the wave packet into the electron and hole branches at $k(t) = 0$, as sketched in Fig. 5.1 (**a**). The repeated sequence of tunneling events between the two branches combined with the subsequent recombination leads to a new set of frequencies, which can be understood by means of a two-band model described in the next section.

5.2. Two-band model for Bloch–Zener oscillations

In the this section we will quantitatively explain the characteristics of Bloch–Zener oscillations using simple model system, consisting of two states described by a periodically modulated one-dimensional Dirac Hamiltonian

$$H(t) = \begin{pmatrix} \frac{2\hbar v}{a} \sin\left(\frac{ak(t)}{2}\right) & g \\ g & -\frac{2\hbar v}{a} \sin\left(\frac{ak(t)}{2}\right) \end{pmatrix}, \tag{5.9}$$

where a is the unit length of the periodic potential, v is the Fermi velocity and g the energy gap between the electron and the hole states. The energy dispersion of the electron and hole branches of this Hamiltonian are given by

$$\epsilon^{\pm}(t) = \pm\sqrt{g^2 + 2(\hbar v/a)^2\,[1 - \cos(ak)]}, \tag{5.10}$$

as shown in Fig. 5.4 (**a**). A comparison with the band structure for the periodically modulated graphene nanoribbon described by the full tight-binding Hamiltonian, which is displayed in Fig. 5.1 (**b**), shows a very good correspondence to this model. We assume a state whose average momentum is driven through the periodic Hamiltonian by an external electric drift field E_D, which enters the equations of motion for $k(t)$ as

$$\hbar \frac{\partial}{\partial t} k(t) = eE_D, \tag{5.11}$$

leading to a linear time evolution of $k(t) = \alpha t$, with the time constant $\alpha = eE_D/\hbar$. Conventional Bloch oscillations with a frequency of $\omega_B = \alpha a$ arise from the periodicity of $k(t)$ in momentum space induced by the recurring Bragg reflections back into the first Brillouin zone, when $k(t)$ reaches the zone boundaries at $\pm\frac{\pi}{a}$. The phase accumulated during the free propagation within a single branch is given by

$$\phi^{\pm} = \frac{1}{\hbar} \int_0^{2\pi/\alpha a} \epsilon^{\pm}(t)\,dt, \tag{5.12}$$

and depending on the propagation time $2\pi/\alpha a$ and the shape of the energy branches $\epsilon^{\pm}$. The interference after the Bloch cycle is only determined by the phase difference between both states, which can be expressed as

$$\phi = \phi^{+} - \phi^{-} = \frac{\mathcal{A}}{eE_D}, \tag{5.13}$$

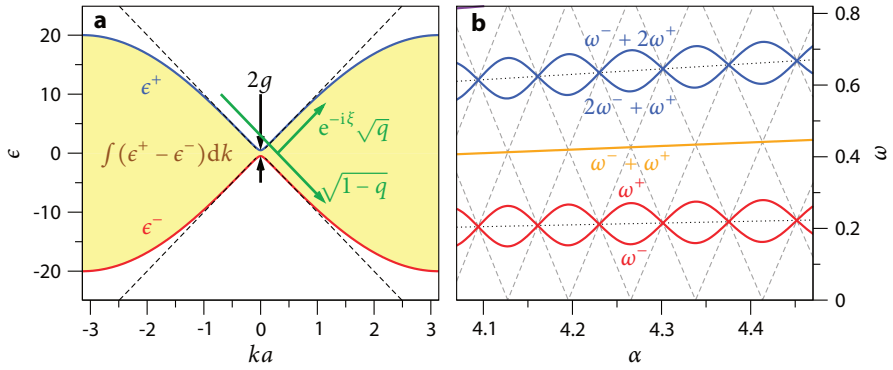

Figure 5.4. | Bandstructure and frequency spectrum of the periodic Dirac model
a, Bandstructure of the Dirac model Hamiltonian (5.9) for $v = 1$, $\hbar = 1$, $a = 1/10$, $g = 1/2$. The shaded (yellow) area denotes the area $\mathcal{A}$ in momentum space from Eq. (5.14). **b,** Frequency spectrum of the Bloch oscillations for different drift accelerations $\alpha = eE_D/\hbar$. Solid lines show the frequencies $n\omega^+ + m\omega^-$ given by Eq. (5.21), dotted (dashed) lines the strong (weak) tunneling limit.

using the area in momentum space,

$$\mathcal{A} = \int_{-\pi/a}^{\pi/a} (\epsilon^+ - \epsilon^-)\mathrm{d}k, \tag{5.14}$$

depicted as yellow shaded area in Fig. 5.4 (**a**). This periodically accumulated phase change between the two branches can be expressed by the matrix

$$U_0 = \begin{pmatrix} \mathrm{e}^{\mathrm{i}\phi/2} & 0 \\ 0 & \mathrm{e}^{-\mathrm{i}\phi/2} \end{pmatrix}, \tag{5.15}$$

where the upper (lower) entry describes the electron (hole) dynamics. In addition to conventional Bloch oscillations on either branch, there is a strong periodic tunneling between the electron and the hole states close to the anti-crossing at $k = 0$. At this point the Hamiltonian (5.9) can be linearized, leading to a Landau–Zener tunneling Hamiltonian [140–142],

$$H_{\mathrm{LZ}} = \begin{pmatrix} \hbar v\ \alpha t & g \\ g & -\hbar v\ \alpha t \end{pmatrix}, \tag{5.16}$$

with a gapped linear dispersion shown by the dashed lines in Fig. 5.4 (**a**). The scattering between the different branches of the Hamiltonian H_{LZ} is described by

$$S_0 = \begin{pmatrix} \mathrm{e}^{-\mathrm{i}\xi}\sqrt{q} & \sqrt{1-q} \\ \sqrt{1-q} & -\mathrm{e}^{\mathrm{i}\xi}\sqrt{q} \end{pmatrix}, \tag{5.17}$$

with the tunneling rate $q = 1 - \mathrm{e}^{-2\pi\delta}$, $\delta = \frac{g^2}{2\hbar^2 v\alpha}$, and an additional tunneling phase $\xi = \frac{\pi}{4} + \arg(1 - \mathrm{i}\delta) + \delta(\log\delta - 1)$. Using the free propagation (5.15) and the tunneling matrix (5.17) we can deduce the scattering matrix

$$S = \begin{pmatrix} \mathrm{e}^{\mathrm{i}(\phi/2-\xi)}\sqrt{q} & \sqrt{1-q} \\ \sqrt{1-q} & -\mathrm{e}^{\mathrm{i}(\xi-\phi/2)}\sqrt{q} \end{pmatrix}, \tag{5.18}$$

which describes the time-evolution of the state for one Bloch cycle with the tunneling at $k = 0$. The scattering eigenstates of this matrix are given by

$$\chi^{\pm} = \frac{1}{\sqrt{\mathcal{N}}} \begin{pmatrix} \sqrt{q}\cos(\phi/2 - \xi) \pm \sqrt{1 - q\sin^2(\phi/2 - \xi)} \\ \sqrt{1-q}\, e^{i\phi/2} \end{pmatrix} \tag{5.19}$$

with the corresponding eigenvalues $e^{i\beta^{\pm}}$, where

$$\beta^{\pm} = \arccos\left(\pm\sqrt{1 - q\sin^2(\phi/2 - \xi)}\right). \tag{5.20}$$

These phases depend periodically on the phase difference ϕ between the electron and the hole branches and induce two new Bloch frequencies

$$\omega^{\pm} = \frac{\alpha a}{\pi} \arccos\left[\pm\sqrt{q}\sin(\phi/2 - \xi)\right]. \tag{5.21}$$

Unlike conventional Bloch oscillations these frequencies do not simply depend linearly on the drift strength α, but show a rapid interweaving pattern strongly changing with α, as shown in Fig. 5.4 (**b**), induced by the coherences from the combined dynamics on the hole and electron branch.

The limiting cases can be understood as follows. For strong coupling, the tunneling rate $q \to 0$ leads to a complete tunneling between the electron and hole branch for every Bloch cycle in momentum space. As a result, the group velocity of the state stays constant at $k = 0$ and thus the corresponding motion in real space is only changing its direction when k reaches the boundaries of the Brillouin zone. Hence, the complete cycle in position space is twice as long as the momentum space cycle, leading to a Bloch frequency of $\omega^{\pm} = \omega_B/2$, depicted as dotted line in Fig. 5.4 (**b**).

In the opposite limit, the coupling between the electron and the hole branch is low, which is resulting in a tunneling rate $q \to 1$. In this case the phase of the free propagation ϕ plays a crucial role for the final frequencies. If the states interfere destructively at $k = 0$, the tunneling time between the branches diverges, leading to the frequencies $\omega^{-} = 0$ and $\omega^{+} = \omega_B$, whereas for constructive interference the resulting frequencies are given by $\omega^{\pm} = \omega_B/2$. For arbitrary phases ϕ the new Bloch frequencies $\omega^{\pm} \to a\alpha[1/2 \pm (\phi/2 - \xi)/\pi] \mod 1$ feature a rhombic frequency pattern represented by the dashed lines in Fig. 5.4 (**b**). In the case of intermediate tunneling rates the frequencies show a smooth transition between these two limiting cases and are in very good agreement with the numerically calculated spectra of Fig. 5.3 (**a,b**).

Furthermore, the scattering eigenstates show a periodically altering polarization into electron- and hole-like states, which depends on the accumulated phase ϕ of Eq (5.13). If the one-dimensional model Hamiltonian (5.9) is considered for $g^2 \gg 2\hbar^2 v\alpha$, the tunneling between the electron and hole branches is weak ($q \to 1$), such that the resulting eigenstates $\chi^{\pm}$ are predominantly characterized by states of a single band for almost all values of ϕ . This amounts to the absolute values of the spinor components being always very close to one or zero, as shown in Fig. 5.5 (**a**). Nevertheless, the

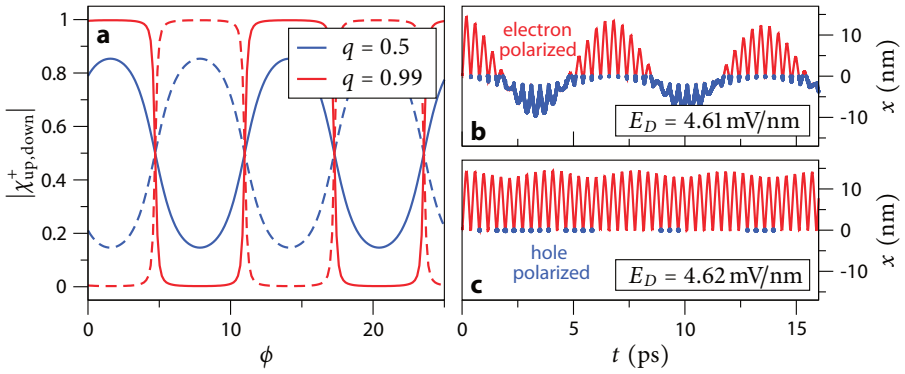

Figure 5.5. | Polarization and example trajectory – a, Polarization dependence on the phase difference between electron and hole branch of the scattering eigenstate χ^+ (solid line shows the upper spinor entry, dashed line the lower spinor entry). Panels (**b**), (**c**) show the center-of-mass motion of an initially electron-polarized wavepacket on a graphene nanoribbon superlattice $M(x) = M_0 + V(x)$ for different drift fields E_D ($M_0 = 50\,\text{meV}$, $V(x) = 300\,\text{meV}\sin(2\pi x/a)$, $a = 10\sqrt{3}a_0$). Blue dots depict regions with a negative amplitude, corresponding to a wavepacket with strong hole character.

polarization vanishes whenever the difference between the phase of the electron and hole branch is

$$\phi = 2(n\pi + \xi) + \pi, \tag{5.22}$$

where $n \in \mathbb{N}$. This alternating character of the spinor between an electron and hole majority for different drift fields E_D can also be deduced from the center-of-mass motion of wave packets with fixed initial polarization. If the drift field is adjusted such that the phase condition (5.22) is approximately satisfied, the center-of-mass motion of the initial electron-like configuration exhibits oscillations ranging from –15 nm to 15 nm for $E_D = 4.61\,\text{mV/nm}$ as shown in Fig. 5.5 (**b**). Since conventional Bloch oscillations in a single band are restricted to positive or negative values, the trajectories imply strong tunneling between the electron and hole states. For values of E_D where condition (5.22) is not fulfilled, *e.g.* $E_D = 4.62\,\text{mV/nm}$ in Fig. 5.5 (**c**), the trajectories of the different polarizations do not significantly cross the origin, thus they preserve their electron-hole character. As a consequence, if the transport of charge carriers through a system comprises a transition from electron to hole states the current should strongly depend on the Bloch–Zener oscillations within the superstructure.

5.3. Transport in graphene-based superlattices

In the following, we consider the current through graphene nanoribbon based superlattices for different bias voltages and demonstrate that Bloch–Zener oscillations lead to clear-cut features in the I-V characteristics. To this end we model a graphene

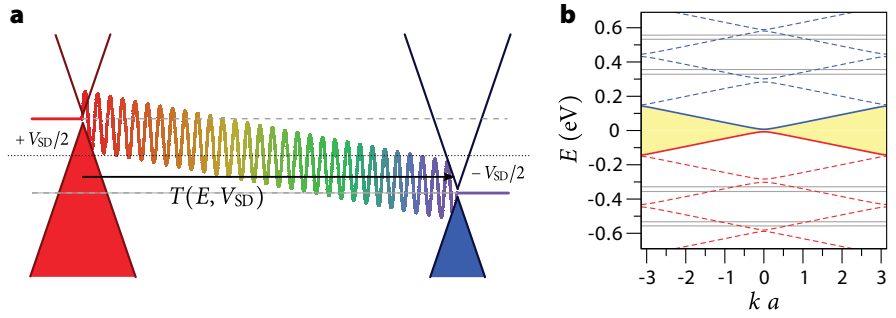

Figure 5.6. | Transport setup for Bloch–Zener oscillations – a, Sketch of the potential landscape composed of a periodic electrostatic potential and a linear potential drop between the two leads with different Fermi levels given by the applied source drain potential V_{SD}. The resulting current (5.24) is depending on the transmission amplitudes $T(E, V_{SD})$ within the bias window, depicted by the dashed lines. **b,** Band structure of a graphene nanoribbon with a periodic electrostatic potential (for $M_0 = 20\text{meV}$, $W = 10a_0$, $a = 30\sqrt{3}a_0$, $V_0 = 500$ meV). The yellow shaded region represents the area $\mathcal{A}$ in momentum space, used to determine the current peaks in Fig. 5.7.

nanoribbon of width W and length L by the tight-binding Hamiltonian of Eq. (5.3), now with a periodic electrostatic potential

$$V(x) = V_0 \sin(2\pi x/a), \tag{5.23}$$

leading to a superlattice mini-bandstructure, as shown in Fig. 5.6 (**b**). A small constant mass term $M(x) = M_0$ is additionally considered, which opens up a gap in the band structure of the metallic armchair nanoribbon. Such band gaps can be also generated by the nanoribbon confinement and are commonly present in experiments on graphene nanoribbons [143]. We assume a linear potential drop $eV_{SD}x/L$ due to the source-drain voltage V_{SD} between the graphene leads at $x = \pm L/2$, which adds up to the tilted sinusoidal total electrostatic potential sketched in Fig. 5.6 (**a**). The current is calculated by means of the Landauer-Büttiker formalism [144],

$$I(V_{SD}) = \frac{2e}{h} \int_{-\infty}^{\infty} T(E, V_{SD})[f^+(E) - f^-(E)]\mathrm{d}E, \tag{5.24}$$

with the Fermi functions $f^{\pm}(E) = \{1+\exp[(E \mp V_{SD}/2)/k_B T]\}^{-1}$. Therefore all transmission amplitudes $T(E, V_{SD})$ within the bias window expressed by the difference of the Fermi functions, $f^+(E) - f^-(E)$, at $-V_{SD}/2$ and $V_{SD}/2$ have to be integrated to the total current, depending on the applied source-drain potential V_{SD}. At zero temperature the bias windows reduces to two step functions at the chemical potential of the left and the right lead, as depicted by the gray dashed lines in Fig. 5.6 (**a**).

The resulting current profile can be separated into three different regimes, as shown in Fig. 5.7. For small source drain voltages V_{SD} the transmission amplitudes $T(E, V_{SD})$ are almost independent of V_{SD}, which results in a linear increase of the current due to

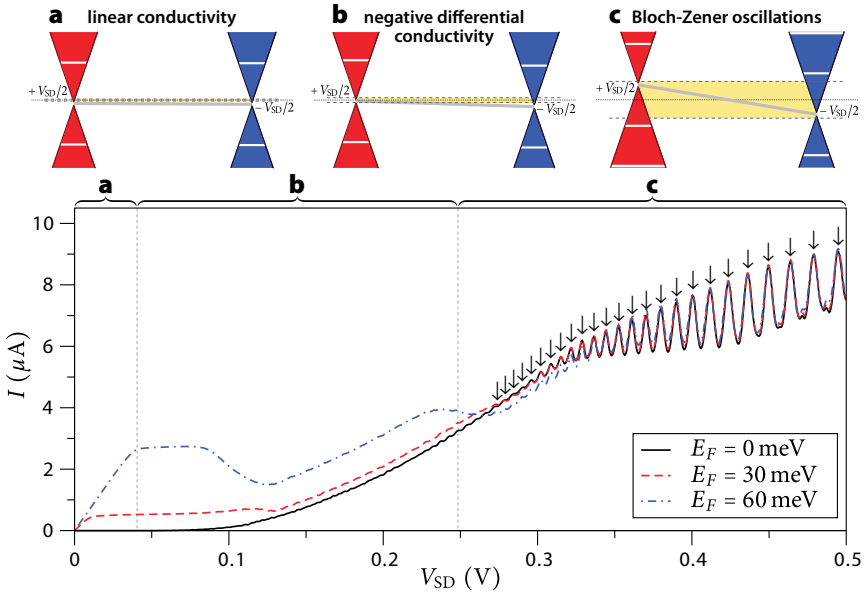

Figure 5.7. | Current signatures of Bloch–Zener oscillations – Current-voltage characteristics of a graphene nanoribbon superlattices ($L = 3000\sqrt{3}a_0$, $W = 10a_0$, $a = 30\sqrt{3}a_0$, $V_0 = 500$ meV, $M_0 = 20$ meV, $T = 20$ K) for different Fermi energies E_F. The sketches describe three different regimes featuring (**a**) linear conductivity, (**b**) negative differential conductivity and (**c**) Bloch–Zener oscillations. The arrows mark the expected current peaks of the Bloch–Zener oscillations given by the phase condition (5.22).

the growing conductance window, as it is the case in Fig. 5.7 (**a**).

If the applied source drain voltage is sufficiently large, the band gap between electron and hole states, which is sketched as gray bar, enters the yellow shaded bias window in Fig. 5.7 (**b**). This leads to a reduction of the transmission amplitudes $T(E, V_{\mathrm{SD}})$ for certain energies E and gives rise to a saturation or even a reduction of the current, as shown in the corresponding part of the I-V dependence in Fig. 5.7 (**b**). Such regions with negative differential conductance are a typical phenomenon indicating Bloch oscillations within the minibands of a superlattice [137].

At higher bias, $V_{\mathrm{SD}} > 0.25\,\mathrm{V}$, we observe the emergence of distinct current oscillations, which can be attributed to Bloch–Zener oscillations. Because of the potential difference between source and drain electrode the band gap between electron and hole states is crossing the entire bias window such that all particles traversing the superlattice must change their electron-hole character, as sketched in Fig. 5.7 (**c**). However, states performing Bloch–Zener oscillations exhibit transitions between the two carrier types only for certain $V_{\mathrm{SD}} = eE_DL$ when the phase ϕ fulfills the condition of Eq. (5.22), as shown in the previous section. If the phase condition is fulfilled and the scattering eigenstates $\chi^{\pm}$ couple the electron and hole branch through the bandgap, the current through the superlattice is strongly enhanced. As shown in Fig. 5.7 the current peaks

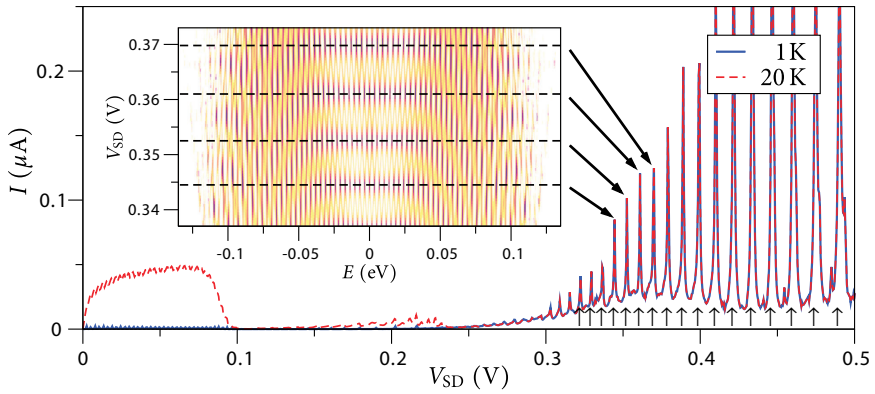

Figure 5.8. | Current and transmission map for Bloch–Zener oscillations – Current-voltage characteristics of a graphene nanoribbon superlattices ($L = 3000\sqrt{3}a_0$, $W = 10a_0$, $a = 30\sqrt{3}a_0$, $V_0 = 500$ meV, $M_0 = 50$meV, $E_F = 0$) for different temperatures. The inset shows the Transmission map $T(E, V_{SD})$ used in Eq. (5.24) to get the current for different temperatures. Dark colors represent high transmissions.

calculated from the Landauer-Büttiker formalism (5.24) coincide perfectly with the expected voltages from the phase condition (5.22), which are marked by arrows. The peak positions are determined by the area $\mathcal{A}$ in momentum space, which is extracted from the minibands around the Fermi energy and shown as shaded area in Fig. 5.6 (**b**).

If the gap between the electron and the hole states is increased, the I-V characteristics of Bloch–Zener oscillations become more pronounced, since the overall transmission is strongly reduced and only raises sharply for gate voltages V_{SD}, which exactly fulfill the phase condition (5.22), as shown in Fig. 5.8. This is in agreement with the polarization properties of the scattering eigenstates $\chi^{\pm}$, which exhibit an increasing separation into electron- and hole-like states for growing q, as revealed in Fig. 5.5 (**a**). Since the left lead is in a hole-like regime and the right lead in an electron-like regime the transmission through the superlattice is suppressed if the transition probability between the two carrier types is reduced. A closer look at the transmission values $T(E, V_{SD})$ shown in the inset of Fig. 5.8 reveals a rhombic structure which features pronounced transmission maxima concentrated at the values of V_{SD} where the phase condition is fulfilled, which are depicted by the dashed lines in the inset. Since the edges of the conductance window shift with the Fermi energy and the transmission maxima appear in a wide energy window, the resulting current profile for Bloch–Zener oscillations is fairly independent of the Fermi energy, as revealed by the I-V characteristics in Fig. 5.7 for $V_{SD} > 0.3$ V, Similarly, the total current for Bloch–Zener oscillations depends only weakly on temperature, because an increase in temperature only softens the borders of the conductance window, which again does only slightly alter the total integral, as revealed by the data in Fig. 5.8.

5.4. Radiation-assisted transport

In the upcoming section we will show that the frequency spectrum of Bloch–Zener oscillations in a graphene superlattice can also be revealed by the transport properties in presence of a driving electromagnetic radiation. By applying an additional laser or microwave source with a sufficiently weak intensity, such that the transport properties are only altered when the laser frequency is in resonance with the wave-packet dynamics due to the Bloch or Bloch–Zener oscillations, we can extract the spectrum of the oscillations by scanning the current through the nanoribbon for different source-drain voltages V_{SD} and radiation frequencies ω_L. This assertion will be verified by calculating the transport through a superstructure in a biased graphene nanoribbon in presence of a driving laser field using a Floquet ansatz, which will be established in the following paragraph.

The electronic properties of the nanoribbon are modeled as in the previous section by the graphene tight-binding Hamiltonian H_{tb} with an additional time-dependent electric field $\boldsymbol{E}_0$ resulting in the Hamiltonian

$$H(t) = H_{\mathrm{tb}} - \boldsymbol{\mu} \cdot \boldsymbol{E}_0 \cos(\omega_L t), \tag{5.25}$$

where $\boldsymbol{\mu}$ is the dipole moment, $\boldsymbol{E}_0$ the electric field and ω_L the angular frequency of the radiation. We assume a coherent field of a microwave or a laser, which induces a time periodicity in the total Hamiltonian

$$H(t) = H(t+T), \quad \text{with} \quad T = \frac{2\pi}{\omega_L}. \tag{5.26}$$

The time-evolution of a state $\psi(t)$ is governed by the time-dependent Schrödinger equation

$$\mathrm{i}\hbar \frac{\partial}{\partial t}\psi(t) = H(t)\psi(t). \tag{5.27}$$

By combining the spatial and time derivatives we get

$$\Bigg(\underbrace{H(t) - \mathrm{i}\hbar \frac{\partial}{\partial t}}_{H_F} \Bigg) u_\alpha(t) = \epsilon_\alpha u_\alpha(t), \tag{5.28}$$

where H_F is the Floquet Hamiltonian. In this representation it is possible to study the time-dependent system using the static eigenvalues $u_\alpha(t)$ of H_F [145], which exhibits an extra dimension t compared to the initial Hamiltonian. Due to the time periodicity of the Hamiltonian the eigenfunctions of the Floquet Hamiltonian are also time periodic, $u_\alpha(t) = u_\alpha(t+T)$. Accordingly, we can apply a Bloch ansatz for the time coordinate and expand the eigenfunctions in a plane-wave basis

$$u_\alpha(t) = \sum_n \mathrm{e}^{-\mathrm{i}n\omega_L t} u_{\alpha,n}, \tag{5.29}$$

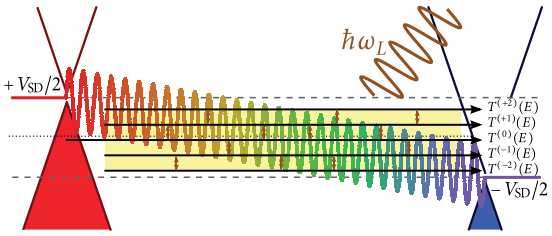

Figure 5.9. | Transport channels for a Floquet Hamiltonian – Sketch of the processes taken into account for the current through a irradiated electrostatic superlattice in presence of a finite source-drain voltage V_{SD}. States entering at the left lead with energy E are scattered into the right lead with a transmission amplitude $T^{(n)}(E)$ under absorption or emission of n photons.

where the plane wave $w_n = \exp(-in\omega_L t)$ in the time domain represents a Floquet mode with index n. In this basis the elements of the Floquet Hamiltonian H_F are given by

$$\langle w_m | H_{tb} | w_n \rangle = H_{tb}\delta_{n,m}, \tag{5.30a}$$

$$\langle w_m | -i\hbar\partial_t | w_n \rangle = -n\hbar\omega_L\delta_{n,m}, \tag{5.30b}$$

$$\langle w_m | \boldsymbol{\mu}\cdot\boldsymbol{E}_0\cos(\omega_L t) | w_n \rangle = \tfrac{1}{2}\boldsymbol{\mu}\cdot\boldsymbol{E}_0\delta_{n\pm1,m}, \tag{5.30c}$$

which are used to express the time-dependent Hamiltonian $H(t)$ as the static matrix Hamiltonian

$$H_F = \sum_{n=-N}^{N}\Big((H_{tb} - n\hbar\omega_L)\,|n\rangle\langle n| + V_t\,(|n\rangle\langle n+1| + |n\rangle\langle n-1|)\Big). \tag{5.31}$$

The diagonal of this matrix is built from multiple copies of the time-independent graphene Hamiltonian H_{tb}, which are energetically shifted by the Floquet energy $-n\hbar\omega_L$. The off-diagonal elements $V_t = \frac{1}{2}\boldsymbol{\mu}\cdot\boldsymbol{E}_0$ connect the different Floquet modes and express the absorption and emission of a single photon with an energy $\hbar\omega_L$. For transport calculations the field $\boldsymbol{E}_0$ has to be zero within the leads to allow for a mode classification of different Floquet states n in the asymptotic regions and is switched on smoothly at the junction between lead and scattering scattering region. In principle, the Hamiltonian (5.31) contains an infinite amount of Floquet modes, however, for a given laser field strength the probability of a high number of absorbed and emitted photons is very low. Thus in practical calculations the Hamiltonian is restricted to N-photon processes and the calculations are repeated with increasing N until the results are converged.

In the following, we study the current passing through the irradiated nanoribbon, which in principle features a rapid time dependent current induced by the radiation field [146]. These oscillations are very fast and usually not resolved by an experimental setup. Fortunately, the signatures of Bloch–Zener oscillations are already visible in the time averaged current at fixed bias,

$$\tilde{I}(V_{SD}) = \frac{e}{h}\int_{-\infty}^{\infty}[T_{RL}(E)f^{+}(E) - T_{LR}(E)f^{-}(E)]\,dE, \tag{5.32}$$

which depends on the Fermi functions $f^{\pm}(E)$ of both leads and the amplitudes

$$T_{RL/LR} = \sum_{n=-N}^{N} T^{(n)}_{RL/LR}, \tag{5.33}$$

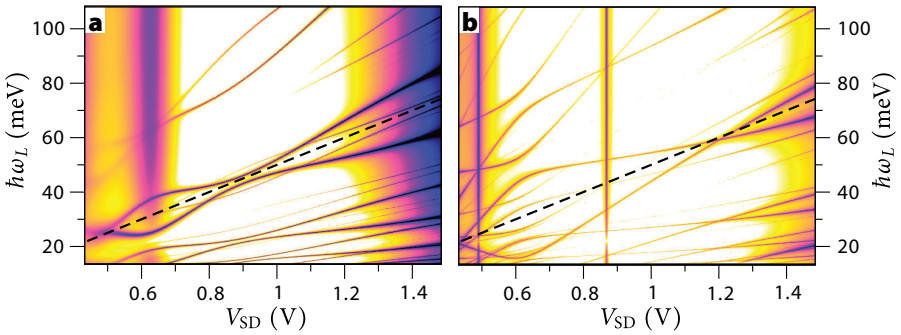

Figure 5.10. | Radiation enhanced transmission – a, Transmission T_{RL}, Eq. (5.33), through a graphene nanoribbon with 10 periods of a sinusoidal mass potential ($W = 3.5\ a_0$, $a = 10\sqrt{3}a_0$, $L = 10\ a$, $M_0 = 0.25\ t$) for different laser energies E_L and different source-drain voltages V_{SD}. The dashed black line represents half of the frequency of conventional Bloch oscillations. The laser field is modeled as $V_t = y \cdot 0.01\, t$, and up to $N = 20$ photon absorptions and emissions are considered by the Floquet Hamiltonian (5.31). Dark colors represent high transmissions. **b,** Transmission through a similar nanoribbon with a stronger mass potential ($M_0 = 0.5\ t$).

where $T^{(n)}_{RL/LR}$ is the transmission under absorption or emission of n photons between the left (L) and the right (R) lead. Accordingly, the total current is given by integrating over different energies the sum of transmission amplitudes T_{LR} for all states entering at the left lead in the Floquet mode $n = 0$, which are scattered into an arbitrary Floquet mode of the right lead after several photon processes, as sketched in Fig. 5.9. Unlike in the static case the transmission amplitudes do not feature a left-right mirror symmetry, $T^{(n)}_{RL} \neq T^{(n)}_{LR}$. Thus the backward flow from the right to the left lead has to be taken into account independently, since the current (5.32) cannot be reduced to the difference of the two Fermi functions as in the static case (5.24).

Using this Floquet transport theory we calculate the current through an armchair graphene nanoribbon with 10 periods long electrostatic superlattice in presence of a finite source-drain potential V_{SD}, leading to the total potential landscape depicted in Fig. 5.9. Additionally, we take a linearly-polarized microwave radiation with a frequency $E_L = \hbar\omega_L$ into account. The resulting transmission T_{RL} for different source-drain voltages V_{SD} and microwave frequencies ω_L is shown in Fig. 5.10. The linear potential drop of the applied source-drain voltage V_{SD} and the lattice periodicity a determine the frequency of the Bloch and Bloch–Zener oscillations. This dependence is visible in the numerically calculated transmission pattern, which features two resonances around half of the Bloch frequency, shown by the black dashed line in Fig. 5.10 (**a**). Since the frequencies of these resonances have a periodic dependence on the applied source-drain voltage, similar to the frequency pattern extracted from the wave packet dynamics in Fig. 5.3, this is a clear signature of Bloch–Zener oscillations in transport. Furthermore, increasing the gap between the electron and the hole branch leads to an amplification of the frequency modulation, as shown in Fig. 5.10 (**b**). This feature is in

close correspondence to the change of the resonance frequencies depending on the band gap g of the model, as presented in Fig. 5.3 (**b**), and has already been demonstrated in the frequency analysis using wave packets in Fig. 5.4. Consequently, we assume such a periodic resonance structure in the I-V characteristics for different laser frequencies as a clear signature of Bloch–Zener oscillations in transport, which might serve as another approach for experimental detection.

5.5. Summary

In this section we revealed that superlattices made of materials with a Dirac-like energy spectrum, such as graphene, feature Bloch–Zener oscillations induced by the interference between the electron and hole states close to the charge neutrality point [17]. The characteristics of these oscillations are explained by a one-dimensional model Hamiltonian. Numerical simulations using wave-packet propagations confirmed the effect in a periodically gated graphene nanoribbon. Furthermore, we demonstrated that Bloch–Zener oscillations manifest themselves as a sequence of pronounced current peaks in quantum transport through biased graphene superlattices. In addition to these current peaks we find the well know negative differential conductance at low bias induced by conventional Bloch oscillations. The sequence of current peaks associated with the Bloch–Zener oscillations are intimately linked to the underlying miniband structure. The entire frequency spectrum of Bloch–Zener oscillations can be measured in the current pattern through a nanoribbon in presence of an additional radiation source. Furthermore, we will demonstrate in Section 7.5 that nanoribbons made of the topological insulator mercury telluride also exhibit Bloch–Zener oscillations, which manifest themselves as a similar frequency pattern and I-V dependence of the current.

We suggest transport measurements through graphene nanoribbons and HgTe strips as promising experimental setups to reveal Bloch–Zener oscillations. For single layer graphene and topological insulators, the periodic electrostatic potential can be imprinted by an array of top gates. For both materials the gap between the electron and hole states can be tuned by the width of the considered nanoribbons. In case of bilayer graphene the band gap can be additionally created via a potential difference in z-direction induced by a top and a bottom gate.

The calculations presented here have been performed for clean, disorder free and coherent systems. Preliminary numerical calculations for graphene-based superlattices with disorder indicate that Bloch–Zener oscillations are still visible in the I-V characteristics, if the mean-free-path of the charge carriers exceeds several periods of the superlattice. This is promising for their experimental detection in solid-state samples. After the publication of our work [17] Bloch–Zener oscillations have been investigated in cold atom setups, where an optically structured honeycomb lattice populated by ultracold, fermionic K-atoms is modeling the electronic structure of graphene, giving rise to similar physical properties [147].

Part II.

Topological Insulators

6 HgTe/CdTe Quantum Wells

In 2005 Kane and Mele revealed that graphene in presence of spin-orbit interaction undergoes a transition from a zero-gap semiconductor to an insulator featuring a quantized Spin Hall effect [4]. The spin-orbit interaction induces a gap in the bulk band structure, leading to electronic properties known as spin Hall insulator [148]. Additionally, the boundaries of a finite piece of graphene feature edge states independent of the zigzag or armchair type of the edge. Since no magnetic field is needed to create those edge states, time-reversal symmetry is still present, and the edge states are protected from backscattering. As a result, one expects a quantized conductance of $\pm e^2/\hbar$, the so called Quantum Spin Hall effect, a pronounced feature in transport of a new state of matter. Shortly afterwards, this new state was integrated into the existing classification of materials[149], showing a novel $\mathbb{Z}_2$ topological invariant distinguishing between an ordinary insulator and a topological insulator [11]. While the spin-orbit coupling of graphene is too small to render experimental evidence [27, 28, 30, 150], several theoretical proposals suggest other two-dimensional materials and heterostructures that are expected to show topological insulator features [151–153]. The prominent transport feature of such topological insulators, the quantum spin hall effect, has subsequently been confirmed for HgTe/CdTe quantum wells [14, 154] as well as for InAs/GaSb heterostructures [155].

The field extended even more, once it was found that topological insulators are not limited to two dimensions but can also appear in three dimensions [156]. Similar to a two-dimensional topological insulator, the bulk of a crystal like BiSe and Bi_2Te_3 has a band gap but the surface features states, which are chiral and governed by a Dirac equation. In this case, possible materials can be classified into weak or strong topological insulators, which can be distinguished by parity eigenvalues at the high symmetry points of the Brillouin zone [157]. The chiral nature of the surface states has already been revealed in experiments with angle-resolved photoemission spectroscopy,

which is especially sensitive to the surface [158, 159]. Furthermore, first steps towards measuring the transport properties of Bi_2Te_3 surface states have been reported [160, 161], which are important for future applications. An overview of topological insulators in two and three dimensions can be found in Refs. [12, 162]. In this work, we restrict ourselves to the two-dimensional topological insulator HgTe, since it is not only the first material system showing transport features of a topological insulator, but also the material system with the most extensive experimental verification of topological insulator properties [14, 154, 163].

HgTe/CdTe quantum wells

As mentioned before, the first theoretical prediction for a material featuring the topological insulator state was graphene with strong spin-orbit interaction [4, 11]. Although it is very unlikely to measure topological insulator features experimentally, due to the small strength of the spin-orbit interaction of graphene, the requirements for a topological insulator have been set. The first theoretical proposal for a material fulfilling these requirements was given by Bernevig, Hughes and Zhang [13, 151]. It employs the inverted band structure of HgTe and creates a two-dimensional confinement within a HgTe/CdTe heterostructure leading to a two-dimensional topological insulator. Shortly after the proposal, experiments have been carried out which show the transport signatures of the topological edge state [14].

In the following chapter, we will introduce the basic features of HgTe/CdTe quantum wells. Starting from the band structure of the bulk materials, we will show how the confinement in z-direction leads to different two-dimensional systems featuring a conventional or an inverted band ordering. We discuss how the effective two-dimensional Hamiltonian can be derived from the three-dimensional system, and check for the quality of this approximation. Based on the obtained two-dimensional Hamiltonian, we will show the emergence of edge states at domain boundaries between conventional and inverted band order and derive their physical properties. Finally, we will provide a derivation of the protection from backscattering by time-reversal symmetry, which excludes the backscattering into the same lead undergoing a flip of spin and is a fundamental ingredient for the spin transistor presented in the next chapter.

6.1. Quantum well band structure

The two main ingredients of the following heterostructure, HgTe and CdTe, are both binary II-VI semiconductors, with the same crystallographic zincblende structure and a very similar lattice spacing. The bulk band structure of both materials shows a direct bandgap at the Γ point and thus the electronic properties can be described by the Γ-point representation of the cubic group. The different bands can be grouped into the

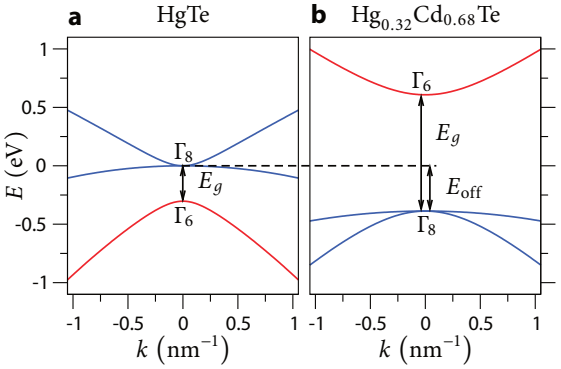

Figure 6.1. | Bulk band structure for HgTe and HgTe – The two panels show the bulk band structure of (**a**) HgTe and (**b**) $Hg_{0.32}Cd_{0.68}Te$ at the Γ point. HgTe features inverted bands with a negative bandgap of $E_g \approx -0.3$ eV whereas the band structure of $Hg_{0.32}Cd_{0.68}Te$ shows a conventional ordering of the spin 1/2 electron band (Γ_6) and the spin 3/2 hole band (Γ_8). A valence band offset of $E_{off} \approx -0.39$ eV and a gap of $E_g \approx 0.6$ eV (see Table A.1) is used.

s-type electron band with total spin 1/2 (Γ_6) and the *p*-type hole bands. Here, we restrict ourselves to the heavy- and light-holes with total spin 3/2 (Γ_8) and neglect the split-off band. The resulting bulk band structure from the 6×6 subgroup of the extended Kane model for HgTe and the HgTe compound used in the following heterostructure is shown in Fig. 6.1. The bands of CdTe are conventionally ordered, like in a typical III-V semiconductor. As shown in Fig. 6.1 (**b**) the electron like Γ_6 bands are separated from the hole-like Γ_8 bands by a positive bandgap. For HgTe this is not the case, as the band edges of the hole-like bands are energetically higher, the Γ_6 band is separated by a negative gap of −300 meV from the Γ_8 band as shown in Fig. 6.1 (**a**). This negative gap stems from a strong relativistic corrections, as heavy atoms like Hg interact very strongly with the atomic electric fields [164–166]. Because of the unusual band ordering, the band structure of HgTe is commonly termed inverted. At a HgTe-CdTe interface, the energies of the valence bands do not match which is taken into account by a valence band offset E_{off}.

Layered heterostructures of different $Hg_{1-x}Cd_xTe$ compounds can be grown by means of molecular beam epitaxy. The stacking order for a symmetrically iodine doped HgTe/CdTe quantum well is sketched in Fig. 6.2, which was used to show the transition between normal and inverted band structure and the associated quantum spin hall effect for different HgTe layer widths d [14]. The electronic structure of both compounds of the heterostructure can be well described by the Hamiltonian

$$\mathcal{H} = \begin{pmatrix} T & 0 & -\frac{1}{\sqrt{2}}Pk_+ & \sqrt{\frac{2}{3}}Pk_z & \frac{1}{\sqrt{6}}Pk_- & 0 \\ 0 & T & 0 & -\frac{1}{\sqrt{6}}Pk_+ & \sqrt{\frac{2}{3}}Pk_z & \frac{1}{\sqrt{2}}Pk_- \\ -\frac{1}{\sqrt{2}}Pk_- & 0 & U+V & 0 & R & 0 \\ \sqrt{\frac{2}{3}}Pk_z & -\frac{1}{\sqrt{6}}Pk_- & 0 & U-V & 0 & R \\ \frac{1}{\sqrt{6}}Pk_+ & \sqrt{\frac{2}{3}}Pk_z & R^\dagger & 0 & U-V & 0 \\ 0 & \frac{1}{\sqrt{2}}Pk_+ & 0 & R^\dagger & 0 & U+V \end{pmatrix}, \tag{6.1}$$

using the momentum operators $k\pm = k_x \pm \mathrm{i}k_y$ in plane. This Hamiltonian only contains the Γ_6 and Γ_8 bands in the sequence $|1\rangle=|\Gamma_6, 1/2\rangle$, $|2\rangle=|\Gamma_6, -1/2\rangle$, $|3\rangle=|\Gamma_8, 3/2\rangle$, $|4\rangle=|\Gamma_8, 1/2\rangle$,

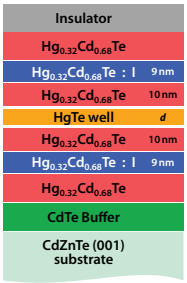

Figure 6.2. | Structure of a HgTe quantum well
Schematics of the layer sequence of a MBE-grown quantum well [167]. Depending on the width d of the HgTe layer the system can be tuned from a band insulator to a topological insulator.

$|5\rangle=|\Gamma_8, -1/2\rangle$, $|6\rangle=|\Gamma_8, -3/2\rangle$. The matrix elements T describe the s-like Γ_6 part while U, V and R describe the heavy-hole and light-hole bands which depend quadratically on $\boldsymbol{k}$. Furthermore, the electron and the light-hole bands are coupled by the Kane matrix element P which is independent of $\boldsymbol{k}$. An overview of the different multi-band Hamilton operators and their corresponding matrix elements can be found in Refs. [168, 169] and the complete definitions of all necessary matrix elements and material parameters for the following calculations are summarized in Appendix A.7.

In the literature [13, 168], the heterostructure sketched in Fig. 6.2 is commonly incorporated into the Hamiltonian (6.1) by an abrupt change of material parameters. Here, we use a softened z-dependent mixing function

$$x(z) = 0.68\left(\frac{1}{1+\mathrm{e}^{(d/2-z)/\delta_d}} + \frac{1}{1+\mathrm{e}^{(d/2+z)/\delta_d}}\right) \tag{6.2}$$

to change the composition of the different $\mathrm{Hg}_{1-x}\mathrm{Cd}_x\mathrm{Te}$ layers, and show that the outcomes only vary slightly from the results with an abrupt change. The material parameters of the different compounds are given by a linear interpolation of the pure material parameters summarized in Table A.1. Assuming translational invariance, the total wave function

$$\Psi_n(\boldsymbol{r}) = \mathrm{e}^{\mathrm{i}(k_x x + k_y y)}\psi_n(z, k_x, k_y) \tag{6.3}$$

can be expressed by plane waves in the x-y-direction and quantum well wave functions $\psi_n(z, k_x, k_y)$ in the z-direction. Exactly at the Γ point ($k_{||} = 0$) the Hamiltonian (6.1) breaks up into four uncoupled blocks, since $k_\pm$ as well as the R matrix elements vanish. As a result, the wave functions of the heavy-hole parts ($|3\rangle$, $|6\rangle$) are just determined by $U + V$, leading to two uncoupled sinusoidal solutions. In Fig. 6.3, the first two modes H1 and H2 are shown for a 7 nm wide quantum well in case of a the smooth material transition.
The electron bands and the light-hole bands are still strongly coupled by the Pk_z entries in the Hamiltonian. Thus, these quantum well bound states are given by superpositions of the $|1\rangle$, $|4\rangle$ and $|2\rangle$, $|5\rangle$ entries. For an abrupt interface the lowest quantum well bound states are exponentially decaying functions within both, the HgTe as well as the HgTe regions. They are localized at the transition between different quantum well layers therefore referred to as interface states [170, 171]. A softened transition between the materials also features such interface states. Fig. 6.3 shows the lowest states which

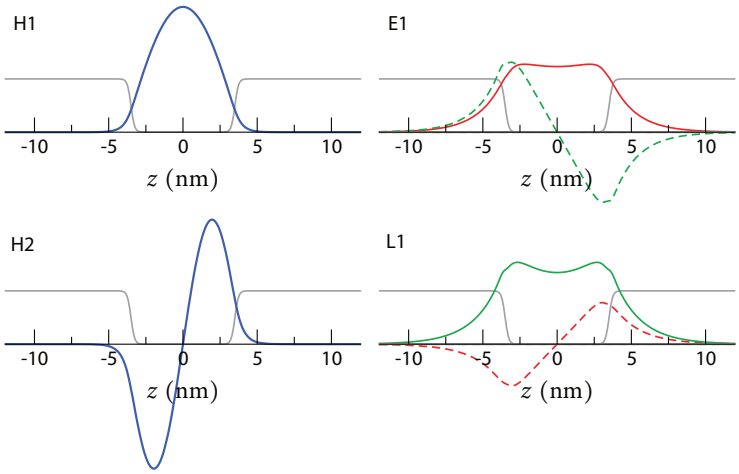

Figure 6.3. | Transversal states of a HgTe quantum well – The panels show the transversal wavefunctions of a 7 nm quantum well made of $Hg_{1-x}Cd_xTe$ at the Γ-point. The transition of the ratio x between the different materials is shown as gray line. The states are labeled by the character of the spinor into heavy-hole (H1,…), light-hole (L1,…) and electron like (E1,…). The following color code is used to distinguish the different spinor entries. Red shows the electron band, blue and green the hole band with $|m| = 3/2$ and $|m| = 1/2$ respectively. Solid line indicate real entries, whereas dashed lines show imaginary entries.

are obtained by numerical diagonalization and labeled by their dominant spinor entry as light-hole (L1, L2), heavy-hole (H1) and electron like (E1). In the following the states are chosen like

$$|\mathrm{E}n,+\rangle = \psi_1^{\mathrm{E}n}(z)\,|1\rangle + \psi_4^{\mathrm{E}n}(z)\,|4\rangle, \tag{6.4a}$$
$$|\mathrm{H}n,+\rangle = \psi_3^{\mathrm{H}n}(z)\,|3\rangle, \tag{6.4b}$$
$$|\mathrm{L}n,+\rangle = \psi_1^{\mathrm{L}n}(z)\,|1\rangle + \psi_4^{\mathrm{L}n}(z)\,|4\rangle, \tag{6.4c}$$
$$|\mathrm{E}n,-\rangle = \psi_2^{\mathrm{E}n}(z)\,|2\rangle + \psi_5^{\mathrm{E}n}(z)\,|5\rangle, \tag{6.4d}$$
$$|\mathrm{H}n,-\rangle = \psi_6^{\mathrm{H}n}(z)\,|6\rangle, \tag{6.4e}$$
$$|\mathrm{L}n,-\rangle = \psi_2^{\mathrm{L}n}(z)\,|2\rangle + \psi_5^{\mathrm{L}n}(z)\,|5\rangle. \tag{6.4f}$$

The key feature of the transversal eigenstates of this HgTe heterostructure is the dependence of the ground state energies on the quantum well width. The electron band E1 and the heavy-hole band H1, which have both opposite effective masses, also change their ordering with respect to their ground state energy, as shown in Fig. 6.4. For a width $d < 6.2$ nm we get a conventional band ordering, since E1 has a higher energy as H1. If the width is increased to values $d > 6.2$ nm, the energy of H1 exceeds that of E1, leading to an inverted ordering. This inverted ordering is necessary to get a topological insulator with edge states and a quantum spin hall effect instead of a conventional insulator. The results of the band-edge energies presented in Fig. 6.4 are

in good agreement with Ref. [13] and small deviations stem from the smooth transition between HgTe and HgTe modeled by Eq. (6.2).

Commonly, the states at $k_{||} = 0$ are used as a basis for an approximate two-dimensional Hamiltonian. Therefore we calculate the matrix elements of the states (6.4) with the Hamiltonian (6.1) as

$$H^0_{ij}(k_x, k_y) = \int_{-\infty}^{\infty} \langle j|\mathcal{H}(k_x, k_y, -\mathrm{i}\partial_z)|i\rangle \, \mathrm{d}z \tag{6.5}$$

and use the momentum operator in z-direction $k_z = -\mathrm{i}\partial_z$. This Hamiltonian is already two-dimensional, but contains all higher bands. In order to get an effective Hamiltonian with a reduced amount of bands, we apply the Löwdin partitioning [169, 172]. To this end,a subset of states close to the Fermi energy is chosen, which will be labeled by m in the following. Other states, not contained in this set, are labeled by l. The influence of the remote bands is subsequently incorporated into the Hamiltonian by the perturbation series

$$H_{mm'} = H^0_{mm'} + \frac{1}{2}\sum_l H^0_{ml} H^0_{lm'} \left(\frac{1}{E_m - E_l} + \frac{1}{E_{m'} - E_l} \right) - \cdots. \tag{6.6}$$

Usually, the set of interest contains the $|H1, +\rangle$ and $|E1, +\rangle$ states. In that case the transformed Hamiltonian reads

$$h_{2\times2}(\boldsymbol{k}) = \begin{pmatrix} C - (B+D)k^2 + M & Ak_+ \\ Ak_- & C + (B-D)k^2 - M \end{pmatrix}, \tag{6.7}$$

if only terms up to second order in $\boldsymbol{k}$ are included. The full Hamiltonian

$$H = \begin{pmatrix} h_{2\times2}(\boldsymbol{k}) & 0 \\ 0 & h^*_{2\times2}(-\boldsymbol{k}) \end{pmatrix} \tag{6.8}$$

comprises an additional 2×2 block, which is obtained by time reversal of the Hamiltonian (6.7) and is given in terms of the basis states $|H1, -\rangle$ and $|E1, -\rangle$. The parameters A, B, C, D and M depend on the width d of the heterostructure and contain the

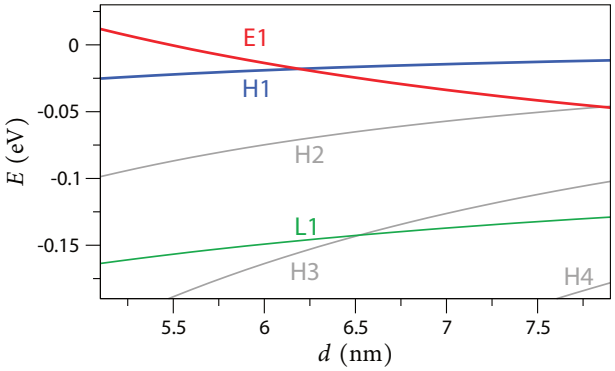

Figure 6.4. | Bandedges for different HgTe quantum well widths – Energies are extracted from a calculation of the transversal states at the Γ point, as shown in Fig. 6.3. The electron band E1 and the hole band H1 cross at $d \approx 6.2\,\mathrm{nm}$ allowing for topological edge states in wells bigger than this critical width.

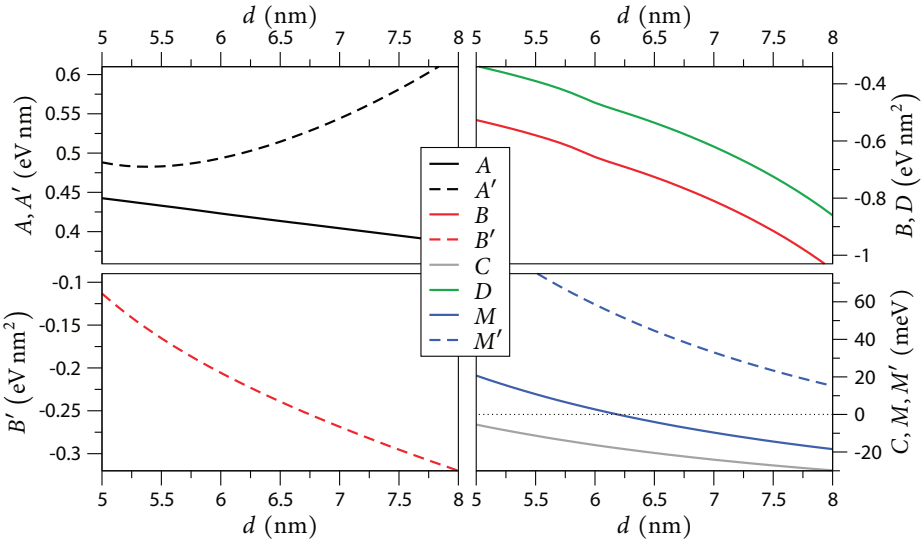

Figure 6.5. | Parameters for the effective two-dimensional Hamiltonians – Panels show the width dependence of the parameters for the effective two-dimensional model of HgTe quantum wells. Solid lines represent parameters needed for the 2×2 and 3×3 Hamiltonian, dashed lines only for the 3×3 Hamiltonian (6.9).

influence of all remote bands given by Eq. (6.6). In Fig. 6.5 their dependence in case of a smooth material transition for the interesting range of quantum well widths is summarized. Here, A is the spin-orbit interaction between the E1 and H1 state and B creates a parabolic dispersion equally for the electron and hole branch. The symmetry between the electron and the hole branch is broken by the D term. C is just an energy offset, and is usually removed from the Hamiltonian in the subsequent calculations.

The key term of this Hamiltonian is the mass parameter M, which fixes the band topology of the system. Quantum wells with a width $d > 6.2\,\mathrm{nm}$ have an inverted band ordering since $M < 0$, as shown in the lower right panel of Fig. 6.5. An inverted ordering is established since the band with higher energy has a hole like character at $k = 0$ and the band with lower energy is electron like. However, there is a gap between the electron and the hole states due to the spin-orbit interaction. For widths $d < 6.2\,\mathrm{nm}$ the band ordering at the Γ point is conventional since the mass $M > 0$. Throughout the following sections this Hamiltonian will be used to describe the electronic structure of HgTe heterostructures.

Since remote bands also influence Berry phase effects like weak localization [21], we also calculate the effective Hamiltonian with the additional H2 band, leading to

$$h_{3\times3}(\boldsymbol{k}) = \begin{pmatrix} C-(B+D)k^2+M & Ak_+ & A'k_-^2 \\ Ak_- & C+(B-D)k^2-M & 0 \\ A'k_+^2 & 0 & C+B'k^2-M' \end{pmatrix}. \quad (6.9)$$

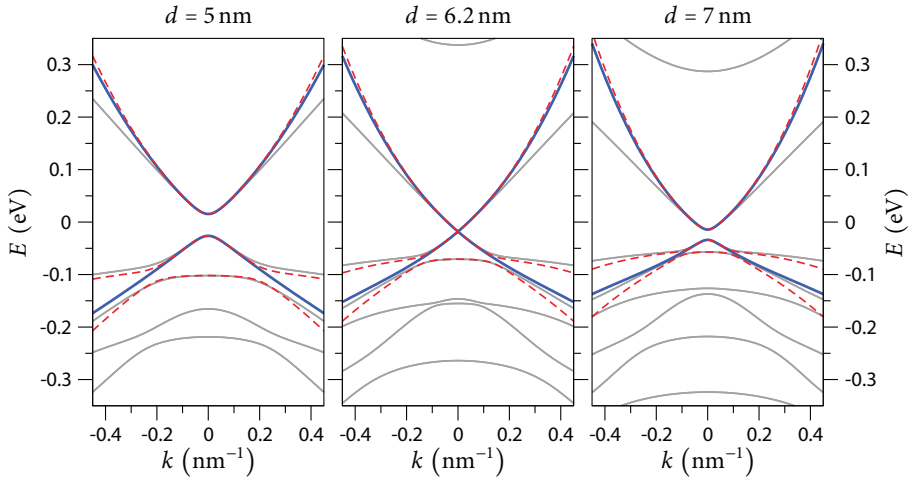

Figure 6.6. | Band structure models for HgTe quantum wells of different widths – Panels show the band structures for a conventional insulator ($d = 5\,\mathrm{nm}$), a gapless system ($d = 6.2\,\mathrm{nm}$) and a topological insulator ($d = 7\,\mathrm{nm}$). The gray lines display the bands given by the full three-dimensional Hamiltonian (6.1) confined by a heterostructure. The blue lines are a two-dimensional approximation resulting from the 2×2 Hamiltonian (6.7) and the red dashed lines for the 3×3 Hamiltonian (6.9).

For this Hamiltonian the dependence of the additional parameters A', B' and M' on the quantum well width d are also summarized in Fig. 6.5. Here, A' is a new spin-orbit interaction, the bending of the H2 band is given by B' and the energy offset by M'. By means of this Hamiltonian, we will show in Section 8.2.2 that the Berry phase texture of the hole branch differs strongly from the electron branch.

Finally, we want to analyze the quality of the two approximations by comparing the band structure of the full three-dimensional system with the two approximations given by Eq. (6.7) and Eq. (6.9). Therefore we calculate the bands for a HgTe heterostructure with all $\boldsymbol{k}$-dependencies of the full Hamiltonian (6.1). The resulting band structure for different quantum well widths d is visualized as gray lines in Fig. 6.6. The same plots also contain the bands of the two approximations. Close to the Γ point, the two-dimensional approximations fit the bands of the full system excellently for all quantum well widths. However, for energies higher than 50 meV the approximations drift away from the exact result and higher orders of $\boldsymbol{k}$ would be required to model the electronic structure properly. For the hole-bands the approximation by the 2×2 Hamiltonian is not very accurate, since the presence of the $H2$ band strongly modifies the band structure. This can be overcome by adding the $H2$ state to the basis of the approximation. The resulting bands, shown as red dashed lines in Fig. 6.6, resemble the electronic structure of the hole part very well. However, if only the physics of the edge states and the states with electronic character are considered the Hamiltonian (6.7) remains a well justified model for the electronic properties of HgTe quantum wells.

Furthermore, Fig. 6.6 does not only show the qualities of the different approximations but also the transition between the different topological states. In order to change from the conventional insulator at small quantum well widths d to a topological insulator for $d > 6.2\,\mathrm{nm}$, the gap between the electron and the hole states has to close. This topological transition is a crucial property of the topological insulator [12] and is nowadays also applied to other systems like for example superconductors [162].

6.2. Edge states

In the preceding section, we derived an effective Hamiltonian for HgTe heterostructures, featuring an inverted band ordering, depending on the quantum well width. Based on these results, we show why there are edge states occurring at domain boundaries between regions with different band topology. Therefore, we use a linear transition between a positive and a negative bandgap and calculate the bound states. We show that one of the occurring states features a linear spectrum, which is independent of the precise shape of transition between the band topologies [173]. It is this bound state, which is also present at the boundaries of a HgTe quantum well, leading to a quantized conductance known as transport signature of the quantum spin Hall effect [14].

In order to get a minimal model featuring edge states, we remove the quadratic terms in $\boldsymbol{k}$ from the Hamiltonian (6.7) leading to the Hamiltonian

$$h(\boldsymbol{k}) = \begin{pmatrix} M & Ak_+ \\ Ak_- & -M \end{pmatrix}, \tag{6.10}$$

and look for states at a model domain boundary given by

$$M(x) = \alpha x. \tag{6.11}$$

Because of the translational invariance in y-direction we can take a plane wave ansatz

$$\psi(x, y) = \mathrm{e}^{\mathrm{i}ky} \begin{pmatrix} \psi_A(x) \\ \psi_B(x) \end{pmatrix}, \tag{6.12}$$

with k the momentum in y-direction and the two transversal wavefunctions $\psi_A(x)$ and $\psi_B(x)$. Employing this ansatz, the Hamiltonian leads to the following two equations:

$$\alpha x \psi_A(x) + A\big(\mathrm{i}k\psi_B(x) - \mathrm{i}\partial_x \psi_B(x)\big) = E\psi_A(x), \tag{6.13a}$$

$$-\alpha x \psi_B(x) - A\big(\mathrm{i}k\psi_A(x) + \mathrm{i}\partial_x \psi_A(x)\big) = E\psi_B(x). \tag{6.13b}$$

These equations can be transformed into a quadratic problem, by applying the first order derivative ∂_x and replacing the obtained expressions with the definitions of $\partial_x \psi_{A/B}$ given by the Eqs. (6.13). The resulting equations read

$$A^2k^2\psi_A(x) + x^2\alpha^2\psi_A(x) + \mathrm{i}A\alpha\psi_B(x) - A^2\partial_x^2\psi_A(x) = E^2\psi_A(x), \tag{6.14a}$$

$$A^2k^2\psi_B(x) + x^2\alpha^2\psi_B(x) - \mathrm{i}A\alpha\psi_A(x) - A^2\partial_x^2\psi_B(x) = E^2\psi_B(x). \tag{6.14b}$$

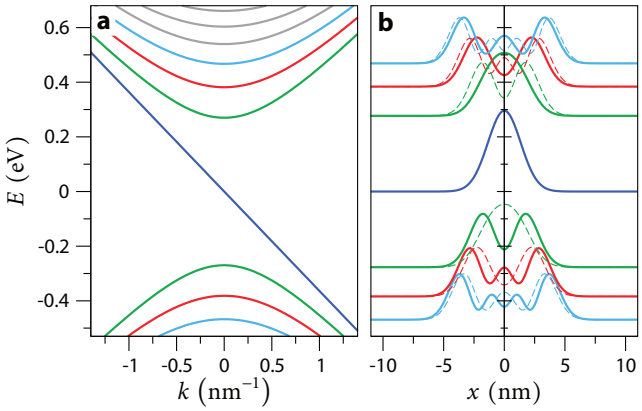

Figure 6.7. | Edge states at a band topology transition
a, Band structure of the edge states featuring one gapless mode ($\alpha = 0.1\,\mathrm{eV\,nm^{-1}}$, $A = 0.364\,\mathrm{eV\,nm}$). **b**, Expectation value of the corresponding transversal eigenstates for $k = 0.5\,\mathrm{nm^{-1}}$ solid lines, $k = -0.5\,\mathrm{nm^{-1}}$ dashed lines.

In the following, we define two new wavefunctions $\phi_\pm(x) = \psi_A(x) \pm \mathrm{i}\,\psi_B(x)$ and use the sum and the difference of Eqs. (6.14) to obtain two new differential equations

$$\alpha^2 x^2 \phi_-(x) - A^2 \partial_x^2 \phi_-(x) = \left(E^2 - A^2 k^2 + A\alpha\right)\phi_-(x), \tag{6.15a}$$

$$\alpha^2 x^2 \phi_+(x) - A^2 \partial_x^2 \phi_+(x) = \underbrace{\left(E^2 - A^2 k^2 - A\alpha\right)}_{\mathcal{E}_n^0} \phi_+(x), \tag{6.15b}$$

which resemble the harmonic oscillator problem. The solutions of this differential equation, corresponding to the eigenenergies $\mathcal{E}_n^0 = (2|n|+1)A\alpha$, are given by

$$\phi_n(x) \propto \mathrm{e}^{-\frac{\alpha}{2A}x^2} H_{|n|}\left(\sqrt{\tfrac{\alpha}{A}}x\right), \tag{6.16}$$

where H_n are Hermite polynomials. In topological insulators we look for gapless excitations, which are often not present in conventional materials due to the zero-point energy. Also the harmonic oscillator solutions ϕ_n have a zero-point energy of $A\alpha$. However, for the given setup this energy is removed from the total eigenenergy, which can be seen in Eq. (6.15a). As a consequence, the gapless state with zero energy at $k = 0$ is given by the ϕ_- state for $n = 0$ and reads

$$\psi_0(x, y) \propto \mathrm{e}^{\mathrm{i}ky} \mathrm{e}^{-\frac{\alpha}{2A}x^2} \begin{pmatrix} 1 \\ \mathrm{i} \end{pmatrix}, \tag{6.17}$$

with the total energy $E_0 = -Ak$. All higher excited states are given by a combination of $\phi_{(n)-}$ and the lower harmonic oscillator eigenstate $\phi_{(n-1)+}$, leading to

$$\psi(x, y) \propto \mathrm{e}^{\mathrm{i}ky} \begin{pmatrix} \sqrt{\alpha A}\,\phi_n(x) + (E_n + Ak)\,\phi_{n-1}(x) \\ \mathrm{i}\sqrt{\alpha A}\,\phi_n(x) - \mathrm{i}(E_n + Ak)\,\phi_{n-1}(x) \end{pmatrix}, \tag{6.18}$$

with an energy dispersion of $E_n = \mathrm{sgn}(n)\sqrt{A^2k^2 + 2|n|A\alpha}$.

To conclude, the model of the transition between conventional and inverted band ordering leads to a linear gapless state between several excited states as shown in

Fig. 6.7 (**a**). The eigenstate of the gapless state in x-direction is independent of k given by a single Gaussian, and surprisingly, the dispersion is independent of the slope α of the transition. In contrast, the excited states feature a gap between the electron and hole states and the transversal eigenstates are depending on the longitudinal momentum k as shown in Fig. 6.7 (**b**).
The preceding calculation was carried out for the upper block of the Hamiltonian. Since the other block is the time inverted copy, the spinors of the lower block can be obtained by complex conjugation. The dispersion is similar to the one of the upper block, except that the dispersion of the gapless state is inverted and has the opposite group velocity.

Similar edge states arise at the boundaries of an inverted HgTe heterostructure. If the bulk of the HgTe heterostructure features inverted bands and the vacuum is assumed to have conventional band ordering, a transition between both band topologies has to exist, and an edge state at the boundary emerges. In the next chapter, we will finally employ these edge states to propose a spin transistor device. However, at first we want to extend the model to include additional spin-orbit interactions and will show that in the presence of edge states the backscattering undergoing a spin-flip is prohibited.

6.3. Spin-orbit interaction

During the derivation of the effective two-dimensional Hamiltonian (6.8) we assumed the used materials HgTe and CdTe to feature bulk inversion symmetry. Furthermore, the layer structure of the quantum well was expected to be symmetric around the HgTe layer, as sketched in Fig. 6.2. As a consequence, the resulting Hamiltonian consists of two strictly uncoupled 2×2 blocks without any spin-orbit terms linking these two blocks. However, this is not the case if the inversion symmetry is broken.

Both materials are characterized by a zincblende structure which is described by a basis containing two different atoms. This breaks the bulk inversion symmetry of the crystal and leads to an additional spin-orbit interaction [174]. In HgTe quantum wells the described spin-orbit interaction enters the effective Hamiltonian as a momentum independent term Δ [167], leading to

$$H = \begin{pmatrix} C_k + M_k & Ak_+ & -\mathrm{i}Rk_- & -\Delta \\ Ak_- & C_k - M_k & \Delta & 0 \\ \mathrm{i}Rk_+ & \Delta & C_k + M_k & -Ak_- \\ -\Delta & 0 & -Ak_+ & C_k - M_k \end{pmatrix}, \tag{6.19}$$

where $k_\pm = k_x \pm \mathrm{i}k_y$, $\boldsymbol{k}^2 = k_x^2 + k_y^2$, $C_k = D\boldsymbol{k}^2$ and $M_k = M - B\boldsymbol{k}^2$.

Furthermore, this Hamiltonian contains the spin-orbit interactions induced by an electric field $\mathcal{E}_z$ perpendicular to the quantum well. This leads to a structure inversion asymmetry which enters the Hamiltonian by additional terms linking the upper and the lower block [175]. Experimentally, structure inversion asymmetry can be either

achieved by growing the quantum well structure asymmetrically, or by directly applying a perpendicular electric field by means of external gating. The corresponding matrix elements for the effective Hamiltonian have been calculated up to several orders in momentum $\boldsymbol{k}$ [176]. However, we limit ourselves to the first order term, which enters the Hamiltonian as R and scales linearly with $\boldsymbol{k}$. Throughout the following chapters we present several numerical calculations which always employ the material parameters for a 7 nm quantum well [167, 176] summarized in Table 6.1.

A	B	D	M	Δ	$R/(e\mathcal{E}_z)$
354.5	−686	−512	−10	1.6	−15.6

Table 6.1. | HgTe quantum well material parameters – Values for a $d = 7$ nm quantum well modeled by the Hamiltonian (6.19) in units of meV and nm [167, 176].

6.4. Absence of backscattering

In the context of topological insulators, the absence of backscattering in presence of elastic scatterers is often mentioned as an important feature [4, 12, 167, 177]. In the preceding section, we have introduced the effects of spin-orbit interactions due to structure inversion asymmetry (SIA) and bulk inversion asymmetry (BIA). This adds several terms to the Hamiltonian (6.8), which looses the initial structure of two uncoupled blocks and results in a dense matrix (6.19). As a consequence, elastic scattering also enables transitions between different spin species corresponding to the two blocks. However, backscattering undergoing a flip of spin is still forbidden and only spin preserving backscattering is allowed. In the following, we will show how this property can be derived from the symmetries of the scattering matrix.

Although most of the symmetries of the Hamiltonian (6.19) are broken, time reversal symmetry is still present and can be expressed by the anti-unitary operator

$$\mathcal{T} = \begin{pmatrix} 0 & 0 & -1 & 0 \\ 0 & 0 & 0 & -1 \\ 1 & 0 & 0 & 0 \\ 0 & 1 & 0 & 0 \end{pmatrix} \mathcal{C}, \tag{6.20}$$

where $\mathcal{C}$ is the complex conjugation. If an additional perpendicular magnetic field B is applied, time reversal leads to a reversal of the applied magnetic field

$$\mathcal{T}\, H(B)\, \mathcal{T}^{-1} = H(-B). \tag{6.21}$$

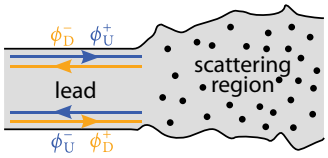

Figure 6.8. | Scattering of edge states
Sketch of a lead carrying two incoming edge states ϕ_U^+ and ϕ_D^+ and two outgoing edge states ϕ_U^- and ϕ_D^- attached to an arbitrary scattering region. .

Assuming very wide leads and a Fermi energy E within the bulk band gap $\pm M$, the remaining traveling lead wave functions are localized at the edges of the lead resulting in a complete spin polarization of these states.[1] Each of the two blocks $\sigma \in \{U, D\}$ of the Hamiltonian (6.19) has an incoming state ϕ_σ^+ and an outgoing state ϕ_σ^- localized at opposite edges, as sketched in Fig. 6.8. From the time reversal symmetry of the Hamiltonian we can deduce the relation

$$\phi_\sigma^+(B) = \mathcal{C}\phi_{\bar{\sigma}}^-(-B), \tag{6.22}$$

between the incoming and outgoing edge states at different magnetic fields, where $\bar{\sigma}$ represents the opposite block. The full state of the lead can be expressed by

$$\Psi(B) = \sum_\sigma \left(a_\sigma(B)\phi_\sigma^+(B) + b_\sigma(B)\phi_\sigma^-(B)\right), \tag{6.23}$$

where a_σ are the complex amplitudes for the incoming states and b_σ for the outgoing states. If a scattering region is attached to the lead, as sketched in Fig. 6.8, the connection between the a_σ and b_σ can be expressed in terms of the scattering matrix $\boldsymbol{S}$ [144], where

$$\begin{pmatrix} b_U(B) \\ b_D(B) \end{pmatrix} = \underbrace{\begin{pmatrix} t_{UU}(B) & t_{UD}(B) \\ t_{DU}(B) & t_{DD}(B) \end{pmatrix}}_{S} \begin{pmatrix} a_U(B) \\ a_D(B) \end{pmatrix}. \tag{6.24}$$

The scattering matrix has to fulfill certain constraints, which can be attributed to certain physical properties. For example, the current conservation requires a unitary scattering matrix $S^\dagger S = 1$, leading to

$$\begin{pmatrix} a_U(B) \\ a_D(B) \end{pmatrix} = \begin{pmatrix} t_{UU}^*(B) & t_{DU}^*(B) \\ t_{UD}^*(B) & t_{DD}^*(B) \end{pmatrix} \begin{pmatrix} b_U(B) \\ b_D(B) \end{pmatrix}, \tag{6.25}$$

when $S^\dagger$ is applied. Furthermore, the system fulfills the time reversal symmetry, which also holds for the scattering matrix. Taking the relation (6.22) between the single modes under complex conjugation into account, the time reversal of the full incoming state leads to

$$\mathcal{T}\Psi(B) = \sum_\sigma \left(a_\sigma^*(B)\,\bar{\sigma}\,\phi_{\bar{\sigma}}^-(-B) + b_\sigma^*(B)\,\bar{\sigma}\,\phi_{\bar{\sigma}}^+(-B)\right) = \tag{6.26}$$

$$\sum_\sigma \left(b_{\bar{\sigma}}^*(B)\,\sigma\,\phi_\sigma^+(-B) + a_{\bar{\sigma}}^*(B)\,\sigma\,\phi_\sigma^-(-B)\right), \tag{6.27}$$

[1] The extent of the edge states is approximately 100 nm and for leads wider than 1000 nm the spin-orbit interactions Δ and $Rk_\pm$ do not lead to an overlap between counter-propagating edge states, as we will explain in detail in the next chapter.

where $\sigma \in \{1, -1\}$ for the different blocks. Accordingly, the amplitudes of the modes transform as $a_\sigma(B) \to \sigma\, b^*_{\bar{\sigma}}(B)$ and $b_\sigma(B) \to \sigma\, a^*_{\bar{\sigma}}(B)$ under time reversal. Since the Hamiltonian fulfills relation (6.21), the same holds for the scattering matrix in Eq. (6.24). Applying the time-inversion operator leads to

$$\mathcal{T}\begin{pmatrix} b_\mathrm{U}(B) \\ b_\mathrm{D}(B) \end{pmatrix} = \begin{pmatrix} t_{\mathrm{UU}}(-B) & t_{\mathrm{DU}}(-B) \\ t_{\mathrm{UD}}(-B) & t_{\mathrm{DD}}(-B) \end{pmatrix} \mathcal{T}\begin{pmatrix} a_\mathrm{U}(B) \\ a_\mathrm{D}(B) \end{pmatrix}. \tag{6.28}$$

The lead amplitudes transform under time reversal in the same way as the time reversal of the edge state wavefunctions given by Eq. (6.27), which results in

$$\begin{pmatrix} a_\mathrm{D}(B) \\ -a_\mathrm{U}(B) \end{pmatrix} = \begin{pmatrix} t^*_{\mathrm{UU}}(-B) & t^*_{\mathrm{DU}}(-B) \\ t^*_{\mathrm{UD}}(-B) & t^*_{\mathrm{DD}}(-B) \end{pmatrix} \begin{pmatrix} b_\mathrm{D}(B) \\ -b_\mathrm{U}(B) \end{pmatrix}. \tag{6.29}$$

By comparing the scattering matrix (6.25) of the unitary transformation and the scattering matrix (6.29) of the time reversal, we can deduce the following relations for the scattering amplitudes:

$$t_{\mathrm{UU}}(B) = t_{\mathrm{DD}}(-B), \tag{6.30}$$

$$t_{\mathrm{UD}}(B) = -t_{\mathrm{UD}}(-B). \tag{6.31}$$

These relations reveal that without broken time reversal symmetry, the scattering between different spin channels is forbidden since $t_{\mathrm{UD}}(0) = -t_{\mathrm{UD}}(0) = 0$. For systems with many leads, the same relation holds within every attached lead. However, transitions between the spin blocks of different leads are allowed. In the following chapter we will take advantage of this property and introduce a spin transistor based on the scattering properties of the edge states.

7 Switching Edge-States in HgTe Constrictions

In the preceding chapter we introduced the basic properties of topological insulators and especially focused on the requirements and consequences of the quantum spin Hall effect in the two-dimensional topological insulator mercury telluride [13, 14]. If the Fermi energy lies within the bulk band gap the transport through the heterostructure is carried only by edge states. In this case the transmission can be conveniently explained by an edge channel picture [178]: Two states of different spin propagate at opposite edges resulting in a quantized conductance of $2e^2/h$. Due to the spatial separation of the spin-states the spin-orbit coupling is suspended, and the system geometry can be employed for spin selection [154]. Spin-selectivity is also a crucial ingredient for the spin transistor proposed by Datta and Das [179]. In this case a spin-polarized current through ferromagnetic contacts is controlled electrically through the gate-dependent Rashba spin-orbit interaction [175] of a conventional two-dimensional semiconductor heterostructure. However, the realization turns out to be difficult because of the spin relaxation in the semiconductor heterostructure and interfacial effects at the ferromagnetic contacts such as the conductivity mismatch [180] between the different materials. HgTe-based topological insulators appear to be promising candidates for spin processing devices [181–183] since they exhibit a gate-dependent chemical potential and considerable spin-orbit interaction but, in contrast to the Datta-Dass proposal

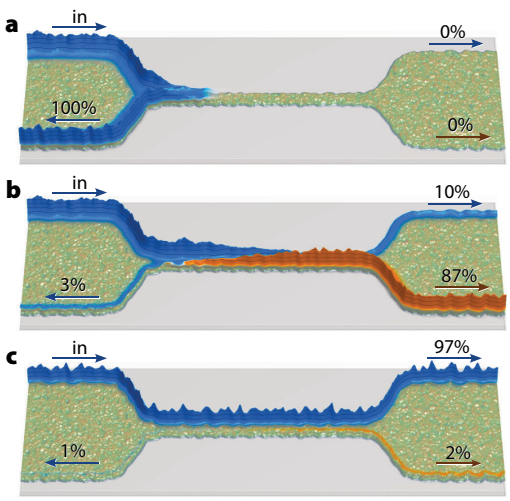

Figure 7.1. | Switching states of a HgTe constriction
Spin-resolved local density of states for charge carriers entering a constriction from the upper left edge. Color code indicates spin polarization [Blue spin-up block (u), orange spin-down block (d)]. **a**, Perfect reflection of the incoming state for an energy within the confinement induced gap [see Fig. 7.3 (**b**) at $\mu = 7$ meV]. **b**, For an energy closely below the gap ($\mu = 4$ meV), the spin-orbit interaction results in a spin flip associated with a switching of the edges. **c**, The effective spin-orbit interaction is reduced for energies far below the gap ($\mu = -5$ meV), and hence the incoming spin-up spin-state leaves the constriction unrotated.

no ferromagnetic contacts are needed to induce spin-polarized current. As a consequence a single material is sufficient to create a spin-transistor action. Moreover, the one-dimensional nature of the edge states suppresses orbital effects present in bulk conductors, leading to high spin polarizations and to a much better spin switching quality.

In the following, we demonstrate how topological edge states can be selectively switched in an elongated constriction etched out of a HgTe heterostructure, leading to an integrated three-state charge- and spin-transistor action of high fidelity. Illustrations of all three possible switching states are shown in Fig. 7.1. An incoming state at the left upper edge, which is spin-up polarized because of the quantum spin Hall effect (and color coded blue in the following images), can either be reflected back to the lower edge as represented by Fig. 7.1 (**a**) or transmitted through the narrow part. The back reflection into the opposite spin channel at the same edge is forbidden, since the combination of time-reversal symmetry and unitarity of the scattering matrix excludes this processes as discussed in the preceding section. Within the constriction the right moving edge-states on the upper and the lower side start to overlap, leading to a finite spin-orbit interaction. This allows for steering the spin orientation and the corresponding path of the electrons traversing the constriction. An incoming spin-up state will leave the channel either by swapping the edge with a simultaneous spin-flip, as shown in Fig. 7.1 (**b**), or by remaining in its spin and edge state as shown in Fig. 7.1 (**c**).

In the following chapter we will show how these switching properties can be understood theoretically. In Section 7.1 we start with the derivation of the edge states for an etched HgTe strip and use those states as a basis for a one-dimensional model Hamiltonian. Subsequently, we show in Section 7.2 by means of a transfer matrix approach using this model how the transmission through an elongated constriction changes by varying external parameters, which ultimately leads to the spin transistor action. Finally, we

employ numerical quantum transport calculations to analyze the impact of system imperfections induced by electrostatic impurities and roughly etched boundaries in Section 7.3. Afterwards we demonstrate the peculiar switching characteristics by means of a top-gate or two side-gates acting on the constriction in Section 7.4. In Section 7.5 we will reveal that periodically modulated HgTe nanoribbons can be further employed to study the frequency spectrum and the transport properties of Bloch–Zener oscillations.

7.1. Topological edge states

In order to understand the switching properties of a HgTe constriction, as sketched in Fig. 7.1, we derive the properties of the edge states at first. Since HgTe quantum wells have a narrow band gap, a confinement of electronic states can only be achieved by taking away parts of the material by etching and not by gating the local chemical potential of certain regions into the band gap. Up to now, the exact type of boundary conditions appearing at the edges of an HgTe heterostructure are not determined. One possible boundary condition arises for example from the vanishing probability current perpendicular to the edge [184]. However, usually the wavefunction is set to zero at the boundaries [185], which we will also apply in the following.

We chose a lead with a constant width W to point in x-direction and search for the transversal eigenfunctions $\psi(y)$, which separately fulfill the boundary conditions $\psi(y \leq 0) = 0$ at the lower side and $\psi(y \geq W) = 0$ at the upper side. We take the Hamiltonian (6.8) consisting of the two uncoupled 2×2 blocks and search for exponentially decaying eigenfunctions

$$\psi_{\mathrm{u}} = \mathrm{e}^{-\lambda y}\begin{pmatrix}1 & \xi & 0 & 0\end{pmatrix}, \tag{7.1a}$$

$$\psi_{\mathrm{d}} = \mathrm{e}^{-\lambda y}\begin{pmatrix}0 & 0 & 1 & \xi\end{pmatrix}, \tag{7.1b}$$

within each of the two blocks for energies in the bulk bandgap $E \in [-M, M]$. Solving the eigenvalue problem for the Hamiltonian leads to two degenerate eigenvalues, corresponding to the different decay lengths

$$\lambda_1^{\pm} = \sqrt{k_x^2 + F^{\pm} - \sqrt{(F^{\pm})^2 - \frac{M^2-(E^{\pm})^2}{B^2-D^2}}}, \tag{7.2a}$$

$$\lambda_2^{\pm} = \sqrt{k_x^2 + F^{\pm} + \sqrt{(F^{\pm})^2 - \frac{M^2-(E^{\pm})^2}{B^2-D^2}}}, \tag{7.2b}$$

where the superscript indicates the propagation direction of the states, with (+) representing the right-moving state and (−) the left-moving one. In Eq. (7.2)

$$F^{\pm} = \frac{A^2 - 2(MB + E^{\pm}D)}{2(B^2 - D^2)}, \tag{7.3}$$

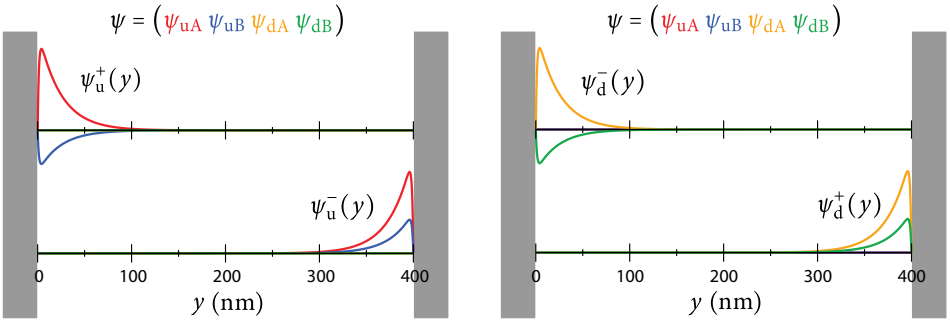

Figure 7.2. | Edge states in a wide HgTe nanoribbon – Transversal wavefunctions given by Eq. (7.6) for a nanoribbon of width $W = 400\,\mathrm{nm}$. The left (right) panel shows the solutions for the upper (lower) block of the spinor. All wavefunctions are real and the color coding displays the different spinor entries.

and the corresponding eigenenergies

$$E^{\pm} = \frac{\mp A\sqrt{B^2 - D^2}k_x - DM}{B} \tag{7.4}$$

are linear in the momentum k_x pointing in lead direction. In order to fulfill the boundary condition at $y = 0$, we build a superposition of an exponentially increasing wavefunction with $\lambda_2^{\pm}$ and an exponentially decreasing one with $\lambda_1^{\pm}$, since $\lambda_2^{\pm} \gg \lambda_1^{\pm}$. This fixes the weight of the second spinor entry in Eq. (7.1) leading to

$$\xi^{\pm} = \pm\frac{\sqrt{A^2 - 4BM + \frac{4D^2M}{B}} - A}{2\sqrt{2}(B - D)M}\sqrt{\frac{A^2B^2 + AB^2\sqrt{A^2 - 4BM + \frac{4D^2M}{B}}}{B^2 - D^2} - 2BM}. \tag{7.5}$$

Furthermore, we can use the opposite superposition of increasing and decreasing solutions at the other boundary $y = W$, leading to four eigenstates

$$\psi_{\mathrm{u}}^{+}(y) \propto \left(\mathrm{e}^{\lambda_1^{+}(y-W)} - \mathrm{e}^{\lambda_2^{+}(y-W)}\right) \begin{pmatrix} 1 & -\xi^{+} & 0 & 0 \end{pmatrix}, \tag{7.6a}$$

$$\psi_{\mathrm{u}}^{-}(y) \propto \left(\mathrm{e}^{-\lambda_1^{-}y} - \mathrm{e}^{-\lambda_2^{-}y}\right) \begin{pmatrix} 1 & -\xi^{-} & 0 & 0 \end{pmatrix}, \tag{7.6b}$$

$$\psi_{\mathrm{d}}^{+}(y) \propto \left(\mathrm{e}^{-\lambda_1^{+}y} - \mathrm{e}^{-\lambda_2^{+}y}\right) \begin{pmatrix} 0 & 0 & 1 & \xi^{+} \end{pmatrix}, \tag{7.6c}$$

$$\psi_{\mathrm{d}}^{-}(y) \propto \left(\mathrm{e}^{\lambda_1^{-}(y-W)} - \mathrm{e}^{\lambda_2^{-}(y-W)}\right) \begin{pmatrix} 0 & 0 & 1 & \xi^{-} \end{pmatrix}, \tag{7.6d}$$

in the limit of a very wide nanoribbon. In Fig. 7.2 the right- and left-moving edge states of the different spin blocks for a 400 nm strip are sketched. The two lines display the amplitudes of the populated spinor entries and are color coded for the spin-up and spin-down solutions respectively. If the width W of the strip is not sufficiently large to neglect the exponential tail of the edge state at the opposite boundary, both boundary conditions ($\psi(y \leq 0) = 0$ and $\psi(y \geq W) = 0$) have to be taken into account simultaneously. This

leads to a small anticrossing between right-moving and left-moving states which is of the size [185]

$$m \approx \frac{2|A(B^2 - D^2)M|}{B^3(A^2B - 4(B^2 - D^2)M)} \mathrm{e}^{-\lambda_1^+ W}. \tag{7.7}$$

The physics of these four uncoupled edge states can be readily described by two one-dimensional Dirac Hamilton operators for the up (u) and down (d) edge

$$H_{\mathrm{eff\,u/d}} = c \mp a\,\sigma_x\,k_x + m\,\sigma_z. \tag{7.8}$$

In each case, it gives rise to a right- and left-moving state with a group velocity

$$a = A\sqrt{\frac{(B^2 - D^2)}{B^2}} \tag{7.9}$$

and an energy offset $c = -DM/B$. The gap induced by a narrow confinement is included into the Hamiltonian by a mass potential, with a strength given by Eq. (7.7).

In order to get transitions between the different spin states, we add a term arising from bulk-inversion asymmetry (BIA) to the effective Hamiltonian. The contribution of the BIA term to the full Hamiltonian (6.19) is given by

$$H_{\mathrm{BIA}} = \begin{pmatrix} & & & -\Delta \\ & & \Delta & \\ & \Delta & & \\ -\Delta & & & \end{pmatrix}, \tag{7.10}$$

with a momentum independent splitting $\Delta \approx 1.6\,\mathrm{meV}$ [167]. The effect of this spin-orbit interaction leads to a nonvanishing coupling and energy splitting

$$\delta^{\pm} \approx \langle \psi_{\mathrm{u}}^{\pm} | H_{\mathrm{BIA}} | \psi_{\mathrm{d}}^{\pm} \rangle \approx -\frac{4\mathrm{e}^{-\lambda_1^{\pm} W} \lambda_1^{\pm} W \xi^{\pm}}{1 + (\xi^{\pm})^2} \Delta, \tag{7.11}$$

between the states with different spin and the same propagation direction. A coupling among states with opposite propagation direction is absent. Note, the parts of the wavefunction with the shorter decay length $\lambda_2^{\pm}$ are neglected in this approximation, since their contribution is small as $\lambda_2^{\pm} \gg \lambda_1^{\pm}$.

At this point we combine the effective Hamiltonian (7.8) without spin-orbit interaction with the energy splitting $\delta^{\pm}$ from BIA leading to

$$H_{\mathrm{eff}} = \begin{pmatrix} c + m & -ak_x & \delta_{\mathrm{m}} & \delta_{\mathrm{p}} \\ -ak_x & c - m & -\delta_{\mathrm{p}} & -\delta_{\mathrm{m}} \\ \delta_{\mathrm{m}} & -\delta_{\mathrm{p}} & c + m & ak_x \\ \delta_{\mathrm{p}} & -\delta_{\mathrm{m}} & ak_x & c - m \end{pmatrix}. \tag{7.12}$$

Since $\delta^{\pm}$ depends on k_x, we get new matrix elements $\delta_{\mathrm{p/m}} = (\delta^{+} \pm \delta^{-})/2$ in the basis of this effective Hamiltonian.

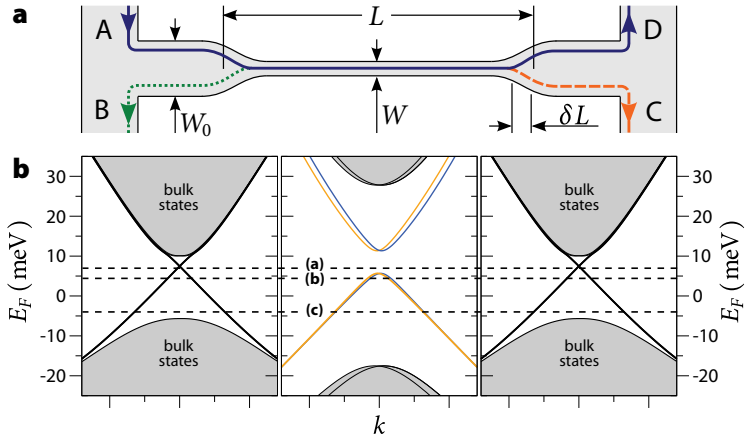

Figure 7.3. | Sketch of the geometry and local band structure – a, An elongated constriction of width W and length L is connected by two bulk regions, which are both attached to two leads. The spin-up channel, entering the system at the upper boundary from lead A, can be scattered to channel B (green), C (orange), D (blue). **b**, Sketch of the band structure for a sequence of a wide (left panel, $W = 1000$ nm), narrow (middle panel, $W = 100$ nm) and wide (right) lateral confinement, as appearing in the constriction sketched in panel (**a**). The dashed lines indicate the Fermi energies of the switching states presented in Fig. 7.1 (**a-c**).

For energies within the bulk band gap, which is the region of interest for the topological spin-transistor presented here, the spin-orbit interaction due to structure-inversion (SIA) is usually much weaker than the BIA part. This is because on the one hand the matrix elements of SIA contain an additional linear dependence on k_x, which is small for the low momenta in the bulk bandgap. On the other hand, SIA is strictly absent for symmetrically grown quantum wells and we expect the symmetry in z-direction only to be marginally broken by an external gating. Hence, we neglect this type of spin-orbit interaction in the effective Hamiltonian (7.12). However, in the numerical calculations presented at the end of this chapter, all spin-orbit interactions are included, and do not significantly change the fundamental switching properties, which we will first derive for the effective Hamiltonian. Instead, SIA can be employed to substantially reduce the constriction length, as we will show at the end of Section 7.4.

7.2. Switching edge states

In the following we utilize the effective Hamiltonian (7.12) to understand the transmission properties of an elongated constriction, as shown in Figs. 7.3 (**a**). We assume two extended regions which are large enough to support gapless edge states. Both are connected by two leads (A, B) and (C, D) in order to allow for a selective determination of the transport carried by the different spin-polarized edge states. The two extended

regions are linked via a sufficiently long channel of width $W(x)$. The width dependence along the longitudinal direction is given by

$$W(x) = W_0 - \left(\frac{W_0 - W}{1 + \mathrm{e}^{\frac{x-L/2}{\delta L}}} - \frac{W_0 - W}{1 + \mathrm{e}^{\frac{x+L/2}{\delta L}}} \right). \tag{7.13}$$

This shapes a transition between the width W_0 of the broad ribbon outside of the constriction and a channel of length L and width W. The transition on a length scale of δL is modeled by a Fermi function, as sketched in Fig. 7.3 (**a**). With these parameters, we are able to describe the geometric properties of a two-dimensional device, as shown in Fig. 7.1 (**a-c**). The position dependent width (7.13) can be further included in the effective one-dimensional Hamiltonian (7.12).

We can already predict three different energy regions important for the switching properties of this setup from the band structure of an extended strip with a fixed width. For a wide ribbon, the mass gap (7.7) as well as the spin-orbit interaction (7.11) vanish exponentially with $\mathrm{e}^{-\lambda_1 W}$, where λ_1 denotes the longer decay length of the eigenstates. Consequently, the band structure of the asymptotic regions features two spin-degenerate gapless bands, as shown in the left and right panels of Fig. 7.3 (**b**). If the ribbon width is on the order of 100 nm, as it should be the case within the constriction, m and $\delta^{\pm}$ are sufficiently strong to open up a band gap and lift the spin degeneracy of the states. This results in a band structure as shown in the middle panel of Fig. 7.3 (**b**).

The three different switching states can be selected by the Fermi energy within the narrowed region. In the following we consider an edge state at the upper edge entering the device at lead A, as sketched in Fig. 7.3 (**a**). If the Fermi energy is situated within the bandgap of the constriction, which is marked by the dashed line (a) in Fig. 7.3 (**b**), the current flow through this region is exponentially suppressed and consequently the transmission to lead B dominates. The reflection into lead A is exactly zero due to the absence of backscattering with a spin-flip, which is a consequence of time-reversal symmetry, as discussed in the previous chapter. This leads to a perfect transmission of 100% to lead B, as shown in Fig. 7.1 (**a**).

For energies outside of the band gap, the edge states are able to enter the constriction and a transmission to lead C or D is possible. The size of the transmission to the opposite lead depends on the channel length and the strength of the spin-orbit interaction. For reasonable configurations a switching with a strong transmission from lead A to C undergoing a spin flip as shown in Fig. 7.1 (**b**) as well as a transmission from lead A to D preserving the spin direction can be achieved [see Fig. 7.1 (**c**)]. In the following the transmission amplitudes of these different switching states will be deduced from the one-dimensional Hamiltonian (7.12).

7.2.1. Transfer matrix approach without spin-orbit interaction

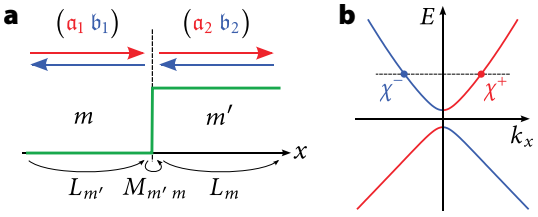

Figure 7.4. | Transfer matrix approach
a, The transfer matrix $M_{m'm}$ relates the incoming and outgoing amplitudes $(\mathfrak{a}_1\ \mathfrak{b}_1)$ and $(\mathfrak{a}_2\ \mathfrak{b}_2)$ at a mass step from m to m'. In the regions with constant mass, the phase evolution is given by L_m and $L_{m'}$. **b,** Sketch of the energies related to the basis states (7.14) extracted from the band structure for different momentum but fixed energy.

To compute the transmission amplitudes through a constriction we apply a transfer matrix approach [186, 187] for the one-dimensional model Hamiltonian (7.12). To this end, we split the system into small regions with constant parameters like the mass m, as sketched in Fig. 7.4 (**a**). In these regions the wavefunction can be described in terms of the amplitudes with the corresponding eigenstates of the asymptotic Hamiltonian. Without spin-orbit interaction, the Hamiltonian breaks up into two blocks, each of them representing a right-moving state $\chi^+_{\mathrm{u/d}}$ and a left-moving state $\chi^-_{\mathrm{u/d}}$. For a transfer matrix approach the eigenstates are needed at a common energy E for different momenta k_x, as sketched in Fig. 7.4 (**b**). Within each of the blocks u/d this leads to the states

$$\chi^{\pm}_{\mathrm{u}} = \frac{1}{\sqrt{1+|u_m|^2}}\begin{pmatrix}\pm u_m\\ 1\end{pmatrix}, \quad \chi^{\pm}_{\mathrm{d}} = \frac{1}{\sqrt{1+|u_m|^2}}\begin{pmatrix}\mp u_m\\ 1\end{pmatrix}, \tag{7.14}$$

where

$$u_m = -\frac{\sqrt{E+m}}{\sqrt{E-m}}. \tag{7.15}$$

In this basis, the wavefunction at any point x can be described by the superposition

$$\psi = \mathfrak{a}\chi^+ + \mathfrak{b}\chi^-, \tag{7.16}$$

where $\mathfrak{a}$ is the amplitude of the right-moving state and $\mathfrak{b}$ is the amplitude of the left-moving state. In the following we derive two different types of matrices required for the total transfer matrix, as depicted in Fig. 7.4 (**a**). The matrix $M_{m'm}$ relates the amplitudes for an abrupt change of the material parameters and L_m describes the phase evolution for free propagation. The matrix $M_{m'm}$ is defined by

$$\begin{pmatrix}\mathfrak{a}_2\\ \mathfrak{b}_2\end{pmatrix} = M_{m'm}\begin{pmatrix}\mathfrak{a}_1\\ \mathfrak{b}_1\end{pmatrix}, \tag{7.17}$$

and connects the amplitudes $(\mathfrak{a}_1\ \mathfrak{b}_1)$ on the left side of the step for a mass m to the amplitudes $(\mathfrak{a}_2\ \mathfrak{b}_2)$ on the right side of the step for a mass m'. Since the Hamiltonian (7.12)

only contains first order derivatives, it is sufficient to match only the wavefunctions, $\psi(0^-) = \psi(0^+)$, on both sides of the step. This leads to the transfer matrix

$$M_{m'm} = \frac{1}{2u_m} \begin{pmatrix} +u_m + u_{m'} & +u_m - u_{m'} \\ +u_m - u_{m'} & +u_m + u_{m'} \end{pmatrix}. \tag{7.18}$$

The matrix for the free precession on a length L is given by the momentum of the right and the left moving states for a common energy E and reads

$$L_m = \begin{pmatrix} e^{i\sqrt{E^2-m^2}L/a} & 0 \\ 0 & e^{-i\sqrt{E^2-m^2}L/a} \end{pmatrix}. \tag{7.19}$$

We are able to get the transmission through arbitrarily shaped constrictions by a successive multiplication of these two building blocks. An example, where the full transmission can be given analytically, is an abrupt change of the constriction width, as sketched by gray lines in Fig. 7.5 (**a**). In terms of the effective Hamiltonian (7.12) this equals the transmission through a mass step, as shown in Fig. 7.5 (**b**). The full transfer matrix from the left to right side of the system is given by

$$M = M_{0m}\, L_m\, M_{m0}, \tag{7.20}$$

containing the transitions M_{0m} and M_{m0} between a gapless region and a gapped region, as well as the free propagation L_m within the constriction. The transmission amplitude[1] $t = (M_{11})^{-1}$ is given by a single entry of the full transfer matrix M [186]. This leads to a quantum transmission

$$T = |t|^2 = \left(1 + \left[\tfrac{m}{a\,k} \sin(k\,L)\right]^2\right)^{-1}. \tag{7.21}$$

The numerical evaluation is shown in Fig. 7.5 (**c**) as a gray line. The result resembles a transmission pattern governed by Fabry-Pérot oscillations, which is a signature of multiple reflections at the constriction boundaries. However, quantum oscillations of this kind are not desired in a switching device and can be sufficiently damped out by smoothing the change of the constriction width $W(x)$ leading to an adiabatic transition.

If the width of the constriction is changed continuously the mass m in the effective model changes in a similar manner, as shown in Fig. 7.5 (**b**) by the blue line. In order to obtain the transfer matrix of this system, we discretize the x-coordinate into N steps with a sufficiently small step size. The full transfer matrix can be obtained by the product of the transfer matrices of the small steps:

$$M = M_{m_N\, m_{N-1}} \prod_{i=N-1}^{1} L_{m_i} M_{m_i\, m_{i-1}}. \tag{7.22}$$

[1]The transmission amplitude t is given by the amplitude of the outgoing state, since for $m = 0$ the group velocity is independent of E and given by a.

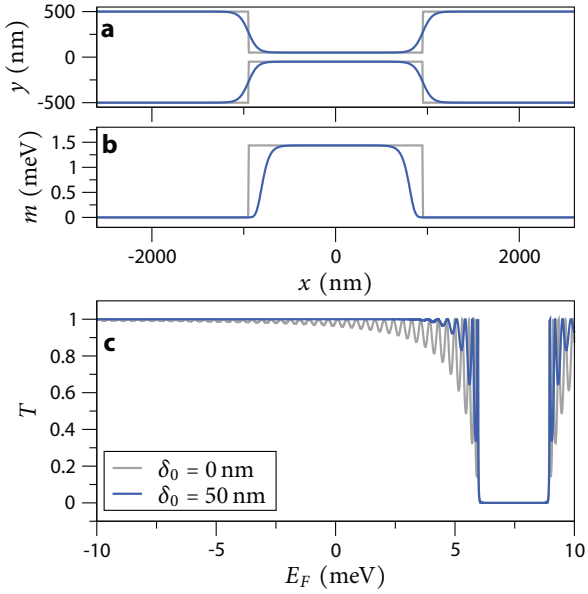

Figure 7.5. | Transport through a constriction without spin-orbit interaction
a, The constriction is modeled by $W(x)$, Eq. (7.13), shaping two bulk regions of width $W_0 = 1000\,\mathrm{nm}$ connected by a smaller channel of width $W = 100\,\mathrm{nm}$ and length $L = 1900\,\mathrm{nm}$ for a transition length of $\delta_0 = 0$ (gray line) and $\delta_0 = 50\,\mathrm{nm}$ (blue line).
b, Corresponding position dependent mass m, Eq. (7.7), of the model Hamiltonian (7.12).
c, Transmission through the constriction for one spin channel given by Eq. (7.21).

The transmission of the smoother constriction shows less resonances than the result for an abrupt change, as shown in Fig. 7.5 (**c**). This effect can be explained by the reflectivity at the crossover between a wide and a narrow region, which is reduced for the adiabatic transition compared to the reflectivity of the abrupt change. As a result, multiple reflections within the constriction are less probable and Fabry-Pérot oscillations tend to vanish. Thus the transmission is dominated by the gap m induced by the width W of the constriction. If the Fermi energy is within this gap, the transmission is zero and transport happens from lead A to B. Out of the gap the transmission is almost unity, except for small oscillations due to multiple reflections at the constriction boundaries.

7.2.2. Transfer matrix approach with spin-orbit interaction

In the following we extend the preceding calculations by taking the spin-orbit interaction between the different blocks of the Hamiltonian (7.12) into account. As in the case without spin-orbit interaction, the eigenstates of the asymptotic system for a common energy E serve as basis for the different amplitudes of the system. For the 4×4 Hamiltonian we obtain the four basis states

$$\chi_+^{\pm} = \frac{1}{\sqrt{2+2|v_{m+}|^2}} \begin{pmatrix} \pm v_{m+} \\ 1 \\ \mp v_{m+} \\ 1 \end{pmatrix}, \quad \chi_-^{\pm} = \frac{1}{\sqrt{2+2|v_{m-}|^2}} \begin{pmatrix} \pm v_{m-} \\ 1 \\ \pm v_{m-} \\ -1 \end{pmatrix}, \tag{7.23}$$

where

$$v_{m\pm} = -\frac{\sqrt{E+m\pm\delta_\mathrm{m}}}{\sqrt{E-m\pm\delta_\mathrm{m}}}. \tag{7.24}$$

The different spinors are grouped into right movers (+) and left movers (−) tagged by the upper index and do not decouple into upper and lower blocks anymore. However, if δ_m is negligibly small, the spinor element $v_{m\pm} = u_m$ and the basis states can be directly written in terms of the two different superpositions of the spinors (7.14) without spin-orbit interaction:

$$\chi^{\pm}_{\pm}\big|_{\delta_\mathrm{m}=0} = \tfrac{1}{\sqrt{2}}\left(\chi^{\pm}_{\mathrm{u}} \pm \chi^{\pm}_{\mathrm{d}}\right). \tag{7.25}$$

The transfer matrix in the basis of the spin-orbit eigenstates (7.23) is given by

$$M_{m'm} = \begin{pmatrix} \frac{v_{m+}+v_{m'+}}{2v_{m+}} & \frac{v_{m+}-v_{m'+}}{2v_{m+}} & 0 & 0 \\ \frac{v_{m+}-v_{m'+}}{2v_{m+}} & \frac{v_{m+}+v_{m'+}}{2v_{m+}} & 0 & 0 \\ 0 & 0 & \frac{v_{m-}+v_{m'-}}{2v_{m-}} & \frac{v_{m-}-v_{m'-}}{2v_{m-}} \\ 0 & 0 & \frac{v_{m-}-v_{m'-}}{2v_{m-}} & \frac{v_{m-}+v_{m'-}}{2v_{m-}} \end{pmatrix}, \tag{7.26}$$

and exhibits a block diagonal form. The free propagation within this basis is given by

$$L_m = \begin{pmatrix} \mathrm{e}^{\mathrm{i}q_+L} & 0 & 0 & 0 \\ 0 & \mathrm{e}^{-\mathrm{i}q_+L} & 0 & 0 \\ 0 & 0 & \mathrm{e}^{\mathrm{i}q_-L} & 0 \\ 0 & 0 & 0 & \mathrm{e}^{-\mathrm{i}q_-L} \end{pmatrix}, \tag{7.27}$$

with the momenta

$$q_\pm = \tfrac{1}{a}\left(\sqrt{(E - m \pm \delta_\mathrm{m})(E + m \pm \delta_\mathrm{m})} \pm \delta_\mathrm{p}\right). \tag{7.28}$$

In order to get spin resolved transmission amplitudes we proceed as follows: The width W_0 of the strip in the asympotic regions is big enough to prevent a spin-splitting as shown in the left and right panels of Fig. 7.3 (**a**). As a result we can transform the spin up and down states to the $\chi^{\pm}_{+}$, $\chi^{\pm}_{-}$ basis in the lead regions given by Eq. (7.25). In a multi-channel transfer matrix approach the transmission amplitudes are

$$\boldsymbol{t} = \begin{pmatrix} M_{11} & M_{13} \\ M_{31} & M_{33} \end{pmatrix}^{-1}, \tag{7.29}$$

and like in the spin-less case, given by the transfer matrix M of Eq. (7.22). However, the off-diagonal elements of M are zero, since every single transfer matrix $M_{m'm}$ is block diagonal. Therefore the total spin-resolved transmission is given by

$$T_{\mathrm{u/d}\leftarrow\mathrm{u}} = \tfrac{1}{4}\left|t_{11} \pm t_{22}\right|^2. \tag{7.30}$$

The phase difference between the transmission amplitudes t_{11} and t_{22} of the two blocks specifies the spin transmission. If the difference between the momenta $q_\pm$ of Eq. (7.28) is small, the transmission amplitudes t_{11} and t_{22} are in phase and $T_{\mathrm{d}\leftarrow\mathrm{u}} \approx 0$. A strong transmission from spin up to spin down can be achieved, if the momentum difference between the blocks fulfills $(q_+ - q_-)L = (1 + 2l)\,\pi$, where $l \in \mathbb{Z}$. This can be achieved

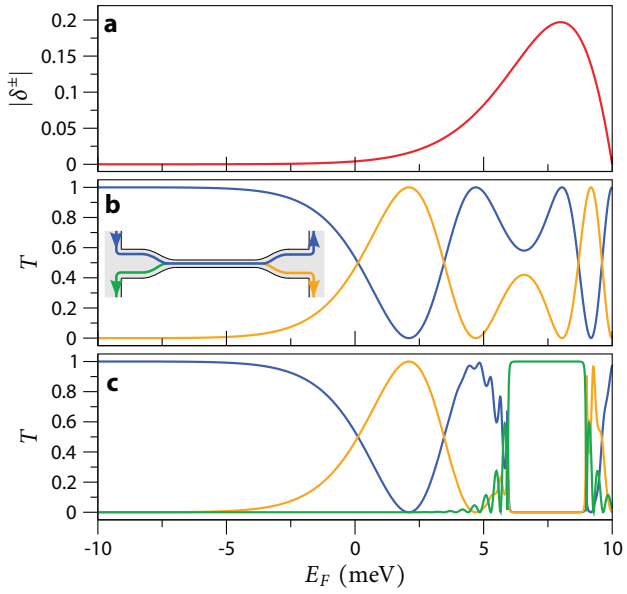

Figure 7.6. | Transport through a constriction with spin-orbit interaction
a, Energy dependence of the spin-orbit splitting $\delta^{\pm}$, Eq. (7.11), for $W = 100\,\mathrm{nm}$.
b, Transmission between initial spin-up to spin-down state for channel length $L = 1900\,\mathrm{nm}$ and vanishing confinement induced gap $m = 0$. Transmission channels are color coded as sketched in the inset.
c, Transmission of the spin-up state through a constriction in presence of spin-orbit interaction into different spin channels given by Eq. (7.30).

by changing external parameters like the Fermi energy. The momentum difference is predominantly given by the strength of the spin-orbit interaction $|\delta^{\pm}|$, which depends exponentially on the decay length $\lambda_1^{\pm}$ of the transversal eigenstates. This decay length is energy dependent and results in a stronger localization of the edge states for energies away from the Dirac point. Correspondingly, the strength of the spin-orbit interaction (7.11) is small for energies close to the opening of the bulk bandgap at $E = -10\,\mathrm{meV}$ and maximal at the crossing point between right and left movers, as shown in Fig. 7.6 (**a**). This leads to a strong spin preserving transmission for small Fermi energies shown by the blue line in Fig. 7.6 (**b**). For increasing energies, the spin-orbit interaction grows and leads to a spin-flip transmission shown as orange line.

If the backscattering due to the mass potential m is taken into account also transport into lead B is enabled and the transmission from lead A into all different leads B, C and D can be tuned by the Fermi energy. As shown in Fig. 7.6 (**c**) there are big energy regions, which in each case feature a dominant transmission into a single outgoing channel. The color code of the different transmission amplitudes is sketched in Fig. 7.3 (**a**). It is this transmission pattern which allows for an application as spin transistor.

7.3. Disorder effects

In the preceding calculations we used a constriction modeled by a one-dimensional Hamiltonian (7.12). In the following we want to show, that the full two-dimensional system features the same switching properties. Therefore we apply the wave-packet transport algorithm presented in Section 4.2. Furthermore, we investigate the stability

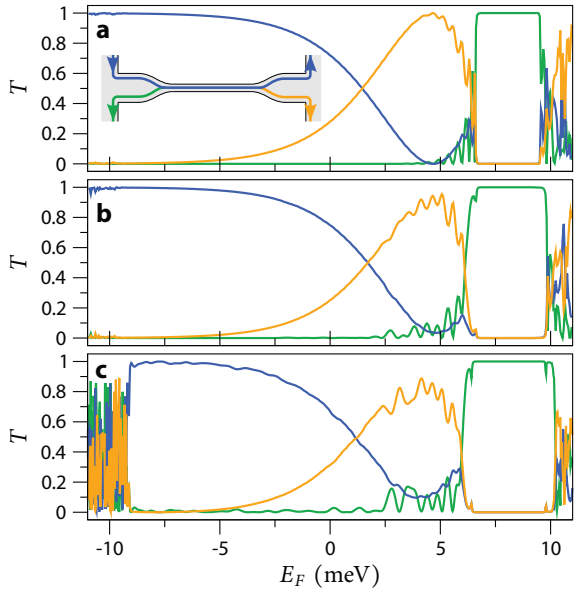

Figure 7.7. | Transport in presence of different disorder types
Energy dependent transmission of the spin-up state through a constriction ($L = 1900\,\text{nm}$, $W_0 = 1000\,\text{nm}$, $W = 100\,\text{nm}$, $\delta L = 50\,\text{nm}$) into different spin channels calculated for the two-dimensional Hamiltonian (8.4). The transmission channels are color coded as sketched in the inset.
a, Clean system.
b, System with a Gaussian impurity potential $U_{\text{imp}}(\boldsymbol{r})$, Eq. (7.31), ($\rho = 10\,\text{nm}$, $U_0 = 2\,\text{meV}$)
c, System with a Gaussian impurity potential and roughened walls modeled by Eq. (7.32) ($W_r = 20\,\text{nm}$).

of the switching properties by adding impurities and rough boundary conditions to the two-dimensional Hamiltonian (6.19).

First of all, we calculate the transmission for a two-dimensional description of a constriction modeled by a strip with a variable position-dependent width given by Eq. (7.13), as applied for the previous one-dimensional model. The resulting transmission amplitudes are summarized in Fig. 7.7 (**a**), using the same color code as in Fig. 7.3 (**a**). The switching properties are similar to the results of the model calculation. For low energies the transmission between lead A and lead D is strong, because of the reduced spin-orbit interaction (7.11). At higher energies, the spin-orbit interaction grants a sufficient precession between different spins and results in a switching from lead A and lead C. Within the confinement induced gap m, Eq. (7.7), the states are not able to enter the constriction and the transmission is steered from lead A and lead B. As in the one-dimensional case there are remains of Fabry-Pérot oscillations. By comparing Fig. 7.6 (**c**) and Fig. 7.7 (**a**) one finds that the one-dimensional model slightly overestimates the spin-orbit interaction with respect to the full two-dimensional Hamiltonian.

In order to incorporate the effect of impurities into the two-dimensional model, we add an electrostatic impurity potential

$$U_{\text{imp}}(\boldsymbol{r}) = \sum_n U_n \mathrm{e}^{-\frac{|\boldsymbol{r}-\boldsymbol{r}_n|^2}{2\rho^2}}, \tag{7.31}$$

to the Hamiltonian (6.19). The sum runs through all grid points n, where the disorder amplitude U_n is drawn from a Gaussian distribution. Additionally, the impurity potential is Gaussian correlated on the length scale ρ, and the strength is determined

by $\langle U_{\mathrm{imp}}(\boldsymbol{r})^2 \rangle = U_0^2$. Numerical calculations reveal that the transport properties of the constriction are mostly unaffected by the electrostatic impurities. Only the strength of the transmission to lead C undergoing a spin-flip is slightly reduced for an impurity strength U_0, which is chosen to be 10% of the bulk band gap of the topological insulator, as shown in Fig. 7.7 (**b**).

An additional source of scattering is given by a rough confinement. Since the constriction has to be etched from a two-dimensional heterostructure, a certain roughness of the walls is unavoidable. As model for this edge roughness we define the width of the strip separately for the upper and the lower boundary by

$$W'(x) = W(x) + \sum_i W_i \sin(x/l_i + \theta_i), \tag{7.32}$$

where $W(x)$ is the smooth variation of the constriction given by Eq. (7.13). In the following calculations we use 21 random oscillation lengths l_i varying from 10 nm to 30 nm with a step size of 1 nm and uniformly distributed random phases θ_i. The amplitudes W_i are chosen uniformly to create a maximal deviation

$$W_r = \max(|W'(x) - W(x)|) \tag{7.33}$$

on the order of a few nanometers. The resulting transport in presence of an electrostatic impurity potential and the rough walls is presented in Fig. 7.7 (**c**). The influence of the rough walls is similar to the effect of electrostatic impurities. Due to the random potential the spin-flip probability within the constriction is slightly reduced [compare orange line in Fig. 7.7 (**c**) with the one in Fig. 7.7 (**a**)]. The rough walls further lead to an increase of the confinement induced gap and an extended region of transmission into lead B, as shown by the green line in Fig. 7.7 (**c**). Furthermore, the fluctuations of the transmission outside the bulk gap ±10 meV are strongly enhanced.

However, none of the two different types of impurities destroys the switching properties of the constriction if the impurities are weak enough to preserve the quantum spin Hall effect. The three different switching states are still very pronounced in the numerical calculations and can be used for a three state spin- and charge-transistor, as shown in the next section.

7.4. Local gating

In the following we consider the possibility of controlled switching between edge currents by two types of local gating. Both setups can be used as spin- and charge-transistor and operate differently with respect to the applied gate voltage. The gating is modeled by a position dependent potential in the vicinity of the constriction. Changing the local Fermi energy via gating has been proven experimentally feasible for the considered HgTe heterostructures [154] and serves as the control for the spin-transistor setups suggested hereafter.

In the first configuration a gate is placed on top of the constriction, which is covering the entire narrow strip and small parts outside of the confined region, as shown in Fig. 7.8 (**a**). We model the gating by the position dependent potential

$$V(x) = V_g \left(\frac{1}{1 + \mathrm{e}^{\frac{x - L_g/2}{\delta L_g}}} - \frac{1}{1 + \mathrm{e}^{\frac{x + L_g/2}{\delta L_g}}} \right), \tag{7.34}$$

with a strength V_g, switched on at the length scale δL_g and covering a length L_g. Similar to the calculations before, we add a random impurity potential as well as edge roughness, as specified in the preceding considerations. The transmission of the spin-up channel entering the device at lead A is calculated by means of the wave-packet algorithm for all Fermi energies in a single run. The resulting transmission amplitudes into lead B, C and D are shown in the panels (**b**), (**c**) and (**d**) of Fig. 7.8, where large (small) transmissions are depicted by dark (bright) colors. All plots show universal conductance fluctuations for energies outside the bulk bandgap, which is approximately given by $E_F - V_g < -|M|$ and $E_F + V_g > |M|$ as marked by dashed lines in Fig. 7.8 (**b-d**). Within the bulk bandgap the device exhibits the switching properties. The Fermi energy of the ungated heterostructure is pinned to a certain value determined by the doping layers incorporated at the fabrication process and can be additionally tuned via a back-gate. Assuming for example a Fermi energy of $E_F = 0$, the transmission can be steered between the three different leads by changing the top-gate voltage V_g. A perfect transmission to lead B is achieved for a voltage of $V_g = -7\,\mathrm{meV}$. By changing the top gate voltage, the effective spin-orbit interaction is changed accordingly [see Fig. 7.6 (**a**)], similar to the Datta-Das proposal based on a gate tunable Rashba spin-orbit interaction [179]. For $V_g = -4\,\mathrm{meV}$ the transmission to lead C is maximal and can be tuned to a transmission to lead D by changing the gate voltage to $V_g = 5\,\mathrm{meV}$. In this region of gate voltages the device acts as a spin transistor.

A similar effect occurs if two side-gates with an opposite applied voltage V_s are attached close to the constriction and used to steer the edge state current, as sketched in Fig. 7.8 (**e**). We assume that the potential induced by the gates drops linearly between the two boundaries, which we model by the potential

$$V(\boldsymbol{r}) = V_s \frac{2y}{W(x)} \left(\frac{1}{1 + \mathrm{e}^{\frac{x - L_g/2}{\delta L_g}}} - \frac{1}{1 + \mathrm{e}^{\frac{x + L_g/2}{\delta L_g}}} \right), \tag{7.35}$$

that is added to the two-dimensional Hamiltonian (6.19). This leads to different chemical potentials for the two spin channels close to the upper and lower side of the constriction. In this way, the momenta k_x of two edge channels with opposite spins get split and the spin-precession within the constriction is strongly reduced. The results of the conductance calculated by the wave-packet algorithm are summarized in Fig. 7.8 (**f-h**). Due to the symmetric gating, an applied gate voltage V_s does not change the average chemical potential within the constriction. Thus the mass gap shows up as a vertical stripe for $E_F > 5\,\mathrm{meV}$ indicating that the constriction is isolating, independent

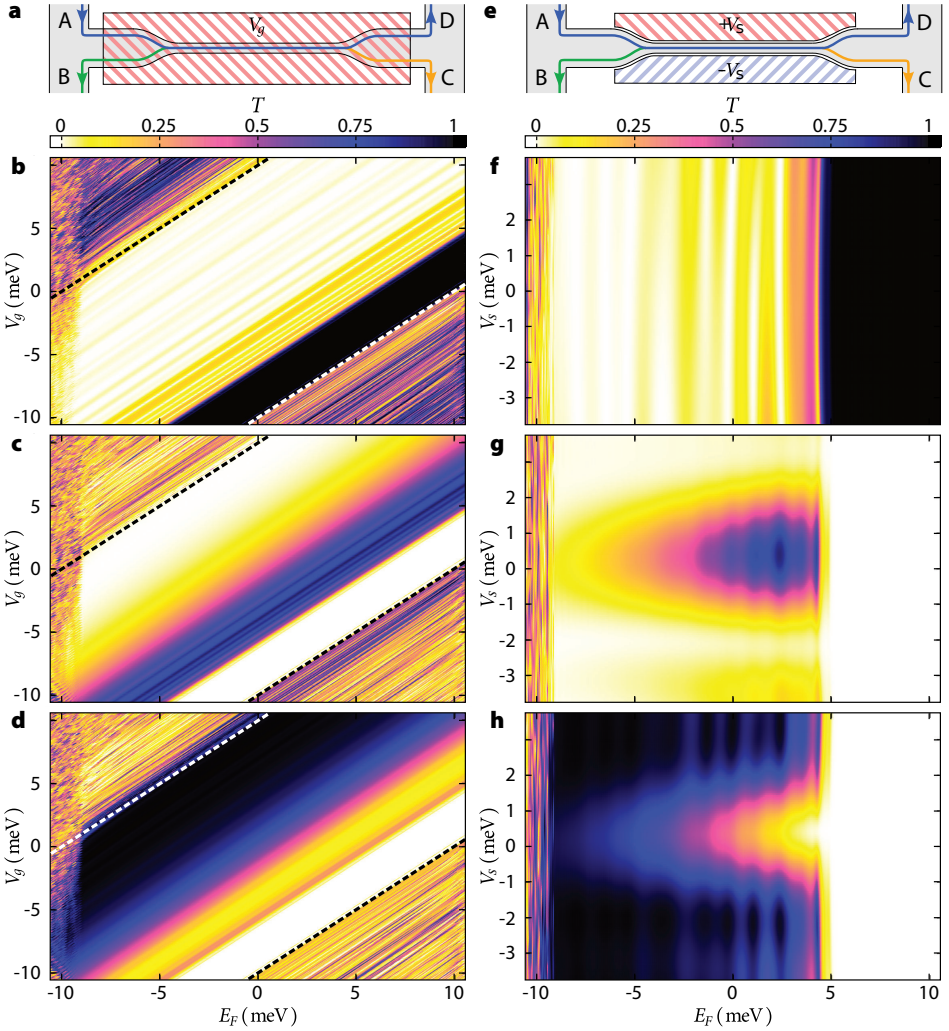

Figure 7.8. | Spin-transistor action by top- and side-gating – a, Scheme of the constriction (width $W = 100\,\mathrm{nm}$, length $L = 1900\,\mathrm{nm}$) coupled to bulk parts (width $W_0 = 1000\,\mathrm{nm}$) and subject to a gate on top of the narrow region (light red area). A random potential with $U_0 = 2\,\mathrm{meV}$ and wall roughness of $W_r = 20\,\mathrm{nm}$ are included as visualized in Figs. 7.1 (**a-c**). **b-d,** Panels show the color coded quantum transmission from lead A to lead B (**b**), C (**c**) and D (**d**) depending on the Fermi energy E_F and the top-gate voltage V_g. **e,** Scheme of a smaller constriction ($W = 60\,\mathrm{nm}$, $W_r = 10\,\mathrm{nm}$, $L = 900\,\mathrm{nm}$, $W_0 = 1000\,\mathrm{nm}$) with two side-gates next to the narrow region. **e-f,** Transmission from lead A to lead B (**f**), C (**g**) and D (**h**) as a function of E_F and side gate voltage V_s. Panels (**b-d**) and (**f-h**) reveal the spin- and charge-transistor action for the different suggested gate configurations.

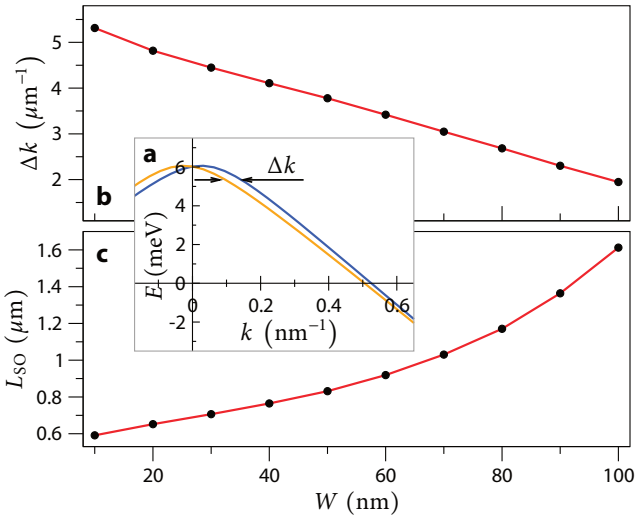

Figure 7.9. | Width dependent spin precession
a, Magnification of the edge-state bandstructure close to the anticrossing between right and left movers in presence of BIA ($\Delta = 1.6$ meV).
b, Momentum difference Δk between the spin-split edge states of a constriction with width W close to the confinement induced gap, as sketched in panel (**a**).
c, Resulting spin precession length L_{SO} for different constriction widths W.

of the external gate voltage, as shown in Fig. 7.8 (**f**). If the constriction is tuned into the conducting state ($E_F < 5$ meV) for example by engineering the Fermi energy by means of properly designed doping layers, the setup works as a spin transistor controlled through the side-gate voltage V_s: For low $|V_s|$ the states entering the device undergo a spin-flip within the constriction leading to a dominant transmission to lead C as depicted in Fig. 7.8 (**g**). In a spin-transistor device, the channel length must be chosen sufficiently long to feature a complete transition between the two spin-states. If a gate voltage $|V_s|$ is applied, the momenta of different spin states differ sufficiently to suppress the spin precession. As a result, the spin state remains unchanged and the spin-up state entering the device at lead A gets transmitted to D, as shown in Fig. 7.8 (**h**). The calculations presented in Fig. 7.8 (**f-h**) were performed for a narrower constriction ($W = 60$ nm) and the same amount of disorder is added to demonstrate that the switching functionality is robust against down scaling to a regime of a few 10 nanometers.

In the preceding part, the channel length was chosen long enough to feature a full spin precession, which is an important ingredient for the spin-transistor action. In view of Eq. (7.11), the effective spin-orbit interaction increases with decreasing width, allowing for faster spin precession and shorter constrictions. The energy region, which shows the strongest spin-orbit splitting, is close to the opening of the confinement induced band gap for $E_F = c - m(W)$, which is also width dependent. As a result, a compromise between a small channel width with a short spin-precession length and a sufficiently small confinement gap m, that still allows for transmission through the constriction, must be found.
Therefore we calculate the band structures of infinitely extended constrictions of different widths W and extract the band splitting Δk, as sketched in Fig. 7.9 (**a**). The splitting between the spin states at the top of the hole-like bands increases with decreasing channel width, as shown in Fig. 7.9 (**b**). This leads to a spin precession length $L_{SO} = \pi/\Delta k$, which is depending on the channel width W as depicted in Fig. 7.9 (**c**). The result shows

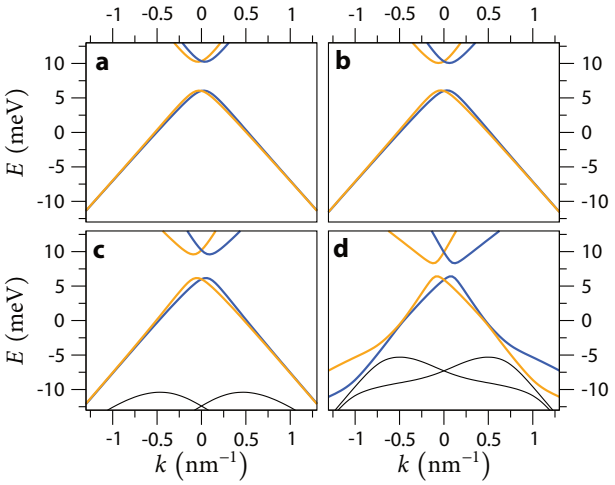

Figure 7.10. | Edge-state spin-splitting from SIA
a, Bandstructure of a strip of width $W = 100\,\mathrm{nm}$ close to the bandgap for a symmetric quantum well ($\Delta = 1.6\,\mathrm{meV}$, $R = 0$). **b-d,** Bandstructure for increasing SIA spin-orbit interaction [(**b**) $R = 0.1\,\mathrm{eV\AA}$, (**c**) $R = 0.2\,\mathrm{eV\AA}$, (**d**) $R = 0.4\,\mathrm{eV\AA}$] and constant BIA $\Delta = 1.6\,\mathrm{meV}$. Most notably the spin-splitting close to the confinement induced gap grows.

a decreasing spin-precession length L_{SO} reaching $L_{SO} = 600\,\mathrm{nm}$ at channel widths of 10 nm. Accordingly, the constriction of a spin-transistor should be as long as the spin-precession length or slightly longer. However, at a width of $W = 30\,\mathrm{nm}$ the confinement induced gap already spans half of the bulk bandgap, which restricts the working area of the transistor. Furthermore, impurity backscattering is more pronounced for smaller channel width. Thus scaling down to lower widths also affects the operating quality of the spin-transistor.

Another possibility to reduce the length of the constriction is to change the strength of the underlying spin-orbit interaction itself. This can be achieved by breaking the symmetry of the heterostructure in z-direction with an asymmetric arrangement of different layers around the HgTe quantum well. Preliminary calculations of the bandstructure for different strengths of SIA and constant BIA indicate that the spin-splitting close to the gap between right and left movers can be amplified by SIA. For increasing SIA of $R = 0.1\,\mathrm{eV\AA}$ [Fig. 7.10 (**b**)], $R = 0.2\,\mathrm{eV\AA}$ [Fig. 7.10 (**c**)] the bands show a strong splitting close to the confinement induced gap, which reduces gradually for increasing momentum. The energy dependence is similar compared to the reference without SIA [see Fig. 7.10 (**a**)], moreover, the splitting is approximately doubled in Fig. 7.10 (**c**), which would already allow for a complete spin flip in a constriction of half the length. If the SIA is further increased, and the term R from SIA gets on the order of the term A, which is responsible for the bulk bandgap and the presence of the topological states, the bandstructure of the edge states becomes more complicated. Besides the strong splitting at the top of the bands, there is an additional anticrossing within in the bulk bandgap, as shown in Fig. 7.10 (**d**). Independent of the composition of different spin-orbit interactions the spin splitting is dominant close to the confinement induced gap. Thus asymmetric quantum wells, which give rise to strong spin-orbit interaction due to SIA, are a second option to increase the effective spin splitting and reduce the required channel lengths in return. Furthermore, the growth of asymmetrically confined quantum wells is also very feasible from an experimental point of view.

7.5. Bloch–Zener oscillations in HgTe nanoribbons

In Chapter 5 we revealed that periodic structures within a zero-gap semiconductor feature both conventional Bloch oscillations and so called Bloch–Zener oscillations in graphene. They arise due to the acceleration of the average momentum of a wave packet in reciprocal space by a constant driving potential in presence of a periodic superlattice, which leads to a periodic motion in momentum space known as Bloch oscillations. If more bands are coupled by small anticrossings the Zener tunneling between those states gains in importance and the effect of Bloch oscillations is enriched by periodic tunneling events within the electron and the hole states close to the Fermi energy, which is explained in detail in Section 5.2. Since the edge states within the bulk bandgap of the topological insulator HgTe are well described by the one-dimensional Dirac Hamiltonian (7.12) we also assume the emergence of Bloch–Zener oscillations in periodically modulated HgTe nanoribbons. In this section we carry out complementary considerations to the Bloch–Zener oscillations in graphene and employ two different types of periodic modulations to investigate the frequency spectrum of Bloch–Zener oscillations as well as their signatures in the current-voltage characteristics.

As introduced at the beginning of this chapter, the finite width of a nanoribbon induces a small mass-like gap m between the right-moving and the left-moving edge-states, as shown in the middle panel of Fig. 7.3 (**b**). The size of the gap can be approximated by Eq. (7.7) and depends exponentially on the width of the ribbon. At first, we want to utilize this dependence to imprint a periodic potential on a nanoribbon by creating a position dependent modulation of the width

$$W(x) = \frac{W_0 + W_1}{2} - \frac{W_0 - W_1}{2} \sin\left(\frac{2\pi x}{a}\right), \tag{7.36}$$

leading to the geometry sketched in Fig. 7.11 (**a**). For the numerical determination of the mini-band structure given by one unit cell of the periodic structure we use an iterative Arnoldi eigenvalue solver implemented in ARPACK [111]. As shown in Fig. 7.11 (**b**), the bandstructure of the modulated nanoribbon features two edge states, which are folded back into the first Brillouin zone multiple times and generate several

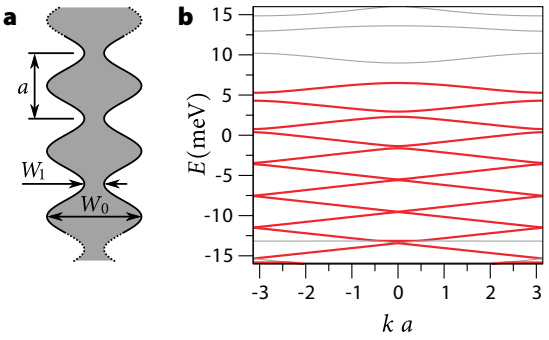

Figure 7.11. | Nanoribbon with periodic width modulation
a, Sketch of a nanoribbon with position dependent width $W(x)$, Eq. (7.36), modulated between the maximal width W_0 and a minimal width W_1 with a periodicity length a.
b, Bandstructure of a periodically modulated HgTe nanoribbon ($W_0 = 300$ nm, $W_1 = 50$ nm, $a = 200$ nm).

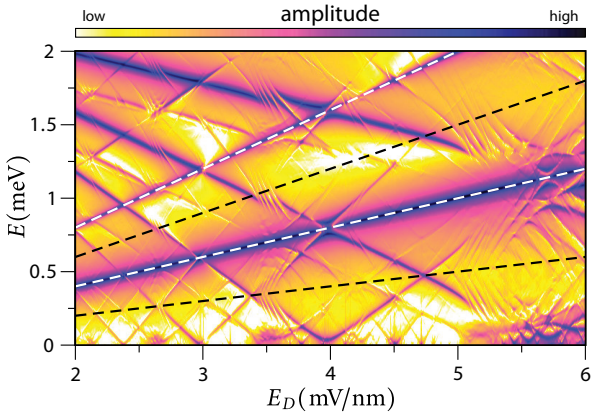

Figure 7.12. | Frequency spectrum for periodic width modulation – Frequencies $E = \hbar\omega$ of the wave packet center-of-mass motion depending on the applied drift field E_D in a periodically modulated HgTe nanoribbon ($W_0 = 300\,\text{nm}$, $W_1 = 50\,\text{nm}$, $a = 200\,\text{nm}$). Amplitudes are color coded, representing stronger amplitudes by darker colors. Dashed lines indicate the frequencies of the Bloch oscillations.

small anticrossings within the energy range of the bulk band gap from −10 meV to 10 meV. This scenario allows for several Landau–Zener tunneling events during the course of Bloch oscillations, which will be visible as additional frequency contributions in the spectrum of the nanoribbon.

In order to obtain this frequency pattern we perform similar wave-packet propagations as in the case of graphene. First we use a spectral method to determine the eigenstate $\psi(E)$ at the energy E utilizing a propagation of a trial wavefunction as presented in Appendix A.4.2. Subsequently we apply a Gaussian envelope on top of this state leading to an initial wave packet, which is localized on one edge and spreads over several periods of the constriction array. The time evolution of this state is computed in presence of a linear drift potential E_D for various Bloch cycles to obtain the center-of-mass motion and subsequently Fourier transformed by Eq. 5.8 to reveal the different frequency contributions, as presented in Fig. 7.12. Due to the sequence of multiple constrictions the wave packet is able to tunnel between the edges, which allows for a inversion of the direction of motion, leading to Bloch and Bloch–Zener oscillations. The frequency pattern of conventional Bloch oscillations is very pronounced in the numerical data and visible as big amplitude at the frequency ω_B marked by the white dashed line in Fig. 7.12. Additionally, there are strong contributions due to the Bloch–Zener oscillations, which reveal themselves as a rhombic frequency pattern in between the frequency of conventional Bloch oscillations and zero frequency, which has been derived in Section 5.2 for the two-band model. In the case of the HgTe superstructure this pattern is comprised of multiple superimposed copies of the rhombic structure, which are induced by a variety of anticrossings in the band structure of the periodically modulated nanoribbon.

A second option for creating a periodic structure is the application of an array of gates, as sketched in Fig. 7.13 (**a**), which can be modeled by the periodic potential

$$V(x) = V_0 \sin(2\pi x/a). \tag{7.37}$$

The band structure of such an electrostatic modulation is quite similar to the pattern

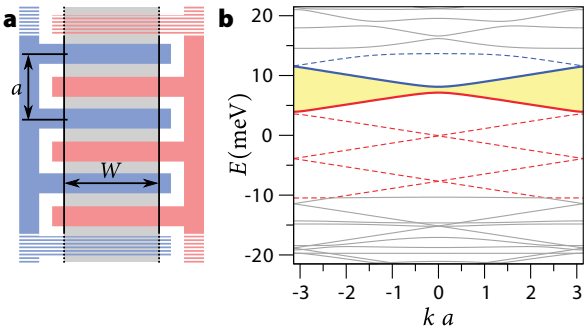

Figure 7.13. | Nanoribbon with periodic electrostatic potential **a,** Sketch of a nanoribbon of width W subject to periodic gating with a periodicity length a. **b,** Bandstructure for a periodically gated HgTe nanoribbon modeled by Eq. (7.37) ($W = 150$ nm, $a = 200$ nm, $V_0 = 5$ meV). Yellow shaded area $\mathcal{A}$ determines the current maxima marked in Fig. 7.14.

achieved by a periodic width modulation, only the band gaps between the higher Bloch bands are not as pronounced, as shown in Fig. 7.13 (**a**). The biggest anticrossing appears at the central energy $c \approx 7.5$ meV, which is the energy of the usual confinement induced gap given by the effective Hamiltonian (7.12). In the following we assume transport through a nanoribbon which is covered with a periodic array of gates in presence of a finite source-drain voltage V_{SD} for different Fermi energies close to the confinement induced gap. We model the voltage drop caused by V_{SD} linear within the scattering region and calculate the induced current by means of the Landauer-Büttiker formalism [144], using Eq. (5.24). Due to the similarity between the bandstructure of the graphene superlattice and the HgTe superlattice we expect similar current voltage characteristics, comparable to the results for graphene presented in Section 5.3.

As shown in Fig. 7.14 the current increases linearly for low applied bias voltages V_{SD}. This stems from the unchanged transmission amplitudes $T(E, V_{\mathrm{SD}})$, which are integrated in an increasing conductance window opened by the voltage difference between the two leads. For higher bias voltages of $V_{\mathrm{SD}} > 1$ mV the transmission amplitudes are reduced since the confinement induced bandgap enters the conductance window, which leads to Bloch oscillations in the dynamical picture. Bloch–Zener oscillations arise for higher voltages $V_{\mathrm{SD}} > 7$ mV and reveal themselves by the typical current peaks presented in Fig. 7.14. This special pattern can be understood by the unique dependence of the coupling between the upper and the lower band, marked by the solid blue and red line in Fig. 7.13 (**b**). Since the states of the left lead are populating the upper branch within the conductance window, and the right lead is described by the lower branch of the mini-band structure, the total current is crucially depending on the coupling between both bands within the scattering region. As show in Section 5.2 the tunneling between the branches in presence of Bloch–Zener oscillations for changing V_{SD} is maximal when the phase condition (5.22) is fulfilled, which leads to a pronounced current peak in the I-V characteristics. The peak position is depending on the accumulated phase of the free propagation and given by the area in momentum space, which can be extracted from the band structure of Fig. 7.13 (**b**). A comparison between the I-V characteristics and the peak positions given by the phase condition (5.22), which are marked by the arrows in Fig. 7.14, reveals a very good correspondence. Since the scattering induced by electrostatic impurities is strongly reduced in topological insulators within the bulk

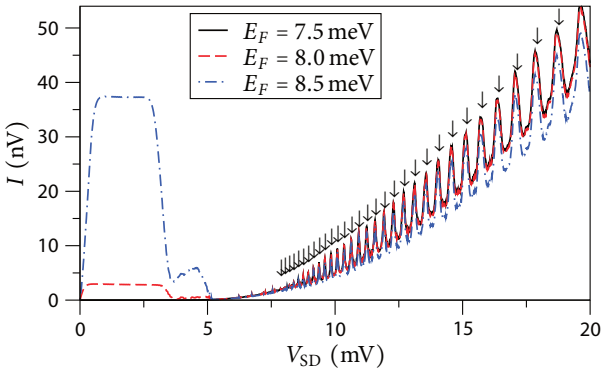

Figure 7.14. | Current dependence for periodic electrostatic potential
I-V_{SD} characteristics of an electrostatically modulated nanoribbon with constant width $W = 150$ nm ($a = 200$ nm). Small vertical arrows mark expected maxima from phase condition (5.22) depending on $\mathcal{A}$ of the bandstructure [see Fig. 7.13 (**b**)].

bandgap, we expect such a setup to be a promising candidate for detecting Bloch–Zener oscillations in a semiconductor setup.

7.6. Summary

In this section we studied the transport properties of HgTe nanoribbons and focused on the possibility to employ a constriction as a novel setup featuring a spin-transistor action. Furthermore we have investigated Bloch–Zener oscillations arising in a periodically modulated zero-gap semiconductor.

At first we have derived a quasi one-dimensional Hamiltonian, which describes the transport due to the edge states in presence of a finite nanoribbon width and spin-orbit interactions. Based on this Hamiltonian we have shown that the transport through a constriction features a transmission pattern, which allows for the construction of a three state spin- and charge-transistor. To verify this statement we have performed two-dimensional transport calculations for realistic device geometries in presence of electrostatic impurities and roughly etched walls. We have studied two setups using a top-gate and a side-gate configuration to steer the current between the different edges solely depending on the applied gate voltages and have been able to reveal a spin-transistor action in this way. For an experimental implementation the dependence of the constriction length on the channel width is crucial. Therefore we have studied the spin-precession length subject to additional spin-orbit interactions and pointed out that the channel length of a transistor can be substantially reduced by the structure-inversion asymmetry induced by an asymmetrically grown quantum well.

In connection to the Bloch–Zener oscillations studied in Chapter 5 for nanoribbons made of graphene, we have conducted similar studies for HgTe structures. We revealed that periodically modulated HgTe strips feature the frequency pattern of Bloch–Zener oscillations as well as the typical current-voltage characteristics. Therefore we have investigated two types of superstructures based on a periodically modulated confinement width or given by an array of gates.

In upcoming studies we will investigate the influence of periodic gating on the switching properties of constrictions. Preliminary calculations show that an electrostatic modulation can be employed to induce topological insulator properties within the confinement induced bandgap, which would increase the working area of the spin-transistor action.

8 Weak Localization in HgTe Heterostructures

Due to the continuous progress in the miniaturization of sample structures and the improvement in material quality and cooling capabilities, unique properties have been discovered in charge transport through semiconductors, which signify the quantum nature of the electrons. For example, the conductance quantization induced by a quantum point contact [188] or the Aharonov-Bohm oscillations emerging in the transmission through ring structures in presence of a perpendicular magnetic field [189], represent an impressive verification of the quantum nature of charge transport. The experimental observation of quantum effects is not only restricted to the ballistic regime, where the mean free path between two scattering events as well as the phase coherence length is on the order of the system size. The diffusive regime, with many phase-coherent scattering events during the transport process, also exhibits interesting quantum effects, like localization [190] and weak localization [191]. The latter is characterized by an increased backscattering probability of waves in random media, which is attributed to constructive interference of time-reversed paths and is present in various systems, like the scattering of electrons in semiconductors [192], the reflection of light by random media [193], or seismic [194], acoustic [195] and atomic matter waves [196].

In this chapter we study the peculiarities of this quantum-mechanical correction to transport in diffusive systems made of HgTe quantum wells, namely the transition between weak localization and weak anti-localization for varying chemical potential. Conventionally the inverted band structure and the associated topological insulator properties of HgTe are experimentally verified by measuring the quantum spin Hall

effect, a quantized conductance of two universal conductance quanta carried by the two topologically protected edge states, which we already introduced in the preceding chapter for the spin transistor. In the following we will reveal that the transitions between weak localization and weak anti-localization feature a significantly different energy dependence, which makes it possible to determine the band ordering by the weak localization response for different chemical potentials.

In general the weak localization properties of systems with inverted band ordering are not yet well explored. For the HgTe heterostructures there are magnetotransport measurements, which feature weak anti-localization in diffusive transport [197] and further studies that revealed an energy dependence of the correction strength [198]. On the theory side, there are diagrammatic studies for the two-dimensional case, which show a transition between weak localization and weak anti-localization upon varying the chemical potential [199] but neglect spin-orbit interactions from bulk inversion or structure inversion asymmetry. Similar transitions arise in thin films of three-dimensional topological insulators, which have also been studied within the framework of diagrammatic perturbation theory [200, 201] and are already supported by experimental investigations [202, 203].

In this chapter we explore the different weak localization regimes of HgTe for both band topologies. We start with an introduction to conventional weak localization in Section 8.1. In Section 8.2 we study the weak localization properties for systems without asymmetry induced spin-orbit interactions and derive an energy dependent transition between localization and anti-localization by means of a Berry phase argument, which is verified by numerical transport calculations. Since the remote bands for negative Fermi energies induce strong deviations from the Berry phase of the 4-band model, we investigate the full Berry phase in Section 8.2.2 and introduce an improved two-dimensional approximation. In Section 8.3 we extend our calculations with different spin-orbit interaction terms and reveal that the inverted band ordering features an energy dependent weak anti-localization, which is not present in conventionally ordered systems and thus can serve as a further way to check the band topology of HgTe quantum wells.

8.1. Weak Localization

Weak localization is a quantum mechanical effect visible in the charge transport through disordered conductors and characterized by an increased backscattering probability in presence of time-reversal symmetry compared to the result expected from the corresponding classical picture [204, 205]. The effect is understood in terms of the interference between waves traveling on different scattering paths, leading to a constructive interference between a trajectory and its time-inverted counterpart. If the phase coherence length τ_ϕ exceeds the mean time τ between successive scattering events, all these pairs of trajectories interfere constructively, resulting in an enhanced backscattering probability.

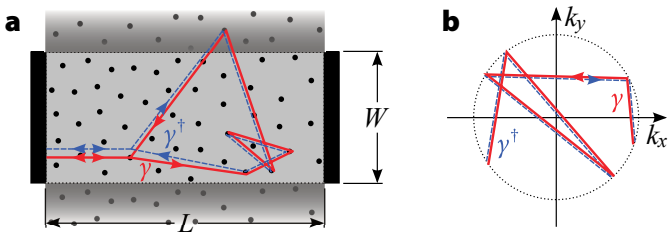

Figure 8.1. | Sketch of the scattering in position and momentum space – a, Periodic scattering region between two non-periodic leads with an exemplary path γ and its time inverted counter path $\gamma^\dagger$ contributing to weak localization. **b,** Corresponding momentum space trajectory $\boldsymbol{k}_n$ for the path γ and $-\boldsymbol{k}_n$ for the counter path $\gamma^\dagger$ of (**a**).

To gain an insight into the backscattering process we consider an initial electron in an eigenstate of momentum $\boldsymbol{k}$, which is described by the plane wave $\exp(\mathrm{i}\boldsymbol{k}\boldsymbol{r})$. After several time steps with an average duration τ this electron is successively scattered between different momentum eigenstates

$$\boldsymbol{k} = \boldsymbol{k}_1' \to \boldsymbol{k}_2' \to \boldsymbol{k}_3' \to \cdots \to \boldsymbol{k}_n' = -\boldsymbol{k}, \tag{8.1}$$

with a finite probability of backscattering into the opposite direction $-\boldsymbol{k} = \boldsymbol{k}_n'$. Upon disorder average closed trajectories γ, as sketched in Fig. 8.1 (**a**), lead to enhanced packscattering, since in an analogous manner the electron can be scattered with the same probability along the trajectory $\gamma^\dagger$ described by the momenta

$$\boldsymbol{k} = -\boldsymbol{k}_n' \to -\boldsymbol{k}_{n-1}' \to -\boldsymbol{k}_{n-2}' \to \cdots \to -\boldsymbol{k}_1' = -\boldsymbol{k}. \tag{8.2}$$

The series of scattering events for the time-inverted path features the same changes of momenta $\Delta\boldsymbol{k}_n$ only in an inverted sequence. Since the total amplitudes A_γ, $A_{\gamma^\dagger}$ of both trajectories depend equally on the scattering phases from the change in momenta $\Delta\boldsymbol{k}_n$ and the dynamical phases from the trajectory lengths, they are perfectly identical $A_\gamma = A_{\gamma^\dagger} = A$, which is also a consequence of time-reversal symmetry [204]. In order to obtain the total intensity of the back reflection these amplitudes have to be added up coherently leading to the total amplitude

$$|A_\gamma + A_{\gamma^\dagger}|^2 = |A_\gamma|^2 + |A_{\gamma^\dagger}|^2 + A_\gamma A_{\gamma^\dagger}^* + A_\gamma^* A_{\gamma^\dagger} = 4|A|^2, \tag{8.3}$$

for the two trajectories γ and $\gamma^\dagger$. If the coherence between the two amplitudes is removed ($A_\gamma A_{\gamma^\dagger}^* = A_\gamma^* A_{\gamma^\dagger} = 0$) the total intensity of γ and $\gamma^\dagger$ only adds up to $2|A|^2$, which is just half of the coherent result. This signifies that the quantum-mechanical backscattering is enhanced compared to the classical incoherent backscattering. More detailed considerations reveal that the size of the reduced transmission is of the order of a universal conductance quantum [206].

Experimentally, weak localization can be measured by means of magnetotransport experiments. In the presence of time-reversal symmetry, back reflection is enhanced

due to the coherence between the time-inverted paths. If the system is subject to a perpendicular magnetic field, the time-reversal symmetry is broken and γ and $\gamma^\dagger$ pick up an opposite magnetic flux. This removes the coherences between the trajectories γ and $\gamma^\dagger$ ($A_\gamma \neq A_{\gamma^\dagger}$), which converts the backscattering amplitude (8.3) of the quantum transmission into the classical result. Therefore it is possible to investigate the effect of weak localization through measuring the average transmission for different magnetic fields, which reveals the presence of enhanced back reflection by a reduced transmission for vanishing field strengths.

In the following, we study the peculiarities of weak localization in diffusive transport through quantum wells made of HgTe. The electronic structure close to the bulk bandgap can be well described by the 4×4 Hamiltonian (6.19),

$$H = \begin{pmatrix} C_k + M_k & Ak_+ & -\mathrm{i}Rk_- & -\Delta \\ Ak_- & C_k - M_k & \Delta & 0 \\ \mathrm{i}Rk_+ & \Delta & C_k + M_k & -Ak_- \\ -\Delta & 0 & -Ak_+ & C_k - M_k \end{pmatrix} \tag{8.4}$$

comprising the states $|E1+\rangle$, $|H1+\rangle$, $|E1-\rangle$ and $|H1-\rangle$ in the z-direction of the quantum well [13], as introduced in Chapter 6. For numerical calculations we use the material parameters summarized in Table 6.1. The topology of the band structure can be changed by the gap M, which represents a conventional ordering of the electron and hole states for $M > 0$ and an inverted ordering for $M < 0$. Additionally, this Hamiltonian contains the spin-orbit interaction terms Δ and R, which are induced by bulk inversion asymmetry (BIA) and structure inversion asymmetry (SIA) [176]. While Δ is fixed, the strength of the spin-orbit interaction due to SIA depends on the quantum well structure, and can be tuned to very small values by growing symmetric wells. Without spin-orbit interaction ($R = \Delta = 0$) the Hamiltonian (8.4) breaks up into two independent 2×2 blocks, each consisting of an s-like electron and a p-like hole band.

Hereafter we employ numerical calculations to study the transport properties of HgTe heterostructures in presence of a perpendicular magnetic field B in the diffusive regime. Therefore we consider coherent two-terminal transport through disordered strip geometries with a Gaussian disorder,

$$U(\boldsymbol{r}) = \sum_i U_i \exp\left(-\frac{(\boldsymbol{r} - \boldsymbol{R}_i)^2}{2\sigma^2}\right), \tag{8.5}$$

correlated on a length scale σ. As a basis for the disorder potential we use a uniform distribution, $-U_0 \leq U_i \leq U_0$, whose strength U_i is chosen randomly for every impurity i located at the grid points $\boldsymbol{R}_i$. To ensure only bulk transport for the inverted and the conventional band ordering we employ periodic boundary conditions in the scattering region, linking the upper and lower edges along transport direction, as sketched in Fig. 8.1 (**a**). The conductance is calculated in linear response within the Landauer formalism [207]

$$G = \frac{e^2}{h} T = \frac{e^2}{h} \sum_{n,m} \sum_{\sigma,\sigma'} |t_{m\,\sigma';n\,\sigma}|^2, \tag{8.6}$$

whereby the transmission amplitudes $t_{m\,\sigma';n\,\sigma}$ are given by the Fisher-Lee relations [208]. If the spin-orbit interaction is switched off in the leads, the modes for the upper and the lower block can be chosen independently and allow for a classification through the index $\sigma \in \{\mathrm{U}, \mathrm{L}\}$ denoting the upper left (U) and the lower right (L) block of the Hamiltonian (8.4) if $R = \Delta = 0$.

8.2. Weak spin-orbit interaction

In this section we start with a negligibly small structure or bulk-inversion asymmetry throughout the whole system, leading to two uncoupled blocks. We will show that the Berry phase accumulated in each of the blocks differs significantly depending on the band ordering, which results in weak localization signatures that allow for a determination of the band ordering by a transport measurement. Without loss of generality we only show the calculation for the Berry phase of the upper subblock

$$H_U = \begin{pmatrix} M - (B+D)\boldsymbol{k}^2 & A(k_x + \mathrm{i}k_y) \\ A(k_x - \mathrm{i}k_y) & -M + (B-D)\boldsymbol{k}^2 \end{pmatrix}, \tag{8.7}$$

since the results for the lower subblock can be obtained by applying the time reversal operator. This Hamiltonian can be easily diagonalized, leading to the energy dispersion for the electron and hole branch,

$$E_{e/h}(\boldsymbol{k}) = -D\boldsymbol{k}^2 \pm F(\boldsymbol{k}), \tag{8.8}$$

with

$$F(\boldsymbol{k}) = \sqrt{A^2\boldsymbol{k}^2 + (B\boldsymbol{k}^2 - M)^2}. \tag{8.9}$$

The corresponding eigenstates are given by

$$\psi_{e/h}(\boldsymbol{k}) \propto \begin{pmatrix} M - B\boldsymbol{k}^2 \pm F(\boldsymbol{k}) \\ A(k_x - \mathrm{i}k_y) \end{pmatrix}. \tag{8.10}$$

As described before, the localization properties are governed by the phases accumulated by different trajectories γ and the interference between those paths, which leads to a substantial quantum correction to the conductance. In a semiclassical description the correction stems from the interference of waves traveling along different impurity-scattered paths. Since disorder and energy averaging removes the contributions from uncorrelated paths, the important remaining contributions for weak localization originate from pairs consisting of the path γ and the time-inverted path $\gamma^\dagger$, as depicted in Fig. 8.1 (**a**). Because of the special spin structure of the momentum eigenstates (8.10) the weak localization signal is governed by additional phases, which can be described by the Berry phase [209]. The strength of this additional phase can be expressed by the Berry curvature tensor given by [210]

$$\mathcal{A}_\sigma(\boldsymbol{k}) = -\mathrm{i}\langle \psi_\sigma(\boldsymbol{k}) | \nabla_k \psi_\sigma(\boldsymbol{k}) \rangle\,, \tag{8.11}$$

in terms of the bulk eigenstates $\psi_\sigma(\boldsymbol{k})$. Assuming an adiabatic transition for a scattering processes from $\boldsymbol{k}_1$ to $\boldsymbol{k}_2$, the additional phase induced by the spin structure is given by [21]

$$\Gamma_\sigma(\Delta\boldsymbol{k} = \boldsymbol{k}_2 - \boldsymbol{k}_1) = \int_{\boldsymbol{k}_1}^{\boldsymbol{k}_2} \mathcal{A}_\sigma(\boldsymbol{k}) \cdot \mathrm{d}\boldsymbol{k}, \tag{8.12}$$

using an integration path with $k = |\boldsymbol{k}_1| = |\boldsymbol{k}_2|$.[1] Accordingly, the total accumulated Berry phase for a trajectory γ consisting of many scattering events, like in Eq. (8.1), is obtained by integrating the vector potential $\mathcal{A}_\sigma$ along a closed loop in momentum space from $\boldsymbol{k}$ to $-\boldsymbol{k}$ with a fixed momentum $k = |\boldsymbol{k}|$ for the number of rotations of the trajectory γ, as sketched in Fig. 8.1 (**b**). For conventional weak localization the path γ and the time-inverted path $\gamma^\dagger$ interfer constructively, leading to a increased back reflection. However, for more complicated spin textures the trajectories also accumulate Berry phases, which have the opposite sign for the time-reversed path because of the inverted rotation orientation in momentum space, as depicted in Fig. 8.1 (**b**). Consequently the difference between the Berry phase of γ and $\gamma^\dagger$ for the simple momentum reversal from $\boldsymbol{k}$ to $-\boldsymbol{k}$ without intersection is given by a full integral of the curvature tensor $\mathcal{A}_\sigma(\boldsymbol{k})$ on the entire Fermi surface:

$$\Gamma_\sigma = \oint_{k=\mathrm{const}} \mathcal{A}_\sigma(\boldsymbol{k}) \cdot \mathrm{d}\boldsymbol{k}\,. \tag{8.13}$$

The circular symmetry of $\mathcal{A}_\sigma(\boldsymbol{k})$ can be used to evaluate the phase Γ_σ by the scalar product $\mathcal{A}_\sigma(\boldsymbol{k}) \cdot (-k_y, k_x)$ at a single point in momentum space leading to a total Berry phase of

$$\Gamma_\sigma = 2\pi \mathcal{A}_\sigma(\boldsymbol{k}) \cdot (-k_y, k_x)\,. \tag{8.14}$$

If the Berry phase given by Eq. (8.14) differs slightly from multiples of 2π, the interference between the trajectories γ is $\gamma^\dagger$ is not entirely constructive and reduces the weak localization [21]. For Γ_σ closed to π, the amplitudes associated with the trajectories γ and $\gamma^\dagger$ interfere destructively, leading to a reversal of the weak localization correction, known as weak anti-localization [211, 212].

In the case of the HgTe quantum wells modeled by the Hamiltonian (8.4), the Berry phase Γ_σ is given by

$$\Gamma_{e/h} = 2\pi \frac{F(\boldsymbol{k}) \pm (M - B\boldsymbol{k}^2)}{2F(\boldsymbol{k})}, \tag{8.15}$$

and features very remarkable properties depending on the two different band topologies. Although a comparison between the band structure of the conventional ordering and the inverted ordering in Fig. 8.2 (**a**,**c**) only reveals marginal differences, the associated Berry phases in Fig. 8.2 (**c**,**d**) are clearly distinct. For the inverted band ordering, the Berry phase spans the whole range of possible Berry phases from 0 to 2π, as shown in Fig. 8.2 (**d**), which introduces an energy range, where the accumulated phase $\Gamma_\sigma \approx \pi$ leading to weak anti-localization as in a "neutrino billiard" [213]. This is not the case if the bands are ordered conventionally, since the region of phases around π is excluded, as

[1] The Hamiltonian (8.4) is spherical symmetric in momentum space, thus energy conserving scatting is equivalent to a constant absolute value $|\boldsymbol{k}|$.

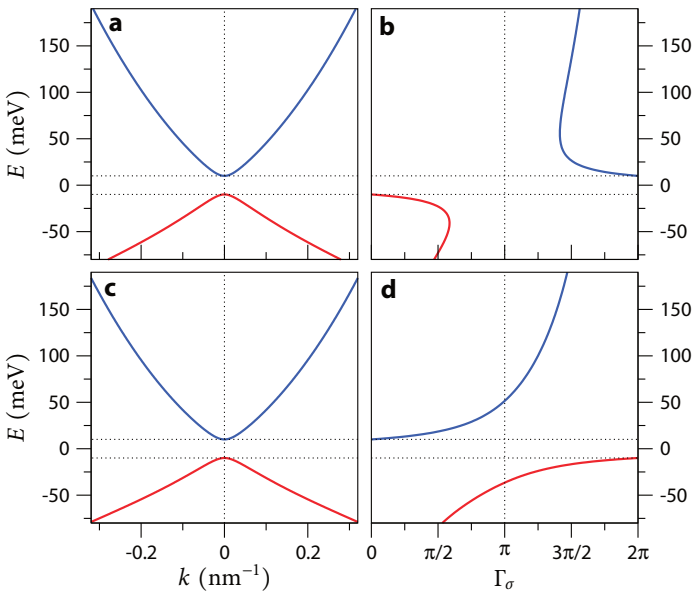

Figure 8.2. | Bulk band structure and Berry phase – The top panels show the bulk band structure (**a**) and the Berry phase (**b**) for a conventional band ordering ($M = 10$ meV), whereas the bottom panels present the bulk band structure (**c**) and the Berry phase (**d**) for an inverted band ordering ($M = -10$ meV). The calculations are based on the 4-band Hamiltonian (8.4) consisting of the E1 and H1 states.

shown in Fig. 8.2 (**b**). As a consequence, we expect distinctly different weak localization behaviors for both systems when the whole range of Fermi energies is considered.

We have examined this behavior by numerical studies of the weak localization in the magnetoconductance through disordered HgTe heterostructures by calculating the change of the quantum transmission

$$\delta T(B) = \big\langle T(B) - T(0) \big\rangle \tag{8.16}$$

in presence of a perpendicular magnetic field B. The averages are taken over a set of 1000 different impurity potentials (8.5) distributing 20000 scatterers, which equals a coverage of 10% of the grid points, within a region of 1000 nm × 5000 nm with a correlation length σ = 15 nm. The Berry phase is tuned by changing the Fermi energy of the system and simultaneously the disorder strength U_0 is adjusted to achieve a constant mean free path of 1200 nm for all energies, leading to comparable shapes of the localization correction for a large range of Fermi energies, as shown in Fig. 8.3.

For energies close to the band gap, the Berry phase deviates only slightly from zero and thus the transport properties can be assumed to be very similar to a conventional electron gas. As a result, we expect a weak localization signature in the magnetotransport, which is indeed present in the numerical calculations and visible as a negative correction to the conductance shown as black line in Fig. 8.3 (**a**). With increasing Fermi energy the Berry phase rises, leading to a reduced weak localization correction. For values of $\Gamma_\sigma = \pi/2$, the minimum in the average transmission at $B = 0$ is supposed to vanish, which is confirmed by the numerical results presented as green line in Fig. 8.3 (**a**). By

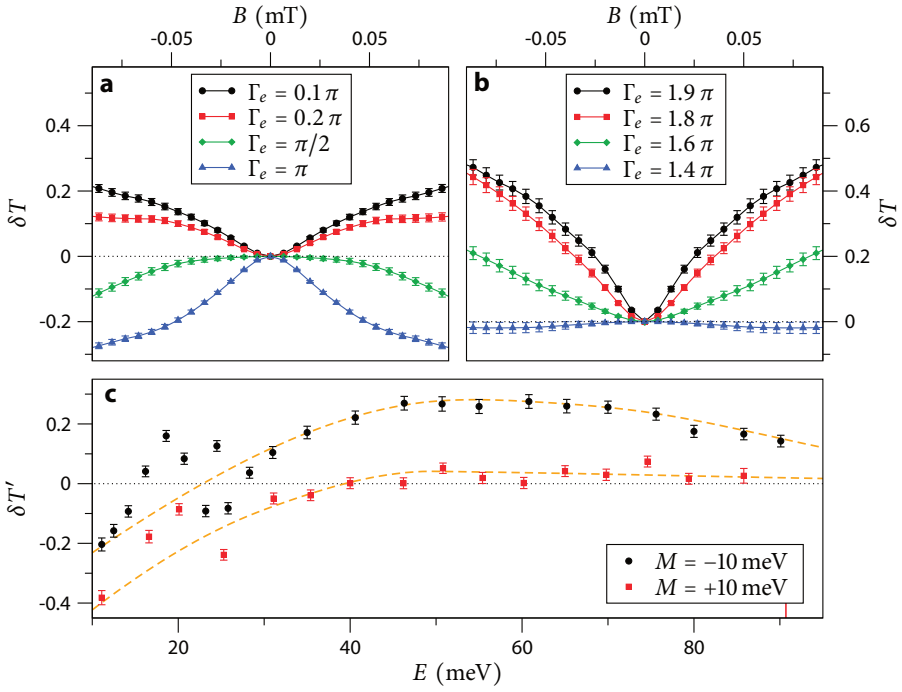

Figure 8.3. | Weak localization without spin-orbit interaction – Magnetoconductance of a HgTe nanoribbon ($L = 5000\,\text{nm}$, $W = 1000\,\text{nm}$) with (**a**) inverted band ordering and (**b**) conventional ordering. Fermi Energies ($E_F = \{11.1\,\text{meV}, 12.5\,\text{meV}, 18.5\,\text{meV}, 52\,\text{meV}\}$) lead to a Berry phase as shown in the panels Impurity potential strength U_0 is varied to obtain a fixed mean free path of 1200nm. **c,** Strength of the weak localization correction $\delta T'$ for inverted and conventional ordering extracted for a magnetic field $B = 0.1\,\text{mT}$.

turning the Fermi energy to

$$E_e^{(\pi)} = -\frac{DM}{B} + \sqrt{\frac{A^2 M}{B}}, \tag{8.17}$$

such that the momentum $\boldsymbol{k}$ fulfills $B\boldsymbol{k}^2 = M$, the electronic states feature a Berry phase of π. In this configuration the system is expected to feature weak anti-localization, since a path and the time inverted counter path accumulate a phase difference of π and therefore interfere destructively, leading to an enhanced transmission at $B = 0$. This is indeed visible in the numerical results showing a pronounced weak anti-localization peak in the blue dataset of Fig. 8.3 (**a**).

The physics changes for a heterostructure with conventional ordering of the electron and hole bands. In Fig. 8.3 (**b**) the average magnetoconductance for the same set of impurity configurations as in Fig. 8.3 (**a**) is shown with a positive bandgap of $M = 10\,\text{meV}$ for different Fermi energies. Close to the bandgap the Berry phase is small as in the case of inverted band ordering, leading to a conventional weak-localization feature.

Unexpectedly, the strength of the weak-localization correction of the conventional regime represented by the black line in Fig. 8.3 (**b**) is almost twice as strong as the result for the inverted regime shown in Fig. 8.3 (**a**). With increasing Fermi energy, the strength of the Berry phase increases, but does not reach π as in the inverted regime. Instead, the maximal phase at $B\boldsymbol{k}^2 = M$ is rather close to $\pi/2$, leading to a strong reduction of any localization correction, which is captured by the numerical results depicted by the blue line in Fig. 8.3 (**b**).

To present the strength of the weak localization for the whole energy range, we extract from various magnetoconductance calculations at different Fermi energies the weak localization correction

$$\delta T' = \left\langle T(B = 0) - T(B = 0.1\,\mathrm{mT}) \right\rangle, \tag{8.18}$$

and summarize the results for both band topologies in Fig. 8.3 (**c**). For conventional ordering, we achieve a transition from weak localization close to the band gap to almost no localization for higher energies. In contrast, a clear-cut transition from weak localization to weak anti-localization and back to weak localization can be found for a system with inverted band ordering. Thus we suggest magnetotransport measurements as a second way to verify an inverted ordering, by the detection of the specific energy dependence of the weak localization transition for variable chemical potentials. Note that for very low energies only few channels contribute to transport, which leads to a reduction of the maximal localization correction and non-universal features noticeable as erratic fluctuations of the localization strength due to the finite number of open channels [206]. These fluctuations at low energies vanish when the width of the scattering region is increased.

8.2.1. Shifted weak localization

On closer examination we find in addition to the expected crossover from weak localization to weak anti-localization shifts of the minima in the magnetotransmission profiles associated with the upper and lower blocks of the Hamiltonian (8.4) induced by the Berry phase. The correction to the classical transmission created by weak localization and weak anti-localization is generated by the interference between a pair of backscattered paths, which are characterized in terms of the enclosed area A and the accumulated angle α, acquired during the series of random scattering processes at impurities along the diffusive path. In conventional electron gases only the enclosed areas A are relevant, with a typical value A_0, which sets the magnetic field scale of the magnetoconductance profile and leads to a transition between the quantum-mechanical and the classical result on the order of $BA_0 \propto \Phi_0$, where B is the perpendicular magnetic field and Φ_0 is the magnetic flux quantum. However, as we have recently shown for ballistic and diffusive two-dimensional hole gases modeled by the heavy-hole and light-hole states of a 4×4 Luttinger Hamiltonian [21], an underlying Berry phase gives

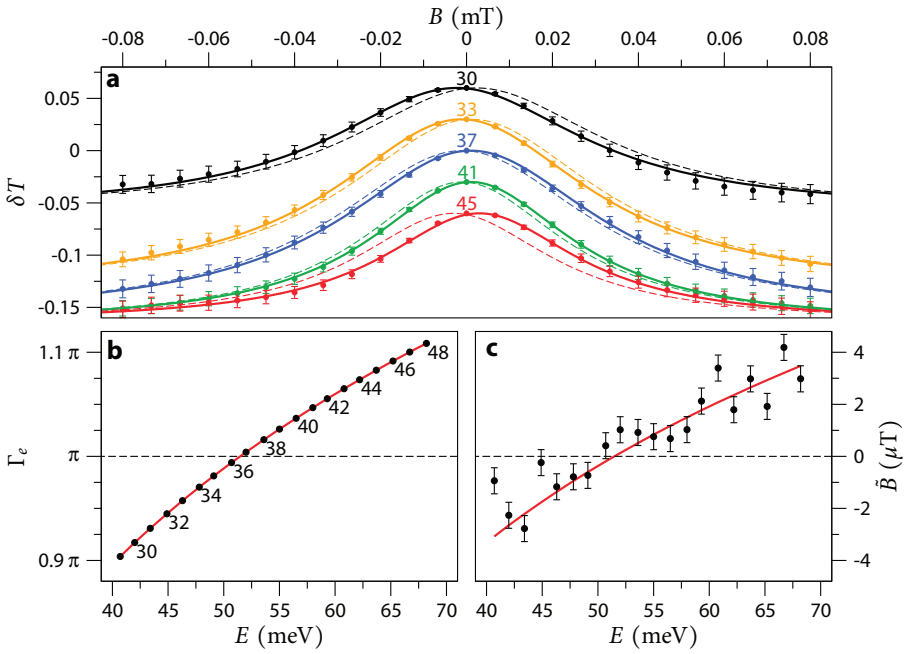

Figure 8.4. | Correlation shifted anti-localization – Shift of the magnetoconductance maximum due to correlations between enclosed area and angle of the contributing trajectories. **a,** Magnetoresistance for different E_F around 52 meV of a diffusive periodic nanoribbon (W = 1000 nm, L = 5000 nm). The index shows the number of open modes without spin degeneracy. **b,** Energy dependence of the Berry Phase around 52 meV. **c,** Energy dependence of the magnetoresistance maximum $\tilde{B}$ extracted from (**a**).

rise to a characteristic shift of the weak localization extrema.[2] This shift depends on the associated Berry phase Γ and the typical accumulated angle α_0. Moreover, for diffusive and chaotic conductors there is a finite classical correlation ρ between the random variables A and α, which characterize a trajectory γ. These different quantities determine an effective magnetic "Berry field" $\tilde{B}$, by which the weak-localization magneto profile is shifted. For a chaotic quantum dot, this shift corresponds to an associated flux [21]

$$\tilde{B}\, A_0 \propto \left(\Gamma\, \rho\, \frac{\alpha_0}{2\pi}\right) \Phi_0, \tag{8.19}$$

which depends linearly on the Berry phase Γ, the average enclosed angle α_0 and the correlation ρ. For the disordered HgTe quantum well we expect a corresponding behavior for Fermi energies with the associated Berry phases close to multiples of π in the weak localization as well as in the weak anti-localization peaks. Fig. 8.4 (**a**) shows the numerically obtained quantum correction to the magnetoconductance (bullets) based

[2] In the supporting material of Ref. [21] we also investigated the shifted weak localization profile in ballistic transport through HgTe cavities.

on the upper block U of the Hamiltonian (8.4). The five different curves correspond to different Fermi energies, close to $E_F = 52\,\mathrm{nm}$, labeled by the number of open transverse modes of one subblock varying from 30 to 45. Fits to the numerical data shown by the solid lines are based on the weak-localization profiles expected for transport through chaotic cavities [21],

$$\delta T_{\mathrm{U(L)}}(B) = \frac{\beta\,\delta T^{(0)}}{1+[2\pi\sqrt{2\beta}A_0(B\mp\tilde{B})/\Phi_0]^2 L_{\mathrm{esc}}/L_b}, \tag{8.20}$$

where β determines the decrease of the weak localization with increasing Berry phase, $\delta T^{(0)}$ the conventional correction strength and L_{esc}/L_b the average number of bounces within the the scattering region. Correspondingly, the dashed lines show the further contribution from the lower block L, which equally add up to the total transmission through the sample. The curves display a small but distinct splitting of the magnetoconductance profiles for different blocks induced by the finite Berry field deviating from a multiple of π and the finite correlation ρ between the areas and angles of the trajectories.

To visualize the relation between the Berry phase and the shift of the localization extrema the phase Γ corresponding to the Fermi energy E and the number of open modes is shown in Fig. 8.4 (**b**). Since Γ is close to π in the depicted energy range, all magnetoconductance curves show weak anti-localization. Most notably, the sign change in $\Gamma - \pi$ between energies corresponding to 36 and 37 channels in Fig. 8.4 (**b**) is reflected in the direction of the energy dependent shift of the weak anti-localization curves in Fig. 8.4 (**a**) with a vanishing shift close to the trace with $n = 37$. The transition from a negative to a positive deviation from Berry phase π between 36 and 37 open channels is also visible in the effective Berry field $\tilde{B}$, extracted from the maxima of various magnetoconductance curves by the same fits used in Fig. 8.4 (**a**). The effective field $\tilde{B}$ depicted in Fig. 8.4 (**c**) indicates a linear dependence between the Berry phase and the shift of the weak anti-localization maximum similar to the results of the chaotic quantum dots [21]. Because of the low correlation ρ between α and A occurring for the diffusive trajectories, the strength of the shift is only a few μT. However, the shift leads to a significant change of the magnetoresistance shape, which is not captured by any diagrammatic approach or description by random matrix theory.

8.2.2. Berry phase modifications by remote bands

In Ref. [21] we demonstrated that the basis truncation used to gain effective two-dimensional Hamilton operators often removes significant Berry phase contributions from the reduced model systems. For example the downfolding of the Luttinger Hamiltonian composed of heavy-hole and light-hole states on a model only comprising heavy-hole basis functions cancels those phase contributions, which induce a shift of the localization minimum, similar to the results presented previously for HgTe. To check the quality of the two-dimensional approximation for the electronic structure of

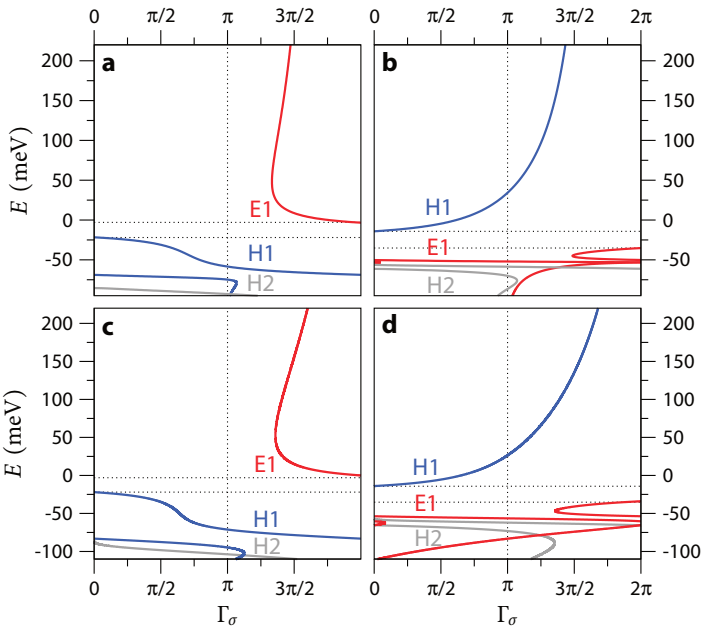

Figure 8.5. | Berry phase for 3D quantum well and three-state model
The top panels show the exact Berry phase of the full three-dimensional heterostructure modeled by Eq. (6.1). The bottom panels represent the Berry phase arising from a model comprised of the E1, H1 and H2 states given by Eq. (6.9). Panels (**a**) and (**c**) are calculated for a thickness of $d = 5.5$ nm and panels (**b**) and (**d**) for a thickness of $d = 7.0$ nm.

HgTe quantum wells, which is commonly used in literature, in the following we compare the Berry phase of a three dimensional calculation with two different two-dimensional models.

For the derivation of the two-dimensional Hamiltonian (6.19) in Chapter 6, we introduced the three-dimensional 6×6 Kane Hamiltonian (6.1), which describes the electron as well as the heavy- and light-hole states close to the Γ-point. We have shown that a heterostructure consisting of a CdTe–HgTe–CdTe sequence is able to confine the wavefunctions in a two-dimensional layer and obtained the full eigenstates in the z-direction $\psi_n(z, k_x, k_y)$ for different momenta k_x and k_y, as shown in Fig. 6.3. Based on these calculations, it is possible to extract the Berry phase of the full three-dimensional system for different HgTe layer widths d. Therefore we compute the eigenstates $\psi_n(z, k_x, k_y)$ of the structure for different in-plane momenta and label the three states closest to the Fermi energy with respect to their spinor character by $\sigma = $ E1 for the electron-like state and H1 or H2 for the two hole-like states. After fixing the phase ambiguity of these eigenstates,[3] the Berry phase for every band σ is calculated by the momentum integral of Eq. (8.11).

Fig. 8.5 (**a**) displays the Berry phase of three different bands for a 5.5 nm confinement, which leads to a bandstructure with a conventional band ordering since the energy of the E1 state is higher than the energies of the H1 and H2 states. A comparison with the Berry phase given by the conventional Hamiltonian (8.4), which only uses the E1 and

[3] The phases of the eigenstates are pinned by choosing the spinor entry with the biggest norm to be real and positive.

Table 8.1. | Parameters for the 3-band model Hamiltonian (6.9) of two HgTe quantum wells with different width d in units of meV and nm obtained.

d	A	B	C	D	M	A'	B'	M'
5.5 nm	433	-580	-11	-390	11	483	-330	75
7.0 nm	404	-810	-24	-620	-10	544	-400	33

H1 states, reveals that the energy dependence of the accumulated phase for the state with positive energy is captured very well, as shown in Fig. 8.2 (**b**). However, the Berry phase of the states with negative energies are not reproduced by the model, as the H1 state of the full system features phases from 0 to $2\,\pi$ whereas the model is restricted to values lower than $0.6\,\pi$. A similar phenomenon appears for the inverted regime, like in the 7 nm quantum well depicted in Fig. 8.5 (**b**). Also in this case the Berry phase of the state with positive energy is reproduced by the approximation in Fig. 8.2 (**d**), while the states with negative energies feature a much richer structure, which is not represented by the approximative Hamiltonian.

Since the deviations of the Berry phase for the negative part of the band structure are large enough to significantly alter the weak localization properties, we have restricted our numerical magnetotransport calculations on the electron branch. In order to investigate the states with negative energy, the model has to be extended by another hole band leading to the 3×3 Hamiltonian (6.9) formed by the E1, H1 and H2 bands. For this approximation the Berry phases of a quantum well with conventional and inverted ordering are depicted in Figs. 8.5 (**c**,**d**) using the material parameters of a 5.5 nm and a 7 nm confinement, as summarized in Table 8.1. For this extended model the resulting energy dependence of the Berry phase follows the behavior of the full three-dimensional calculation in the associated upper panels quite accurately, and therefore we expect the 3×3 Hamiltonian (6.9) as a good candidate to study the weak localization properties of the hole branches in upcoming investigations.

8.3. Strong spin-orbit interaction

In addition to the spin-orbit coupling A between the E1 and H1 bands forming the 2×2 blocks of the Hamiltonian (8.4), there are further spin-orbit interactions present in HgTe heterostructures, which can be divided based on their physical origin into terms arising from bulk inversion asymmetry (BIA) and structure inversion asymmetry (SIA). BIA is given by the bipartite nature of the II-V semiconductor HgTe and the corresponding zinc blende crystal structure, and thus can only be modified by changing the material system. SIA depends on internal and external electric fields, and consequently changes its size depending on the thicknesses and distances of the doping layers as well as the external gating. However, for symmetric HgTe quantum wells and small external gating we can assume the SIA to be negligibly small.

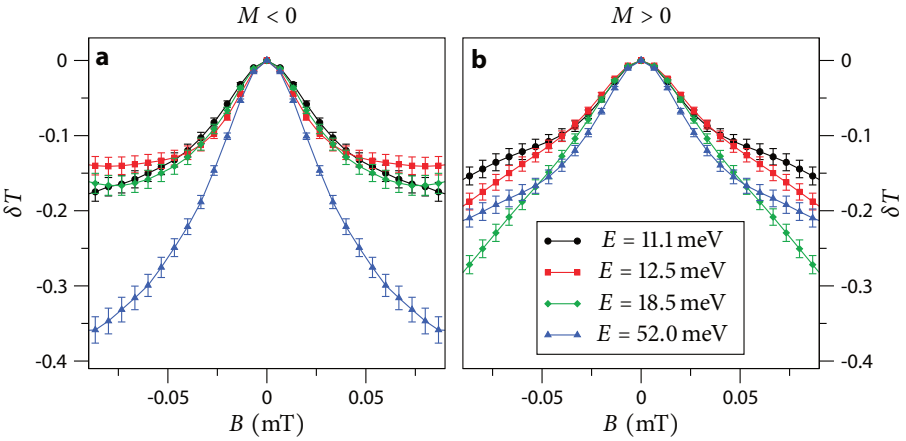

Figure 8.6. | Weak anti-localization by spin-orbit interaction – Correction δT of the average magnetoconductance in the presence of spin-orbit interaction due to structure inversion asymmetry ($\Delta = 1.6\,\text{meV}$) for (**a**) inverted band order ($M = -10\,\text{meV}$) and (**b**) conventional band order ($M = +10\,\text{meV}$).

In the following, we study the weak localization profile for a symmetrically grown quantum well and assume a naturally sized BIA and no SIA. To this end, we calculate as in the previous section the magnetoconductance in the diffusive regime averaged over different impurity configurations for a set of Fermi energies, as summarized in Fig. 8.6 (**a**) for inverted band ordering and in Fig. 8.6 (**b**) for conventional band ordering. Every Fermi energy corresponds to a certain Berry phase, which is chosen such that the entire range of Berry phases from 0 to π is covered, as in the previous calculations without BIA presented in Fig. 8.3 (**a**). In comparison to systems without additional spin-orbit interaction terms the average magnetoconductance always features weak anti-localization already for very low Berry phases independent of the band ordering. This is in line with the common diffusive transport theory developed for two-dimensional electron gases [205] which shows that strong spin-orbit interaction leads to spin relaxation and thereby weak anti-localization. However, in the case of HgTe there exists a significant change of the weak anti-localization correction amplitude depending on the band ordering. For conventionally ordered bands, the weak anti-localization correction is almost constant and also the shape of the correction does not change significantly with the Fermi energy, as shown in Fig. 8.6 (**b**). This is not the case for the inverted ordering, which features a weak anti-localization profile with almost twice the amplitude at a Fermi energy of $E_e^{(\pi)}$, as depicted in Fig. 8.6 (**a**).

This effect can be explained by a new conserved quantity, which is given by a superposition of different spins that remain uncoupled in the presence of spin-orbit interaction,

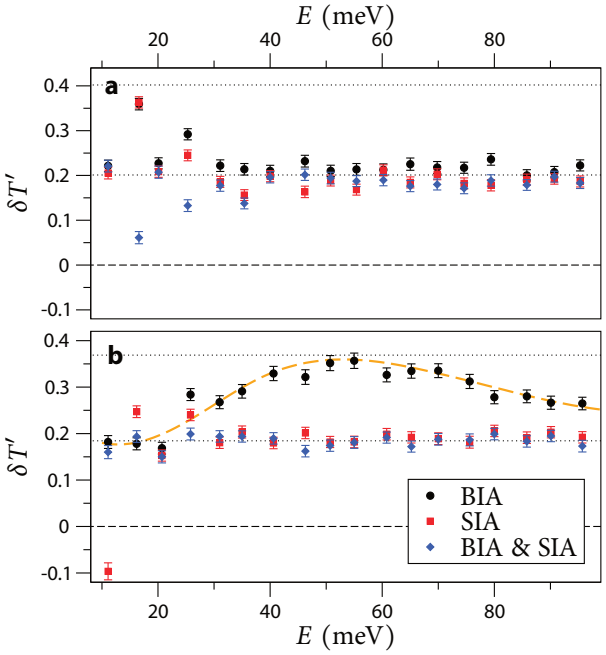

Figure 8.7. | Energy dependent weak anti-localization Strength of the magnetoconductance correction $\delta T'$ for different spin-orbit interactions ($\Delta = 1.6$ meV, $R = 35$ eVÅ). The results are extracted from the transmission at 0.1 mT. **a,** The localization strength for conventional band ordering ($M = 10$ meV) features a constant localization strength for all combinations of structure-inversion asymmetry and bulk-inversion asymmetry. **b,** For inverted band ordering ($M = -10$ meV) and solely structure inversion asymmetry, the strength of the anti-localization correction at $E_\pi = 52$ meV is doubled .

as we will see in the following. To this end, we apply the unitary transformation

$$\mathcal{T} = \frac{1}{\sqrt{2}} \begin{pmatrix} 1 & 0 & 0 & 1 \\ 0 & -1 & 1 & 0 \\ -1 & 0 & 0 & 1 \\ 0 & 1 & 1 & 0 \end{pmatrix} \tag{8.21}$$

to the Hamiltonian (8.4), which mixes the initial spin states to $|1\rangle = |E1+\rangle + |H1-\rangle$, $|2\rangle = |E1-\rangle - |H1+\rangle$, $|3\rangle = |H1-\rangle - |E1+\rangle$ and $|4\rangle = |H1+\rangle + |E1-\rangle$. In this rotated basis the initial Hamiltonian reads

$$H = \begin{pmatrix} C_k - \Delta & -Ak_+ & -M_k & -\mathrm{i}\frac{1}{2}Rk_- \\ -Ak_- & C_k - \Delta & -\frac{1}{2}\mathrm{i}Rk_+ & M_k \\ -M_k & \frac{1}{2}\mathrm{i}Rk_- & C_k + \Delta & -Ak_+ \\ \frac{1}{2}\mathrm{i}Rk_+ & M_k & -Ak_- & C_k + \Delta \end{pmatrix}, \tag{8.22}$$

which allows us to identify a new block structure. If no spin-orbit interaction due to SIA is present ($R = 0$), this Hamiltonian consists of two blocks which are only coupled by the matrix element $M_k = M - B\boldsymbol{k}^2$. In the case of an inverted band ordering there exists a momentum $\boldsymbol{k}$, where $M_k \approx 0$ since M and B are both negative, which occurs for an energy of 52 meV in a heterostructure with a band gap of $M = -10$ meV. At this energy the Hamiltonian decouples into two independent 2×2 blocks, that both show weak anti-localization, due to a Berry phase of π. Thus the combined weak anti-localization strength is twice as high as the results for energies remote from this condition, as shown in Fig. 8.6 (**a**).

If spin-orbit interaction terms from SIA are present, it is impossible to find a unitary transformation into two uncoupled blocks. As a consequence, the weak anti-localization correction stays roughly constant throughout the whole range of different Fermi energies. In order to check this behavior we have calculated the energy dependence of the weak anti-localization correction $\delta T'$, Eq. (8.18), for different combinations of BIA and SIA, which is summarized in Fig. 8.7. As expected, the weak anti-localization with conventional band ordering is independent of the type of spin-orbit interaction, since all weak anti-localization peaks show an amplitude of about 0.2, as shown in Fig. 8.7 (**a**). However, this is not the case for a heterostructure with inverted band ordering. If only BIA is present, weak anti-localization is approximately doubled at 52 meV and shows a smooth transition between values from 0.2 to 0.4, represented by black symbols in Fig. 8.7 (**b**). For non-zero SIA a block diagonalization is not possible, and hence the weak anti-localization correction is constant, independent of additional spin-orbit interaction terms. Similar to the calculations without spin-orbit interaction, there are erratic fluctuations of the localization strength at low energies, which can be attributed to the limited amount of open channels in the numerical calculations yet can be suppressed by increasing the system size.

Using the energy dependence of the weak anti-localization peak it is also possible to deduce the band ordering of an symmetrically grown HgTe quantum well by transport measurements away from the bulk band gap, similar to a HgTe heterostructure without spin-orbit interaction. If the weak anti-localization features a maximum at a Fermi energy of 52 meV, which is twice as high as the weak anti-localization peak for very low and high energies, the band ordering of the quantum well is inverted. On the other hand a constant weak anti-localization peak can either originate from a conventionally ordered band structure or spin-orbit contributions due to SIA.

8.4. Summary

In this chapter we have studied the weak localization properties of HgTe heterostructures with different band topologies in the diffusive regime. In the context of topological insulators the inverted band ordering is the key ingredient which has to be accomplished to obtain the special properties of topological insulators, like spin-polarized edge or surface states. We have found that the inverted band ordering also leads to notable features in the weak localization response visible in diffusive magnetotransport profiles. Therefore, we have used a Berry phase argument to explain the transitions between weak localization and weak anti-localization for small spin-orbit interactions and checked the dependence on the Fermi energy by means of numerical transport calculations. We revealed a full transition between localization and anti-localization for systems with inverted band ordering, which is not present in systems with conventional band ordering. Hence, we expect that for systems with negligibly small spin-orbit interaction the band topology can be deducted by a gate dependent measurement of the weak-localization transition. In the presence of spin-orbit interactions within a symmetrically grown

quantum well a similar implication on the band ordering can be made, if the structure inversion asymmetry is small. Since an inverted band ordering gives rise to a new conserved spin quantity, which is only present for a certain Fermi energy, the energy dependence of a weak anti-localization peak is a clear evidence for an inverted band structure.

Furthermore, we found that the Berry phase texture of the hole states is not adequately described by the model commonly used in literature. Therefore we developed a three band model for the HgTe quantum well, which can be employed in further investigations to study the weak-localization response of hole-doped heterostructures. Additionally, a semiclassical theory can be developed, which describes the weak-localization profile in presence of correlations between the accumulated areas and angles of the backscattered trajectories, similar to the theory we have established for ballistic transport.

9 Conclusion and Outlook

9.1. Summary

In this thesis we studied the electronic properties of the zero-gap semiconductors graphene and mercury telluride (HgTe). The quantum transport through such systems is usually investigated in the stationary limit by means of time-independent Green's function techniques. We developed a multipurpose time-dependent quantum transport library [16], whose most important parts are introduced in Section 4. By means of this numerical tool we were able to compute the time-evolution governed by a broad range of Hamilton operators, which can be either expressed by an atomistic tight-binding description or by a mixed position and momentum-space representation given by $\boldsymbol{k} \cdot \boldsymbol{p}$ perturbation theory. From the time evolution we extracted various physical observables like the center-of-mass motion, the polarization dynamics, the density of states or the transport properties for wave packets in different mesoscopic systems. These observables have been employed throughout this thesis to gain an insight into the electronic properties of graphene or topological insulators and revealed the following phenomena:

Wave-packet revivals

In Chapter 3 we investigated the revival dynamics arising in the time evolution of excited wave packets on a sheet of graphene subject to a perpendicular magnetic field. We showed that the wave-packet motion features a significant sequence of collapses and revivals similar to the dynamics of highly excited electrons in Rydberg atoms [15]. An initially localized wave packet becomes circularly spread during the first few cyclotron orbits. This motion is reversed after a certain propagation time and finally leads to a

wave-packet which resembles the initial one. The effect stems from the non-equidistant spacing of the Landau levels in graphene and is thus not present in conventional two-dimensional electron gases. We presented the signatures of the revivals in the center-of-mass motion as well as the autocorrelation function, based on numerical wave-packet propagations. Furthermore, we introduced a model based on a superposition of classical orbits in different Landau levels, which is able to reproduce the quantum-mechanical center-of-mass motion very accurately. The times featuring fractional revivals and full revivals have been extracted from the autocorrelation function, which can be expressed by the accumulated phases of the contributing Landau levels.

Looking to experimental settings, we studied the effect of impurities and revealed that long-range potentials solely remove the signatures of revivals in the autocorrelation function, whereas the signatures in the center-of-mass motion remain present. This motion, which can be related to the polarization dynamics, also exhibits the revival physics and can be considered in the context of a four-wave-mixing setup. We showed that short laser pulses can be employed to excite initial zero energy wave-packets into highly excited Landau levels. By applying a second time-delayed laser pulse the motion of these excited states can be probed. The combination of both lasers induces higher order processes in the diffracted signals, which feature a pronounced dependence on the delay of the second laser pulse and indicate the presence of wave-packet revivals. Our numerical calculations demonstrated that the diffracted signals depend significantly on the underlying revival dynamics and thus are well suited to detect wave-packet revivals on a sheet of graphene by means of a four-wave-mixing setup.

Bloch–Zener oscillations

Furthermore, we studied the effect of Bloch–Zener oscillations in Chapter 5, which arise alongside conventional Bloch oscillations if the dynamics of accelerated electrons in a periodically modulated zero-gap semiconductor are considered [17]. We carried out numerical wave-packet simulations in atomistic graphene nanoribbons which show that Bloch–Zener oscillations feature additional frequency contributions compared to conventional Bloch oscillations. The underlying physics can be reduced to a one-dimensional model Hamiltonian based on a periodically modulated Dirac equation, which exhibits the same additional frequency contributions. The effect is understood via the coherent dynamics in the electron and the hole branches of the periodic bands and successive Zener tunneling events for every Bloch cycle. Furthermore, the tunneling rate between the upper and the lower Bloch bands shows distinct variations depending on the frequencies of the Bloch–Zener oscillations. This tunneling dependence is visible in the transport properties and manifests itself in pronounced peaks in the current through periodically modulated nanostructures in the presence of a variable gate voltage. To this end, we carried out several numerical transport calculations in graphene nanoribbons. These all revealed pronounced current voltage characteristics induced by the Bloch–Zener oscillations. Finally, we recommended the observed

current pattern as an experimentally accessible observable, both in the dc current and in driven quantum transport, to verify the presence of Bloch–Zener oscillations in a zero-gap semiconductor. Considering HgTe strips, we also found a similar frequency pattern and current voltage characteristics, as presented in Section 7.5.

HgTe spin-transistor

In Chapter 7 we studied the switching properties of constrictions etched out of the two-dimensional topological insulator HgTe and proposed a novel setup featuring a spin-transistor [18]. First, we derived the edge states arising at the boundaries of a HgTe heterostructure starting from the full three-dimensional electronic properties of the constituents HgTe and CdTe. Based on the edge-state wavefunctions we established a one-dimensional model Hamiltonian to describe the electronic properties of a confined region for a fixed width. This model was then applied to demonstrate the switching properties of a constriction by means of a transfer matrix approach [19]. We revealed that depending on the chemical potential within the constriction the current can be steered between all four different edge states very selectively. Subsequently, we carried out numerical transport calculations using our wave-packet transport scheme to study the switching properties of realistically modeled devices connected to four leads [18]. All calculations were carried out with electrostatic impurities as well as a boundary disorder, which does not affect the switching properties of the system. This robustness can mainly be attributed to the topological protection of the edge states. The presented spin transistor only consists of a single material, which is utilized in two ways by combining the spin selectivity of the extended topological-insulator regions and the spin precession within the constriction. Compared to a conventional Datta-Das spin-transistor, which requires ferromagnetic contacts to create the spin-polarization, this setup is not affected by spin-injection problems. Consequently, we expect the proposed setup to be a promising implementation of a combined charge and spin-transistor of high fidelity.

Weak localization in HgTe heterostructures

Finally, we investigated in Chapter 8 the weak localization properties of HgTe heterostructures with a special focus on the dependence of the quantum mechanical corrections to magnetotransport on the band topology. We found that the inverted and the conventional band ordering feature distinctly different transitions between weak localization and weak anti-localization upon variation of the Fermi energy [20]. In particular we studied the energy dependence of the Berry phase of the electronic states confined inside a quantum well and found a pronounced topology and energy dependent texture of the accumulated phase. Based on this energy dependence the magnetotransport undergoes different transitions between weak localization and weak

anti-localization, which has been confirmed by numerical transport calculations in diffusive HgTe strips.

If the spin orbit interaction is weak, the inverted band structure leads to a transition from weak localization to complete weak anti-localization, which is not present in conventionally ordered systems. For stronger spin-orbit interaction the magnetoconductance shows weak anti-localization which exhibits a pronounced energy dependent increase of the correction strength if the bands of the quantum well are inverted. In both cases the magnetotransport of a diffusive system with inverted band ordering has a specific energy dependence, which is not present in the conventionally ordered case. In conclusion, we suggest the measurement of the energy dependent weak localization correction to magnetotransport as an additional way to classify the band topology of HgTe heterostructures without relying on the quantum spin Hall effect. Thus a classification is possible even if the system cannot be gated into the bulk band gap.

9.2. Outlook

Based on the developments and results of this thesis several further investigations can be considered.

The numerical scheme to employ wave packets for a determination of the transport properties of mesoscopic systems presented in Chapter 4 can, for example, be extended to time-periodic systems. For this method the numerical effort to calculate the transmission amplitudes does not increase with N_t^3, as it is the case for a Floquet ansatz with N_t Floquet states, since the time-dependent treatment circumvents an extra dimension. Furthermore, the commutation relation of the time-evolution operator for one periodicity cycle can be exploited to restrict the necessary propagation time of the outgoing lead wave-packets. By means of this fully time-dependent transport scheme, one could explore more deeply time-dependent effects in quantum transport, like the valley-valve time-delay presented in Appendix A.4.3 or the radiation induced Bloch–Zener oscillations of Section 5.4.

In Chapter 7 we presented a novel spin-transistor based on a constriction etched out of a HgTe heterostructure. Our considerations revealed that the energy region, which features a spin-transistor action is exponentially reduced with decreasing channel width given by the confinement induced band gap. However, a small channel width is favorable for short constriction lengths. We found that the gap can be closed upon imposing a few periods of an electrostatic superstructure, which restores the topological insulator properties. Preliminary calculations already showed that this effect can be indeed employed to create a spin flip within very narrow constrictions, which are conventionally blocked by a confinement-induced gap. These studies need to be extended to consider the impact of impurities and rough boundaries arising in typical experimental settings. Furthermore, it would be desirable to derive an analytical

model, which allows a determination of the required properties of the superstructure to close the confinement induced gap.

In this thesis we investigated the weak localization properties of HgTe heterostructures and revealed a distinct energy dependence of the quantum correction to the average magnetoconductance, which ultimately allows for a determination of the band topology by magnetotransport signatures. We also found in Chapter 8 that the Berry texture of the hole branch given by the conventionally used two band model differs significantly from the full three-dimensional result. To improve the description of the quantum well we derived a three band model, which includes an additional heavy-hole band and is able to capture the special energy dependence of the Berry phase in the p-doped region. It should be checked if our improved model induces changes in the transport signatures, like the energy dependence of weak localization properties. Also the robustness of the quantum spin Hall effect with additional hole bands could be investigated.

Furthermore, we revealed that the two band Hamiltonian of an HgTe heterostructure can be converted by an unitary transformation into two uncoupled blocks for energies corresponding to a Berry phase of π. This characteristics is very similar to a two-dimensional electron gas, where the spin-up and the spin-down block can be decoupled by a special unitary transformation, if the Rashba and Dresselhaus spin-orbit interaction are of the same strength. This suggests that the counterpart of a persistent spin helix in HgTe heterostructures has similar capabilities as the spin helix in two-dimensional electron gases, which should be checked by numerical transport calculations and analytic considerations.

In the past years the rapid developments in condensed matter physics, like the discovery of novel topological phases, have attained great interest and revealed unexpected physical properties. The techniques of this thesis are pertinent to these new developments and should be applied in the upcoming fields. Especially from the time-dependent treatment of the quantum transport we expect an extended insight into the emerging effects.

A Appendix

A.1. Classical propagation and quantization of Landau levels in graphene

In chapter 3 we have studied the time-evolution and the corresponding revivals of wave packets in a perpendicular magnetic field. In the following, we want to specify the properties of the classical time-evolution of a wave packet governed by a Dirac equation in a magnetic field and obtain the semiclassical quantization. In order to be localized in position and momentum space, the initial wave packet $\psi(\boldsymbol{r}, t)$ has to have a small extent in both coordinates. The expectation value of the position operator and the kinetic momentum are defined by

$$\boldsymbol{r}(t) = \langle\psi(t)|\hat{\boldsymbol{r}}|\psi(t)\rangle, \quad \boldsymbol{k}(t) = \langle\psi(t)|\hat{\boldsymbol{k}}|\psi(t)\rangle. \tag{A.1}$$

As a first step we analyze the free solutions of the Hamiltonian and classify the resulting bands by the index λ. For the Dirac Hamiltonian of graphene we obtain electron-like ($\lambda = +1$) and hole-like states ($\lambda = -1$) with an energy dispersion $\mathcal{E}_\lambda = \lambda\, v\, \hbar|\boldsymbol{k}|$. The time-evolution of the momentum $\boldsymbol{k}$ and the center $\boldsymbol{r}$ of a wave packet only restricted to one band λ is defined by the two coupled equations of motion [214]

$$\dot{\boldsymbol{r}} = \frac{\partial\mathcal{E}_\lambda}{\hbar\partial k} - \dot{\boldsymbol{k}} \times \Omega_\lambda(\boldsymbol{k}), \tag{A.2}$$

$$\hbar\dot{\boldsymbol{k}} = -e\boldsymbol{E}(\boldsymbol{r}) - e\dot{\boldsymbol{r}} \times \boldsymbol{B}, \tag{A.3}$$

where $\boldsymbol{B} = B\boldsymbol{e}_z$ stands for an isotropic magnetic field perpendicular to the plane and $\boldsymbol{E}(\boldsymbol{r})$ is a position dependent electric potential. The Berry curvature $\Omega_\lambda(\boldsymbol{k})$ enters the equations of motion in momentum space but is zero in case of a gapless Dirac equation. The relation (A.2) can be reduced to $\dot{\boldsymbol{r}} = \lambda v \boldsymbol{k}/|\boldsymbol{k}|$ because of the linear dispersion and

therefore describes a center-of-mass, which always travels with the speed v parallel or anti-parallel to the wave vector $\boldsymbol{k}$. For a vanishing electric field the equations of motion can be solved. The momentum of the wave packet is controlled by the differential equation

$$\hbar\dot{\boldsymbol{k}} = -ev\frac{\boldsymbol{k}}{|\boldsymbol{k}|} \times \boldsymbol{B}(\boldsymbol{r}), \tag{A.4}$$

given by (A.3), which is solved by

$$\boldsymbol{k} = k_0 \begin{pmatrix} \cos(\omega_c t + \varphi) \\ \sin(\omega_c t + \varphi) \end{pmatrix}, \tag{A.5}$$

where the initial momentum of the wave packet is given by k_0 in direction φ. The cyclotron frequency depends on the momentum and is given by

$$\omega_c = \frac{evB}{\hbar k_0}. \tag{A.6}$$

The resulting real space propagation (A.2) is given by

$$\boldsymbol{r} = \boldsymbol{r}_0 + \lambda\ l_c \begin{pmatrix} \sin(\omega_c t + \varphi) \\ -\cos(\omega_c t + \varphi) \end{pmatrix}. \tag{A.7}$$

Thus electron-like and hole-like states propagate in opposite directions on orbits with the radius

$$l_c = \frac{\hbar k_0}{eB}. \tag{A.8}$$

In order to obtain the quantization of the Landau levels from the closed cyclotron orbits the phase changes along the trajectories have to be studied. The main contribution is given by the classical action, while an additional contribution enters which is known as Berry's phase. Although the Berry curvature is vanishing, Berry's phase [209] is still present and defined by the vector potential

$$\vec{\mathcal{A}}_\lambda(\boldsymbol{k}) = -\mathrm{i}\langle u_\lambda(\boldsymbol{k})|\nabla_k u_\lambda(\boldsymbol{k})\rangle, \tag{A.9}$$

and the spinor parts $u_\lambda(\boldsymbol{k})$ of the plain-wave solutions of the Hamiltonian. These spinors are given by

$$u_\pm(\boldsymbol{k}) = \frac{1}{2}\sqrt{2}\begin{pmatrix} 1 \\ \mathrm{e}^{\pm\mathrm{i}\varphi} \end{pmatrix}, \tag{A.10}$$

where φ is the direction of the vector $\boldsymbol{k}$. Hence the vector potential gets

$$\vec{\mathcal{A}}_\pm(\boldsymbol{k}) = \pm\frac{1}{2k^2}\begin{pmatrix} k_y \\ -k_x \end{pmatrix}, \tag{A.11}$$

which is used to calculate the additional phase-change

$$\Gamma_\lambda(\omega) = \oint_\omega \vec{\mathcal{A}}_\lambda(\boldsymbol{k})d\boldsymbol{k} \tag{A.12}$$

for an arbitrary adiabatic transition on the path $\omega(t)$ in momentum space. The result is the well known Berry's phase

$$\Gamma_{\pm}(\omega) = \pm\pi \tag{A.13}$$

for a single closed orbit on graphene [25]. The adiabatic transition in momentum space is fulfilled for common magnetic field strengths, since all trajectories are cyclotron orbits and thus sufficiently smooth. The classical phase change and Berry's phase have to be added up to build a new EBK quantization condition which reads [215]

$$\frac{1}{2}\boldsymbol{e}_z \oint_{\omega} \boldsymbol{k} \times d\boldsymbol{k} = 2\pi\frac{eB}{\hbar}\left(n' + \frac{\nu}{4} - \frac{\Gamma_{\pm}(\omega)}{2\pi}\right) \tag{A.14}$$

where ν is the Maslov index depending on the caustics traversed on one cyclotron orbit (here $\nu = 2$). Plugging the formula for the cyclotron motion into the quantization condition results in the equation

$$\pi k_0^2 = 2\pi\frac{eB}{\hbar}\left(n' + \frac{1}{2} \mp \frac{1}{2}\right). \tag{A.15}$$

The momentum quantization yields

$$k_0 = \operatorname{sign}(n)\sqrt{2\frac{eB}{\hbar}|n|}, \tag{A.16}$$

with a Landau level index n defined for hole-like and electron-like states. All the other quantized parameters follow from the relations calculated before

$$\mathcal{E}_n = \nu\ \operatorname{sign}(n)\sqrt{2eB\hbar|n|}, \tag{A.17}$$

$$l_n = \operatorname{sign}(n)\sqrt{2\frac{\hbar}{eB}|n|}, \tag{A.18}$$

$$\omega_n = \nu\ \operatorname{sign}(n)\sqrt{\frac{eB}{2\hbar|n|}} \quad \text{if} \quad n \neq 0. \tag{A.19}$$

In chapter 3 these properties have been used to give an explanation for the center-of-mass revivals and an expression for the motion, which approximates the quantum mechanical result very accurately.

A.2. Magnetic field in mixed momentum- and position-space representation

In solid-state physics the electronic properties of mesoscopic structures are frequently investigated in presence of a perpendicular magnetic field $\boldsymbol{B} = B\boldsymbol{e}_z$, which can be for example used to break the time reversal symmetry for low B, like in the case of weak localization for diffusive transport in bulk HgTe (see chapter 8), or in order to induce a quantization into Landau levels for large field strengths as employed in chapter 3. In all cases the effect of the magnetic field is added to the Hamiltonian by minimally coupling a vector potential $\boldsymbol{A}$ to the momentum operator with the substitution $\boldsymbol{p} \to \boldsymbol{p} - e\boldsymbol{A}$. Several different possible vector potentials $\boldsymbol{A}$ exist that fulfill

$$\boldsymbol{B} = \nabla \times \boldsymbol{A}, \tag{A.20}$$

for a given magnetic field $\boldsymbol{B}$, which is known as freedom of gauge. In the following, we will show how the magnetic field is added into the action of an arbitrary $\boldsymbol{k} \cdot \boldsymbol{p}$ Hamiltonian $\hat{H}$ of Eq. (4.5) in a mixed momentum- and position-space representation and use the gauge invariance for an efficient implementation.

The action of a single matrix element $\hat{H}_m$ on the wavefunction $\psi(\boldsymbol{r})$ can be calculated by

$$\hat{H}_m \ \psi(\boldsymbol{r}) = c_{m_x m_y}(\boldsymbol{r}) \ \ \mathcal{F}_x^{-1} k_x^{m_x} \mathcal{F}_x \ \ \mathcal{F}_y^{-1} k_y^{m_y} \mathcal{F}_y \ \ \psi(\boldsymbol{r}), \tag{A.21}$$

where m_x and m_y represent the different powers of the momentum operators k_x and k_y, as introduced in chapter 4. In order to add the magnetic field to $\hat{H}_m$, the momentum operators have to be replaced by

$$k_x^{m_x} \to \left(k_x - \mathrm{i}\frac{e}{\hbar}A_x(\boldsymbol{r})\right)^{m_x} \quad \text{and} \quad k_y^{m_y} \to \left(k_y - \mathrm{i}\frac{e}{\hbar}A_y(\boldsymbol{r})\right)^{m_y}, \tag{A.22}$$

which introduces an unfavorable position dependence in momentum space. As a consequence, the action of the operator is not just a multiplication with the scalar $k_x^{m_x}$ or $k_y^{m_y}$, but all commutators of k_x and $A_x(\boldsymbol{r})$ have to be taken into account and calculated separately, which is especially inconvenient for higher orders of $k_x^{m_x}$, $m_x > 2$. However, this problem can be avoided if the gauge invariance of the vector potential is utilized.

The perpendicular magnetic field $\boldsymbol{B} = B(\boldsymbol{r})\boldsymbol{e}_z$ can be expressed by several different special gauges like the symmetric gauge

$$\boldsymbol{A}^{[0]} = \frac{1}{2}\begin{pmatrix} -a_x(x,y) \\ a_y(x,y) \end{pmatrix} \tag{A.23}$$

or the Landau gauges in x and y direction,

$$\boldsymbol{A}^{[-1]} = \begin{pmatrix} -a_x(x,y) \\ 0 \end{pmatrix} \quad \text{and} \quad \boldsymbol{A}^{[+1]} = \begin{pmatrix} 0 \\ a_y(x,y) \end{pmatrix}. \tag{A.24}$$

For all these different gauges the position dependence of the vector potential is given by

$$a_x(x,y) = \int_{y_0}^{y} B(x,y')dy' \quad \text{and} \quad a_y(x,y) = \int_{x_0}^{x} B(x',y)dx', \tag{A.25}$$

and can be unified to

$$\boldsymbol{A}^{[\mu=-1,0,1]} = \frac{1}{2}\begin{pmatrix} a_x(x,y)(\mu-1) \\ a_y(x,y)(\mu+1) \end{pmatrix}, \tag{A.26}$$

with $\mu = 0$ for the symmetric gauge and $\mu = \mp 1$ for the Landau gauge in x and y direction. The transformation of the vector potential from gauge i to gauge f is given by

$$\boldsymbol{A}_f(\boldsymbol{r}) = \boldsymbol{A}_i(\boldsymbol{r}) + \nabla\chi(\boldsymbol{r}), \tag{A.27}$$

using the scalar potential

$$\chi_{f\leftarrow i}(\boldsymbol{r}) = \frac{i-f}{2}\int_{x_0}^{x}\left(\int_{y_0}^{y} B(x',y')dy'\right)dx'. \tag{A.28}$$

Furthermore, the potential χ can be used to calculate the transformation of the wavefunction from gauge i to gauge f:

$$\psi_f(\boldsymbol{r}) = \underbrace{\exp\left(-\frac{\mathrm{i}e}{\hbar}\chi_{f\leftarrow i}(\boldsymbol{r})\right)}_{\mathcal{G}_{f\leftarrow i}}\psi_i(\boldsymbol{r}). \tag{A.29}$$

Because of the gauge invariance, the time evolution of all physical observables stays unchanged, if the wavefunction and the Hamiltonian are converted in the same way. This can be exploited to calculate the action of the Hamiltonian in a more convenient way. Conventionally, we use a symmetric gauge to represent the perpendicular magnetic field and compute every matrix element by the operator[1]

$$\hat{H}_m\psi(\boldsymbol{r}) = c_{m_x m_y}(\boldsymbol{r})\ \ \mathcal{F}_x^{-1}\left(k_x - \mathrm{i}\tfrac{e}{\hbar}A_x^{[0]}(\boldsymbol{r})\right)^{m_x}\mathcal{F}_x\ \ \mathcal{F}_y^{-1}\left(k_y - \mathrm{i}\tfrac{e}{\hbar}A_y^{[0]}(\boldsymbol{r})\right)^{m_x}\mathcal{F}_y\ \ \psi(\boldsymbol{r}). \tag{A.30}$$

If the wavefunction is given in the Landau gauge in x direction $\boldsymbol{A}^{[-1]}$, the action of the $k_y^{m_y}$ operator is position independent since $A_y^{[-1]} = 0$ and the operator $k_y^{m_y}$ can be calculated by a simple multiplication in momentum space. The same holds for the $k_x^{m_x}$ operator in the gauge $\boldsymbol{A}^{[+1]}$. As a consequence, it is advantageous to compute the matrix element by

$$\hat{H}_m\psi(\boldsymbol{r}) = c_{m_x m_y}(\boldsymbol{r})\ \mathcal{G}_{0\leftarrow+1}\left[\mathcal{F}_x^{-1}k_x^{m_x}\mathcal{F}_x\right]\mathcal{G}_{+1\leftarrow-1}\left[\mathcal{F}_y^{-1}k_y^{m_y}\mathcal{F}_y\right]\mathcal{G}_{-1\leftarrow 0}\ \psi(\boldsymbol{r}), \tag{A.31}$$

acting with three gauge transformations $\mathcal{G}_{f\leftarrow i}$ on the wavefunction. We calculate the scalar potential $\chi(\boldsymbol{r})$ from the definition of the magnetic field $B(\boldsymbol{r})$ before the

[1] A symmetric gauge is used to equally distribute numerical errors into the k_x and the k_y operator.

propagation starts and store the different gauge transformations $\mathcal{G}_{-1\leftarrow 0}$, $\mathcal{G}_{1\leftarrow -1}$ and $\mathcal{G}_{0\leftarrow -1}$ for every grid point. Additionally, the last gauge transformation can be merged with the matrix elements $c_{m_x m_y}(\boldsymbol{r})$. This scheme can be implemented very efficiently, since the action of the magnetic field only comprises two additional multiplications with a phase vector, which is unchanged during the whole propagation. A calculation using the permutations of the momentum operator and the vector potential is more demanding. Furthermore, the same gauge transformations are needed to place lead wave-packets into the scattering region in presence of a magnetic field, as shown in Section 4.2.2.

A.3. Open boundary conditions

All mesoscopic systems studied in this thesis consist of a finite scattering region connected to several semi-infinite leads thereby describing an actually infinitely extended system, as sketched in Fig. 4.4. However, only the properties of the finite scattering region are of interest and techniques which restrict the simulated area can be applied. In recursive Green's function calculations the truncation is achieved by attaching the surface Green's functions of the semi-infinite leads, which describes the scattering of the states into an asymptotic channel at a fixed energy [91]. A single wave packet contains a variety of different energies and other methods have to be used for the open boundary conditions at the edges of the simulated area.

The best results can be achieved by so called transparent boundary conditions, which are mathematically constructed such that the time evolution in the simulated area is equal to the solution of the whole problem restricted to the system of interest [216]. This scheme assures the highest numerical accuracy, which amounts to a vanishing probability of spurious reflections of the wave function at the boundaries. Therefore the entire history of the time evolution at the edges of the system has to be stored to compute a time-dependent change of the differential equation, which is numerically demanding and by now not implemented in TQT.

The numerical calculations presented in this thesis use methods which do not require a history of the time evolution, like the perfectly matched layer technique (PML) [217] or absorbing boundary conditions [218]. In order to study the influence of these two techniques we first apply them on a one dimensional Schrödinger equation

$$\mathrm{i}\partial_t \psi(x,t) = \partial_x^2 \psi(x,t) + V\psi(x,t). \tag{A.32}$$

As initial state we choose a Gaussian wave packet

$$\psi(x,t) \propto \mathrm{e}^{-x^2/2a}\mathrm{e}^{ikx}, \tag{A.33}$$

with an extent a and a momentum k. For this type of wave packet the time evolution in an infinite system can be calculated analytically by a propagation in momentum space. In the following we want to study the time evolution in a restricted simulation domain $(-x_B, x_B)$ and compare the results to the exact propagation.

The PML technique can be understood as a coordinate stretch at the boundary with a coordinate transformation

$$x \to x + R\int_0^x \sigma(\xi)d\xi, \tag{A.34}$$

which at the same time modifies the derivative operator

$$\partial_x \to \frac{1}{1+R\sigma}\partial_x. \tag{A.35}$$

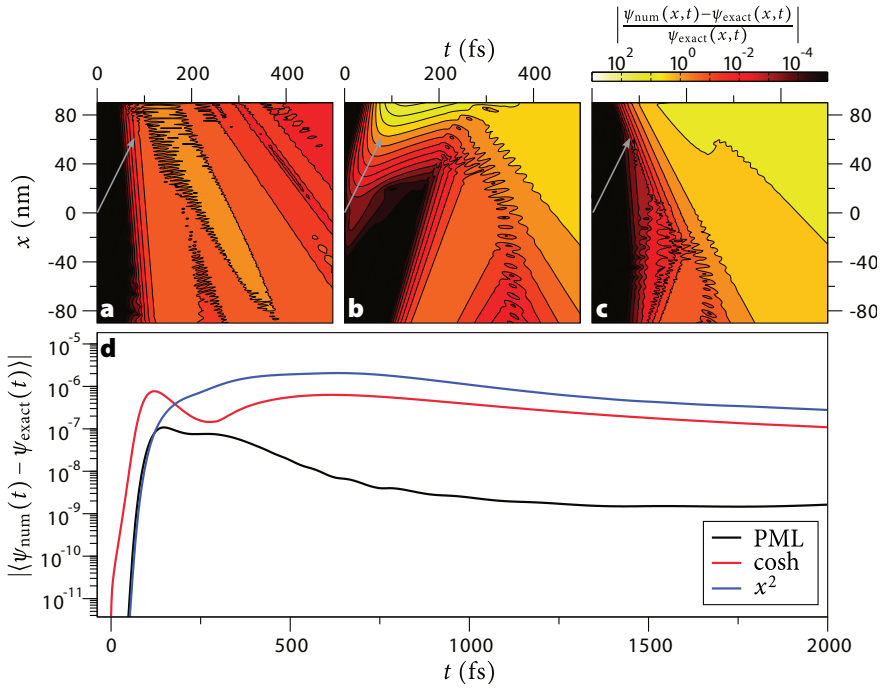

Figure A.1. | Error of absorbing boundaries – Comparison of the error arising for the propagation of a kicked Gaussian wave-packet (gray error represents the propagation direction, $a = 15$, $k = 0.4$) in a finite scattering region $(-x_B, x_B)$, $x_B = 128$, for different absorbing boundary conditions. The deviation between the exact result and the numerical calculations is color coded, where yellow represents stronger deviations. **a,** PML boundaries ($W = 20$, $R = \exp(-i\pi/4)$, $\sigma_0 = 4$). **b,** Complex absorbing boundaries with a cosh dependence (A.38) ($a_b = 4$). **c,** Complex absorbing boundaries wit a x^2 dependence (A.39) ($W = 20$). **d,** Time evolution of the integrated error between exact and numerical time evolution for the different absorbers (**a**,**b**,**c**).

As a consequence, the time evolution of the Gaussian wave-packet is governed by the new differential equation

$$i\partial_t \psi = \frac{1}{1+R\sigma}\partial_x \left(\frac{1}{1+R\sigma}\partial_x \psi\right) + V\psi. \tag{A.36}$$

For the numerical calculations we use a quadratic dependence of σ at the boundaries

$$\sigma = \begin{cases} \sigma_0 (x - x_L)^2, & -x_B < x < x_L = W - x_B, \\ 0, & x_L < x < x_R, \\ \sigma_0 (x - x_R)^2, & x_B > x > x_R = x_B - W, \end{cases} \tag{A.37}$$

where x_L and x_R are the starting points of the coordinate stretch and σ_0 the strength. In Fig. A.1 (**a**) the deviation between the analytical result of the infinite system and the numerical calculation in a bounded domain using PML boundaries is visualized for a

kicked wave packet, which has a propagation direction along the gray arrow. For low times (black area) no deviation is present, however, after a certain time the wave packet hits the boundary and some parts are reflected (orange stripe). The local error is less than 0.1% and can be easily decreased by increasing the width of the absorbing layer.[2] In total the wave packet is absorbed very well, and the integrated error in Fig. A.1 (**d**) shows that only 10^{-8} of the wave packet remains in the simulation area.

A much easier approach is the application of complex potentials [218]. In this way the time-evolution with a small imaginary part leads to a local reduction of the absolute value of the wave packet. Different complex potentials can be used, like

$$V(x) = -\mathrm{i}V_{\mathrm{at}}\left(\cosh\left(\left(\frac{x-x_B}{a_B}\right)^2\right)+\cosh\left(\left(\frac{x+x_B}{a_B}\right)^2\right)\right) \tag{A.38}$$

in Fig. A.1 (**b**), or

$$V(x) = -\mathrm{i}\frac{V_{\mathrm{at}}}{W}\begin{cases}(x-x_L)^2, & -x_B < x < x_L = W - x_B,\\ 0, & x_L < x < x_R,\\ (x-x_R)^2, & x_B > x > x_R = x_B - W,\end{cases} \tag{A.39}$$

in Fig. A.1 (**c**). A comparison shows that the complex absorbing potentials perform not as well as the PML. The reflection of the boundary is enhanced, as shown in Fig. A.1 (**b,c**) and a higher amount ($\approx 10^{-6}$) of the wave packet stays in the simulated area, as apparent from time evolution of the integrated error in Fig. A.1 (**d**). Absorbing potentials which do not vanish completely inside of the scattering may generate a better longterm result but already show deviations for very short propagation times, like in the case of the cosh potential in Fig. A.1 (**b**).

The preceding calculations with the one-dimensional Schrödinger equation show that PML boundaries and complex boundaries can be added to the Hamiltonian to model an infinite system. For the same width W of the absorbing layer, the PML performs best and should be preferred. However, there are also Hamilton operators for which even complex absorbers do not lead to backscattering, like in the case of topological insulators where the edge states are topologically protected. In this thesis PML boundaries and complex potentials have been applied to model the escape of the wavefunction from the mesoscopic system into semi-infinite leads, and it is worth mentioning that both methods have to be optimized carefully by hand to get sufficient numerical accuracy.

[2] At this point in time the analytical solution of the wave packet has already left the scattering region, leading to an amplification of the plotted error because of the normalization.

A.4. Observables from a wave-packet propagation

During the propagation of a quantum wave-packet several observables can be extracted from the time evolution, like for example the quantum transport properties introduced in Chapter 4. In the following we will demonstrate how spectral properties of the underlying system can be extracted from the time evolution of a trail state, which is frequently used in this thesis. Furthermore, we will show how the mode-resolved current can be extracted from the time evolution of a scattered wave-packet, which gives for example further insight into the tunneling through a p-n junction in a graphene nanoribbon. The integrated time-dependent current is also very suitable for calculating energy averaged transport properties, which can be for instance employed to extract weak localization properties.

A.4.1. Correlation and density of states

The time evolution of a wave packet $\psi(t)$ in a system with a discrete set of eigenstates ψ_n with corresponding eigenvalues E_n can be calculated by the expansion

$$\psi(t) = \sum_n c_n \psi_n \mathrm{e}^{-\mathrm{i}E_n t/\hbar}, \tag{A.40}$$

where c_n represents the spectral weight of the eigenstates contributing to the initial state. In the same way it is possible to extract the spectrum $n(E)$ of the system by means of the quantum time-evolution of a wave packet $\psi(t)$ by [219]

$$n(E) = \frac{1}{2\pi} \int_{-\infty}^{\infty} \underbrace{\langle \psi(0) | \psi(t) \rangle}_{C(t)} \mathrm{e}^{\mathrm{i}Et/\hbar} dt. \tag{A.41}$$

Therefore the correlation $C(t)$ between the initial state $\psi(0)$ and the propagating wave packet $\psi(t)$, which is for example calculated by one of the numerical methods introduced in Section 4.1, is tracked and translated into the spectrum by a Fourier transform. The connection between the correlation and the spectrum is evident once the expansion in eigenstates (A.40) is inserted into Eq. (A.41), which can be reduced to

$$n(E) = \sum_n \frac{1}{2\pi} \int_{-\infty}^{\infty} |c_n|^2 \mathrm{e}^{-\mathrm{i}E_n t/\hbar} \mathrm{e}^{\mathrm{i}Et/\hbar} dt, \tag{A.42}$$

using the orthonormality of the eigenstates $\langle \psi_n | \psi_m \rangle = \delta_{nm}$. Every single addend of this sum equals the Fourier representation of a Dirac delta function, leading to the spectrum

$$n(E) = \sum_n |c_n|^2 \, \delta(E - E_n). \tag{A.43}$$

If the correlation $C(t)$ is only computed for a propagation forward in time, which is usually the case for the results presented in this thesis, the very same spectrum can be extracted my means of the Laprace transform

$$n(E) = \frac{1}{\pi} \mathfrak{Re} \int_0^{\infty} \langle \psi(0) | \psi(t) \rangle \, \mathrm{e}^{\mathrm{i}Et/\hbar} dt. \tag{A.44}$$

In numerical calculations the correlation can only be computed for a limited interval and an abrupt truncation of the integrals in Eqn. (A.41) and (A.44) would lead to spurious fluctuations in the spectrum. This can be circumvented by introducing an envelope function, which suppresses the oscillations of the correlation function for long propagation times. In this thesis we generally use a Gaussian envelope corresponding to a temperature T which is modifying the correlation

$$C(t) = \frac{1}{2\pi\hbar} \exp\left(-\tfrac{1}{2}\left(\tfrac{k_B T t}{\hbar}\right)^2\right) \langle\psi(0)|\psi(t)\rangle. \tag{A.45}$$

After a Fourier transformation of the damped $C(t)$ the initial Dirac delta functions obtain a Gaussian broadening with a variance of $k_B T$.

A.4.2. Eigenstates

In a similar manner the eigenstates ψ_n of the system can be extracted out of the time evolution of the wavefunction. Since the initial wave packet is generally made up of a superposition of different eigenstates, the Fourier transformation of the time evolution $\psi(t)$ can be used to extract the eigenstate

$$\psi_n \propto \int \psi(t) \mathrm{e}^{\mathrm{i}E_n t/\hbar} dt, \tag{A.46}$$

at the energy E_n. Usually it is not possible or efficient to store the time evolution of the state $\psi(t)$ so that the energies of the interesting eigenstates already have to be selected before the propagation. This scheme was for example used to calculate the switching states of the HgTe contriction in Fig. 7.1 and the initial edge-state wave-packets for the with-modulated nanoribbon showing Bloch–Zener oscillations in Fig. 7.12.

A.4.3. Time-resolved current

Besides the energy resolved transmission amplitudes presented in Chapter 4, interesting transport properties can be also captured by the time-dependent and mode-resolved current of a wave-packet through the attached leads. Weak localization properties can be for example not only extracted from the energy averaged transmission amplitudes but also from the integrated time-dependent current. In the following we will show, how the time-resolved current through a lead modeled by an arbitrary Hamilton operator can be calculated. If the system under investigation is described by a Hamiltonian comprising of various different momentum operators, it is advantageous to describe the current through the surface of the lead $\mathcal{S}_L$ by the general probability current

$$j(t) = \int_{\mathcal{S}_L} \hat{\boldsymbol{v}} |\psi(\boldsymbol{r})|^2 d\boldsymbol{S}, \tag{A.47}$$

and assume the surface $\mathcal{S}_L$ to be perpendicular on the lead direction, as shown in Fig. 4.4. For this configuration the transversal eigenstates $\chi_i(E)$ as well as the group velocities

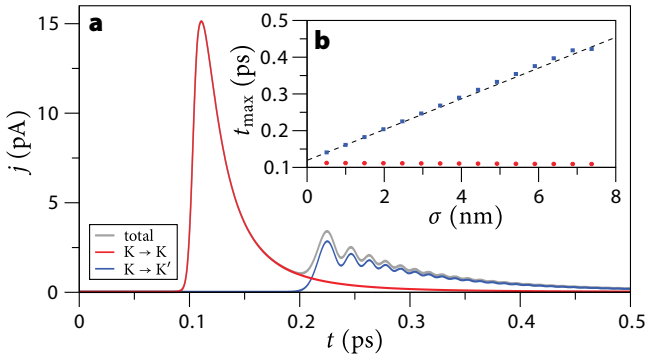

Figure A.2. | Valley tunneling delay – a, Current induced by a wave packet polarized in valley K through a p-n junction in a zig-zag nanoribbon modeled by Eq. (4.60) with $V_0 = 0.5\text{eV}$, $\sigma = 2.46\text{nm}$. Parts undergoing a tunneling into the valley K' display a time delay.
b, Dependence of the time delay on the spread σ of the p-n junction.

$v_i(E)$ are given by the lead Hamiltonian (4.41) and have been already calculated for the creation of the lead wave-packets in Section 4.2.2. Since the expectation values of the velocity operator $\hat{\boldsymbol{v}}$ are known in the basis of the lead eigenstates, it is possible to use a transformation between the time domain and the energy domain to calculate the current

$$j_i(t) = e \int v_n(E) \left(\int \chi_i(x,E) \int \phi(x,t) \mathrm{e}^{\mathrm{i}Et/\hbar} \mathrm{d}t\mathrm{d}x \right) \mathrm{e}^{-\mathrm{i}Et/\hbar} \mathrm{d}E, \tag{A.48}$$

where $\phi(x,t)$ is the wavefunction leaving the system, which is tracked during the time evolution on the lead surface $\mathcal{S}_L$.[3]

In the following we study the time-dependent current induced by a wave packet tunneling through a p-n junction in a zig-zag graphene nanoribbon, as sketched in Fig. 4.7 (**a**), which already served as the example system for the comparison of the transmission properties calculated by the recursive Green's function method and the wave-packet scheme. If a valley-polarized wave-packet is propagated through the potential step (4.60), parts of the wavefunction can be scattered from the valley K to the valley K'. The time-dependence of the current through the right lead reveals that those parts which have switched the valleys arrive at later times, as shown in Fig. A.2 (**a**). This scattering is governed by the dynamics of the edge states linking the two valleys[114], as sketched in Fig. 4.7 (**b**), and thus the time delay is governed by the propagation of the edge state from K to K'. The time evolution of their average momentum k is described by

$$\hbar \frac{\partial k}{\partial t} = eE(x), \tag{A.49}$$

with the electric field $E(x)$, which is induced by the potential step (4.60). Because of the vanishing group velocity of the edge states their real space motion can be neglected and $E(x)$ can be approximated by the field value at the origin $E(0) = V_0/4\sigma$, which is

[3] In presence of a magnetic field, a gauge transformation is applied on the wavefunction before $\phi(x,t)$ is tracked, such that the $\boldsymbol{A}$ field is perpendicular on the current and thus not entering Eq. (A.48). Previously the vector potential was incorporated into the current operator [220], which leads to numerical instabilities for high magnetic fields.

only depending on the spreading of the potential step σ. The minimal distance between the valleys in momentum space is given by

$$\Delta k = \frac{2(9 - 4\sqrt{3})\pi}{9a_0}, \tag{A.50}$$

and results in a propagation time between K and K' of

$$\Delta t = \frac{4\hbar\Delta k}{eV_0}\sigma. \tag{A.51}$$

Fig. A.2 (**b**) shows the time delays of the current with and without valley tunneling for different steepnesses σ of the potential step. The $K \to K$ tunnel event is independent of the potential gradient, whereas the $K \to K'$ tunneling time grows linearly with σ. The associated time delay between the two processes is perfectly described by Eq. (A.51), which is displayed as back dashed line in Fig. A.2 (**b**). This illustrates the dynamics of tunneling process which occurs at the p-n junction and gives an intuitive insight into the physics of the valley-valve effect.

A.5. Lead wave-packet normalization

In order to calculate the transmission through a scattering region by means of a propagation, as introduced in Section 4.2.3, the pain-wave contributions of the involved wave packets have to be normalized. The incoming (+) and outgoing (−) wave packets are generally assembled in momentum space by

$$\Phi_\alpha^\pm = \int_{-\infty}^{\infty} \eta_\alpha^\pm(k)\ \chi_\alpha(k)\ \mathrm{e}^{\mathrm{i}ky}\ \mathrm{d}k, \tag{A.52}$$

using the transversal eigenstates $\chi_\alpha(k)$ of the lead weighted by the factor $\eta_\alpha(k)^\pm$ for the longitudinal momentum k . The different pain-wave contributions can be extracted by

$$\psi_\alpha^\pm(E) = \frac{1}{\mu_\alpha^\pm(E)} \int_{-\infty}^{\infty} \mathrm{e}^{-\mathrm{i}\hat{H}_\alpha t/\hbar}\ \Phi_\alpha^\pm\ \mathrm{e}^{\mathrm{i}Et/\hbar}\ \mathrm{d}t, \tag{A.53}$$

comprising the propagation with the lead Hamilton operator $\hat{H}_\alpha$. To obtain a normalized transmission, the weights of the energies in the wave packet have to be determined, which allows us to define a correction factor $\mu_\alpha^\pm(E)$, such that the pain waves are orthonormal

$$\langle \psi_\beta^\pm(E')|\psi_\alpha^\pm(E)\rangle = \delta_{\beta,\alpha}\ \delta(E-E'). \tag{A.54}$$

The following calculation determines this overlap between two incoming or outgoing wave packets $\psi_\beta^\pm(E')$ and $\psi_\alpha^\pm(E)$ in the same lead for different modes. First we combine the definition of the plain-wave parts (A.53) and the wave packets (A.52) leading to

$$\begin{aligned}\langle \psi_\beta^\pm(E')|\psi_\alpha^\pm(E)\rangle = \int \Bigg(\int \mathrm{e}^{\mathrm{i}\hat{H}_\beta t'/\hbar}\ \frac{\eta_\beta(k')}{\mu_\beta^\pm(E')}\ \chi_\beta^*(k')\ \mathrm{e}^{-\mathrm{i}k'y}\ \mathrm{e}^{-\mathrm{i}E't'/\hbar}\mathrm{d}t'\ \mathrm{d}k' \Bigg) \\ \cdot \Bigg(\int \mathrm{e}^{-\mathrm{i}\hat{H}_\alpha t/\hbar}\ \frac{\eta_\alpha(k)}{\mu_\alpha^\pm(E)}\ \chi_\alpha(k)\ \mathrm{e}^{\mathrm{i}ky}\ \mathrm{e}^{\mathrm{i}Et/\hbar}\mathrm{d}t\ \mathrm{d}k \Bigg) \mathrm{d}x\ \mathrm{d}y.\end{aligned} \tag{A.55}$$

The action of the Hamilton operators $\hat{H}_\beta$ and $\hat{H}_\alpha$ can be replaced by the respective eigenvalues $\epsilon_\beta(k')$ and $\epsilon_\alpha(k)$, since the wave functions $\chi_\beta(k')$ and $\chi_\alpha(k)$ are constructed as eigenstates of the leads. Furthermore, the $\mathrm{d}y$ integration leads to

$$\int_{-\infty}^{\infty} \mathrm{e}^{\mathrm{i}y(k-k')}\mathrm{d}y = 2\pi\delta(k-k')$$

and removes one momentum dependence,

$$\begin{aligned}\langle \psi_\beta^\pm(E')|\psi_\alpha^\pm(E)\rangle = 2\pi \int \Bigg(\int \tfrac{\eta_\beta(k)}{\mu_\beta^\pm(E')}\ \chi_\beta^*(k)\ \mathrm{e}^{-\mathrm{i}(E'-\epsilon_\alpha(k))t'/\hbar}\mathrm{d}t' \Bigg) \\ \cdot \Bigg(\int \tfrac{\eta_\alpha(k)}{\mu_\alpha^\pm(E)}\ \chi_\alpha(k)\ \mathrm{e}^{\mathrm{i}(E-\epsilon_\alpha(k))t/\hbar}\mathrm{d}t \Bigg) \mathrm{d}k\ \mathrm{d}x.\end{aligned} \tag{A.56}$$

Since the transversal wave functions are chosen to form a complete set for fixed momentum k,

$$\int \chi_\beta^*(k)\ \chi_\alpha(k)\ \mathrm{d}x = \delta_{\alpha,\beta},$$

the x integration yields

$$\begin{aligned}&\langle\psi^{\pm}_{\beta}(E')|\psi^{\pm}_{\alpha}(E)\rangle\\&= 2\pi\,\delta_{\alpha,\beta}\int\left(\int\frac{\eta_{\alpha}(k)}{\mu^{\pm}_{\alpha}(E')}\,\mathrm{e}^{-\mathrm{i}(E'-\epsilon_{\alpha}(k))t'/\hbar}\mathrm{d}t'\right)\left(\int\frac{\eta_{\alpha}(k)}{\mu^{\pm}_{\alpha}(E)}\,\mathrm{e}^{\mathrm{i}(E-\epsilon_{\alpha}(k))t/\hbar}\mathrm{d}t\right)\mathrm{d}k.\end{aligned}\tag{A.57}$$

In every bracket the time integration t and the t' can be performed and results in two energy delta functions:

$$\langle\psi^{\pm}_{\beta}(E')|\psi^{\pm}_{\alpha}(E)\rangle = (2\pi)^3\hbar^2\delta_{\alpha,\beta}\int\frac{\eta_{\alpha}(k)}{\mu^{\pm}_{\alpha}(E')}\,\delta(E'-\epsilon_{\alpha}(k))\,\frac{\eta_{\alpha}(k)}{\mu^{\pm}_{\alpha}(E)}\,\delta(E-\epsilon_{\alpha}(k))\,\mathrm{d}k.\tag{A.58}$$

The final momentum integration projects all k dependencies by means of the two delta functions $\delta(E-\epsilon_{\alpha}(k))$ and $\delta(E-\epsilon_{\beta}(k))$ on the energy branch $\epsilon^{\pm}_{\alpha}(k)$, which is populated by the incoming (+) or outgoing (−) wave packet. The weight of the wave packet $\eta^{\pm}_{\alpha}(E)$, which was initially defined in momentum space as $\eta^{\pm}_{\alpha}(k)$, is now assigned to the energy $E=\epsilon^{\pm}_{\alpha}(k)$. Accordingly, the overlap between different pain-wave parts of the wave packet are given by

$$\langle\psi^{\pm}_{\beta}(E')|\psi^{\pm}_{\alpha}(E)\rangle = (2\pi\hbar)^3\delta_{\alpha,\beta}\frac{1}{\hbar|\partial\epsilon^{\pm}_{\alpha}/\partial k|}\left(\frac{\eta^{\pm}_{\alpha}(E)}{\mu^{\pm}_{\alpha}(E)}\right)^2\,\delta(E'-E).\tag{A.59}$$

Note, there are no ambiguities $\epsilon^{\pm}_{\alpha}(k)=\epsilon^{\pm}_{\alpha}(k')$, since the bands are cut in such a way that for positive and negative group velocity there is only one momentum k in every single wave packet which corresponds to the energy $\epsilon^{\pm}_{\alpha}(k)$, as discussed in Section 4.2.2. The derivative of the band energy $\epsilon^{\pm}_{\alpha}$ corresponds to the group velocity $v^{\pm}_{\alpha}(E)$ for the right or left moving states at the energy E. This results in a correction factor of

$$\mu^{\pm}_{\alpha}(E)=\frac{\eta^{\pm}_{\alpha}(E)(2\pi\hbar)^{3/2}}{\sqrt{v^{\pm}_{\alpha}(E)}},\tag{A.60}$$

which is providing the energy normalization of the quantum transmission amplitudes extracted from the time evolution of a wave packet in Section 4.2.3.

A.6. Transmission through a p-n junction in a graphene nanoribbon

The code of listing A.1 employs the TQT library to evaluate the transmission amplitudes through a p-n junction in a graphene nanoribbon. This layout is used to demonstrate in Section 4.2.3 and A.4.3 how the valley-valve effect can be studied by the time evolution of a quantum wave-packet. The dependencies of the necessary TQT classes are illustrated in Fig. A.3 and the code of an implementation in C++ is structured as follows.

In order to obtain all transmission amplitudes the time evolution for every single incoming wave packet has to be calculated separately, which is accomplished by the loop in line 15. From line 19 to 27 the basic properties of the setup are defined by the instantiation of a **`Grid`** class for the geometric sizes, a **`GrapheneZZ2`** class for the tight-binding Hamiltonian of a zig-zag nanoribbon, a **`Timestate`** class which holds the wavefunction and a **`Timeline`** class to handle the time steps of the propagation.

The leads are defined by the creation of two **`LeadWavePacket`** classes, which share the common parameters given by the **`LeadParam`** class. Since the band structure of graphene features two valleys, all bands have to be separated into K and K' leading to valley-polarized wave packets, which is accomplished by switching on the splitting algorithm with `set(`**`LeadParam`**`::SPLIT)`. After the constructor has completed, the entire wave-packet data consisting of the transversal wavefunctions, energies and splitting informations, are stored in the folders `lead1` and `lead2` and will be automatically reloaded if the classes are recreated. The band structure of the leads and the indices of the corresponding wave packets are stored in the files `band_lead1.plt` and `band_lead1.plt`.

In lines 45 to 60 the potential step as well as the absorbing boundary conditions are imprinted on the Hamiltonian by the public vectors `hamiltonian.V(ix,iy)` and `hamiltonian.Vat(ix,iy)` respectively. Since the system contains a complex absorbing potential we initialize a **`FaberPropagator`** `prop` for an energy domain $\Delta E = 20\,\mathrm{eV}$ and $d = 0.4$. By means of the function `prop.add(`**`Observable`**`&IN_obs)` all observables are registered at the propagator. In this way the interface functions of the observables

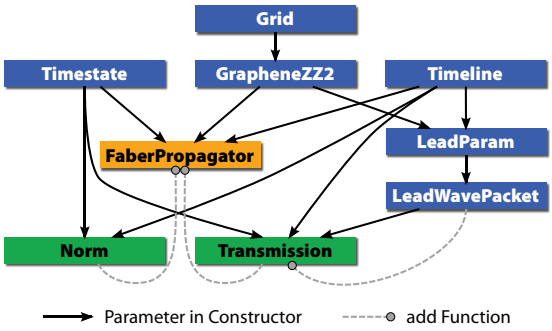

Figure A.3. | Class dependencies of the code example – Sketch of the used TQT classes in listing A.1 and the dependencies amongst themselves. Solid lines with arrows indicate the requirements of the constructor. Classes like the observables **`Norm`** and **`Transmission`** are attached to the propagator **`FaberPropagator`** by an `add(`**`Observable`**`&IN_obs)` function, depicted by the gray dashed lines.

are automatically called during the propagation and allow the tracking of the time evolution.

The example program calculates time evolution of the absolute value by the **Norm** class as well as the the transmission through the p-n junction. An instance of the **Transmission** class determines the transport from `lead1` as specified in the constructor into all the leads added by the `add(LeadWavePacket &IN_lead)` function. Furthermore, the reflection back into the outgoing lead is calculated automatically. After adding all observables to the propagator the function `prop.runall()` is launched to calculate the time evolution. From line 82 to 95 the information gathered by the observables is stored to output files. The files `norm(0-19).nc` contain the decay of the absolute value of the wave packet, `all_transmissions(0-19).dat` the mode resolved transmission from one lead to all other leads and `sum_transmissions(0-19).nc` the total transmission and reflection.

Listing A.1 | Program to calculate the transmission amplitudes through a p-n junction

```
#include "tqt.h"

using namespace TQT;

//Define a Fermi function used for potential steps
REAL pot(REAL x, REAL x0, REAL a0)
{
  return 1. / (1. + exp((x - x0) / a0));
}

int main()
{

  //Run through all different bands
  for (INDEX wp_id = 0; wp_id < 20; wp_id++)
  {

    //Define a graphene nanoribbon (length=500 unit cells, with=6*2 unit cells)
    Grid grid(500, 6, 2.46 * SI_ANGS, 2.46 * SI_ANGS);

    //Define atomistic graphene Hamiltonian and corresponding state to propagate
    GrapheneZZ2 hamiltonian(grid);
    Timestate state(hamiltonian);

    //Define a time discretization and split it every 50 time steps
    Timeline timeline(500.0e-15, .1e-15);
    timeline.add_equalsplit(50);

    //Define global parameters (split multiple valleys, energy bounds) of the leads
    LeadParam leadparam(timeline, hamiltonian);
    leadparam.set(LeadParam::SPLIT);
    leadparam.set_Emin(-7.*SI_CHARGE_ELECTRON);
    leadparam.set_Emax(5*SI_CHARGE_ELECTRON);
    leadparam.info();

    //Initialize two leads at -9nm and +9nm of the p-n junction and write bands
    LeadWavePacket lead1(leadparam, -9. * SI_NM, grid.get_y0(), -9. * SI_NM,
        grid.get_y1(), "lead1");
    LeadWavePacket lead2(leadparam, 9. * SI_NM, grid.get_y1() - 1.e-10, 9. * SI_NM,
        grid.get_y0(), "lead2");
    lead1.write_band("band_lead1.plt");
    lead2.write_band("band_lead2.plt");

    //Add potential and left/right absorber to the Hamiltonian
    {
      REAL border = 40 * SI_NM;
      REAL border_width = grid.get_x1()-border;
```

```
      REAL x;
      for (INDEX ix = 0; ix < grid.get_NX(); ix++)
        for (INDEX iy = 0; iy < grid.get_NY(); iy++)
        {
          x = grid.get_x0() + ix * grid.get_dx();
          hamiltonian.V(ix, iy) = .6 * pot(-x, 0., 1.492 * SI_NM) *
              SI_CHARGE_ELECTRON;
          hamiltonian.M(ix, iy) += .000001 * SI_CHARGE_ELECTRON;
          hamiltonian.Vat(ix, iy) -= 0.15 * pot(x, -border-0.5*border_width,
              border_width*0.3) * SI_CHARGE_ELECTRON;
          hamiltonian.Vat(ix, iy) -= 0.15 * pot(-x, -border-0.5*border_width,
              border_width*0.3) * SI_CHARGE_ELECTRON;
        }
    }

    //Initialize a propagator using Faber polynomials with DeltaE=20, E0=0, d=0.4
    FaberPropagator prop(timeline, state, 20. * SI_CHARGE_ELECTRON, 0., 0.4);
    prop.set_Hamiltonian(hamiltonian);

    //Define the norm observable and add it to the propagator
    Norm norm(timeline, state);
    prop.add(norm);

    //Define the transmission observable for the band wp_id and analyze all
    //amplitudes through lead1 and lead2 between -2.5eV and 1.8eV
    Transmission transmission(timeline, state, lead1, wp_id, -2.5 *
        SI_CHARGE_ELECTRON, 1.8* SI_CHARGE_ELECTRON);
    transmission.add(lead2);
    //Add the transmission to the propagator
    prop.add(transmission);

    //Calculate the time evolution
    prop.runall();

    //Write the time evolution of the norm
    std::stringstream filename;
    filename << "norm" << wp_id << ".nc";
    norm.write_t(filename.str().c_str());

    //Write the energy dependent transmission into all modes
    filename.str("");
    filename << "all_transmissions" << wp_id << ".dat";
    transmission.write_E(filename.str().c_str());

    //Write the energy dependent transmission into different leads
    filename.str("");
    filename << "sum_transmissions" << wp_id << ".dat";
    transmission.write_E_sum(filename.str().c_str());

  }//End loop through all different bands

  return 0;
}
```

A.7. Kane Hamiltonian for HgTe quantum wells

In the previous sections about topological insulators the electronic structure of HgCdTe quantum wells have been commonly described by an effective two-dimensional Hamiltonian. However, in order to derive this two-dimensional approximation the electronic structure of the bulk materials has to be modeled appropriately. Close to the Γ-point materials like HgTe and CdTe can be well described by the Kane Hamiltonian

$$H = \begin{pmatrix} T & 0 & -\frac{1}{\sqrt{2}}Pk_+ & \sqrt{\frac{2}{3}}Pk_z & \frac{1}{\sqrt{6}}Pk_- & 0 \\ 0 & T & 0 & -\frac{1}{\sqrt{6}}Pk_+ & \sqrt{\frac{2}{3}}Pk_z & \frac{1}{\sqrt{2}}Pk_- \\ -\frac{1}{\sqrt{2}}Pk_- & 0 & U+V & 0 & R & 0 \\ \sqrt{\frac{2}{3}}Pk_z & -\frac{1}{\sqrt{6}}Pk_- & 0 & U-V & 0 & R \\ \frac{1}{\sqrt{6}}Pk_+ & \sqrt{\frac{2}{3}}Pk_z & R^\dagger & 0 & U-V & 0 \\ 0 & \frac{1}{\sqrt{2}}Pk_+ & 0 & R^\dagger & 0 & U+V \end{pmatrix}, \tag{A.61}$$

containing the Γ_6 representation of the electron bands and Γ_8 representation of the hole bands. All necessary matrix elements are given by

$$k_\parallel^2 = k_x^2 + k_y^2, \quad k_\pm = k_x \pm i k_y, \tag{A.62}$$

$$T = E_g + \frac{\hbar^2}{2m_{\text{eff}}}\left(k_x^2 + k_y^2 + k_z^2\right), \tag{A.63}$$

$$U = E_{\text{off}} - \frac{\hbar^2}{2m_0}\left(\gamma_1 k_\parallel^2 + k_z \gamma_1 k_z\right), \tag{A.64}$$

$$V = -\frac{\hbar^2}{2m_0}\left(\gamma_2 k_\parallel^2 - 2k_z \gamma_2 k_z\right), \tag{A.65}$$

$$R = -\frac{\hbar^2}{2m_0}\left(\sqrt{3}\mu k_+^2 - \sqrt{3}\bar{\gamma} k_-^2\right). \tag{A.66}$$

The material parameters of the pure materials are summarized in Table A.1. We use a linear interpolation between the two pure material parameters to model the layers of the heterostructure with different $Hg_{1-x}Cd_xTe$ constituents given by the position dependent mixing parameter x of Eq. (6.2). The valence band offset between HgTe and CdTe is taken to be $E_{\text{off}} = 570$ meV [168]. Since the split-off band is not present in this

Table A.1. | Band structure parameters of HgTe and CdTe at $T = 0$ K. [168]

	E_g	Δ	$E_P = \frac{2m_0P^2}{\hbar^2}$	F	γ_1	γ_2	γ_3
HgTe	-0.303 eV	1.08 eV	18.8 eV	0	4.1	0.5	1.3
CdTe	1.606 eV	0.91 eV	18.8 eV	-0.09	1.47	-0.28	0.03

representation, its influence has to be taken into account by a modified effective mass of the electron band [169]

$$m_{\text{eff}} = m_0 * \left(1 + \frac{2m_0 P^2}{3\hbar^2(E_g + \Delta)}\right)^{-1}. \tag{A.67}$$

This three dimensional description of HgCdTe was used in chapter 6 to derive the bound states of the quantum well, to calculate the effective Hamiltonian and to compare the resulting band structure with the full three dimensional result.

Bibliography

[1] H. P. Boehm, A. Clauss, G. O. Fischer and U. Hofmann, *Das Adsorptionsverhalten sehr dünner Kohlenstoff-Folien*, Z. anorg. allg. Chemie **316**, 119 (1962).

[2] K. S. Novoselov, A. K. Geim, S. V. Morozov, D. Jiang, M. I. Katsnelson, I. V. Grigorieva, S. V. Dubonos and A. A. Firsov, *Two-dimensional gas of massless Dirac fermions in graphene*, Nature **438**, 197 (2005).

[3] K. S. Novoselov, A. K. Geim, S. V. Morozov, D. Jiang, Y. Zhang, S. V. Dubonos, I. V. Grigorieva and A. A. Firsov, *Electric Field Effect in Atomically Thin Carbon Films*, Science **306**, 666 (2004).

[4] C. L. Kane and E. J. Mele, *Quantum Spin Hall Effect in Graphene*, Phys. Rev. Lett. **95**, 226801 (2005).

[5] P. R. Wallace, *The Band Theory of Graphite*, Phys. Rev. **71**, 622 (1947).

[6] Y.-M. Lin, C. Dimitrakopoulos, K. A. Jenkins, D. B. Farmer, H.-Y. Chiu, A. Gill and P. Avouris, *100-GHz transistors from wafer-scale epitaxial graphene*, Science **327**, 332 (2010).

[7] Y. Wu, Y.-M. Lin, A. A. Bol, K. A. Jenkins, F. Xia, D. B. Farmer, Y. Zhu and P. Avouris, *High-frequency, scaled graphene transistors on diamond-like carbon.*, Nature **472**, 74 (2011).

[8] S. Bae *et al.*, *Roll-to-roll production of 30-inch graphene films for transparent electrodes.*, Nat. Nanotechnol. **5**, 574 (2010).

[9] J. Wu, M. Agrawal, H. a. Becerril, Z. Bao, Z. Liu, Y. Chen and P. Peumans, *Organic light-emitting diodes on solution-processed graphene transparent electrodes.*, ACS nano **4**, 43 (2010).

[10] N. Savage, *Come into the light.*, Nature **483**, 38 (2012).

[11] C. L. Kane and E. J. Mele, *Z_2 Topological Order and the Quantum Spin Hall Effect*, Phys. Rev. Lett. **95**, 146802 (2005).

[12] M. Z. Hasan and C. L. Kane, *Colloquium: Topological insulators*, Rev. Mod. Phys. **82**, 3045 (2010).

[13] B. A. Bernevig, T. L. Hughes and S.-C. Zhang, *Quantum Spin Hall Effect and Topological Phase Transition in HgTe Quantum Wells*, Science **314**, 1757 (2006).

[14] M. König, S. Wiedmann, C. Brüne, A. Roth, H. Buhmann, L. W. Molenkamp, X.-L. Qi and S.-C. Zhang, *Quantum Spin Hall Insulator State in HgTe Quantum Wells*, Science **318**, 766 (2007).

[15] V. Krueckl and T. Kramer, *Revivals of quantum wave packets in graphene*, New J. Phys. **11**, 93010 (2009).

[16] T. Kramer, C. Kreisbeck and V. Krueckl, *Wave packet approach to transport in mesoscopic systems*, Phys. Scr. **82**, 38101 (2010).

[17] V. Krueckl and K. Richter, *Bloch-Zener oscillations in graphene and topological insulators*, Phys. Rev. B **85**, 115433 (2012).

[18] V. Krueckl and K. Richter, *Switching Spin and Charge between Edge States in Topological Insulator Constrictions*, Phys. Rev. Lett. **107**, 86803 (2011).

[19] V. Krueckl and K. Richter, *Switching spin and charge between edge states in topological insulator constrictions: a transer matrix approach*, Proc. SPIE **8416**, Spintronics V, 84610Z (2012).

[20] V. Krueckl and K. Richter, *Probing the band topology of mercury telluride through weak localization and antilocalization*, Semicond. Sci. Technol. **27**, 124006 (2012).

[21] V. Krueckl, M. Wimmer, I. Adagideli, J. Kuipers and K. Richter, *Weak Localization in Mesoscopic Hole Transport: Berry Phases and Classical Correlations*, Phys. Rev. Lett. **106**, 146801 (2011).

[22] H. W. Kroto, J. R. Heath, S. C. O'Brien, R. F. Curl and R. E. Smalley, *C60 Buckminsterfullerene*, Nature **318**, 162 (1985).

[23] S. Iijima and T. Ichihashi, *Single-shell carbon nanotubes of 1-nm diameter*, Nature **363**, 603 (1993).

[24] Y. Zheng and T. Ando, *Hall conductivity of a two-dimensional graphite system*, Phys. Rev. B **65**, 245420 (2002).

[25] Y. Zhang, Y.-W. Tan, H. L. Stormer and P. Kim, *Experimental observation of the quantum Hall effect and Berry's phase in graphene*, Nature **438**, 201 (2005).

[26] A. H. C. Neto, F. Guinea, N. M. R. Peres, K. S. Novoselov and A. K. Geim, *The electronic properties of graphene*, Rev. Mod. Phys. **81**, 109 (2009).

[27] H. Min, J. E. Hill, N. a. Sinitsyn, B. R. Sahu, L. Kleinman and A. MacDonald, *Intrinsic and Rashba spin-orbit interactions in graphene sheets*, Phys. Rev. B **74**, 165310 (2006).

[28] M. Gmitra, S. Konschuh, C. Ertler, C. Ambrosch-Draxl and J. Fabian, *Band-structure topologies of graphene: Spin-orbit coupling effects from first principles*, Phys. Rev. B **80**, 235431 (2009).

[29] S. Reich, J. Maultzsch, C. Thomsen and P. Ordejón, *Tight-binding description of graphene*, Phys. Rev. B **66**, 035412 (2002).

[30] D. Huertas-Hernando, F. Guinea and A. Brataas, *Spin-orbit coupling in curved graphene, fullerenes, nanotubes, and nanotube caps*, Phys. Rev. B **74**, 155426 (2006).

[31] R. S. Deacon, K.-C. Chuang, R. J. Nicholas, K. S. Novoselov and A. K. Geim, *Cyclotron Resonance study of the electron and hole velocity in graphene monolayers*, Phys. Rev. B **76**, 081406 (2007).

[32] F. D. M. Haldane, *Model for a Quantum Hall Effect without Landau Levels: Condensed-Matter Realization of the "Parity Anomaly"*, Phys. Rev. Lett. **61**, 2015 (1988).

[33] G. W. Semenoff, *Condensed-Matter Simulation of a Three-Dimensional Anomaly*, Phys. Rev. Lett. **53**, 2449 (1984).

[34] J. W. McClure, *Diamagnetism of graphite*, Phys. Rev. **104**, 666 (1956).

[35] T. Kramer, C. Kreisbeck, V. Kruecki, E. J. Heller, R. E. Parrott and C.-T. Liang, *Theory of the quantum Hall effect in finite graphene devices*, Phys. Rev. B **81**, 81410(R) (2010).

[36] A. K. Geim and K. S. Novoselov, *The rise of graphene*, Nat. Mater. **6**, 183 (2007).

[37] T. M. Rusin and W. Zawadzki, *Zitterbewegung of electrons in graphene in a magnetic field*, Phys. Rev. B **78**, 125419 (2008).

[38] J. Schliemann, *Cyclotron motion in graphene*, New J. Phys. **10**, 43024 (2008).

[39] R. Saito, G. Dresselhaus and M. Dresselhaus, *Trigonal warping effect of carbon nanotubes*, Phys. Rev. B **61**, 2981 (2000).

[40] J. Schliemann, *Cyclotron motion and magnetic focusing in semiconductor quantum wells with spin-orbit coupling*, Phys. Rev. B **77**, 125303 (2008).

[41] A. Chaves, L. Covaci, K. Y. Rakhimov, G. A. Farias and F. M. Peeters, *Wave-packet dynamics and valley filter in strained graphene*, Phys. Rev. B **82**, 205430 (2010).

[42] H. Tal-Ezer and R. Kosloff, *An accurate and efficient scheme for propagating the time dependent Schrödinger equation*, J. Chem. Phys. **81**, 3967 (1984).

[43] M. D. Feit, J. A. Fleck Jr. and A. Steiger, *Solution of the Schrödinger equation by a spectral method*, J. Comput. Phys. **47**, 412 (1982).

[44] T. Kramer, E. J. Heller and R. E. Parrott, *An efficient and accurate method to obtain the energy-dependent Green function for general potentials*, J. Phys.: Conf. Ser. **99**, 12010 (2008).

[45] W. Zawadzki and T. M. Rusin, *Zitterbewegung (trembling motion) of electrons in semiconductors: a review.*, J. Phys.: Cond. Mat. **23**, 143201 (2011).

[46] J. Parker and C. R. Stroud Jr., *Coherence and decay of Rydberg wave Packets*, Phys. Rev. Lett. **56**, 716 (1986).

[47] A. ten Wolde, L. D. Noordam, A. Lagendijk and H. B. van Linden van den Heuvell, *Observation of Radially Localized Atomic Electron Wave Packets*, Phys. Rev. Lett. **61**, 2099 (1988).

[48] J. A. Yeazell, M. Mallalieu and C. R. Stroud Jr., *Observation of the collapse and revival of a Rydberg electronic wave packet*, Phys. Rev. Lett. **64**, 2007 (1990).

[49] R. W. Robinett, *Quantum wave packet revivals*, Phys. Rep. **392**, 1 (2004).

[50] I. S. Averbukh and N. F. Perelman, *Fractional revivals: Universality in the long-term evolution of quantum wave packets beyond the correspondence principle dynamics*, Phys. Lett. A **139**, 449 (1989).

[51] Z. D. Gaeta and C. R. Stroud Jr., *Classical and quantum-mechanical dynamics of a quasiclassical state of the hydrogen atom*, Phys. Rev. A **42**, 6308 (1990).

[52] S. D. Boris, S. Brandt, H. D. Dahmen, T. Stroh and M. L. Larsen, *Quantum-mechanical motion of Gaussian wave packets on elliptical and hyperbolic Kepler orbits in the Coulomb field*, Phys. Rev. A **48**, 2574 (1993).

[53] C. Leichtle, I. S. Averbukh and W. P. Schleich, *Generic Structure of Multilevel Quantum Beats*, Phys. Rev. Lett. **77**, 3999 (1996).

[54] J. Wals, H. H. Fielding, J. F. Christian, L. C. Snoek, W. J. van der Zande and H. B. van Linden van den Heuvell, *Observation of Rydberg wave packet dynamics in a Coulombic and magnetic field*, Phys. Rev. Lett. **72**, 3783 (1994).

[55] W. Merkel, I. S. Averbukh, B. Girard, G. G. Paulus and W. P. Schleich, *Factorization of numbers with physical systems*, Fortschr. Phys. **54**, 856 (2006).

[56] M. Štefaňák, W. Merkel, W. P. Schleich, D. Haase and H. Maier, *Factorization with Gauss sums: scaling properties of ghost factors*, New J. Phys. **9**, 370 (2007).

[57] M. Mehring, K. Müller, I. Averbukh, W. Merkel and W. Schleich, *NMR Experiment Factors Numbers with Gauss Sums*, Phys. Rev. Lett. **98**, 1 (2007).

[58] M. Gilowski, T. Wendrich, T. Müller, C. Jentsch, W. Ertmer, E. Rasel and W. Schleich, *Gauss Sum Factorization with Cold Atoms*, Phys. Rev. Lett. **100**, 1 (2008).

[59] D. Bigourd, B. Chatel, W. Schleich and B. Girard, *Factorization of Numbers with the Temporal Talbot Effect: Optical Implementation by a Sequence of Shaped Ultrashort Pulses*, Phys. Rev. Lett. **100**, 1 (2008).

[60] S. Das Sarma, S. Adam, E. H. Hwang and E. Rossi, *Electronic transport in two dimensional graphene*, Rev. Mod. Phys. **83**, 407 (2011).

[61] K. I. Bolotin, K. J. Sikes, J. Hone, H. L. Stormer and P. Kim, *Temperature-Dependent Transport in Suspended Graphene*, Phys. Rev. Lett. **101**, 96802 (2008).

[62] C. R. Dean *et al.*, *Boron nitride substrates for high-quality graphene electronics*, Nat. Nano **5**, 722 (2010).

[63] T. O. Wehling, S. Yuan, A. I. Lichtenstein, A. K. Geim and M. I. Katsnelson, *Resonant Scattering by Realistic Impurities in Graphene*, Phys. Rev. Lett. **105**, 056802 (2010).

[64] O. V. Yazyev and S. G. Louie, *Electronic transport in polycrystalline graphene*, Nat. Mater. **9**, 806 (2010).

[65] A. Fasolino, J. H. Los and M. I. Katsnelson, *Intrinsic ripples in graphene*, Nat. Mater. **6**, 858 (2007).

[66] P. E. Lammert and V. H. Crespi, *Geometrical perturbation of graphene electronic structure*, Phys. Rev. B **61**, 7308 (2000).

[67] A. Cortijo and M. A. H. Vozmediano, *Electronic properties of curved graphene sheets*, EPL **77**, 47002 (2007).

[68] N. Levy, S. A. Burke, K. L. Meaker, M. Panlasigui, A. Zettl, F. Guinea, A. H. Castro Neto and M. F. Crommie, *Strain-induced pseudo-magnetic fields greater than 300 tesla in graphene nanobubbles.*, Science **329**, 544 (2010).

[69] A. Rycerz, J. Tworzydło and C. W. J. Beenakker, *Anomalously large conductance fluctuations in weakly disordered graphene*, EPL **79**, 57003 (2007).

[70] C. H. Lewenkopf, E. R. Mucciolo and A. H. Castro Neto, *Numerical studies of conductivity and Fano factor in disordered graphene*, Phys. Rev. B **77**, 081410(R) (2008).

[71] J. Wurm, M. Wimmer and K. Richter, *Symmetries and the conductance of graphene nanoribbons with long-range disorder*, Phys. Rev. B **85**, 245418 (2012).

[72] Y. Adamov, I. V. Gornyi and A. D. Mirlin, *Loschmidt echo and Lyapunov exponent in a quantum disordered system*, Phys. Rev. E **67**, 56217 (2003).

[73] M. F. Gelin, D. Egorova and W. Domcke, *Efficient Calculation of Time- and Frequency-Resolved Four-Wave-Mixing Signals*, Acc. Chem. Res. **42**, 1290 (2009).

[74] A. L. Cavalieri *et al.*, *Intense 1.5-cycle near infrared laser waveforms and their use for the generation of ultra-broadband soft-x-ray harmonic continua*, New J. Phys. **9**, 242 (2007).

[75] E. Goulielmakis *et al.*, *Single-cycle nonlinear optics.*, Science **320**, 1614 (2008).

[76] S. Haessler *et al.*, *Attosecond imaging of molecular electronic wavepackets*, Nat. Phys. **6**, 200 (2010).

[77] T. Brabec and F. Krausz, *Intense few-cycle laser fields: Frontiers of nonlinear optics*, Rev. Mod. Phys. **72**, 545 (2000).

[78] F. Krausz, *Attosecond physics*, Rev. Mod. Phys. **81**, 163 (2009).

[79] C. Lanczos, *An iteration method for the solution of the eigenvalue problem of linear differential and integral operators*, J. Res. Natl. Bur. Stand. **45**, 255 (1950).

[80] D. Bauer, D. B. Milošević and W. Becker, *Strong-field approximation for intense-laser–atom processes: The choice of gauge*, Phys. Rev. A **72**, 023415 (2005).

[81] D. Xiao, W. Yao and Q. Niu, *Valley-Contrasting Physics in Graphene: Magnetic Moment and Topological Transport*, Phys. Rev. Lett. **99**, 236809 (2007).

[82] J. Stoer and R. Bulirsch, *Introduction to Numerical Analysis* (Springer, New York, 2002).

[83] L. Seidner, G. Stock and W. Domcke, *Nonperturbative approach to femtosecond spectroscopy: General theory and application to multidimensional nonadiabatic photoisomerization processes*, J. Chem. Phys. **103**, 3998 (1995).

[84] W. T. Pollard and R. A. Mathies, *Analysis of femtosecond dynamic absorption spectra of nonstationary states*, Annu. Rev. Phys. Chem. **43**, 497 (1992).

[85] S. Mukamel, *Principles of Nonlinear Optical Spectroscopy*, *Oxford series on optical sciences* (Oxford University Press, New York, 1999).

[86] W. Domcke and G. Stock, *Theory of Ultrafast Nonadiabatic Excited-State Processes and their Spectroscopic Detection in Real Time*, Adv. Chem. Phys. **100**, 1 (1997).

[87] S. Meyer and V. Engel, *Non-perturbative wave-packet calculations of time-resolved four-wave-mixing signals*, Appl. Phys. B **71**, 293 (2000).

[88] M. F. Gelin, D. Egorova and W. Domcke, *Efficient method for the calculation of time- and frequency-resolved four-wave mixing signals and its application to photon-echo spectroscopy*, J. Chem. Phys. **123**, 164112 (2005).

[89] A. V. Pisliakov, T. Mancal and G. R. Fleming, *Two-dimensional optical three-pulse photon echo spectroscopy. II. Signatures of coherent electronic motion and exciton population transfer in dimer two-dimensional spectra*, J. Chem. Phys. **124**, 234505 (2006).

[90] L. Pfeiffer, K. W. West, H. L. Stormer and K. W. Baldwin, *Electron mobilities exceeding 107 cm2/V s in modulation-doped GaAs*, Appl. Phys. Lett. **55**, 1888 (1989).

[91] S. Datta, *Electronic Transport in Mesoscopic Systems*, *Cambridge Studies in Semiconductor Physics and Microelectronic Engineering* (Cambridge University Press, Cambridge, 1995).

[92] E. Schrödinger, *Quantisierung als Eigenwertproblem (Erste Mitteilung)*, Ann. Phys. **79**, 361 (1926).

[93] E. Schrödinger, *Quantisierung als Eigenwertproblem. 2. Mitteilung*, Ann. Phys. **79**, 489 (1926).

[94] P. A. M. Dirac, *On the theory of quantum mechanics*, Proc. R. Soc. Lond. A **112**, 661 (1926).

[95] J. M. Luttinger and K. W, *Motion of Electrons and Holes in Pertubed Periodic Fields*, Phys. Rev. **97**, 869 (1955).

[96] M. Wimmer and K. Richter, *Optimal block-tridiagonalization of matrices for coherent charge transport*, J. Comput. Phys. **228**, 8548 (2009).

[97] J. W. Cooley and J. W. Tukey, *An Algorithm for the Machine Calculation Complex Fourier Series*, Math. Comp. **19**, 297 (1965).

[98] H. Nielsen, *Absence of neutrinos on a lattice (I). Proof by homotopy theory*, Nucl. Phys. B **185**, 20 (1981).

[99] H. Tal-Ezer, *Polynomial Approximation of Functions of Matrices and Applications*, J. Scient. Comput. **4**, 25 (1989).

[100] R. Kosloff, *Propagation methods for quantum molecular dynamics*, Annu. Rev. Phys. Chem. **45**, 145 (1994).

[101] G. Faber, *Über polynomische Entwickelungen*, Math. Ann. **57**, 389 (1903).

[102] W. Huisinga, L. Pesce, R. Kosloff and P. Saalfrank, *Faber and Newton polynomial integrators for open-system density matrix propagation*, J. Chem. Phys. **110**, 5538 (1999).

[103] A. Nauts and R. E. Wyatt, *New approach to many-state quantum dynamics: The recursive-residue-generation method*, Phys. Rev. Lett. **51**, 2238 (1983).

[104] T. J. Park and J. C. Light, *Unitary quantum time evolution by iterative Lanczos reduction*, J. Chem. Phys. **85**, 5870 (1986).

[105] M. Hochbruck and C. Lubich, *On Krylov subspace approximations to the matrix exponential operator*, SIAM J. Numer. Anal. **34**, 1911 (1997).

[106] W. E. Arnoldi, *The Principle of Minimized Iterations in the Solution of the Matrix Eigenvalue Problem*, Quart. Appl. Math. **9**, 17 (1951).

[107] Y. Saad and M. H. Schultz, *GMRES: A Generalized Minimal Residual Algorithm for Solving Nonsymmetric Linear Systems*, SIAM J. Sci. Stat. Comput. **7**, 856 (1986).

[108] D. J. Tannor and D. E. Weeks, *Wave packet correlation function formulation of scattering theory: The quantum analog of classical S-matrix theory*, J. Chem. Phys. **98**, 3884 (1993).

[109] J. R. Taylor, *Scattering Theory: The Quantum Theory of Nonrelativistic Collisions* (John Wiley & Sons, New York, 1972).

[110] J. E. Bresenham, *Algorithm for computer control of a digital plotter*, IBM Systems Journal **4**, 25 (1965).

[111] R. B. Lehoucq and D. C. Sorensen, *Deflation techniques for an implicitly restarted Arnoldi iteration*, SIAM J. Matrix Anal. Appl. **17**, 789 (1996).

[112] M. Wimmer, I. Adagideli, S. Berber, D. Tomanek and K. Richter, *Spin Currents in Rough Graphene Nanoribbons: Universal Fluctuations and Spin Injection*, Phys. Rev. Lett. **100**, 177207 (2008).

[113] A. Rycerz, J. Tworzydło and C. W. J. Beenakker, *Valley filter and valley valve in graphene*, Nature Physics **3**, 172 (2007).

[114] A. R. Akhmerov, J. H. Bardarson, A. Rycerz and C. W. J. Beenakker, *Theory of the valley-valve effect in graphene nanoribbons*, Phys. Rev. B **77**, 205416 (2008).

[115] F. Bloch, *Über die Quantenmechanik der Elektronen in Kristallgittern*, Z. Phys. A **52**, 555 (1929).

[116] C. Zener, *A Theory of the Electrical Breakdown of Solid Dielectrics*, Proc. R. Soc. Lond. A **145**, 523 (1934).

[117] J. Feldmann, K. Leo, J. Shah, D. A. B. Miller, J. E. Cunningham, T. Meier, G. von Plessen, A. Schulze, P. Thomas and S. Schmitt-Rink, *Optical investigation of Bloch oscillations in a semiconductor superlattice*, Phys. Rev. B **46**, 7252 (1992).

[118] K. Leo, P. H. Bolivar, F. Brüggemann, R. Schwedler and K. Köhler, *Observation of Bloch oscillations in a semiconductor superlattice*, Solid State Commun. **84**, 943 (1992).

[119] C. Waschke, H. G. Roskos, R. Schwedler, K. Leo, H. Kurz and K. Köhler, *Coherent submillimeter-wave emission from Bloch oscillations in a semiconductor superlattice*, Phys. Rev. Lett. **70**, 3319 (1993).

[120] M. B. Dahan, E. Peik, J. Reichel, Y. Castin and C. Salomon, *Bloch Oscillations of Atoms in an Optical Potential*, Phys. Rev. Lett. **76**, 4508 (1996).

[121] S. R. Wilkinson, C. F. Bharucha, K. W. Madison, Q. Niu and M. G. Raizen, *Observation of Atomic Wannier-Stark Ladders in an Accelerating Optical Potential*, Phys. Rev. Lett. **76**, 4512 (1996).

[122] T. Pertsch, P. Dannberg, W. Elflein, A. Bräuer and F. Lederer, *Optical Bloch Oscillations in Temperature Tuned Waveguide Arrays*, Phys. Rev. Lett. **83**, 4752 (1999).

[123] R. Morandotti, U. Peschel, J. S. Aitchison, H. S. Eisenberg and Y. Silberberg, *Experimental Observation of Linear and Nonlinear Optical Bloch Oscillations*, Phys. Rev. Lett. **83**, 4756 (1999).

[124] H. Sanchis-Alepuz, Y. A. Kosevich and J. Sánchez-Dehesa, *Acoustic Analogue of Electronic Bloch Oscillations and Resonant Zener Tunneling in Ultrasonic Superlattices*, Phys. Rev. Lett. **98**, 134301 (2007).

[125] H. Fukuyama, R. A. Bari and H. C. Fogedby, *Tightly bound electrons in a uniform electric field*, Phys. Rev. B **8**, 5579 (1973).

[126] J. Rotvig, A.-P. Jauho and H. Smith, *Bloch Oscillations, Zener Tunneling, and Wannier-Stark Ladders in the Time Domain*, Phys. Rev. Lett. **74**, 1831 (1995).

[127] D. W. Hone and X.-G. Zhao, *Time-periodic behavior of multiband superlattices in static electric fields*, Phys. Rev. B **53**, 4834 (1996).

[128] B. M. Breid, D. Witthaut and H. J. Korsch, *Bloch-Zener oscillations*, New J. Phys. **8**, 110 (2006).

[129] B. M. Breid, D. Witthaut and H. J. Korsch, *Manipulation of matter waves using Bloch and Bloch-Zener oscillations*, New J. Phys. **9**, 62 (2007).

[130] P. Abumov and D. W. L. Sprung, *Interminiband Rabi oscillations in biased semiconductor superlattices*, Phys. Rev. B **75**, 165421 (2007).

[131] Y. Shimada, N. Sekine and K. Hirakawa, *Terahertz emission due to interminiband resonant Zener tunneling in wide-miniband GaAs/Al0.3Ga0.7As superlattices*, Appl. Phys. Lett. **84**, 4926 (2004).

[132] F. Dreisow, A. Szameit, M. Heinrich, T. Pertsch, S. Nolte, A. Tünnermann and S. Longhi, *Bloch-Zener Oscillations in Binary Superlattices*, Phys. Rev. Lett. **102**, 76802 (2009).

[133] S. Kling, T. Salger, C. Grossert and M. Weitz, *Atomic Bloch-Zener Oscillations and Stückelberg Interferometry in Optical Lattices*, Phys. Rev. Lett. **105**, 215301 (2010).

[134] C.-H. Park, L. Yang, Y.-W. Son, M. L. Cohen and S. G. Louie, *New Generation of Massless Dirac Fermions in Graphene under External Periodic Potentials*, Phys. Rev. Lett. **101**, 126804 (2008).

[135] M. Barbier, P. Vasilopoulos and F. M. Peeters, *Extra Dirac points in the energy spectrum for superlattices on single-layer graphene*, Phys. Rev. B **81**, 75438 (2010).

[136] L. Brey and H. A. Fertig, *Emerging Zero Modes for Graphene in a Periodic Potential*, Phys. Rev. Lett. **103**, 46809 (2009).

[137] G. J. Ferreira, M. N. Leuenberger, D. Loss and J. C. Egues, *Low Bias Negative Differential Resistance in Graphene Nanoribbon Superlattices*, Phys. Rev. B **84**, 125453 (2011).

[138] T. Hartmann, F. Keck, H. J. Korsch and S. Mossmann, *Dynamics of Bloch oscillations*, New J. Phys. **6**, 2 (2004).

[139] K. Nakada, M. Fujita, G. Dresselhaus and M. S. Dresselhaus, *Edge state in graphene ribbons: Nanometer size effect and edge shape dependence*, Phys. Rev. B **54**, 17954 (1996).

[140] L. D. Landau, *On the theory of transfer of energy at collisions II*, Phys. Z. Sowjetunion **2**, 46 (1932).

[141] C. Zener, *Non-adiabatic crossing of energy levels*, Proc. R. Soc. Lond. A **137**, 696 (1932).

[142] E. C. G. Stueckelberg, *Theorie der unelastischen Stosse zwischen Atomen*, Helv. Phys. Acta **5**, 369 (1932).

[143] M. Y. Han, J. C. Brant and P. Kim, *Electron Transport in Disordered Graphene Nanoribbons*, Phys. Rev. Lett. **104**, 56801 (2010).

[144] M. Büttiker, Y. Imry, R. Landauer and S. Pinhas, *Generalized many-channel conductance formula with application to small rings*, Phys. Rev. B **31**, 6207 (1985).

[145] J. H. Shirley, *Solution of the Schrödinger equation with a Hamiltonian periodic in time*, Phys. Rev. **138**, B979 (1965).

[146] S. Kohler, J. Lehmann and P. Hänggi, *Driven quantum transport on the nanoscale*, Phys. Rep. **406**, 379 (2005).

[147] L. Tarruell, D. Greif, T. Uehlinger, G. Jotzu and T. Esslinger, *Creating, moving and merging Dirac points with a Fermi gas in a tunable honeycomb lattice*, Nature **483**, 302 (2012).

[148] S. Murakami, N. Nagaosa and S.-C. Zhang, *Spin-Hall Insulator*, Phys. Rev. Lett. **93**, 156804 (2004).

[149] A. Altland and M. R. Zirnbauer, *Nonstandard symmetry classes in mesoscopic normal-superconducting hybrid structures*, Phys. Rev. B **55**, 1142 (1997).

[150] Y. Yao, F. Ye, X.-L. Qi, S.-C. Zhang and Z. Fang, *Spin-orbit gap of graphene: First-principles calculations*, Phys. Rev. B **75**, 041401(R) (2007).

[151] B. A. Bernevig and S.-C. Zhang, *Quantum Spin Hall Effect*, Phys. Rev. Lett. **96**, 106802 (2006).

[152] S. Murakami, *Quantum Spin Hall Effect and Enhanced Magnetic Response by Spin-Orbit Coupling*, Phys. Rev. Lett. **97**, 236805 (2006).

[153] C. Liu, T. Hughes, X.-L. Qi, K. Wang and S.-C. Zhang, *Quantum Spin Hall Effect in Inverted Type-II Semiconductors*, Phys. Rev. Lett. **100**, 236601 (2008).

[154] A. Roth, C. Brüne, H. Buhmann, L. W. Molenkamp, J. Maciejko, X.-L. Qi and S.-C. Zhang, *Nonlocal Transport in the Quantum Spin Hall State*, Science **325**, 294 (2009).

[155] I. Knez, R.-R. Du and G. Sullivan, *Evidence for Helical Edge Modes in Inverted InAs/GaSb Quantum Wells*, Phys. Rev. Lett. **107**, 136603 (2011).

[156] L. Fu, C. L. Kane and E. J. Mele, *Topological Insulators in Three Dimensions*, Phys. Rev. Lett. **98**, 106803 (2007).

[157] L. Fu and C. L. Kane, *Topological insulators with inversion symmetry*, Phys. Rev. B **76**, 45302 (2007).

[158] D. Hsieh *et al.*, *Observation of unconventional quantum spin textures in topological insulators*, Science **323**, 919 (2009).

[159] H. Beidenkopf, P. Roushan, J. Seo, L. Gorman, I. Drozdov, Y. S. Hor, R. J. Cava and A. Yazdani, *Spatial fluctuations of helical Dirac fermions on the surface of topological insulators*, Nat. Phys. **7**, 939 (2011).

[160] D.-X. Qu, Y. S. Hor, J. Xiong, R. J. Cava and N. P. Ong, *Quantum Oscillations and Hall Anomaly of Surface States in the Topological Insulator Bi_2Te_3*, Science **329**, 821 (2010).

[161] F. Xiu *et al.*, *Manipulating surface states in topological insulator nanoribbons*, Nat. Nano **6**, 216 (2011).

[162] X.-L. Qi and S.-C. Zhang, *Topological insulators and superconductors*, Rev. Mod. Phys. **83**, 1057 (2011).

[163] C. Brüne, A. Roth, E. G. Novik, M. M. König, H. Buhmann, E. M. Hankiewicz, W. Hanke, J. Sinova and L. W. Molenkamp, *Evidence for the ballistic intrinsic spin Hall effect in HgTe nanostructures*, Nat. Phys. **6**, 448 (2010).

[164] R. Dornhaus and G. Nimtz, *"The properties and applications of the HgCdTe alloy system" Springer Tracts in Modern Physics: Narrow-gap semiconductors* (Springer, Berlin, 1983), S. 119–281.

[165] K. C. Hass, H. Ehrenreich and B. Velický, *Electronic structure of HgCdTe*, Phys. Rev. B **27**, 1088 (1983).

[166] P. Carrier and S.-H. Wei, *Calculated spin-orbit splitting of all diamondlike and zinc-blende semiconductors: Effects of p½ local orbitals and chemical trends*, Phys. Rev. B **70**, 035212 (2004).

[167] M. König, H. Buhmann, L. W. Molenkamp, T. L. Hughes, C.-X. Liu, X.-L. Qi and S.-C. Zhang, *The Quantum Spin Hall Effect: Theory and Experiment*, J. Phys. Soc. Jpn. **77**, 31007 (2008).

[168] E. Novik, A. Pfeuffer-Jeschke, T. Jungwirth, V. Latussek, C. Becker, G. Landwehr, H. Buhmann and L. W. Molenkamp, *Band structure of semimagnetic Hg1−yMnyTe quantum wells*, Phys. Rev. B **72**, (2005).

[169] R. Winkler, *Springer Tracts in Modern Physics: Spin-orbit Coupling Effects in Two-Dimensional Electron and Hole Systems* (Springer, Berlin, 2003).

[170] N. A. Cade, *Quantum well bound states of HgTe in CdTe*, J. Phys. C: Solid State Phys. **18**, 5135 (1985).

[171] O. A. Pankratov, S. V. Pakhomov and B. A. Volkov, *Supersymmetry in heterojunctions: Band-inverting contact on the basis of PbSnTe and HgCdTe*, Solid State Commun. **61**, 93 (1987).

[172] P.-O. Löwdin, *A Note on the Quantum-Mechanical Perturbation Theory*, J. Chem. Phys. **19**, 1396 (1951).

[173] B. A. Volkov and O. A. Pankratov, *Two-dimensional massless electrons in an inverted contact*, JETP Lett. **42**, 178 (1985).

[174] G. Dresselhaus, *Spin-Orbit Coupling Effects in Zinc Blende Structures*, Phys. Rev. **100**, 580 (1955).

[175] Y. A. Bychkov and E. I. Rashba, *Properties of a 2D electron gas with lifted spectral degeneracy*, JETP Lett. **39**, 78 (1984).

[176] D. G. Rothe, R. W. Reinthaler, C.-X. Liu, L. W. Molenkamp, S.-C. Zhang and E. M. Hankiewicz, *Fingerprint of different spin-orbit terms for spin transport in HgTe quantum wells*, New J. Phys. **12**, 65012 (2010).

[177] J. Maciejko, T. L. Hughes and S.-C. Zhang, *The Quantum Spin Hall Effect*, Annu. Rev. Condens. Matter Phys. **2**, 31 (2011).

[178] M. Büttiker, *Absence of backscattering in the quantum Hall effect in multiprobe conductors*, Phys. Rev. B **38**, 9375 (1988).

[179] S. Datta and B. Das, *Electronic analog of the electro-optic modulator*, Appl. Phys. Lett. **56**, 665 (1990).

[180] G. Schmidt, D. Ferrand, L. W. Molenkamp, A. T. Filip and B. J. van Wees, *Fundamental obstacle for electrical spin injection from a ferromagnetic metal into a diffusive semiconductor*, Phys. Rev. B **62**, 4790 (2000).

[181] J. Maciejko, E.-A. Kim and X.-L. Qi, *Spin Aharonov-Bohm effect and topological spin transistor*, Phys. Rev. B **82**, 195409 (2010).

[182] F. Dolcini, *Full electrical control of charge and spin conductance through interferometry of edge states in topological insulators*, Phys. Rev. B **83**, 165304 (2011).

[183] L. B. Zhang, F. Cheng, F. Zhai and K. Chang, *Electrical switching of the edge channel transport in HgTe quantum wells with an inverted band structure*, Phys. Rev. B **83**, 81402 (2011).

[184] A. Medhi and V. B. Shenoy, *Continuum theory of edge states of topological insulators: variational principle and boundary conditions*, J. Phys.: Cond. Mat. **24**, 355001 (2012).

[185] B. Zhou, H.-Z. Lu, R.-L. Chu, S.-Q. Shen and Q. Niu, *Finite Size Effects on Helical Edge States in a Quantum Spin-Hall System*, Phys. Rev. Lett. **101**, 246807 (2008).

[186] J. H. Davies, *The Physics of Low-Dimensional Semiconductors* (Cambridge University Press, New York, 1998).

[187] J. Viana Gomes, N. M. R. Peres and J. V. Gomes, *Tunneling of Dirac electrons through spatial regions of finite mass*, J. Phys.: Cond. Mat. **20**, 325221 (2008).

[188] B. J. van Wees, H. van Houten, C. W. J. Beenakker, J. G. Williamson, L. P. Kouwenhoven, D. van der Marel and C. T. Foxon, *Quantized conductance of point contacts in a two-dimensional electron gas*, Phys. Rev. Lett. **60**, 848 (1988).

[189] R. A. Webb, S. Washburn, C. P. Umbach and R. B. Laibowitz, *Observation of h/e Aharonov-Bohm oscillations in normal-metal rings*, Phys. Rev. Lett. **54**, 2696 (1985).

[190] E. Abrahams, P. W. Anderson, D. C. Licciardello and T. V. Ramakrishnan, *Scaling theory of localization: Absence of quantum diffusion in two dimensions*, Phys. Rev. Lett. **42**, 673 (1979).

[191] B. L. Altshuler, D. Khmel'Nitzkii, A. I. Larkin and P. A. Lee, *Magnetoresistance and Hall effect in a disordered two-dimensional electron gas*, Phys. Rev. B **22**, 5142 (1980).

[192] Y. Kawaguchi and S. Kawaji, *Negative Magnetoresistance in Silicon (100) MOS Inversion Layers*, J. Phys. Soc. Jpn. **48**, 699 (1980).

[193] M. P. van Albada and A. Lagendijk, *Observation of weak localization of light in a random medium*, Phys. Rev. Lett. **55**, 2692 (1985).

[194] E. Larose, L. Margerin, B. van Tiggelen and M. Campillo, *Weak Localization of Seismic Waves*, Phys. Rev. Lett. **93**, 048501 (2004).

[195] G. Bayer and T. Niederdränk, *Weak localization of acoustic waves in strongly scattering media*, Phys. Rev. Lett. **70**, 3884 (1993).

[196] F. Jendrzejewski, K. Müller, J. Richard, A. Date, T. Plisson, P. Bouyer, A. Aspect and V. Josse, *Coherent Backscattering of Ultracold Atoms*, Phys. Rev. Lett. **109**, 195302 (2012).

[197] E. B. Olshanetsky, Z. D. Kvon, G. M. Gusev, N. N. Mikhailov, S. A. Dvoretsky and J. C. Portal, *Weak antilocalization in HgTe quantum wells near a topological transition*, JETP Letters **91**, 347 (2010).

[198] G. M. Minkov, A. V. Germanenko, O. E. Rut, A. A. Sherstobitov, S. A. Dvoretski and N. N. Mikhailov, *Weak antilocalization in HgTe quantum well with inverted energy spectrum*, Phys. Rev. B **85**, 235312 (2012).

[199] G. Tkachov and E. M. Hankiewicz, *Weak antilocalization in HgTe quantum wells and topological surface states: Massive versus massless Dirac fermions*, Phys. Rev. B **84**, 035444 (2011).

[200] H.-Z. Lu and S.-Q. Shen, *Weak localization of bulk channels in topological insulator thin films*, Phys. Rev. B **84**, 125138 (2011).

[201] I. Garate and L. Glazman, *Weak localization and antilocalization in topological insulator thin films with coherent bulk-surface coupling*, Phys. Rev. B **86**, 035422 (2012).

[202] H.-T. He, G. Wang, T. Zhang, I.-K. Sou, G. Wong, J.-N. Wang, H.-Z. Lu, S.-Q. Shen and F.-C. Zhang, *Impurity Effect on Weak Antilocalization in the Topological Insulator Bi_{2}Te_{3}*, Phys. Rev. Lett. **106**, 166805 (2011).

[203] M. Liu *et al.*, *Crossover between Weak Antilocalization and Weak Localization in a Magnetically Doped Topological Insulator*, Phys. Rev. Lett. **108**, 036805 (2012).

[204] G. Bergmann, *Weak localization in thin films: a time-of-flight experiment with conduction electrons*, Phys. Rep. **107**, 1 (1984).

[205] S. Chakravarty and A. Schmid, *Weak localization: The quasiclassical theory of electrons in a random potential*, Phys. Rep. **140**, 1986 (1986).

[206] C. W. J. Beenakker, *Random-matrix theory of quantum transport*, Rev. Mod. Phys. **69**, 731 (1997).

[207] R. Landauer, *Electrical resistance of disordered one-dimensional lattices*, Philosophical Magazine **21**, 863 (1970).

[208] D. S. Fisher and P. A. Lee, *Relation between conductivity and transmission matrix*, Phys. Rev. B **23**, 6851 (1981).

[209] M. V. Berry, *Quantal phase factors accompanying adiabatic changes*, Proc. R. Soc. Lond. A **392**, 45 (1984).

[210] M.-C. Chang and Q. Niu, *Berry phase, hyperorbits, and the Hofstadter spectrum: Semiclassical dynamics in magnetic Bloch bands.*, Phys. Rev. B **53**, 7010 (1996).

[211] H. Suzuura and T. Ando, *Crossover from Symplectic to Orthogonal Class in a Two-Dimensional Honeycomb Lattice*, Phys. Rev. Lett. **89**, 266603 (2002).

[212] E. McCann, K. Kechedzhi, V. I. Fal'ko, H. Suzuura, T. Ando and B. L. Altshuler, *Weak-Localization Magnetoresistance and Valley Symmetry in Graphene*, Phys. Rev. Lett. **97**, 146805 (2006).

[213] M. V. Berry and R. J. Mondragon, *Neutrino billiards: time-reversal symmetry-breaking without magnetic fields*, Proc. R. Soc. Lond. A **412**, 53 (1987).

[214] G. Sundaram and Q. Niu, *Wave-packet dynamics in slowly perturbed crystals: Gradient corrections and Berry-phase effects*, Phys. Rev. B **59**, 14915 (1999).

[215] M.-C. Chang and Q. Niu, *Berry phase, hyperorbits, and the Hofstadter spectrum*, Phys. Rev. Lett. **75**, 1348 (1995).

[216] B. Engquist and A. Majda, *Radiation boundary conditions for acoustic and elastic wave calculations*, Comm. on Pure and Appl. Math. **32**, 313 (1979).

[217] J.-P. Berenger, *A perfectly matched layer for the absorption of electromagnetic waves*, J. Chem. Phys. **114**, 185 (1994).

[218] B. Engquist and A. Majda, *Absorbing boundary conditions for numerical simulation of waves*, Math. Comp. **31**, 629 (1977).

[219] E. J. Heller, *The semiclassical way to molecular spectroscopy*, Acc. Chem. Res. **14**, 368 (1981).

[220] K. E. Aidala, R. E. Parrott, T. Kramer, E. J. Heller, R. M. Westervelt, M. P. Hanson and A. C. Gossard, *Imaging magnetic focusing of coherent electron waves*, Nat. Phys. **3**, 464 (2007).

List of Publications

2012 [1] **V. Krueckl** and K. Richter, *Probing the band topology of mercury telluride through weak localization and antilocalization*, special issue on "Topological Insulators", Semicond. Sci. Technol. **27**, 124006. [Chapter 8]

[2] **V. Krueckl** and K. Richter, *Switching spin and charge between edge states in topological insulator constrictions: a transer matrix approach*, Proc. SPIE 8461, Spintronics V, 84610Z. [Chapter 7]

[3] **V. Krueckl** and K. Richter, *Bloch-Zener oscillations in graphene and topological insulators*, Phys. Rev. B **85**, 115433. [Chapter 5]

2011 [4] **V. Krueckl** and K. Richter, *Switching Spin and Charge between Edge States in Topological Insulator Constrictions*, Phys. Rev. Lett. **107**, 086803. [Chapter 7]

[5] **V. Krueckl**, M. Wimmer, I. Adagideli, J. Kuipers and K. Richter, *Weak Localization in Mesoscopic Hole Transport: Berry Phases and Classical Correlations*, Phys. Rev. Lett. **106**, 146801.

2010 [6] T. Kramer, **V. Krueckl**, E. Heller and R. Parrott, *Self-consistent calculation of electric potentials in Hall devices*, Phys. Rev. B **81**, 205306.

[7] T. Kramer, C. Kreisbeck, **V. Krueckl**, E. Heller, R. Parrott and C.-T. Liang, *Theory of the quantum Hall effect in finite graphene devices*, Phys. Rev. B **81**, 081410.

[8] T. Kramer, C. Kreisbeck and **V. Krueckl**, *Wave packet approach to transport in mesoscopic systems*, Phys. Scr. **82**, 038101.

2009 [9] **V. Krueckl** and T. Kramer, *Revivals of quantum wave packets in graphene*, New J. Phys. **11**, 093010. [Chapter 3]

Acknowledgements

First and foremost, I would like to express my sincere gratitude to Prof. Dr. Klaus Richter for giving me the opportunity to work in his group and his support during my whole PhD period. He made it possible to pick very freely different fields of research, showed great trust in own ideas and encouraged their further development.

I also want to thank Dr. Tobias Kramer for introducing me to time-dependent physics, which allowed me to gain a deeper, more intuitive understanding of physical processes in general.

I would like to express my gratitude to Dr. İnanç Adagideli and Dr. Michael Wimmer for many fruitful discussions.

Over the past years, I have been sharing offices with various colleagues and want to thank Dr. Birgit Hein, Dr. Christoph Kreisbeck, Dr. Henri Saarikoski and Dr. Jürgen Wurm for a pleasant working atmosphere.

I am very grateful to my brother Markus Krückl for his patient revising of this thesis and Fedor Tkatschenko, Dr. Henri Saarikoski, Dr. Jack Kuipers, Jan Bundesmann, Josef Michl, Dr. Juan Diego Urbina, Lisa Hesse, Dr. Ming-Hao Liu, Sven Essert and Tobias Dollinger for proofreading my drafts.

I acknowledge the financial support from the Deutsche Forschungsgemeinschaft within GRK 1570 and the Emmy-Noether programme KR 2889-2/1.

Finally, I want to thank my parents Monika und Viktor for all the support during my years of study.